



5-1-2022

Mathematical Modeling Of Pre And Post Combustion Processes In Coal Power Plant

Ashish Pramod Kotwal

Follow this and additional works at: <https://commons.und.edu/theses>

Recommended Citation

Kotwal, Ashish Pramod, "Mathematical Modeling Of Pre And Post Combustion Processes In Coal Power Plant" (2022). *Theses and Dissertations*. 4271.
<https://commons.und.edu/theses/4271>

This Dissertation is brought to you for free and open access by the Theses, Dissertations, and Senior Projects at UND Scholarly Commons. It has been accepted for inclusion in Theses and Dissertations by an authorized administrator of UND Scholarly Commons. For more information, please contact und.common@library.und.edu.

MATHEMATICAL MODELING OF PRE AND POST COMBUSTION PROCESSES IN
COAL POWER PLANT

By

Ashish Kotwal

Bachelor of Engineering

University of Mumbai, 2013

Master of Science

University of North Dakota, 2017

A Dissertation

Submitted to the Graduate Faculty

of the

University of North Dakota

in partial fulfilment of the requirements

for the degree of

Doctor of Philosophy

Grand Forks, North Dakota

May 2022

Copyright 2022 Ashish Kotwal

Name: Ashish Pramod Kotwal
Degree: Doctor of Philosophy

This document, submitted in partial fulfillment of the requirements for the degree from the University of North Dakota, has been read by the Faculty Advisory Committee under whom the work has been done and is hereby approved.

DocuSigned by:
Michael Mann
Michael Mann

DocuSigned by:
Gautham Krishnamoorthy
Gautham Krishnamoorthy

DocuSigned by:
Daniel Laudal
Daniel Laudal

DocuSigned by:
Srivats Srinivasachar
Srivats Srinivasachar

DocuSigned by:
Clement Tang
Clement Tang

Name of Member 6 - delete if not needed

This document is being submitted by the appointed advisory committee as having met all the requirements of the School of Graduate Studies at the University of North Dakota and is hereby approved.

DocuSigned by:
Chris Nelson
Chris Nelson
Dean of the School of Graduate Studies

5/4/2022
Date

PERMISSION

Title Mathematical Modeling of Pre and Post combustion Processes in Coal Power Plant

Department Energy Engineering

Degree Doctor of Philosophy

In presenting this thesis in partial fulfillment of the requirements for a graduate degree from the University of North Dakota, I agree that the library of this University shall make it freely available for inspection. I further agree that permission for extensive copying for scholarly purposes may be granted by the professor who supervised my thesis work or, in their absence, by the chairperson of the department or the dean of the School of Graduate Studies. It is understood that any copying or publication or other use of this dissertation or part thereof for financial gain shall not be allowed without my written permission. It is also understood that due recognition shall be given to me and to the University of North Dakota in any scholarly use which may be made of any material in my thesis.

Name: Ashish Kotwal

Date: May 13, 2022

TABLE OF CONTENTS

TABLE OF CONTENTS.....	iv
LIST OF FIGURES	vii
LIST OF TABLE	xii
ACKNOWLEDGMENTS	xiii
ABSTRACT.....	xiv
NOMENCLATURE	xvii
1. INTRODUCTION	1
1.1 Coal Definition.....	1
1.2 Purpose.....	1
1.3 Does coal hold future then?.....	4
1.4 Pre- and Post- Combustion Technologies	4
1.4.1 Extractive Metallurgical Processes from Coal	5
1.4.2 Post-Combustion Carbon Capture Process.....	5
1.5 Key Takeaways from the Novel Technologies	6
1.6 Scope, Goals and Hypothesis	6
1.7 Objectives to Achieve	7
1.8 Research Significance	9
2. LITERATURE REVIEW	11
2.1 REE Recovery via Hydrometallurgical Extractions.....	11
2.1.1 REE Extraction Resources.....	13
2.1.2 REE Recovery Using Aqueous Resources	16
2.2 Rare Earths Separation Technologies	21
2.3 Rare Earth Metallization Technologies.....	25
2.4 Carbon Dioxide Capture Technologies	29
2.4.1 Process Modeling Studies.....	34
2.4.2 Numerical Modeling Studies	37
3. RARE EARTH ELEMENTS PROCESS MODELING.....	39
3.1 Process Modeling Using METSIM	40
3.1.1 METSIM Unit Operations	48
3.2 Results and Discussion.....	50

3.2.1	UND Process for Hydrometallurgical Extraction of REE.....	51
3.2.1.1	Lab-Scale Testing of H-Bed Lignite Coal	51
3.2.1.2	Bench-Scale Parametric Testing of H-Bed lignite coal	55
3.2.2	Semi-continuous UND Process modification.....	59
3.2.2.1	Semi-Continuous Testing on Bench-Scale with H-Bed Lignite Coal	62
3.2.3	UND Process Modeling of REE Extraction	67
3.2.3.1	Process Modeling Diagrams	67
3.3	Conclusion.....	85
4.	CO ₂ CAPTURE MODELING	86
4.1	Introduction: Past CO ₂ Modeling efforts	86
4.2	Presented multiphase CFD modeling.....	87
4.2.1	Surface forces and their implementation	91
4.2.2	Film layer mass transfer modeling and implementation	93
4.3	Multiphase modeling setup	95
4.3.1	Introduction to Packings with Numerical Strategies	95
4.3.2	OpenFOAM file structure and introduction	97
4.3.3	OpenFOAM hydrodynamics problem setup.....	100
4.3.3.1	Geometrical development	100
4.3.3.2	Discretization Grid Algorithm Development.....	103
4.3.3.3	Computational Solver Development.....	107
4.3.3.3.1	Single-Phase Flow Study Solver Setup.....	107
4.3.3.3.2	Multiphase Flow Solver and Case Advancement	110
4.4	Results and Discussions	118
4.4.1	OpenFOAM Computational Environment Creation.....	118
4.4.1.1	Single-Phase Simulations.....	119
4.4.1.2	Multiphase Simulations	120
4.4.2	3D REU Multiphase Flow Hydrodynamics.....	123
4.4.3	Grid Independent test.....	124
4.4.4	Transient flow with hybrid BCs	126
4.4.5	Effect of Solvent Properties.....	127
4.4.6	Code-to-Code Comparison & Simplified Geometric Modeling.....	133
4.4.7	Comparison with Existing Correlations	140

4.5	Conclusion.....	142
5.	OVERALL CONCLUSION AND FUTURE WORK.....	144
5.1	UND Hydrometallurgical Process Synopsis	144
5.2	Current Work in Process Modeling.....	146
5.3	Future Work in Process Modeling Required.....	147
5.4	Current Numerical Modeling Status	149
5.5	Future Work in CO₂ Capture CFD Analysis	150
5.6	Efficient Coal Power Plants	152
	BIBLIOGRAPHY	155
	APPENDIX A.....	171
	APPENDIX B.	178
	APPENDIX C.	198

LIST OF FIGURES

<i>Figure 1.1: 2019 CO₂ Emissions from Fossil Fuel Combustion by Sector and Fuel Type (EPA, 2020) [1].....</i>	2
<i>Figure 1.2: A graph from 2020 Annual energy outlook report showing comparisons of sources for energy generation (energy information admin, 2020) [2].....</i>	3
<i>Figure 2.1: Simplified Recycling flowsheet of rare earth magnets. [32] [38].....</i>	15
<i>Figure 2.2: Leaching Processes used in Baotou rare earth complex in China Simplified flowsheet [29].....</i>	18
<i>Figure 2.3: A multistep leaching process developed by OSRAM to recover rare earth metals present in the phosphor powder [48].....</i>	21
<i>Figure 2.4: The figure showing Three stage counter current extraction in a mixer settler set up [50].....</i>	24
<i>Figure 2.5: The first figure showing solubility data presented in terms of graph rare earth oxides in fluorides molten salts, the second figure shows Nd₂O₃ solubility in fluoride melts with different NdF₃-LiF compositions and at different temperatures in Guo, et al' work [63].....</i>	28
<i>Figure 2.6: 'Climate Diamond' an overall ecosystem defining diagram.</i>	30
<i>Figure 2.7: The figure showing Different technologies for CO₂ separation and capture (PSA/TSA/ESA: Pressure swing adsorption/temperature swing adsorption/electric swing adsorption) [67]</i>	31
<i>Figure 2.8: The figure showing pseudo 1st-order reaction approaches reaction verses mass transfer, process-based modeling insight [78].....</i>	35
<i>Figure 2.9: The figure showing process modeling tool ASPEN representation of a stage [78]... ..</i>	36
<i>Figure 3.1: The figure showing example of METSIM window, providing process modeling insight.....</i>	42
<i>Figure 3.2: A generalized flowchart of METSIM functionality and standard operating procedure.</i>	43
<i>Figure 3.3: 'Select Element' dialog box where first elements are selected before beginning of any METSIM operations</i>	45
<i>Figure 3.4: 'Select Components' menu which is automated operation in METSIM after choosing elements required in the Process Model.</i>	46

<i>Figure 3.5: A menu showing list of selected components after addition of desired components based on the component phase these are categorized under 5 sections.</i>	<i>47</i>
<i>Figure 3.6: METSIM's 'ICOM Edit Components' menu where different components are added which are by default are not present in the database.</i>	<i>47</i>
<i>Figure 3.7: Process schematic of major unit operations for Phase 2 testing.....</i>	<i>52</i>
<i>Figure 3.8: Total REE concentration for each drum of coal collected from an outcrop of the H Bed seam in Slope County, ND.</i>	<i>53</i>
<i>Figure 3.9: Leaching efficiency vs acid concentration for as-received H Bed lignite.</i>	<i>54</i>
<i>Figure 3.10: Leaching kinetics (through association with Al) in the as-received H Bed lignite.</i>	<i>54</i>
<i>Figure 3.11: Extraction efficiency of REE from lignite coal using a pH-based leaching process at various pH values, with pH A being the high pH, pH B being the medium pH, and pH C being the low pH.</i>	<i>56</i>
<i>Figure 3.12: Removal efficiencies of REE, iron, thorium, and uranium in the impurity removal step at both pH 3 and pH 3.5.</i>	<i>57</i>
<i>Figure 3.13: Cumulative recovery of REE at different oxalic acid concentrations. oxalic acid concentration increases from left to right (Concentration A is the lowest and Concentration D is the highest).</i>	<i>58</i>
<i>Figure 3.14: Purity of REE products on an oxide basis, which were precipitated at various oxalic acid concentrations. oxalic acid concentration increases from left to right (Concentration A is the lowest and Concentration D is the highest).</i>	<i>59</i>
<i>Figure 3.15: Piping and instrumentation diagram for the as-installed semi-continuous REE extraction system.</i>	<i>60</i>
<i>Figure 3.16: REE recovery from coal during leaching tests.</i>	<i>64</i>
<i>Figure 3.17: Overall REE extraction from the coal, acid consumption during leaching tests. ...</i>	<i>64</i>
<i>Figure 3.18: Extraction of elements during the impurity removal step for each testing week.</i>	<i>65</i>
<i>Figure 3.19: Recovery of REE from the PLS for each of the weeks of testing.</i>	<i>66</i>
<i>Figure 3.20: The apparent reaction mechanism describing the leaching process insights. Several inorganic species in lignite coal are organically associated in the form of Carboxylic acid salts (monovalent cations). Or complexes of carboxyl functional groups (multivalent cations).</i>	<i>68</i>
<i>Figure 3.21: Spiraling Process Flow diagram in METSIM consisting of major unit operations</i>	<i>69</i>

<i>Figure 3.22: Leaching Process Flow diagram in METSIM consisting of major unit operations</i>	70
<i>Figure 3.23: Impurity removal process Flow diagram in METSIM consisting of major unit operations</i>	71
<i>Figure 3.24: Stage-1 oxalate precipitation process flow diagram in METSIM consisting of major unit operations</i>	72
<i>Figure 3.25: Stage-2 oxalate precipitation process Flow diagram in METSIM consisting of major unit operations</i>	73
<i>Figure 3.26: METSIM convergence testing for each iteration in steady-state calculations the green color in cell represents acceptable value by software.</i>	82
<i>Figure 3.27: Extraction efficiency of REE from blend of two types of coals with respect to their ratios Type 1 and Type 2.</i>	84
<i>Figure 4.1: Definition of the contact angle, θ_w, unit vector normal to the wall, n_{wall} and unit vector tangential to wall, t_w.</i>	92
<i>Figure 4.2: Metallic structured packings above shown packings are ‘MellapakPlus,252.Y’ while the lower pictures are of ‘MellapakPlus,250.X’ packing.</i>	96
<i>Figure 4.3: Overview of OpenFOAM architecture.</i>	98
<i>Figure 4.4: Directory structure of an OpenFOAM case in general scenario.</i>	99
<i>Figure 4.5: A corrugated sheet structured assembly, a predominant motivation towards the REU development for present project.</i>	101
<i>Figure 4.6: Finalized 3D CAD model of Representative Elementary Unit (REU) Multiple levels of REU is shown 3 Sections, 2 Sections, 1 Sections.</i>	103
<i>Figure 4.7: Finalized 3D grid of REU the meshes above are tetrahedral prism-based elements, multilayered hexahedral snappyHexMesh tool based elements, and uniform ICEM-CFD based CutCell based mesh. Below two images are showing enlarged views of ICEM-CFD based mesh showing uniformity with single layer inflation at boundary for capturing hydrodynamics of flow along boundary layers.</i>	106
<i>Figure 4.8: Snapshot of the vertical plane along Y axis of REU indicating velocity and pressure contours using single-phase flow.</i>	120
<i>Figure 4.9: Temporal profile Snapshots of the wetting of left wall of the column using gas-liquid two-phase flow solver. The transport properties of liquid utilized were water.</i>	121

<i>Figure 4.10: A time varying snapshots of the 1-part corrugation of REU with simplified conditions of boundary, which is gravity driven flow, inspired by Dam break case in OpenFOAM tutorials.</i>	122
<i>Figure 4.11: Snapshot of the gas-liquid interface depicting the temporal evolution of the wetting along corrugated sheet. Water ($Ka = 3969$) at $qL = 180\text{m}^3/\text{m}^2$ here gas indicated by blue</i>	126
<i>Figure 4.12: Snapshot of the liquid interface in one side of REU, for four indicated solvents by Ka number with fix load $qL=72\text{m}^3/\text{m}^2$ and fix contact angle(γ) of 70°</i>	128
<i>Figure 4.13: Variations of Normalized wetted, and interfacial area compared against Ka number of fluid loads varying $qL=72, 180, 270 \text{ m}^3/\text{m}^2$ and fix contact angle(γ) of 70°</i>	129
<i>Figure 4.14: Variations of Normalized liquid holdup compared against Ka number of fluid $qL=72 \text{ m}^3/\text{m}^2$ and fix contact angle(γ) of 70°</i>	131
<i>Figure 4.15: Variations of Normalized wetted and interfacial area compared against contact angles of fluid $qL=72 \text{ m}^3/\text{m}^2$ and fix liquid = 40% – MEA</i>	132
<i>Figure 4.16: The normalized wetted area comparisons for all four solvents in the full scale REU geometry and half (symmetric)REU geometry fixed constant contact angle $\gamma = 70^\circ$</i>	134
<i>Figure 4.17: The REU geometries employed in the OpenFOAM simulations.</i>	135
<i>Figure 4.18: The normalized wetted area comparisons for all four solvents in the full scale REU geometry and half (symmetric)REU geometry fixed constant contact angle $\gamma = 70^\circ$</i>	136
<i>Figure 4.19: The normalized wetted and interfacial area comparisons for MEA 40% in the full scale REU geometry and half (symmetric)REU geometry and previous research study by Singh and others, varying constant contact angle γ</i>	137
<i>Figure 4.20: The liquid holdup comparison for all four solvents with respect to their Ka number in the previous computational study by Singh and others and half (symmetric)REU geometry in present investigation, fixed constant contact angle $\gamma = 70^\circ$ and liquid = Water</i>	138
<i>Figure 4.21: The liquid holdup comparison with respect to contact angle in the previous computational study by Singh and others and half (symmetric)REU geometry in present investigation, varying constant contact angle γ, and liquid = 40%MEA.....</i>	139
<i>Figure 4.22: The liquid holdup against liquid load in comparison with previous computational and experimental studies by various researchers and half (symmetric)REU geometry applied in present investigation, constant contact angle $\gamma = 60^\circ$, and liquid = 40%MEA</i>	140

Figure 4.23: The interfacial area against liquid load in comparison with previous computational and experimental studies by various researchers and half (symmetric)REU geometry applied in present investigation, constant contact angle $\gamma = 60^\circ$, and liquid = 40%MEA 141

Figure 5.1: A schematic of a typical Neural Network showing hidden layers, an input layer, and an output layer as well as biases. 148

Figure 5.2: Opportunities to recover REE from various sections of coal value added chain management.(courtesy: NETL, DoE)..... 153

Figure 5.3: Proposed Near future or next generation coal operated power plant system process flow..... 154

LIST OF TABLE

<i>Table 2-1: Separation factors for extraction of rare earths by DEHPA and PC 88A (Maharana and Nair,</i>	24
<i>Table 3-1. Flowrates and feedrate controllers implemented in METSIM process modeling calculations.</i>	75
<i>Table 3-2. Flowrates and feedrate controllers implemented in METSIM process modeling calculations.</i>	76
<i>Table 3-3. Tank equipment inventory analysis of the REE extraction bench-scale system using METSIM calculations.</i>	78
<i>Table 3-4. Filtration equipment inventory analysis of the REE extraction bench-scale system using METSIM calculations.....</i>	80
<i>Table 4-1: The dimensions of the triangular section which are utilized for development of REU.</i>	102
<i>Table 4-2: The Boundary Conditions (BC's) are asserted for REU under single-phase solver configuration [88].</i>	108
<i>Table 4-3: The Boundary Conditions (BC's) are asserted for REU under two phase gas-liquid solver configuration.</i>	114
<i>Table 4-4: Transport properties of selected liquids solutions.</i>	115
<i>Table 4-5: Design of Experiment using Taguchi design showing number of cases in this project</i>	116

ACKNOWLEDGMENTS

I will never be able to finish my thesis without help and guide from my committee members, friends, my family. Especially, I would like to express my deepest gratitude to my advisor, Dr. Michael Mann, for his great support, good patience, consistent encouragement and excellent guidance for my thesis and Ph.D. program. I would like to express my sincere appreciation to Dr. Gautham Krishnamoorthy, Dr. Daniel Laudal, Dr. Clement Tang, and Dr. Srivats Srinivasachar for their useful advice and experience sharing. I would like to thank my friends, especially my best friend and fiancée Dr. Shilpi Jain for her generous and valuable advises and help. Finally, I want to thank my Mom, Dad, and Sister for supporting and financing me. In addition, I would like to thank Spotify, for letting me hear awesome, magnificent Rock and Metal songs, and keeping my spirit high 24/7, along with many podcasters such as Joe Rogan improving my knowledge.

ABSTRACT

Coal is a brownish-black sedimentary rock with organic and inorganic constituents. It has been a vital energy resource for humans for millennia. Coal accounts for approximately one quarter of the world's energy consumption, with 65% of this is energy utilized by residential consumers, and 35% by industrial consumers. Coal operated power stations provide 42% of U.S. electricity supply. The United States hold 96% of coal reserves in North America region, out of which 26% are known for commercial usage. The coal combusted in these power generating facilities requires certain pre-combustion processing, while by-products of coal combustion go through certain post-combustion processing.

The application of hydrometallurgical extraction of Rare Earth Elements (REE) from North Dakota Lignite coal feedstock can assist coal value amplification. Extraction of REE from lignite coals liberates REEs and CMs that are vital to electronics, power storage, aviation, and magnets industries. The REE extraction process also reduces the sulfur content of ND lignite coal, along with ash components that foul heat exchange surfaces and can have benefits for post-combustion scrubbing units.

When coal is combusted, the exhaust gasses contain carbon dioxide (CO_2), sulfur dioxide (SO_2), oxides of nitrogen (NO_x), water (H_2O) and nitrogen (N_2). Carbon dioxide comprises approximately 8-10 vol% of the flue gas and is reported to contribute to the greenhouse effect, a primary reason for climate change. Carbon Capture and Storage (CCS) involves of CO_2 by use of liquid or solid absorbents to separate CO_2 from combustion flue gas. Little data is available on gas-liquid interfacial area correlations in the literature for use of second generation solvents, such as

MonoEthanolAmine (MEA), in structured packing absorber columns consisting of thin corrugated metal plates or gauzes, designed to force fluids on complicated paths. While mathematical model development for existing post-combustion carbon capture (PCCC) technologies, such as carbon capture simulations using computational fluid dynamics (CFD) for prediction of mass transfer coefficients is well developed, models describing the behavior of third generation solvents is lacking.

Two main research opportunities exist: (i) due to the complex chemistry of coal, there is a requirement for a modeling tool that can account for the coal composition and complex hydrometallurgical extraction processes to assist in designing and sizing pre-combustion REE extraction plants; and (ii) CFD models are required that can capture the mass transfer coefficients of third generation CO_2 solvents using structured packing.

Two primary hypotheses have been developed to address the research opportunities: (1.) Process modeling of hydrometallurgical extraction of REE provides some theory-based understanding that is complementary to experimental validation and, with the help of chemical kinetics and percentage carboxylation existing in feedstocks, can forecast the efficiency and leachability of other feedstocks, and (2.) A detailed Volume of Fluid (VOF) simulation of coupled mass and momentum transfer problems in small intricate regions of corrugated structured and packed panels placed at 45° angle can be used to predict mass transfer coefficients for third generation solvents by using open-source numerical C/C++ based framework called Open Fields-Operations-And-Manipulations (OpenFOAM).

The hydrometallurgical process modeling is developed using METSIM, a leading hydrometallurgical process modeling software tool. The steady state process model provides an overview of REE production along with equipment inventory sizing. The model also has functions

to define percentage of organic carboxylic acid bonds present in coal, since, the prior research has identified that the primary association of REE in lignite coal is as weakly-bonded complexes of carboxyl groups, which are targets of the extraction technology.

The CFD modeling work is expected to determine critical mass transfer coefficients for CO_2 capture using structured packing columns. Further, the developed CFD model and its validity will be tested against experimental data from various industrial and literature sources.

NOMENCLATURE

Symbol	Unit	Meaning
a_{ch}	[m]	Length of packing channel side
A	[m ²]	Area
B	[m]	Base of channel
C_0		Courant number
\mathcal{F}	[N.m ⁻³]	Surface tension force per unit volume
σ	[N.m ⁻²]	Surface tension
g	[m.s ⁻²]	Gravitational Acceleration
H		Height of Channel
K_a		Kapitza Number
n		Unit normal vector
Q		Solvent flow rate
Re		Reynolds number
S	[m]	Side of Channel
We		Weber Number
x		Mole fraction
δ		Film thickness
∇		Gradient operator
κ		Interface curvature
a_G	[m ² .m ⁻³]	Packing geometric area density
D_{pk}	[m]	Packing Diameter

H_{pk}	[m]	Packing Element Height
α_{ch}	[°]	Channel inclination angle
θ_{ch}	[°]	Angle between packing channel sides
d_h	[m]	Hydraulic diameter
Ω		Geometrical Domain
Ω^h		Discretized Spatial Domain
Ω_P^h		Discretized Spatial Domain with Phase
ρ_l	[kg.m ⁻³]	Density of Liquid
ρ_g	[kg.m ⁻³]	Density of Gas
u	[m.s ⁻¹]	Velocity
\mathfrak{R}^+		Set of real numbers
ξ	[N.m ⁻²]	viscous stress tensor
p	[Pa]	Pressure
μ	[N.s.m ⁻²]	Dynamic Viscosity
ν	[m ² .s ⁻¹]	Kinematic viscosity
Q		Solution domain
Q^h		Discretized solution domain
\mathcal{H}		Interface mathematically define
\mathbf{S}_f		Vector normal to the face f
Φ_f^ϕ		Flux of the quantity Φ through f
α		Volume fraction function
Δt	[s]	Time step

t	[s]	Time
Ω_p^h		Centroid cell
α_p^h		Discretized domain containing volume fraction
UD		Phase A calculated using upwind scheme
HR		Phase B calculated using high resolution scheme
H		Henry's Constant
D		Diffusion
β		Contact Angle of Liquid in 'constantContactAngle' BC
REE		Rare Earth Element
CM		Critical Mineral
REO		Rare Earth Oxide
LREE		Light Rare Earth Elements
MREE		Middle Rare Earth Elements
HREE		Heavy Rare Earth Elements
CREE		Critical Rare Earth Elements
TREE		Total Rare Earth Elements
PLS		Pregnant Leach Solution
AMD		Acid Mine Drainage
PFD		Process Flow Diagrams
P&ID		Piping and Instrumentation Diagram
SX-EW		Solvent extraction-electrowinning
CFD		Computational Fluid Dynamics
BC		Boundary Condition

NSE	Navier-Stokes Equations
MULES	Multidimensional Universal Limiter for Explicit Solution
VoF	Volume of Fluid
PIMPLE	Combination of PISO and SIMPLE algorithm
PISO	Pressure Implicit with Splitting of Operator
SIMPLE	Semi-Implicit Method for Pressure-Linked Equations
OpenFOAM	Open Field Operations And Manipulations

1. INTRODUCTION

This chapter provides a brief introduction to the coal-based fossil fuel power plants and the novel pre-combustion and post-combustion processes that are developed to improve their emissions and economic performance and competitiveness in rapidly changing electricity generation market. Also, chapter introduces the modeling involved in these pre- and post-combustion power plant processes.

1.1 Coal Definition

Coal is a complex sedimentary rock carrying organic and inorganic matter. The organic matter also is referred as maceral matter, while the inorganic matter commonly known as mineral matter. There are four types of coal, namely, anthracite, bituminous, sub-bituminous, and lignite. Coal deposited sediments also known as coal beds of coal seams, and can range from fractions of an inch to hundreds of feet in thickness. Coal changes its composition from one rank to another rank, and within any particular coal seam the coal can show vast variations in composition. With its relatively high heating value (8000 to 15000 Btu/lb.) and relatively low cost, coal has been major source of energy for past couple of centuries.

1.2 Purpose

Since the late 1600's, fossil fuel power plants especially coal fueled power plants propelled the progress in socio-economic establishment in modern human civilization by providing consistent, reliable and low-cost electricity or power. The key working principle of working of coal powered electricity generation station is to burn the coal in boiler which increases the

temperature and pressure of water to create super-heated steam which is used to spin a turbines and generate electricity. Burning of coal essentially generates a large amount of atmospheric gases, together known as flue gas, consisting mainly of carbon dioxide (CO_2), sulfur dioxide (SO_2), various nitrous oxides (NO_x). Out of these gaseous entities, SO_2 and NO_x are actively reduced to levels lower than acceptable standards of U.S. Environmental Protection Agency (EPA). While the CO_2 is a major constituent of these flue gases, which although not commonly regulated, is a greenhouse gas known to contribute to global warming.

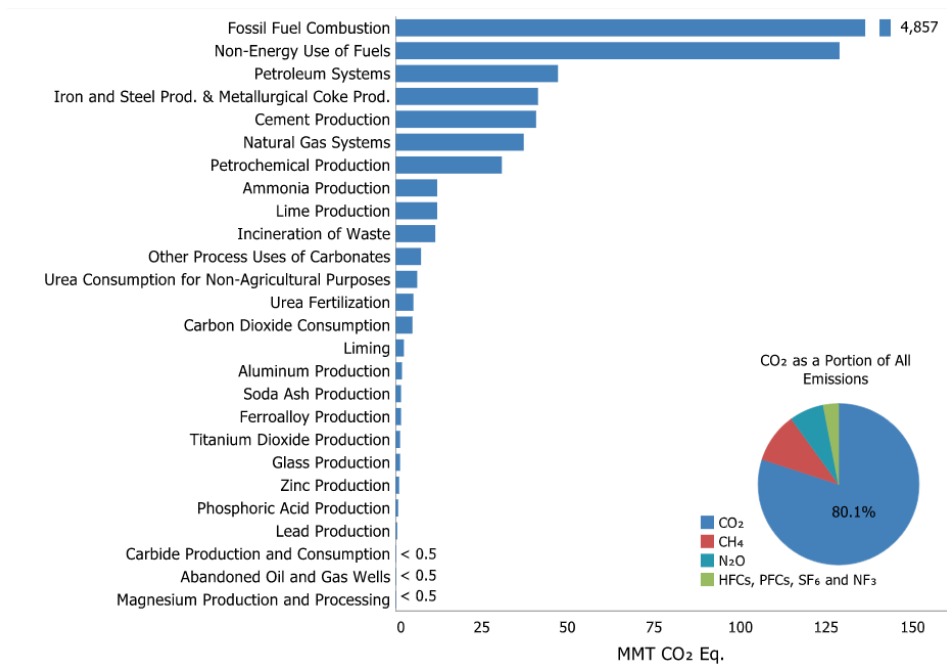


Figure 1.1: 2019 CO₂ Emissions from Fossil Fuel Combustion by Sector and Fuel Type (EPA, 2020) [1]

Based upon data from EPA 2020 report, the present energy generation scenario shows fossil fuel-based energy generation stations lead to approximately 4857 MMT CO₂ equivalent release in the atmosphere. However, CO₂ emissions can be reduced using various novel technologies. Figure 1.1 shows evidence of high use of fossil fuel-based energy generation effectively generating higher

emissions of CO_2 on multi-magnitude level compared to other industrial sectors. As a largest source of U.S greenhouse gas emissions, CO_2 from fossil fuel combustion has accounted for approximately 76 percentage of Global Warming Potential (GWP) – weighted total U.S. gross emissions across the time series from 1990 – 2019 [1].

Thus, coal shows a less promising future for energy generation. An annual energy outlook report from 2020 in *Figure 1.2* shows the increasing use of renewable energy resources, such as solar, wind, geothermal etc.

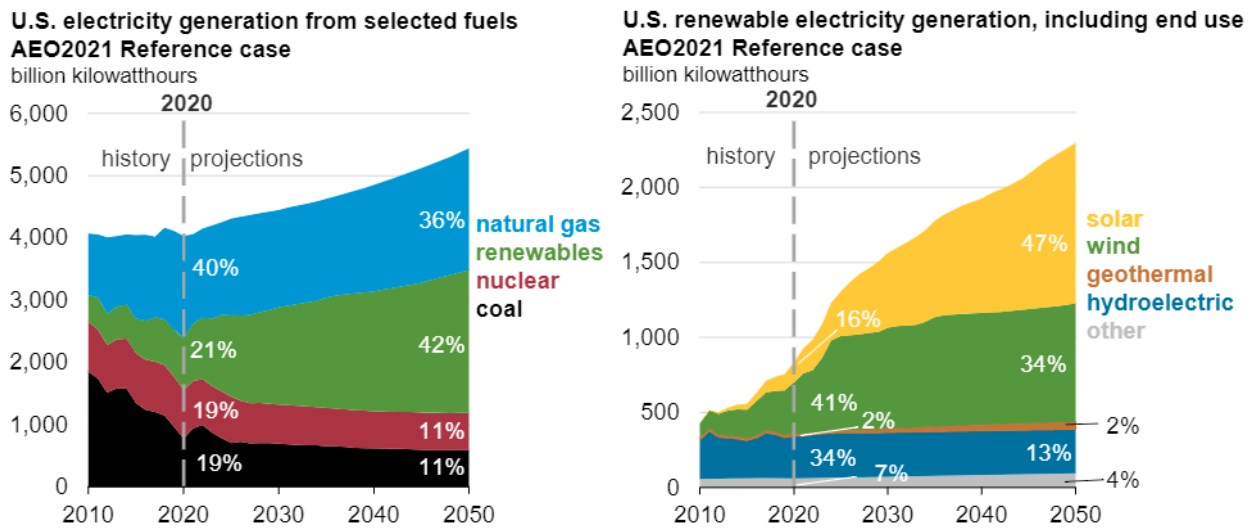


Figure 1.2: A graph from 2020 Annual energy outlook report showing comparisons of sources for energy generation (energy information admin, 2020) [2]

By 2050 the projections for growth in solar energy harvesting and usage shows 47%, while the natural gas utilization is forecasted to decrease to 36% from its current 40% utilization level. In addition, with new generation (Generation – IV) reactors, the use of nuclear energy is envisaged to increase as well. With the constraints from various socio-economical levels and rising competitive financial establishments, coal does not show encouraging investment market for

investors. Rising environmental awareness also creates the challenges for upcoming coal fuel-based power generations stations.

1.3 Does coal hold future then?

With the economic and environmental adversaries driving coal from the market, the author does take liberty and asks the question to the readers, 'Is coal still relevant in the future?' Although, the environmental impact is causing coal-based power plants to show a bleak future, coal however remains a critical component for electricity generation, as well as a critically contributing component in the other types of product development.

Even though being a higher calorific value holding sedimentary rock useful for combustion, the coal can be utilized in many chemical industries such as activated carbon production, humic acid development, extraction of minerals from coal, development of petrochemical products, syngas, hydrogen production, etc. [3, 4] In addition, novel pre- and post- combustion technologies, for example: CO_2 capture and storage from flue gases, applied to previously existing coal operated power plants, provide a possible future for power plants to produce low-carbon emission based energy allowing to compete against market penetrating renewable energy resources. [3, 5, 6].

1.4 Pre- and Post- Combustion Technologies

Novel technologies are being implemented in coal operated power plants. Some technologies are implemented as pre-combustion processes such as coal upgrading for improved power plant efficiency and reduction of pollutants in flue gases. Other types of technologies are applied at the post-combustion stage, for example, capturing CO_2 and other polluting gases from the flue gas system, also known as point carbon capture.

The author discusses two relevant technologies briefly in the current chapter and provides explanations in detail throughout the dissertation. These technologies are as follows:

1. Extractive metallurgy using aqueous medium from coal before combustion of coal in power plant as a pre-combustion technology.
2. Post – combustion carbon dioxide (CO_2) capture from flue gases using third- or second-generation solvents.

1.4.1 Extractive Metallurgical Processes from Coal

The process of extracting critical minerals such as Rare Earth Elements (REE) from coal by decomposing either weak bonds between organic matter and inorganic minerals or completely decomposing organic matter of coal with the use of an aqueous medium or by use of a heating process is known to mankind for many decades. The use of coal which is a complex sedimentary rock, unlike clays, provides value-added functionality in addition to its use for combustion to generate power.

In 2015, the geological survey of North Dakota promisingly shows it is possible acquire rare earth elements and critical minerals by using North Dakota lignite coal feedstock. [7] [8] Thus, the use of aqueous medium to extract precious elements from coal and further utilizing the upgraded coal towards power plant combustion is a novel and unique process showing favorable economics and encouraging results [9].

1.4.2 Post-Combustion Carbon Capture Process

Coal and natural gas power plants emit environmentally harmful constituting gases such as SO_2 , NO_x , CO_2 , etc. [6, 5] After capture of SO_2 , and NO_x gases, CO_2 capture by absorption into amine solution within packed column absorber has been regarded as one of the most viable options

for implementing carbon capture and storage within existing coal and natural gas power plants. [10] Thus, Carbon dioxide removal by second or third generation amine based liquid solvents in post-combustion processes allow power generation facilities to continue operations as per future environmental standards or equivalent European standards. [11]

1.5 Key Takeaways from the Novel Technologies

The author promotes following key takeaways to readers of this dissertation.

Unlike multiple types of coals being utilized in for mineral extraction, which has been researched and commercially applied over many years, the North Dakota lignite coal feed stock utilization for Rare Earth Elements (REE) and other critical materials is a novel and unique process. Currently, for this process no predictive and reactive modeling is present, and the modeling depends upon experimental data. Thus, experimental data is also far less available for current process for various types of coals. Hence, calibration of model based on existing experimental data is essential, as well as aiming to predict the forecasted coal types is necessary.

The research and academic literature studies show various types of mathematical modeling development for solvents and sorbents for CO_2 capture systems. [12, 13, 14] A coarse-grained or coarse mesh CFD model which can perform faster simulations and generate results quicker and more accurate than the previously established models, utilizing less computational resources is rarely available. Only a handful of publications show the use of open-source CFD software with inclusion of complex geometrical domain and results validation. [15, 16]

1.6 Scope, Goals and Hypothesis

Therefore, the author addresses two critical opportunities here. These are: 1) development of a process model for REE extraction and purification using electrochemical metallization, and 2)

advancement of CO_2 capture processes by developing an open-source software established computational fluid dynamics (CFD) model capable of using coarse mesh for simulations for prediction of interfacial area and mass transfer.

Hence from these critical opportunities. The author plans to test two ‘research opportunities’ derived hypothesis throughout the Ph.D. studies, which are as follows:

1. Process modeling of hydrometallurgical extraction of Rare Earth Elements (REE) using premier metallurgical software provides a conceptual understanding, complementary to experimental calibration using bench-scale and lab-scale experiments, to find parameters such as chemical kinetics and percentage carboxylation existing in coal feedstocks. Purification of REE by applying an electrochemical metallization process will also be included.
2. A coarse-grained Volume of Fluid (VoF) simulation with coupled mass and momentum transfer equations can predict mass transfer coefficients for third or second generation solvents in small intricate regions of corrugated structured packings placed at 45° angle by using open-source numerical framework based upon C/C++ computing language. The software to be used is **Open – Fields Operations And Manipulations (OpenFOAM)**

1.7 Objectives to Achieve

The objective of this dissertation and overall Ph.D. experimental and modeling work, gleaned from previous takeaways and hypotheses, is formulated below.

A predictive and reactive model is necessary for hydrometallurgical extraction of rare earth elements as well as an electrochemical metallization process for extracted rare earth purification. Thus, establishing a process flow diagram (PFD) is critical since these diagrams conveniently

provide an overall idea of what the process going to look like as well as the size and amount of process dependent equipment inventory required. Specific steps to be followed in this research include:

- A steady-state process model is established for the overall process using the process flowsheets as inputs.
- Although the model is steady-state, the reactive and predictive abilities of this model shall be able to provide the complimentary understanding to experimental evidence.
- The calibrated predictive model should be able to forecast the performance of other upcoming coals based upon their carboxylic bonds associations, which can be determined by ‘vitrinite reflectance’ or other relevant analytical techniques.
- The process of electrochemical metallization for REE purification is established using conceptualized PFDs. The process then simulated using a steady-state model.

Multiphase flow computational fluid dynamics is required to model the details of CO_2 capture by second generation solvents, a crucial part of models is time-dependent, multi-dimensional, and simulations at the micro-scale with high-fidelity interface reconstructions. The following objectives are critical to accomplish this modeling task:

- Micro-scale simulations utilizing the volume of fluid (VOF) interface capturing methodology in OpenFOAM (InterFoam) will be performed to predict wetted area/interfacial exchange areas for fluids (solvents) and configurations (packing shapes and dimensions) at different levels of uptake of interest to NETL.

- By developing the simplified geometric modeling approach, the all hexahedral meshing size is reduced to perform these high-fidelity simulations with higher iterations per time-step for computational time reductions.
- Utilizing the results from fine-scale and coarse-scale simulations, in conjunction with the Higbie Penetration Model [17, 18], a methodology for estimating mass transfer coefficients will be developed.
- Documentation for utilizing open-source solvers for future aspirants in the field of computational fluid dynamics will be developed.

The author contributes novel understanding and theory to the scientific community, through these modeling efforts. Publications in technical literature about the results from these projects ensures wide spread of dissemination of these results.

1.8 Research Significance

North Dakota hosts the world's largest lignite coal deposits [19, 20, 9, 21] with an economic and energy portfolio heavily invested in lignite mining and utilization. The modeling efforts of this dissertation provide a complimentary mathematical understanding to an on-going effort to develop a novel process for the extraction of rare earth elements from North Dakota lignite coal. This dissertation and overall Ph.D. experimental and modeling work will provide a better understanding of this innovative process allowing more rapid development of the extraction process with process optimization of extraction efficiencies and economics. [22] [23]

Carbon capture and storage or sequestration is one of the prime challenges facing the continued use of fossil fuel since the global warming has been identified as an existential threat to planet and humans. CO_2 capture at fossil fuel power plants is essential for the reversal of

exponential growth of CO_2 in the atmosphere. The use of second or third generation solvents such as cyclic amines, hindered amines, etheramines, amino acids, phase change solvents, ionic liquids, or mixtures for CO_2 capture depict promising results for power plants. The current predictive capability using faster and smarter CFD simulations provide assessments for forecasted packings and associated solvents with better mass transfer rates while minimizing pressure losses and liquid holdup which can investigate to reduce the large energy requirements for the carbon capture facilities associated with fossil fuel power plants.

2. LITERATURE REVIEW

2.1 REE Recovery via Hydrometallurgical Extractions

Rare Earth Elements (REE's) are critical materials for the manufacturing of electronic devices, batteries, magnets, sensors and other critical products. The demand for these critical minerals in industries is sharp due to advancement of the information technology age. A group of 15 lanthanides and 2 transition metal elements accounting total of 17 elements are consider as Rare Earth Elements, these are lanthanum (*La*), cerium (*Ce*), praseodymium (*Pr*), neodymium (*Nd*), promethium (*Pm*), samarium (*Sm*), europium (*Eu*), gadolinium (*Gd*), terbium (*Tb*), dysprosium (*Dy*), holmium (*Ho*), erbium (*Er*), thulium (*Tm*), ytterbium (*Yb*), and lutetium (*Lu*), Yttrium (*Y*), and Scandium (*Sc*). The misnomer 'Rare' does not prove them to be rarer than platinum group elements, as the exploration observation show that these are 200 to 250 times more abundant than Gold (*Au*), one of platinum group elements [7] [9]. The period when these elements discovered enabled them to be less useful in industrial development, thus researchers across industry and academia deemed them as 'Rarely used', thus the term Rare is applied as prefix to these elements. These elements are categorized in two factions as Light Rare Earth Elements (LREE) comprised of *La* through *Sm*, and Heavy Rare Earth Elements (HREE), comprised of *Eu* through *Lu* including *Sc* and *Y*. Only *Pm* is radioactive and observed only in artificial environments such as radioactive wastes, etc.

Presently, multiple market segments show heavy usage of these elements in the form of compounds or as pure metals. LREE shows importance as catalysts and circuitry components, while the HREE holds criticality in the magnet industry essential for virtually any high efficiency, high power electric motor or electricity generator. [9] [24] Due to China's early entry into the market and high-quality rare earth mining resources, China holds a major section of REE mining

and recovery processes, capturing maximum export in the global economy. As a result of their monopoly on the market, China has been able to control the price of rare earth elements causing pricing fluctuations and tend to rise prices over time. The United States is an importer of these elements, and therefore has dependency over China for access to material that are critical to its economy and national security. Another major concern is that the natural occurrence of REE in Chinese land is depleting, forecasting a global shortage of REE by 2025, since China holds maximum economy of REE trading. This ultimately leads to the need for discovering novel REE recovery technologies, while resurrecting previous industrial process such as the Mountain Pass Mine in California. In this chapter, the author reviews the major REE extraction and recovery technologies offered in industry.

Extraction of REE from coal or ore by means of aqueous medium is called hydrometallurgical extraction of REE. If an abundant amount of heat is employed to recover these critical elements, then it is termed pyrometallurgical extraction of REE. The hydrometallurgical process involves leaching which essentially is a separation method for substances from a solid by dissolving it in a liquid acid solution. However, as noted by Gupta and Krishnamoorthy [22, 25] due to the unique nature of lanthanides and their similarity among each other, the process becomes complex due to chemical bonding between the REE's and the other elements which cannot be broken down easily. Thus, various chemical and physical process have been developed with extraction ranging from 30%, in which the maceral matter such as coal or ore can still be used for other purposes, to 95% in which the maceral matter is completely decomposed and all the REEs are liberated in aqueous medium in form of trivalent ions.

2.1.1 REE Extraction Resources

The resources suitable for extraction of REE are segregated in two groups namely natural and artificial. These are explained in this section:

Natural (Primary) Resources: According to Jordan and other researchers, along with Ozbayoglu, Atalay, Huang [26] [27] [28] [29] bastnaesite, a fluorocarbonate mineral containing approximately 70% Rare Earth Oxides (REOs) mainly comprised of LREE is one of the most primary naturally occurring rare earth extraction source. Based on economic analysis, major revenue generating mines such as Mountain Pass, USA, Bayan Obo, are created to extract REEs from this ore.

Monazite which is another naturally occurring rare earth phosphate mineral shows similar properties as Bastnaesite, holding slightly more HREE compared to Bastnaesite. Monazite also contains a higher percentage of naturally occurring Radioactive Elements (NREs). They are mainly mined as heavy mineral rich sands and mining is mostly conducted in the Southeast Asian peninsula such as India. [30] [22]

Xenotime is also a phosphate-based mineral containing ~67% of REOs and holds richness in Yttrium. Mining of Xenotime is mainly conducted in India, Brazil, and Australia. It is a critical mineral for HREEs, and these ion-absorbed clays naturally occur in metamorphic rocks. Apart from natural occurrence of this ore, it can also be recovered from Monazite by floatation and magnetic separation techniques. [26] [31]

In addition to the notable ore resources defined above which are primarily utilized in the production of Rare Earth Elements, there are other ores that are considered as primary resources. These ores include the phosphate-bearing mineral known for Ce as Britholite

$[(Ce, Ca)_5(SiO_4, PO_4)_3(OH, F)]$, silicate-bearing mineral for Eu production known as Eudialyte $[Na_4(Ca, Ce)_2(Fe^{2+}, Mn^{2+}, Y)ZrSi_8O_{22}(OH, Cl)_2]$, and the halide mineral for Nb production called Pyrochlore $[(Ca, Na, REE)_2Nb_2O_6(OH, F)]$. [32] [33]

Recently, lignite and sub-bituminous coal have been identified as one of the critical primary resources for extraction and recovery of rare earth metals and compounds. For example, a newly process was developed for the extraction of REE from fire-clay coal which is type of bituminous coals in Eastern Kentucky region [34] [35]. One caveat of the process is that the by-product, which is coal, and the product which is extracted REE of the process; both are critical, thus achieving optimized ratio of extracted REE and demineralized coal is important. As per the Honaker's article, the research team less likely recover the coal, hence show higher concentration of acid utilization. [34]

Unlike the process at University of Kentucky, the process developed at University of North Dakota uses lignite coal for extraction of REEs and CMs. In lignite, the REE are weakly bound as organic complexes, rather than in hard mineral forms that are typical of higher-rank coals and most existing REE mineral ores. These organic associations permit a simple dilute acid leaching process to be highly effective in selective extraction of the REEs and CMs, such as Ge and Ga. The leaching process is also a coal beneficiation process, offering value-added opportunities for the upgraded lignite byproduct. These characteristics allow for a relatively simple system using conventional processing equipment with mild processing conditions (ambient pressure and temperature and moderate acid concentrations). [9] [24] [36]

Artificial (Secondary) Resources: The absence of cost-effective and operational primary deposits is encouraging many nations to actively research technologies to extract REE from consumer electronics scrap, industrial residue, and end-of-life products. One of the advantages of

secondary resources is less environmental impact factors which are significantly higher in terms of mining.

Permanent magnets such as Neodymium-Iron-Boron (*NdFeB*) alloys with some of admixtures of other rare earths such as Praseodymium, etc. are substantially used in Hard Disk Drives (HDDs), Solid State Drives (SSD), and Random-Access Memories (RAM) which is observed by Gutfleisch and others, along with Binnemans [37] [38] . These electronic “scrap” materials are generally recycled using combinations of chemical and physical processes. Firstly, physical processes separate out parts rich in rare earths from other transitional metals. Later hot concentrated acid digestion dissolves all non-metal parts and what remains is rare earths and other critical elements. [39] [38] A simplified diagram is shown in the following *Figure 2.1*

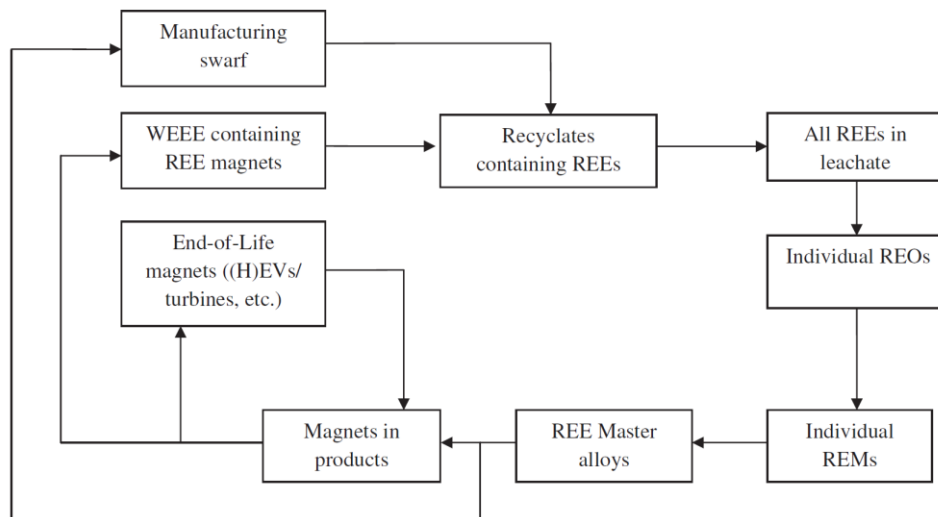


Figure 2.1: Simplified Recycling flowsheet of rare earth magnets. [32] [38]

Based on research by Binnemans, Muller and Friedrich [40] fluorescent lamps hold 10 to 20 Wt.% rare-earth phosphorus, thus the fluorescent lamps are increasing recycled by many industries. The process involves beneficiation (grinding), sieving, leaching, impurity removal such as Fe, and recovery of REEs. In addition, in certain cases the process of mercury removal (Hg) is

required after leaching with an aqueous medium this process of pyrolysis forms the final product. [40] [41]

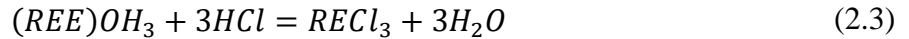
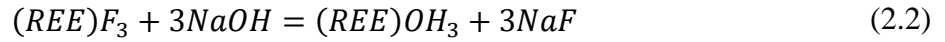
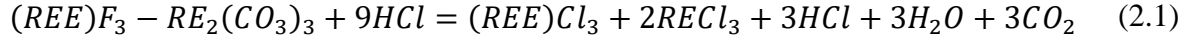
Due to the use of cerium oxide powder mixed with water as the best polishing reagent for glass, the cathode ray televisions and its components are a prime target for REE and other critical material recycling plants [42, 30]. According to reports of Yu and Chen, [41, 8] the use of REEs as fluidized catalytic cracking catalysts in petrochemical industry allows recycling of used fluidized bed consist of these REEs towards renewal for the fluidized bed components.

2.1.2 REE Recovery Using Aqueous Resources

The processed materials from primary and secondary sources are hydrometallurgy treated using strongly acidic or basic solutions which leads to selected dissolution and precipitation of metals of interest. The typical hydrometallurgical extraction process involves leaching followed by solvent extraction, or ion exchange, and precipitation chemistry.

The research group of Akkurt in 1993 and Fatherly in 2008, studied the physically beneficiated concentrates leached in suitable lixiviant directly or after heat treatment to dissolve its metallic value. Several mineral acids such as HCl , H_2SO_4 , HNO_3 are utilized in various concentrations, while some organizations developed synthesized organic acids, such as Cynex 272 (Di-2,4,4-trymethylpentyl Phosphonic Acid), or Versatic-10 (having chemical nomenclatures as Alkyl monocarboxylic acids, etc.) acting as selective leaching agents according to [43] [25]. Chi and others show that Bastnaesite has also been roasted with ammonium chloride, which decomposes into gaseous HCl that forms rare earth chlorides, which are readily leached with hot water. One of the caveats of the process is that it does not extract rare earth fluorides. This issue

was later on effectively resolved by utilizing pre/post treatment with alkaline or sulfuric acid roasting using reactions below.



In above reaction equations, *REE* denotes Rare Earth Element.

Another process shows a pathway where after heating with concentrated sulfuric acid (98%) at $\sim 500^\circ C$, REEs are precipitated in an aqueous *NaCl* solution. The heating removes the CO_2 and *HF* in gaseous form from the process as discussed by Peelman and research group. The adverse environmental effects of this process are discussed as well. The following flowsheet (*Figure 2.2*) defines the processes in Baotou rare earth extraction facility in China:

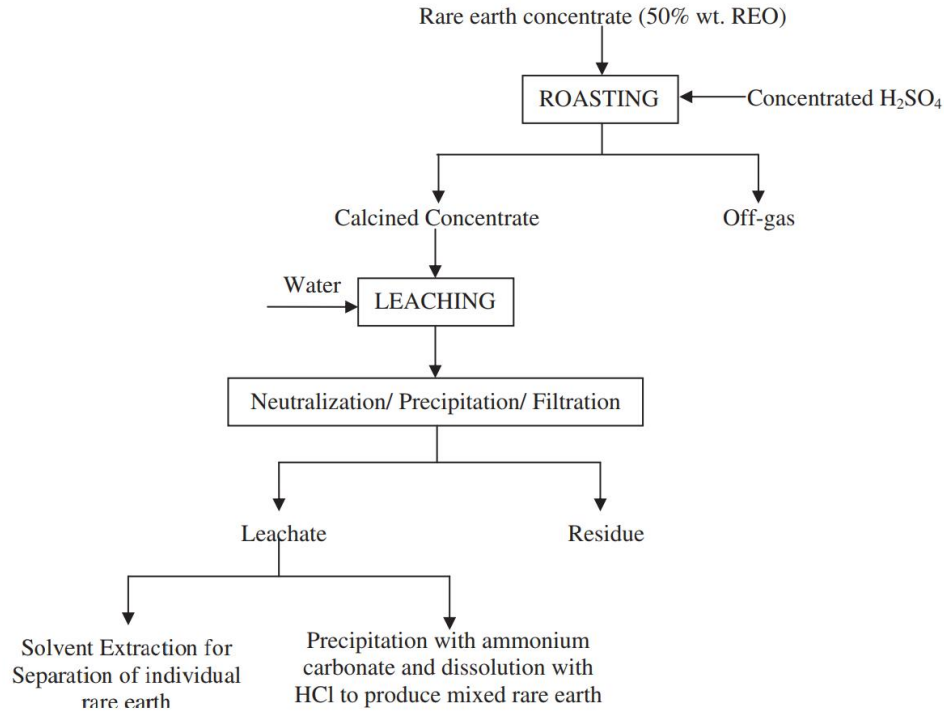
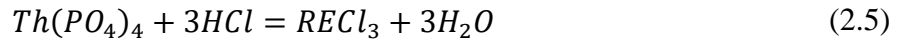
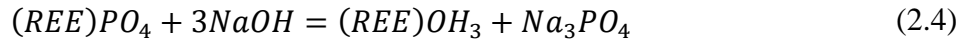


Figure 2.2: Leaching Processes used in Baotou rare earth complex in China Simplified flowsheet [29]

Huang and Zhang's research group [29] describe the process as one of the most accepted technologically and economically feasible processes in China for rare earth production on mass scale. In the concentrate generation process, first the bastnaesite is roasted with H_2SO_4 and gaseous byproducts are disposed. Later the roasted source is calcinated and leached with water, the neutralized solution processed, and rare earths are recovered up to 90% and hydrofluoric acid (HF) is generated as a by-product. This process was studied by Yorukoglu's research team and investigated by Kuzmin and others [44] [45] and showed environmentally dangerous effects near the Baotou region.

Due to a higher percentage of naturally occurring radioactive deposits, Monazite needs suitable conditions unlike Bastnaesite. Monazite leaching is conducted in less harsher

environments, and one of the leaching variables is sodium hydroxide ($NaOH$) and $140^{\circ}C - 150^{\circ}C$. Prior to the chemical processes the ores need to be grinded finely ~98% as studied by Kuzmin [44]. The reactions are shown below:



Different authors investigated direct leaching of Monazite under various experimental conditions to either generate the concentrate or to remove the undesirable products to reach the final step as concentrates. However, to increase the extraction and recovery, the Monazite ore needs to be treated with a suitable beneficiation circuit. Without proper particle size the leaching and other processes are less efficient [22, 25, 32]. In 1990 Merritt proposed another novel process for Monazite preparation and rare earth extraction, where the Monazite was heated with $CaCl_2$ and $CaCO_3$ under reducing atmosphere with sulphadiazine. As a result, conversion of rare earth phosphates to oxysulphides and oxychlorides of REE and a stable oxide of thorium and chlorapatite formed in less than an hour. From this mixture, rare earth metals can be selectively leached in HCl .

Similar to Monazite and Bastnaesite, Xenotime ore-based concentrates and their extraction and recovery were investigated by Kumar and others [41]. Either sulfuric acid or alkali leaching is used as one of the methods for the extraction of rare earth from Xenotime ores. Vikery in 1990 and Gupta and Krishnamoorthy in 1992 [22] reported that there are different possible leaching methods, for example, using sulfuric or nitric acid, alkaline solutions, or water leaching after providing pre-treatment such as roasting with an ammonium salt. $(NH_4)_2SO_4$ and $NaCl$ are frequently used leaching reagents for the ion absorb clays and the kinetics of this leaching process is very fast. For clays, usually no beneficiation processes are required before leaching and as a

result, the process economics show better NPV and a shorter payback time according to Moldoveanu and Papangelakis. [46]. In China, the ion clays containing 0.08 – 0.8 Wt. % rare earths are being processed using 7% $NaCl$ and 1 – 2 % $(NH_4)_2SO_4$ at a pH of 4 achieving 95% of rare earths recorded on commercial-scale reported by Peelman and research group in 2014. [47]

Secondary Resources Extraction Methodologies: In secondary waste sources, the control over organics is more prominent than that of the primary resources which are ores or coal. Hence, after few unit operations the process can lead towards separation and again metallization process. Here we are discussing secondary extraction of recovery source as permanent magnets. In 1992 Lyman and Palmer discuss a development of a process for separation of rare earth from $Nd - Fe - B$ magnets where 1 kg of magnetic scrap was dissolved in 10 L of 2M H_2SO_4 . The pH of the leachate was increased to 1.5 at which Nd precipitated in form of salt, which is then leached in HF to form NdF_3 . Itakura and others discuss the usage of HCl and oxalic acid $H_2C_2O_4$ as a medium for leaching rare earths from electronic waste. In their process, Ni-coated $Nd - Fe - B$ sintered magnets were treated with an aqueous solution containing 3M HCl and 0.2 N oxalic acid. 99% of the Nd present is then recovered as neodymium oxalate $NdCOOH$. In 1994 Elis and research group invented a process of conversion of these magnets using a medium of nitric acid (HNO_3) in concentrated form. In this process the magnets were completely dissolved in HNO_3 , later to form neodymium iron fluoride double salt with the additions of HF . This salt was dried and calciothermically reduced to the metallic state. For elements from ‘phosphor lamps’ recycling, the process was developed by OSARAM A.G. consisting of multistep leaching. The process is targeting specific compounds in phosphors, and it is reviewed by Otto and Wojtalewicz Kasprzac [48]. It shown in *Figure 2.3* as simplified flowsheet:

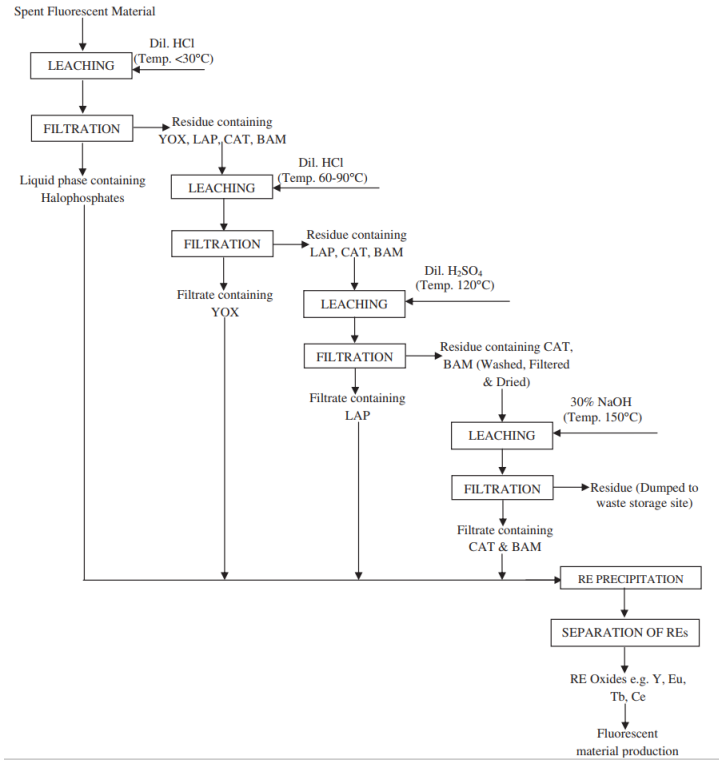


Figure 2.3: A multistep leaching process developed by OSRAM to recover rare earth metals present in the phosphor powder [48]

In a generalized overview, for any hydrometallurgical process, regardless of primary or secondary source, dissolution in acidic or basic media is critical for the extraction of Rare Earths or any required precious mineral with further downstream reaction with a base to form solid precipitates in a stable form so that they can be recovered. [49]

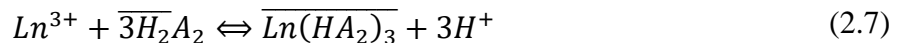
2.2 Rare Earths Separation Technologies

The separation of trivalent lanthanides from each other, multivalent actinides, and other transition metals from lanthanides is a formidable challenge in the field of separation science. Physical forces (e.g.: electromagnetic separation), chemical reactions (e.g.: selective reagent dependent separation), electrochemical forces, etc., are used for separating REEs from each other.

Lanthanides are usually separated in multistage extraction in counter-current mode using mixer settlers which are monotonous and time consuming. To develop feasible and eco-friendly processes, R&D studies are being conducted for rare earth extraction from leached solution using various solvents depending upon material and media. Some of the well-known solvents in the mining industry including Cyanex 272 (Di-2,4,4,-trimethylpentyl phosphinic acid), D2EHPA (Di-2-ethylhexyl phosphoric acid), Versatic-10 (Alkyl monocarboxylic acids). In 1958, Peppard and research team investigated the generalized overall reaction in extractants. [49]



In the above equation the Ln stands for any lanthanide series rare earth metal, A is an organic anion and over scoring denotes that the species present in organic phase. However, acidic extractants aggregated as dimers in non-polar organic solutions, thus lowering the polarity. As a result, the modeling of reactions as cationic extractants are more intricate. Therefore, rare earth complexes formed may contain undissociated organic acid. So the equation is depicting the process as;



Equations 2.6 and 2.7 distinctively represent the fact that the extent of rare earth extraction with cation exchangers increases by increasing the pH of the aqueous phase while the stripping process increases with acidity of the aqueous stripping solution. After extensive research, many researchers concluded that D2EHPA (*Di – (2 – ethylhexyl) phosphoric acid*) and HEHEHP/PC 88A (*2 – ethylhexyl 2 – ethylhexyl phosphonic acid*) are considered to be suitable extractants for the separation of rare earth metals. These acids are also called

organophosphorous acids and show the same mechanism which is reported as equation 2.7. In 1989, Reddy investigated that D2EHPA can be used with dilute kerosene for the extraction of *Y*, *Er*, *Dy*, *Tb*, *Gd*, and *Ho* from aqueous chloride solution. The relationship between the *HCl* solution and DEHPA is inversely proportional. *Er* separated from solution in first stage, while *Gd* remains as an end solution. Peppard and Wason in 1961, investigated separation of lanthanides and found separation in following fashion in Toluene with addition of 0.75M of D2HPA as $Lu > Yb > Tm > Tb > Eu > Pm > Pr > Ce > La$. These rare earths were extracted from 0.5M *HCl* solution. The separation factor for all the rare earths was uniform at 2.5.

The solvent extraction process has been used for chloride solutions of Monazite ore for extracting LREEs using D2EHPA. However, PC 88A as weaker acid compared to D2EHPA has been created by Hitachi and it shows better performance of extraction of REEs. Figure 2.4 shows the mixer-settler arrangement in typical industrial environment. At first, the light and heavy rare earth metals were removed from chloride medium of Monazite using mixer settlers. This mixer-settler arrangement operated in the continuous counter-current mode by maintaining the required organic to aqueous (O/A) ratio and maintaining flow rates of both streams. These processes were reviewed by Thakur in 2000. [50]. The *Table 2-1* below shows the extracted values of elements.

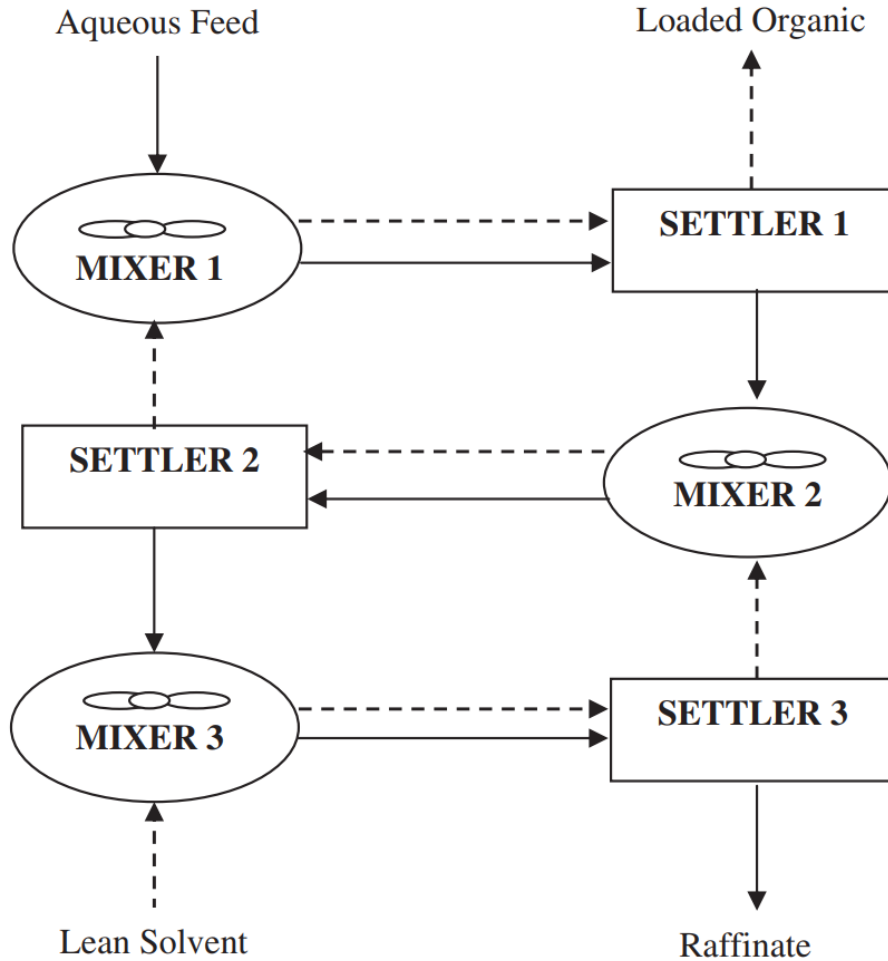


Figure 2.4: The figure showing Three stage counter current extraction in a mixer settler set up [50]

Table 2-1: Separation factors for extraction of rare earths by DEHPA and PC 88A (Maharana and Nair, 2005).

Rare Earth Element pair	DEHPA	PC 88A
<i>Ce/La</i>	2.98	6.83
<i>Pr/Ce</i>	2.05	2.03
<i>Nd/Pr</i>	1.38	1.55
<i>Sm/Nd</i>	6.58	10.60
<i>Eu/Sm</i>	1.90	2.30
<i>Gd/Eu</i>	1.43	1.50

<i>Tb/Gd</i>	0.98	5.80
<i>Dy/Tb</i>	2.40	2.82
<i>Ho/Dy</i>	1.90	2.00
<i>Er/Ho</i>	2.25	2.73
<i>Er/Y</i>	1.37	1.43
<i>Tm/Er</i>	2.90	3.34
<i>Yb/Tm</i>	3.09	3.56
<i>Lu/Yb</i>	1.86	1.78

The use of various carboxylic acids, including naphthenic and versatic acids, for extraction and separations of rare earth elements has been discussed by Bauer and Lindstrom in 1964 [51] and Korpusov and others in 1974. [52]. Preston in 1994 followed by Xu [53] and his research team in 2003, further in 2006, Singh others [54] reported that extractants having lower solubility such as cekanoic, neo-heptanoic, and some 2-bromo alkanoic acids also act as good extractants for rare earths separation process. Much of the past research using carboxylic acids is concreted on the extraction behavior of Y and its association either with the acidity of the extractant or steric hindrance caused by the carboxylic acid structure and the atomic number of rare earth ions. Generally, Versatic 10 and naphthenic acid are employed for Y extraction. However, utilization of naphthenic acid alters the composition of the extractants and is also highly soluble in water which leads to substantial loss of the reagent. [55]

2.3 Rare Earth Metallization Technologies

In field of magnet production, pure metal forming processes are critical. The higher the metal purity, the better magnetic properties are produced. The most common working technologies are electrochemical depositions showing efficient energy usage. The first recorded investigation

into the idea of electrically decomposing rare earth oxides to generate rare earth metals in a fluoride bath happened in 1907. [56]. Researchers Morrice and Henrie in 1967, Morrice and Wong in 1979, [56], [57], [58] from the Bureau of Mines conducted a series of foundational investigations on the electrolysis of rare earth metals in the fluoride molten salt system from the 1960s to the late 1980s, laying the groundwork for the later development of oxide-fluoride molten salt electrolysis technology. Based on the study, many patents were claimed by Goldsmith and Kruesi in 1973 and claimed by Sharma in 1987 for electrowinning rare earth metals and related alloys. [54]. As the Neodymium Iron Boron mixture ($B - Nd - Fe$) started growing its applications in industries such as wind turbine industries and computer hard drives (HDDs), the demand for rare earth elements led the substitution of oxide-fluoride electrolysis for chloride molten salt electrolysis.

Reported by Pang Siming in 2011 [59], rare earth oxides are less expensive than chlorides and do not necessitate any additional pre-treatment processes. In the oxide-fluoride process, the anode products are more favorable, which are carbon dioxide (CO_2) and carbon monoxide (CO). With the advancement of technology over the last few decades, the recovery and current efficiency have increased to the point where they favor oxide-fluoride electrolysis, with the reported recovery in the process being more than 92 percent and the current efficiency being 70-80 percent which is also discussed by Pang Siming and others. [59] The cell capacity with fluoride baths is typically 4,000-6,000 amps, however some manufacturers have increased the unit cell capacity to 25,000 amps mentioned by Liu and coworkers. [60]

In early 2000 Zhang [30] and research team measured the density for the $NdF_3 - LiF$ electrolyte system along with addition of Nd_2O_3 with the method of Archimedes generating the following empirical correlation, which is function of temperature, $t(^{\circ}C)$ and content of NdF_3

c (wt. %). The correlation also holds true for c in range between $73\text{wt. \%} < c < 83\text{wt. \%}$ and $1000^\circ\text{C} < t < 1100^\circ\text{C}$.

$$\rho = -4.11 \times 10^{-4}(c^2) + 0.14(c) + 4.134 \times 10^{-4}(t) - 1.5 \times 10^{-5}(c \cdot t) - 3.82 \quad (2.8)$$

Porter and colleagues [61] completed a series of studies on the oxide solubility in molten fluorides in 1961. Representative samples from an oxide-saturated melt were acquired for oxygen analysis and a graphite filtration system was built to extract analytical samples free of suspended oxide. The sample's oxide content was determined using an inert-gas fusion method. The solubility of CeO_2 in the $\text{CeF}_3 - \text{BaF}_2 - \text{LiF}$ (63 – 16 – 21 wt. %) in this research was reported with an average of 2.1 wt. % at 850°C and 1.4 wt. % at 800°C . Guo et al. [62] [63] suggested a semi-analytical model for rare earth oxide solubility in molten fluorides salts. In this study, they collated available literature data on the solubility of REOs in fluoride melts, as shown in Figure 2.5. The solubility of Nd_2O_3 in the $\text{NdF}_3 - \text{LiF}$ system with varied compositions and temperatures is forecasted and compared with existing literature data using the model created in their work.

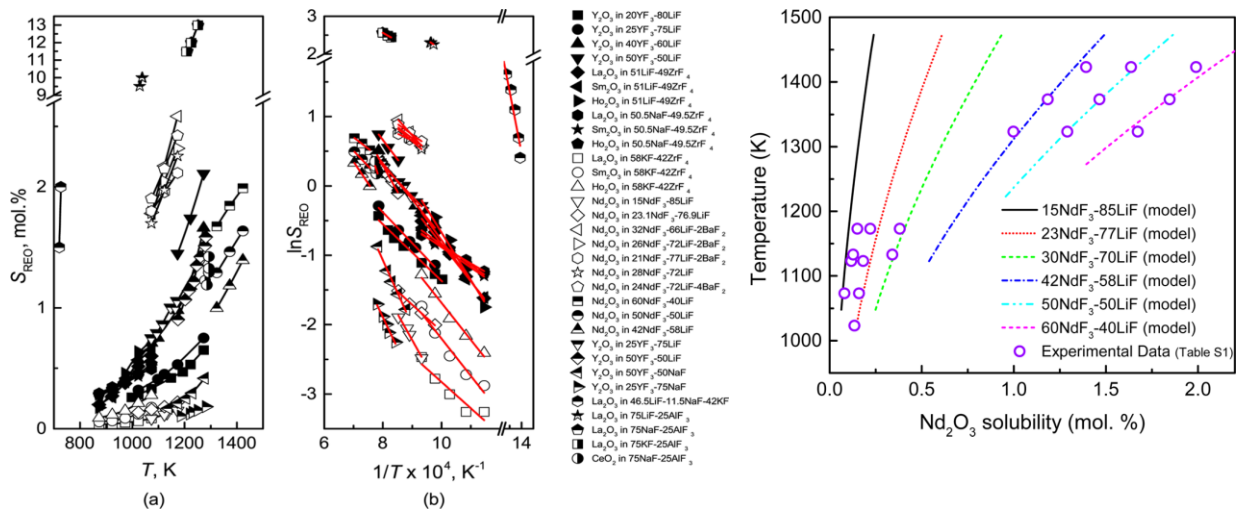


Figure 2.5: The first figure showing solubility data presented in terms of graph rare earth oxides in fluorides molten salts, the second figure shows Nd₂O₃ solubility in fluoride melts with different NdF₃-LiF compositions and at different temperatures in Guo, et al' work [63]

One of the most important electrochemical properties for the electrolysis process is the electrical conductivity of the REE fluoride electrolyte. High electrolyte conductivity is essential for reducing resistance loss and improving energy efficiency. In terms of the rare earth fluoride electrolyte system, little study has been documented in the literature. Keller and others [64] conducted the measurement of the electrical conductivity for the (REE)F₃ – LiF fluoride melt with the conductance cell, however due to lack of data points and no intent of accurate measurement of electrical conductivity in their research, their work does not provide fundamental aspects of research. Zheng and Zhu [25] research team continuously manipulated the cell Constant Voltage, Constant Current (CVCC) technique for measurement of specific electrical conductivity of the rare earth fluoride system with the addition of rare earth oxides. The change of the conductivity in the melt with the temperature was noted, and is inversely proportional to the oxide content. One of the reasons attributed towards lack of ample data points in past research is that the measurement involves high temperature and corrosive fluorides. Obtaining good data for electrical conductivity measurement is difficult due to decomposition of measuring probe unless it is made from platinum group elements. Thus, Kim and coworkers designed a conductance cell to suit this purpose using an Iridium plating probe and described their efforts on the electrical conductivity determination of molten alkaline-earth fluorides. The specific electrical conductivity was determined by the following equation:

$$\kappa = \left(\frac{dZ_{cell}}{dl} \right)_{Z'=0}^{-1} \times \frac{dG}{dl} \quad (2.9)$$

In above equation, $\left(\frac{dZ_{Cell}}{dl}\right)_{Z'=0}^{-1}$ refers to the change in cell impedance with changing electrode distance when imaginary parts Z' equals to zero, while $\frac{dG}{dl}$ represents the change of the cell constant with regards to change in electrode distance.

A review of the fundamental property investigation of the $Nd_2O_3 - NdF_3 - LiF$ molten electrolysis system reveals that little work has been done on the electrical conductivity of the fluoride melt, and there is uncertainty about the source of fluoride breakdown in the molten electrolysis process. However, both are critical for understanding the electrolysis process and addressing issues related to energy efficiency and PFC emissions. This study is motivated primarily to concentrate on these two issues and perform fundamental studies to provide guidance on boosting energy efficiency and lowering PFC emissions.

2.4 Carbon Dioxide Capture Technologies

The earth system has natural carbon dioxide sinks and sources which balance out the overall carbon utilization and production throughout the global dynamics by means of complex mechanisms. Human activities cause a rise in concentration of greenhouse gases in the atmosphere due to artificial carbon production sources such as fossil fuel plants and internal combustion engine vehicles. The following diagram called ‘Climate Diamond’ shown in *Figure 2.6*. graphically depicts the activities of humans contributing to the rising greenhouse effect, while nature is trying to adapt the human modified earth system architecture. [65] [66]

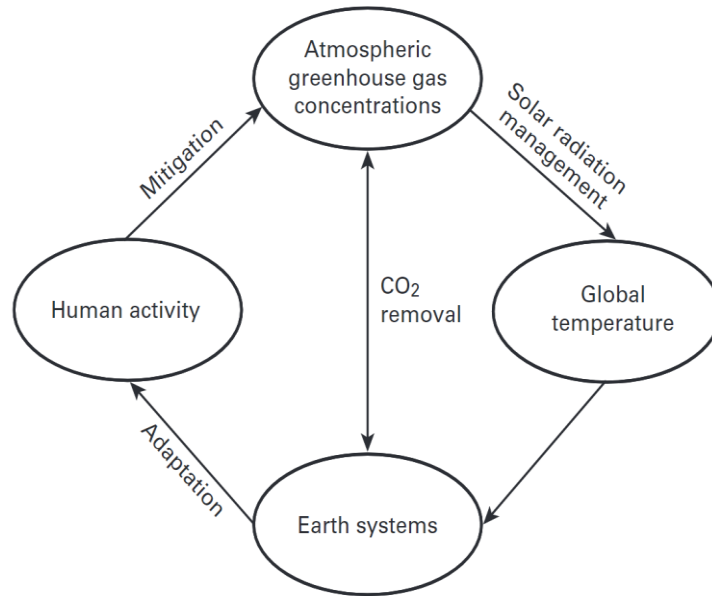


Figure 2.6: ‘Climate Diamond’ an overall ecosystem defining diagram.

There are three principle technologies which deliver the objective of capturing of CO_2 : Direct Air Capture (DAC), Point Capture (PC), and Mobile/Distributed Point Capture (MPC). The technologies involving DAC of CO_2 operate to capture maximum CO_2 in the atmosphere using biological processes or chemical processes. The process is also known as also known as non-point source. On the other hand, point capture technologies involve aspects of capturing CO_2 at the flue gas systems of fossil fuel power plants. Mobile/distributed point capture technologies involve IC engine vehicles, airplanes etc. prior releasing flue gases to atmosphere. Based on results of large-scale techno-economic analysis of capturing of CO_2 through atmosphere, the carbon capture is most effective on gas releasing systems of large stationary sources of CO_2 . It is much easier and cheaper to implement CCS on the flue gas systems of fossil fuel power plants and factories than it is for tailpipe of IC engine automobiles or the chimney of residential place.

After substantially steep rising global temperatures in past decades and fear of runaway greenhouse effect, Carbon Capture and Storage/Sequestration is one of many technologies which

captured attention of common people through popular cultural showcases and media outlets. Subsequently work towards finding solutions performed by researchers in academia and industries also received captive insights from media to showcase to common people. Various technologies for carbon capture involving chemical, biological, mechanical/physical processes have been developed over period of decades. While biological technologies are still under development, the chemical and physical technologies are summarized in *Figure 2.7* and discussed as follow:

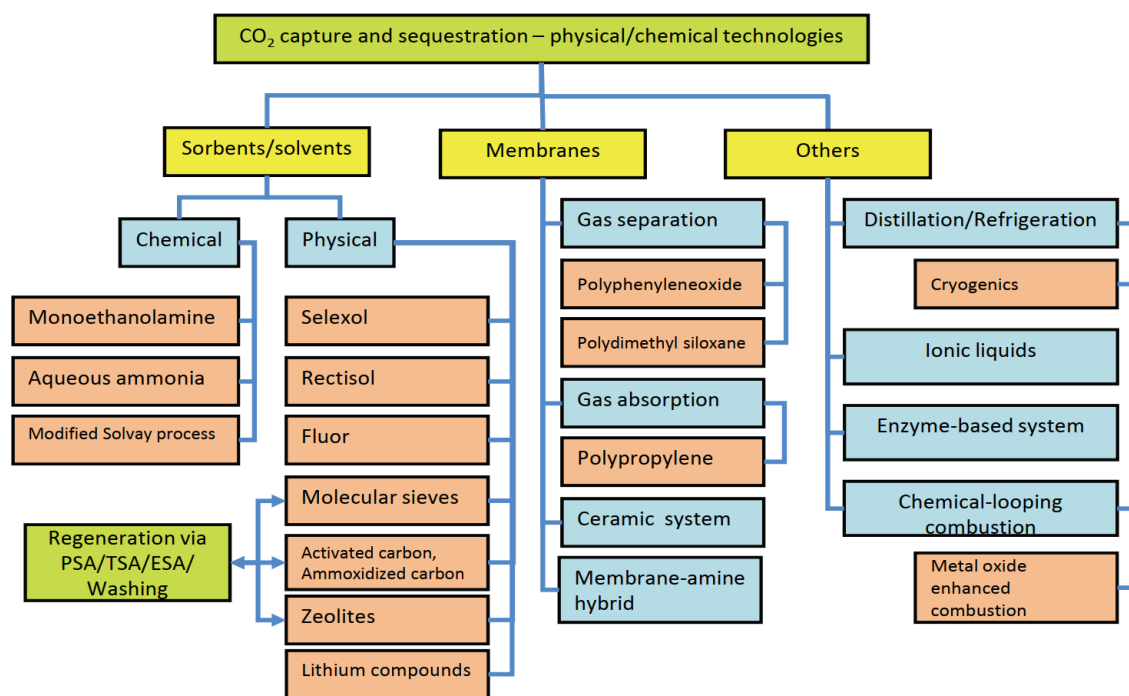
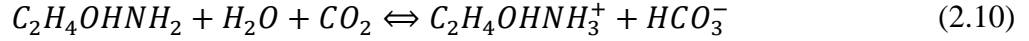
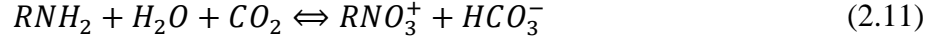


Figure 2.7: The figure showing Different technologies for CO₂ separation and capture (PSA/TSA/ESA: Pressure swing adsorption/temperature swing adsorption/electric swing adsorption) [67]

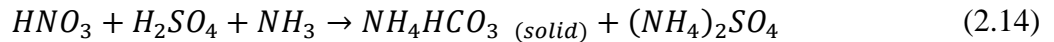
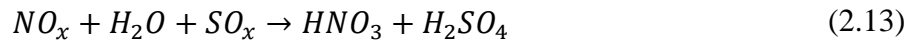
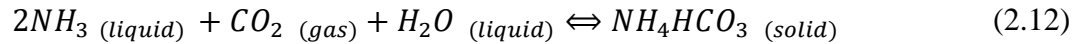
Sorbents/Solvents: This technology includes methodologies to capture CO_2 by means of chemical and physical reactions. The chemical reactions such as ‘2nd generation’ amine hindered solvent dependent reactions, for example the reaction of MonoEthanolAmine with CO_2 , is defined below:



The process is also defined as:



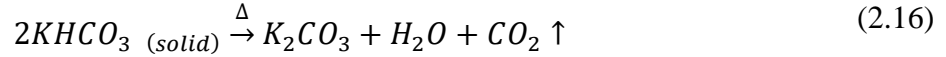
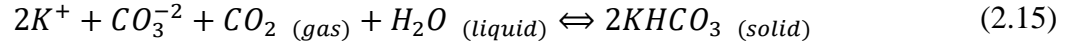
The aqueous ammonia process, also known as ammonia-based wet scrubbing, is similar to the amine process in many aspects but holds multiple advantages over MEA process. The aqueous ammonia process is less corrosive to the equipment inventory compared to the MEA process, has the potential for high CO_2 absorption capacity, and shows no degradation during absorption/regeneration. Tolerance for oxygen in the flue gas, cost economics, and the potential for regeneration using pressure swing are promising features for commercial feasibility. The process is described as follows:



The modified Solvay process, also known as dual-alkali process approach, where CO_2 and $NaCl$ react with each other in presence of ammonia (acting as primary alkali) as a catalyst under aqueous environment produces Na_2HCO_3 and ammonium chloride. The process is energy intensive due stripping of CO_2 from Na_2HCO_3 . The use of secondary alkali in the process captures 2 moles of CO_2 simultaneously liberating 1 mole of CO_2 . The overall process is inefficient.

Carbonate systems have been researched extensively, and are an example of CO_2 capture where solid sorbent is utilized. The Carbonate-based CO_2 Capture systems strip CO_2 from flue

gases using a soluble carbonate. The CO_2 selectively reacts to form bicarbonate salts. The following equations show the overall process:



The process of physical absorption involves capturing of CO_2 where the diffusion represents the fundamental process of mass transport. The energy usage required for these types of processes is comparatively lower than the chemical-based system as the physical solvents selectively absorb CO_2 according to Henry's Law without any chemical interactions. The Henry's law generalizes the overall process of diffusion, for isothermal conditions:

$$p = k_H \times c \quad (2.17)$$

Where p is partial pressure of CO_2 in the gas phase above the physical solvent, c is concentration of CO_2 in the physical solvent and k_H is constant of Henry's law dependent of temperature. The physical absorption process is mostly dependent upon partial pressure of CO_2 , and temperature. [68] [69]. With use of a suitable solvent along with lower temperatures, higher loadings of CO_2 can be achieved. Thus, the overall the process is economically and efficiency favorable.

In this category, Selexol and Rectisol are the two most common physical solvent processes. The processes usually operate around temperatures of $0^\circ C - 5^\circ C$ [70] [67]. Another process, the Fluor process uses Propylene Carbonate ($C_4H_6O_3$), the chemical used as a polar solvent to strip CO_2 from the gases. The physical binding of CO_2 the with Fluor solvent makes this process energy efficient as result of solvent regeneration. [67].

Other physical solvents in CO_2 capture applications are methanol, N-methyl-2-pyrrolidone, polyethylene glycol, dimethyl-ether, propylene carbonate and sulfolane [71]. While many studies and results of many technologies has been published in past decades, the current scope of literature reviewed for this dissertation is limited to chemical and physical solvent and sorbent-based CO_2 capture in support of the modeling efforts that were performed.

2.4.1 Process Modeling Studies

Multiple researchers investigating process modeling of CO_2 capture has been through the use of equilibrium models as a traditional way of modeling absorption and desorption columns for CO_2 capture. [72] [73] These models are established upon empirical co-relations developed from numerous experimental and theoretical investigations and involved solving fundamental equations. [74] [75] The process modeling tends to provide results by using empirical algebraic correlations to reduce the computation time. Thus, many research and development studies in Academia as well as industry are inclined towards ASPEN, gPROMs, ChemCAD based process modeling studies, rather than focusing on models developed from fundamental equations using iterative solver algorithms.

In this section of literature review, a brief explanation of post process modeling towards are laid out. ASPEN plus and other ASPENtech family products are chosen as representative of empirical-based tools for process modeling. [76] Using APEN, the process models for CO_2 capture are established with absorption columns in flowsheet format. These columns are divided into a number of stages and the assumption is that the vapor and liquid phase leaving a stage in the column are at equilibrium [77]. Although this model approach answers the problem statement, these simplistic model assumptions do not provide insights into the accuracy for real-time cases, thus, a rate-based approach is beneficial.

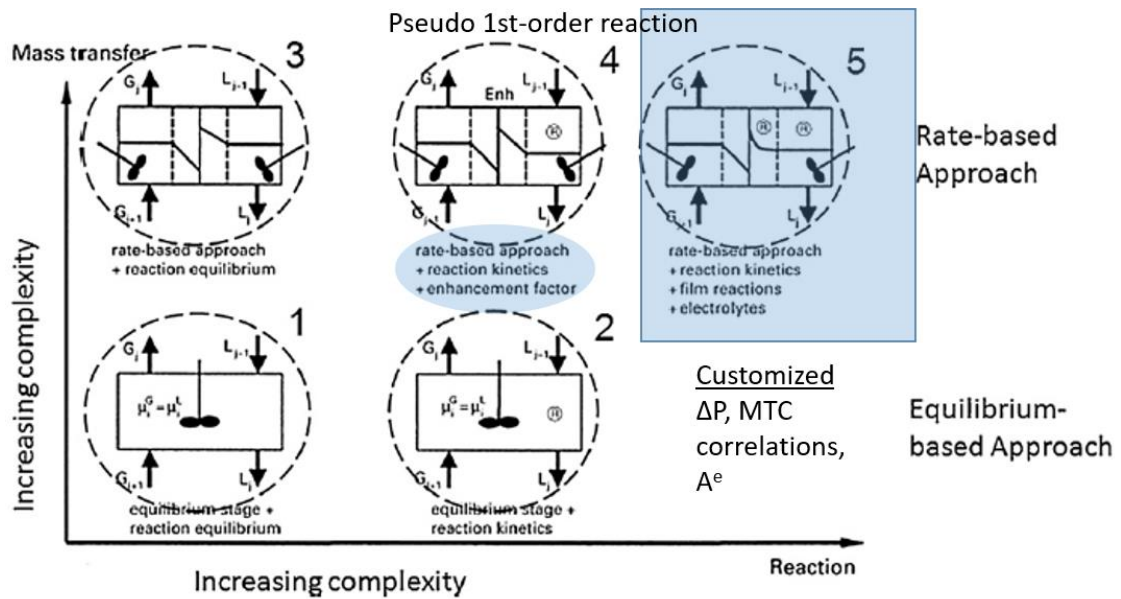


Figure 2.8: The figure showing pseudo 1st-order reaction approaches reaction versus mass transfer, process-based modeling insight [78]

Figure 2.8 represents different modeling strategies, and shows that as we move upwards and rightwards on the graph, the complexity increases. Additional effects like electrolyte influence can be taken into account. The process hydrodynamics such as liquid holdup, mass transfer coefficient, pressure drop, etc. can be directly involved via correlations in kinetics models. The rate-based approach also enables the absorber column outputs to be related to geometrical aspects and operating conditions allowing design optimization.

ASPEN RateSep, the rate-based mode of RadFrac allows for the rate-based modeling of absorption and desorption columns [79]. This rate-based modeling of mass and heat mass and heat transfer phenomena as well as kinetics of chemical reactions allowed with stage-based model as shown in Figure 2.9.

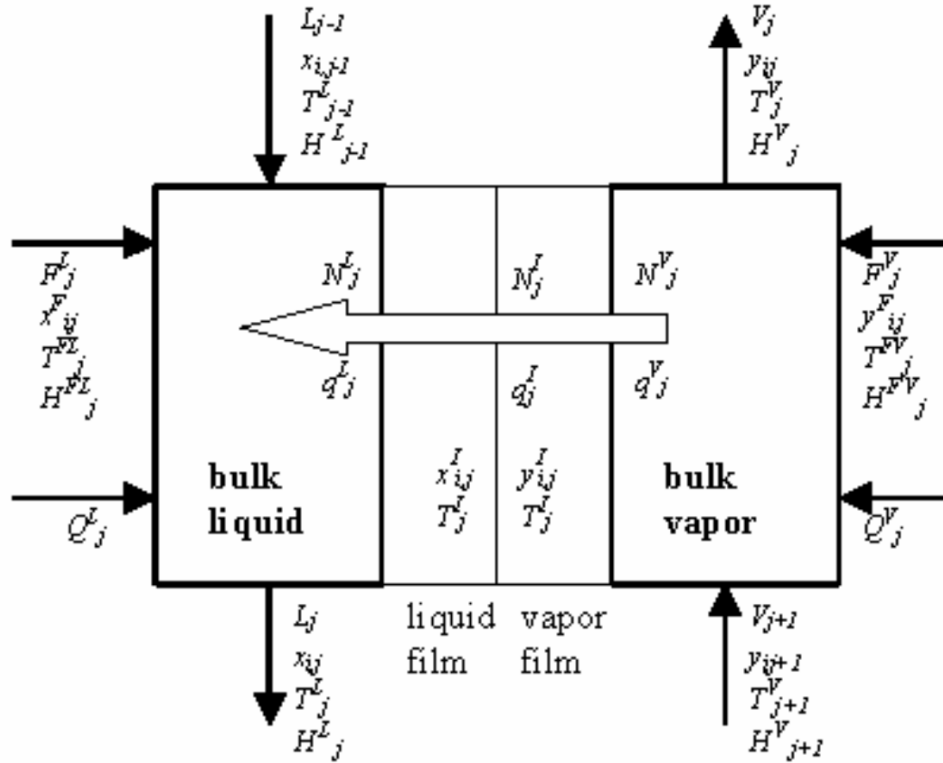


Figure 2.9: The figure showing process modeling tool ASPEN representation of a stage [78]

Usually in process modeling software, the following equations are solved:

- Mass and heat balances for the vapor and liquid phases
- Mass and heat transfer rate models to determine interphase transfer rates
- Vapor-liquid equilibrium equations for the interphase etc.

The ASPEN RateSep uses the solution proposed by Alopaeus to solve the Maxwell-Stefan multicomponent mass transfer equation [80] [81]. The modeling approach utilizes the two-film theory and allows for film discretization which is valuable to get a concentration profile at higher accuracy in the film for fast reaction. A Combination of film equation with separation balance equation for liquid and vapor phase, diffusion and reaction kinetics, electrolyte solution chemistry and thermodynamics. [81]

2.4.2 Numerical Modeling Studies

The aspirational and motivational force behind the current theoretical and numerical investigation is previously published study by Rajesh Singh and research group at the National Energy Technology Laboratory (NETL) [82]. The numerical investigation study unfolds the understanding of contact angle, liquid holdup, and wetted as well as interfacial area, and its dependence as transport properties of fluids which are tested in the numerical simulations. [83] The study also unveils its validation by comparing results with previously published experimental co-relations. Using ANSYS FLUENT tool the simulations performed in the multiple studies including NETL researchers are based on 3D geometrical domain. [15] [84] [16] [85]

Multiple researchers at NETL investigated liquid interfacial area and wetting area over inclined surfaces using ANSYS and OpenFOAM computational solvers [86]. These investigations looked at solvent properties and contact angle over an inclined flat plate for rivulet film flow analysis and later identical investigation of hydrodynamics with corrugated sheets instead of a flat plate. All the examinations were performed with multiphase volume of fluid methodology with ANSYS FLUENT software implementing PISO scheme for pressure velocity coupling, and MULES algorithm for interfacial area understanding. [82] [87]

Investigation of the dynamics of rivulet flow and other types of multiphase flows flowing through structured packings on multiple levels of magnitude, starting with a flat inclined plate surrogate model build and ending at detailed CFD investigation of a whole column section is conducted by Isoz and others [88] [89]. The exploration of phenomenon is purely organized using OpenFOAM numerical framework with multiphase flow Volume of Fluid (VoF) predictive strategy. The investigator also delves into simplified geometric modeling. [90]

Many examiners observe the packing pressure drop as well. Certain studies use single-phase simulations, by passing flow of various gasses ranging from air to cyclohexenes to determine dry pressure drop. [91] [92] [93] [15] [94] Either steady state or transient behavior is modeled by accounting for turbulence in the geometrical domain. Utilized tools are usually FLUENT or OpenFOAM along with that Star CCM+. ANSYS CFX is employed to calculate the pressure drop across the domain. [95] [96] In terms of open-source software development, due to versatility and verbosity of OpenFOAM, no other software is utilized other than OpenFOAM. The literature shows MFiX, an open-source software developed by NETL, is implemented [97] [98].

Although, many researchers have been investigating the numerical analysis of various packings, fewer researchers have implemented multidisciplinary optimization architecture, code-to-code comparison, or uncertainty quantification. The current research reported in this dissertation addresses the code-to code comparison to explore the fidelity of numerical simulations and also shows uncertainty quantification and reduced-order modeling. With the advancement of Machine Learning in CFD and with the help of orders of magnitude coarser grid, it possible to calculate accurately the time evolution of solutions to non-linear partial differential equations (PDEs), speeding the computational simulations ~41-fold faster. Although the research shows various developments using single-phase flow solution algorithms techniques, the overall development in the field of multiphase flows is primordial. [99]

3. RARE EARTH ELEMENTS PROCESS MODELING

The University of North Dakota (UND) Institute for Energy Studies (IES) has developed a process to extract rare earth elements and other critical materials from lignite coals. Results from research and development work funded by the U.S. Department of Energy, North Dakota Industrial Commission, and a number of industry sponsors are presented in the final reports for the first two Phases of this work [36]. Three major goals of UND's hydrometallurgical extraction project were to i) identify promising lignite or lignite-related feedstocks with total rare earth element content above 300 parts per million (ppm), ii) evaluate the lab and bench-scale process extractability of the REE using the identified resources, iii) determine and establish the process to recover REEs from lignite and iv) develop a process modeling framework for the REE extraction process for plant scale-up and predicting its performance using lignite coals from various areas. The study focused on resource evaluation and lab-scale extractability during Phase I, whereas Phase II involved the development of an economically and technologically viable extraction process where a method for cost-effective generation of higher purity concentrates (up to 65%) was developed and the preliminary framework for modeling was established. The results from that work formed the basis of the modeling work presented in this chapter.

In this chapter, the general process of modeling studies using METSIM software is discussed in the first section. A brief introduction to the novel hydrometallurgical process for extraction of rare earth elements being developed by the Institute for Energy Studies including data used to calibrate the METSIM model developed as a part of this dissertation is presented next.

The chapter then delves further into process modeling of the above-mentioned process, and standard operating/building manual for building processes in METSIM.

3.1 Process Modeling Using METSIM

The use of process simulation software is becoming increasingly common in various disciplines, particularly in chemical and metallurgy plant design. Experts and engineers benefit greatly from process simulation software since it allows them to analyze novel processes and compute heat/material balances, and are capable of modeling complicated processes that standard spreadsheet tools such as EXCEL cannot. This section discusses process simulation software, primarily explaining the application of METSIM and SYSCAD software in metallurgical processes. [100] The computational process and the application status of the process simulation software as related to the UND rare earth extraction process are also presented.

Metallurgical calculations are frequently isolated from process design software and therefore need to be performed using Excel manual computations. It is a high burden and work efficiency is very poor. At the same time, spreadsheet calculations are not sufficiently sophisticated to perform required calculations, especially in the face of more complicated processes, the need for multiple and variable raw materials, "three wastes," and the amount of output which are all difficult to estimate. [101] Process simulation technology computes by establishing a mathematical model using unit operations and thermodynamic techniques. Process simulation technology can compute material balances, heat balances, equipment size estimation, and energy analysis, as well as conducting environmental and economic calculations. The majority of the process simulation software is used in the petrochemical industry. [102] In the subject of hydrometallurgy, SYSCAD and METSIM are the primary process simulation software applications.

Modeling software packages typically fall within three categories:

1. Thermochemical property calculation software, such as HSC, OLI, STABCAL, and FACTSAGE;
2. Mineral process simulation and optimization software, such as JKSimMet, JKSimfloat, and USIMPAC;
3. Process simulation software, such as METSIM, SYSCAD, and IDEAS.

The research focus of this dissertation is on the process simulation software METSIM, a general-purpose process simulation system designed to help engineers perform mass and energy balances on complex processes. METSIM, in accordance with the sequential modular method, is made up of modules that contain subsets of equations that describe the design specifications and performance characteristics for each process stage. The system solves the equation subsets for each module, allowing for separate examination of each flow-sheet unit operation. Each module computes all of the outgoing stream variables dataset on design variables and input stream components, which can then be used as input stream values during the next process step. Actual data acquired from operational or pilot plants, comparable processes, or estimations given by the engineer may be submitted by the user. The modules use data arrays in the APL global workspace to acquire information on all autonomous stream variables. [103]

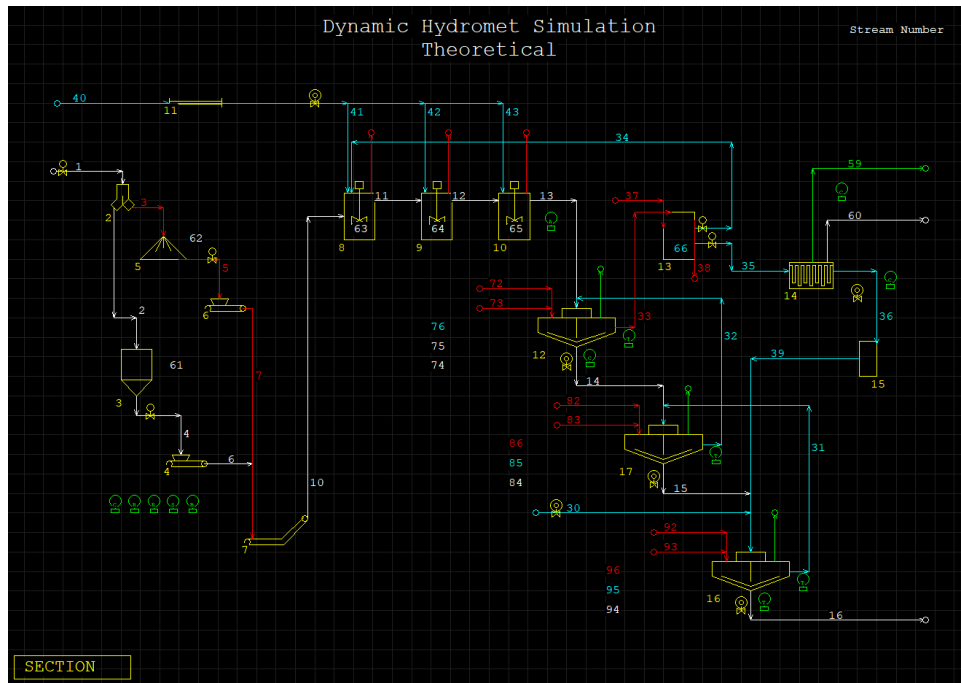


Figure 3.1: The figure showing example of METSIM window, providing process modeling insight

Figure 3.1 presents one of the examples of METSIM theoretical processes, depicting complexity in flowsheet modeling.

A modeling strategy is required and used while creating a METSIM model. The process modeling may be divided into eight major steps shown as flowchart in Figure 3.2:

1. Enter the project's fundamental information and choose characteristics like quality and time units.
2. Choose the components and create a system phase table that includes a list of all the elements and compounds in the system, as well as the phase of each compound.
3. Create a process flow chart that includes all operational and logistical components.
4. Enter the input stream's name, flow rate, and composition.
5. Enter the chemical reaction of each working unit and configure the required parameters.

6. Add the process controller, input function command(s) in order to obtain the required results.
7. Examine the results, input values, and process mechanism, and debug the model until no errors are displayed.
8. Present the outcomes.

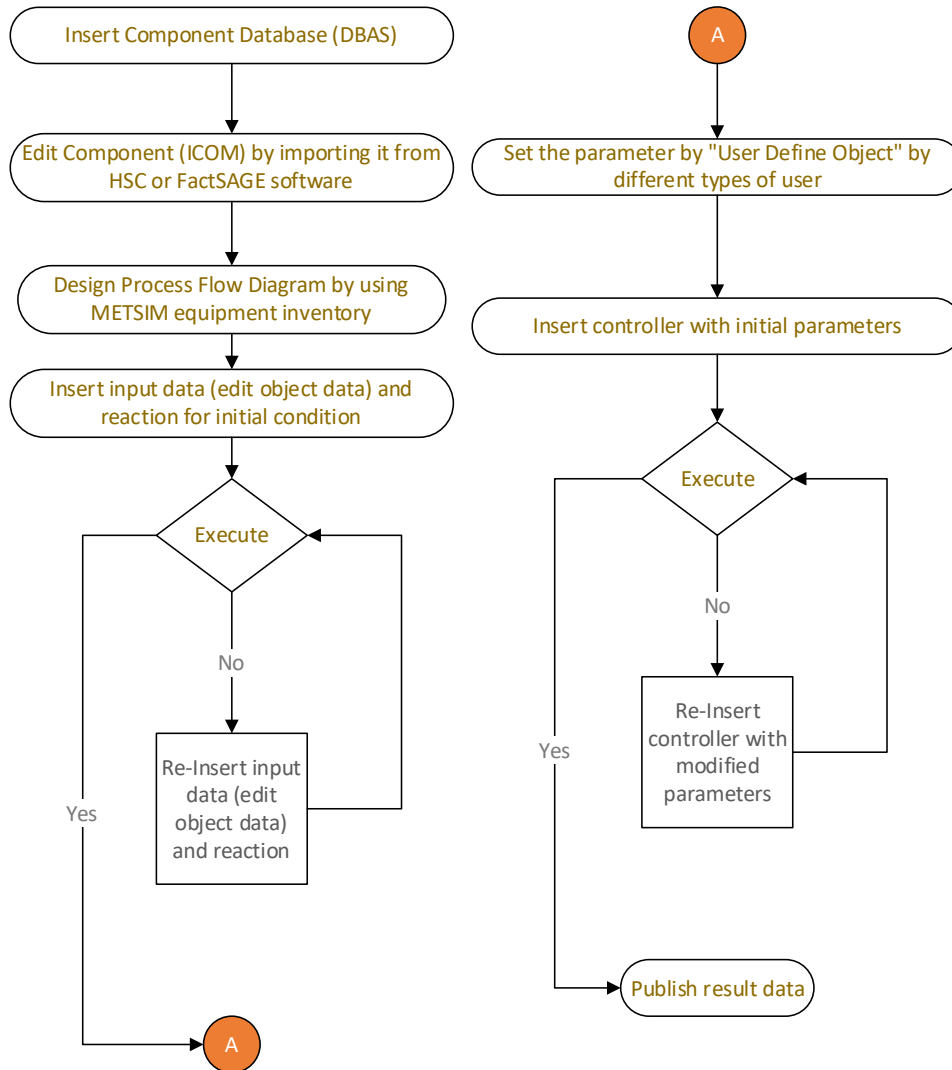


Figure 3.2: A generalized flowchart of METSIM functionality and standard operating procedure.

Only a handful of research is available in literature about the METSIM software and its metallurgical process modeling, primarily due to proprietary process paths that are devised using the software, which prohibits the open literature publications. [104] [103] Zhao et.al. have simulated the leaching of ionic rare earth carbonates with *HCl* using METSIM. [103] Kumari and others also simulated the steady-state leaching with *HCl* as solvent to optimize the extraction of Bastnaesite ore. [32] Yaqui and others, theoretically analyzed the radiation damage resistance of the $LaPO_4$ based Monazite type ceramics using atomistic modeling techniques. The molecular dynamics simulations were performed using LAMMPS to understand the radiation-induced amorphization process in monazite. [8] [105]

The research presented in this dissertation shows a process modeling framework using METSIM. With METSIM, it is possible to develop dynamic datasheets as inputs and outputs and to perform modeling and simultaneously exchange data dynamically between Excel and other applications. In this framework, METSIM performs the vital role of plant scale-up and equipment sizing while receiving essential data from other applications such as Excel and ASPEN. METSIM holds a vast inventory of readily designed unit operations such as filter presses, mixer-settler assemblies, tanks with agitators, rotary vacuum drum filters, coal spirals, and other unit operations critical to mining and hydrometallurgical extraction plants.

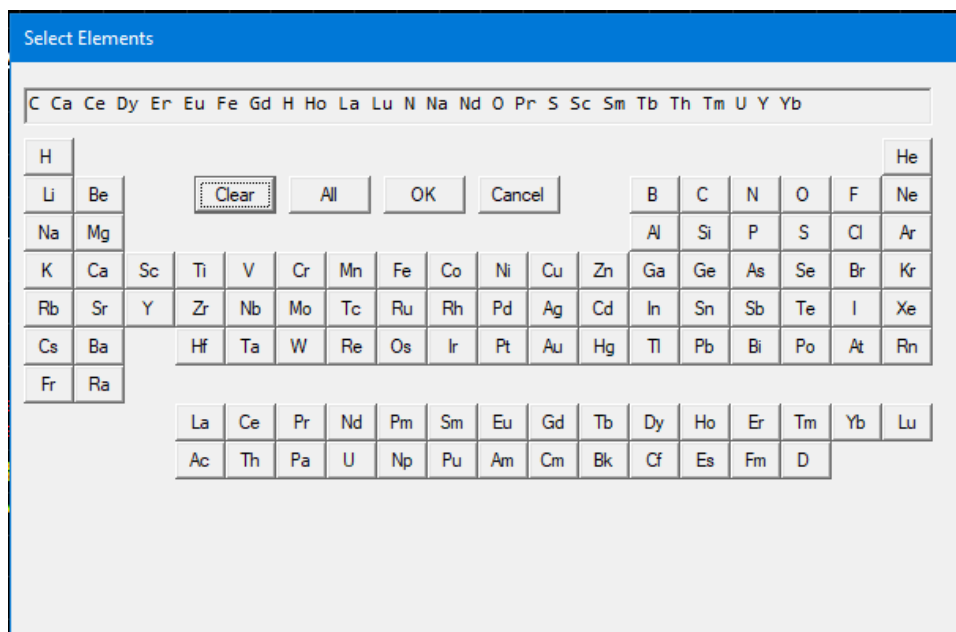


Figure 3.3: 'Select Element' dialog box where first elements are selected before beginning of any METSIM operations

The required elements for the process modeling are selected first from the 'Select Elements' menu as shown in *Figure 3.3*. The required elements selected in this menu essentially allows the METSIM software to provide the compounds which are present in METSIM's default database and available to the user as reactants and products. The software team at PROWARE has planned to couple the software with other database software packages such as FactSAGE, etc. After selecting elements, METSIM provides an automated response by opening 'Select Components' menu which allow user to select required compounds based on the elements which were elected to be part of process modeling as shown in *Figure 3.4*.

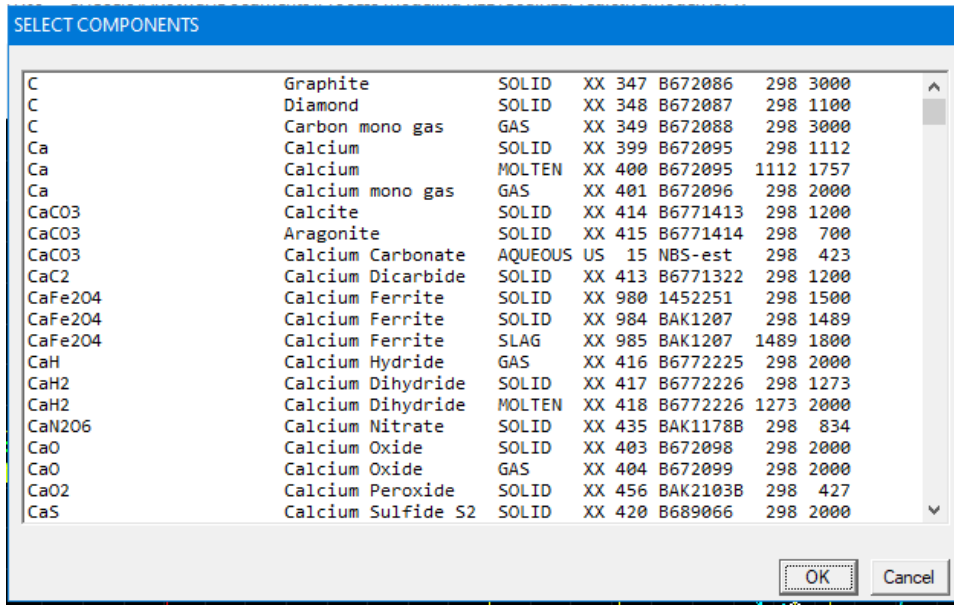


Figure 3.4: ‘Select Components’ menu which is automated operation in METSIM after choosing elements required in the Process Model.

After selecting the desired components for process modeling, the user can review selected components in the ‘Elements & Components’ menu which is *Figure 3.5*. Through this iterative process the research team defined the required components for the process modeling of REEs and CMs. The METSIM default database does not contain many of the required components which are recognized in the hydrometallurgical process developed at UND. To overcome this issue, METSIM’s ‘ICOM Edit Components’ menu option is utilized which opens an application dialog box shown in *Figure 3.6*. This option allows the user to include components which are present as product or reactants in the global METSIM software environment. These components are recognized by METSIM in all the streams which are defined in all process areas.

With the successful selection of components, project information such as process modeling flowsheet title, modeler’s information, flowsheet revision, units, and convergence tolerance for process modeling, etc. are defined.

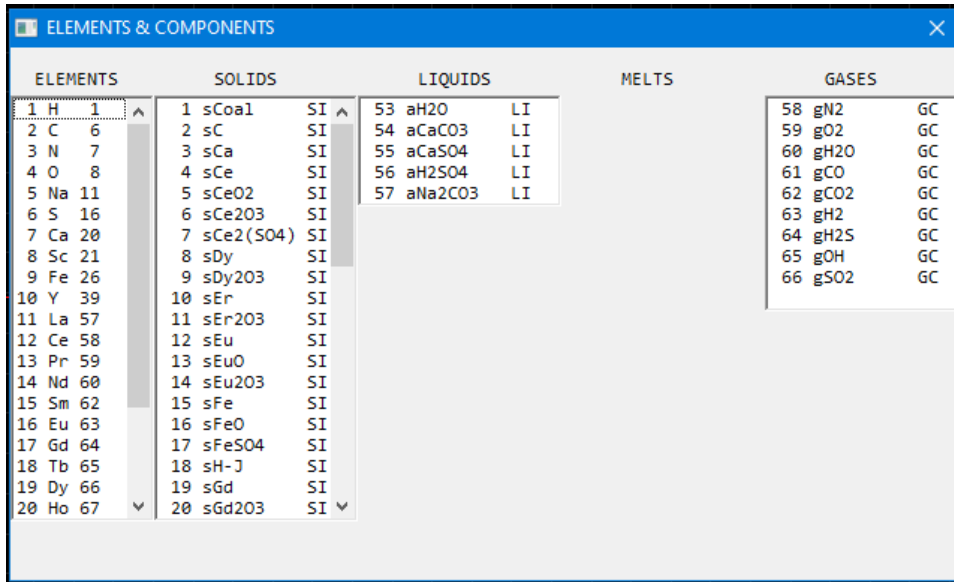


Figure 3.5: A menu showing list of selected components after addition of desired components based on the component phase these are categorized under 5 sections.

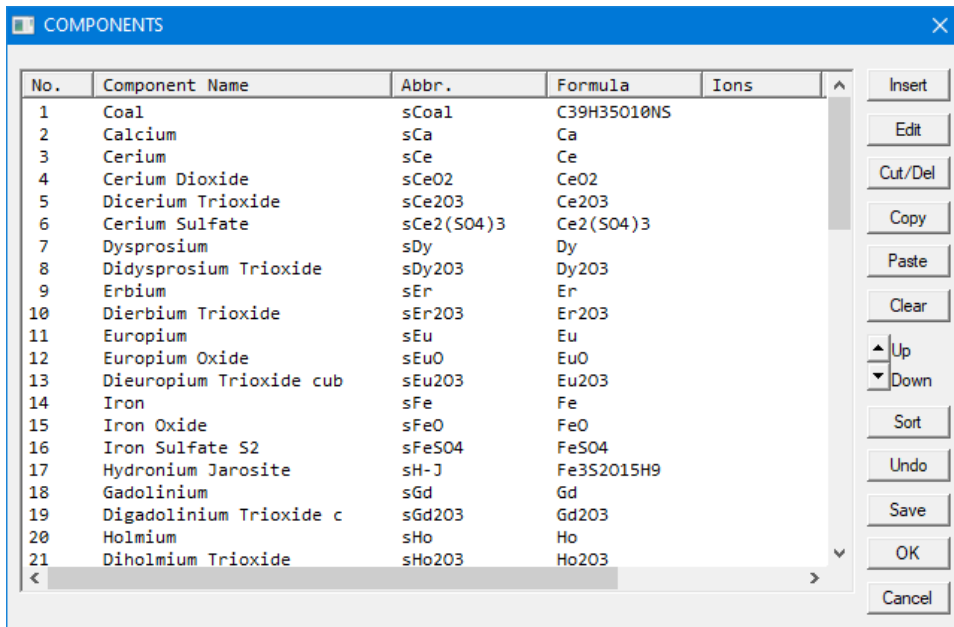


Figure 3.6: METSIM's 'ICOM Edit Components' menu where different components are added which are by default are not present in the database.

3.1.1 METSIM Unit Operations

METSIM, being designed and programmed specifically for mining and metallurgical extraction industries, holds a unique set of unit operations. For example, the UND process requires pumps of two categories: diaphragm pumps and positive displacement peristaltic pumps. METSIM has both types of pumps as unit operations in a ready-to-deploy format with no additional programming. METSIM has separate modules for hydrometallurgy, along with other modules such as coal beneficiation, all which are essential for designing of flowsheets. As a result, using METSIM it is possible to design and scale-up the plant equipment inventory and sizes based on available METSIM unit operations. However, algorithms of METSIM expect that the process modeler holds past commercial experience of mining plant equipment manufacturing or designing and/or procurement, and to use this knowledge to guide the design using unit operations given by METSIM for accurate sizing and estimation of capital and operating costs.

The following unit operations are available for designing flowsheets in METSIM.

Agitated Tank – Tanks are crucial equipment to mix material and conduct chemical reactions. The essential inputs to this unit operation are feed and discharge streams in the First tab. On the second tab, METSIM requires critical information from the user to either ‘simulate’ or ‘design’ the unit operation and based on feed stream material values, METSIM calculates required tank dimensions. On the third tab of the unit operation, the agitation related inputs are provided; ‘Mixing’ option is selected for agitation operation. In fourth tab, reactions are added to calculate reaction kinetics while mixing in tank.

Gravity Spiral – Since the REEs and other CMs are discovered in lighter fractions of coal, beneficiation of coal is needed to segregate tailing from middlings and concentrates. Thus, in METSIM the ‘Gravity Spiral’ unit operation is applied for the process of spiraling. Similar to the

‘Agitated Tank’ the first tab needs feed and discharge stream composition and flow rates. Here discharge streams are divided in two fractions tailings, and concentrates. A certain percentage of concentrates are recycled back in the spiraling process termed as middlings. In the second tab it is essential to define concentrates solids ratio. On the fourth tab of the unit operation, split factors are defined as percentages of REEs and CMs are separated in concentrates. Since the reactions occurring during the spirals are unknown but expected to be minimal, no reactions are defined.

Filter Press – Pressurized filtration is used during solids and liquid separation in the UND process after the slurry is fed from positive displacement pumps. After attaching feed and discharge streams which are defined in the first tab of the unit operation, parameters are defined under the second tab where first the system is defined as ‘design’ state. Using values of material balance in discharge and feed streams, parametrized values are calculated by METSIM. Under the dimensions tab, plate area, filtration area, filtration thickness, etc. are calculated. If reactions are occurring, they are defined under the reaction tab.

Pumps – Due to METSIM having unique mining related unit operations in its inventory, the software provides valuable information about the unit operation which can be delivered to manufacturer during procurement/designing of plant. Thus, the pump unit operation is added between various unit operations and can provide desirable parameters for designing pumping systems for particular media transport.

Thickener – During the development of REE extraction process, the lack of a filtration system in the impurity removal process led to decision of applying first an impurity thickening system and then applying a filtration system for maximum impurity removal. Thus, in METSIM, prior to impurity filtration, a thickener unit operation is deployed. The first tab is where feed streams and discharge streams are attached. In the second tab the first design option is applied and

balanced feed and discharge stream values are provided. METSIM calculates the design parameters and designs the desired impurity removal system. Later, the ‘Simulate Single Unit Operation’ option is selected and used to remove values from the discharge streams and based on varied feed streams the unit operation-based modeling is simulated. Later in the third tab Thickener specific parameters are added such as Underflow, Overflow, Particle size partitions, Overflow weir factors, etc. In the fourth tab, the lab tested thickening data is essential to model and simulate the thickener.

Screw Feeder – To feed solids, a screw conveyor unit operation is added to flowsheets. For steady-state process modeling, only feed and discharge streams are sufficient to attach the screw feeder. METSIM however requires experiential data of dust analysis and control to simulate this unit operation with dust control and capture option.

These unit operations are essential to calculate and simulate the UND extraction process. In addition to these unit operations, the process modeling involved stream splitters and stream mixers, assigning components of streams to be redirected towards each area. The use of stream mixers and splitters makes it possible to include stream recycling. The process modeling flowsheets and modeling results are discussed in the next section of this chapter.

3.2 Results and Discussion

The results of the testing completed in Phase-2 of UND’s DOE funded project demonstrated that extraction of REE from lignite is technically feasible [97]. The UND process generates concentrates in the form of REE oxalates and further into REOs. Additionally, the organically associated REEs and CMs in lignite provide a distinct advantage, allowing extraction of these elements with dilute acid at milder conditions compared to other metallurgical extraction

with coal associated projects, particularly using a pH-controlled mechanism. Downstream, the concentrated REOs are separated using specialized processes based on electrochemical reaction kinetics-based mechanisms. After separation of the REEs and other CMs associated in a combined material, four lanthanides namely, Neodymium (*Nd*), Praseodymium (*Pr*), Terbium (*Tb*), and Dysprosium (*Dy*) converted to pure metals in traditional method of electrochemically metallization. The results of these processes are discussed in this section. Further details of this process can be found in DOE report [36].

3.2.1 UND Process for Hydrometallurgical Extraction of REE

The following section discusses the REEs and CMs extraction process developed at UND using H-Bed lignite. While other coals were tested, for the scope of this dissertation, only H-bed lignite coal and its results are discussed. Further sections present the results of lab-scale and bench-scale parametric testing including continuous testing of the same coal. These results provide model specific information required for the METSIM simulation.

3.2.1.1 Lab-Scale Testing of H-Bed Lignite Coal

The UND process of REEs and CMs extraction from lignite coal is summarized in the block flow diagram presented as *Figure 3.10* the PFD is based on series of tests and their results which are discussed in further sections.

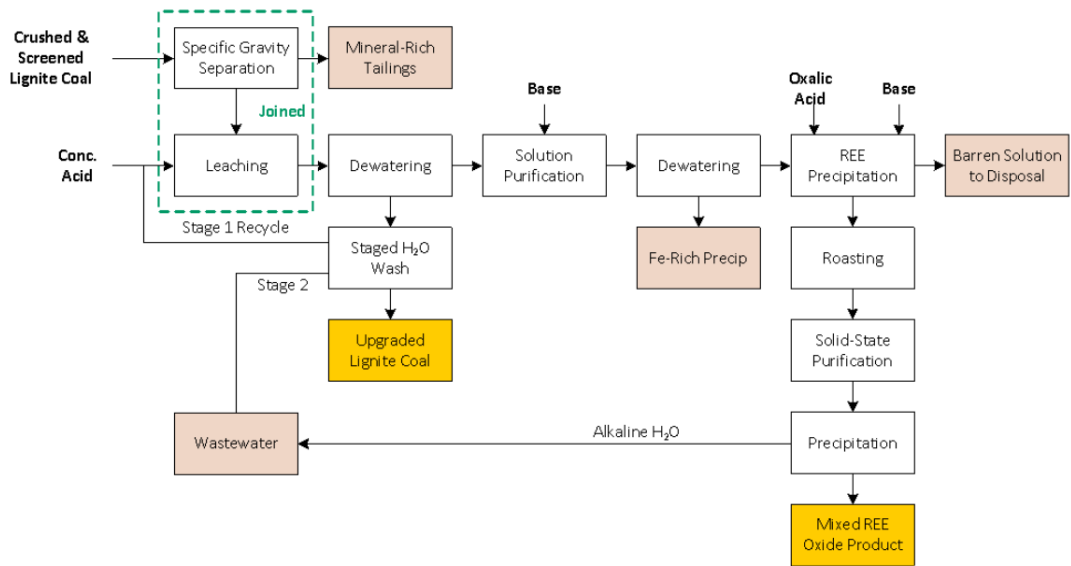


Figure 3.7: Process schematic of major unit operations for Phase 2 testing.

The manual excavation efforts of H-Bed lignite coal from Slope County, ND resulted in 18, 55-gallon drums totaling ~7000 lbs of sample. Each drum was dried and crushed to -10 mesh size and split for ICP-MS sampling. The REE concentration on a dry whole coal basis for each drum is shown in Figure 3.9. The drums range from 350 ppm to 830 ppm, with weighted average of 645 ppm, these values are significantly above pragmatic target of 300 ppm.

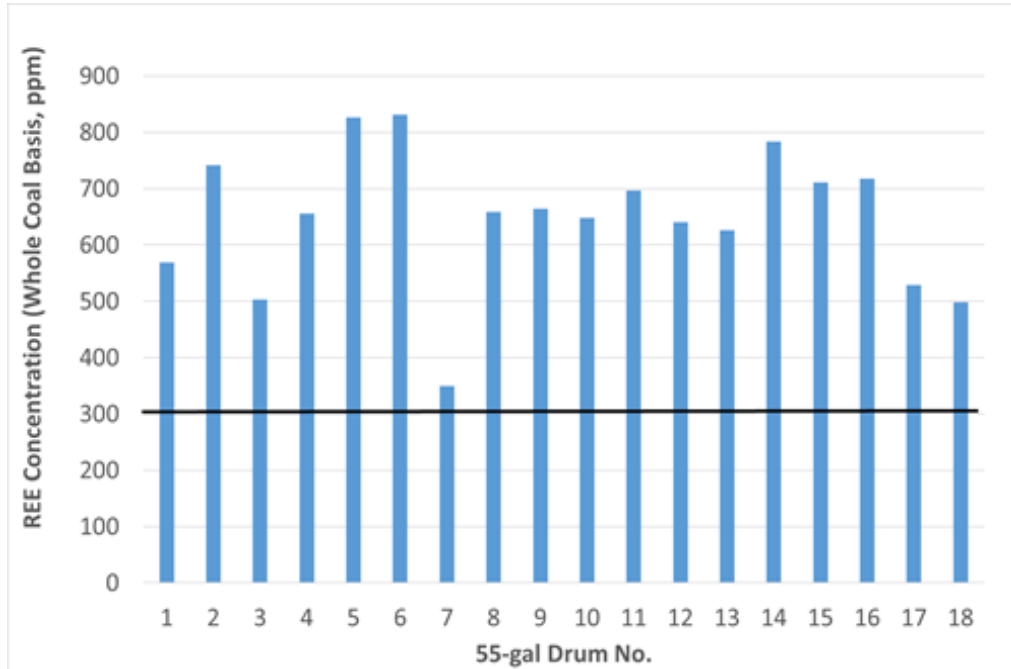


Figure 3.8: Total REE concentration for each drum of coal collected from an outcrop of the H Bed seam in Slope County, ND.

A blended H-Bed lignite was used to perform the tests on bench-scale system. *Figure 3.9* shows the leaching efficiency of H-Bed lignite with the increasing acid concentration (decreasing pH) in solution most suitable for leaching REEs and CMs. The acid requirement increases drastically to reduce the pH further while the extraction efficiency of elements plateaus at the higher acid concentration. Thus, as determined through economic factors, the second highest acid concentration was selected, due to similar leaching performance with considerably lower cost associated (acid and subsequent base consumption). An hour-long residence time is considered adequate based on aluminum leaching behavior and its leaching efficiency with respect to time (see *Figure 3.11*). Here, aluminum (*Al*) is analog to other trivalent elements associated in coal. The pH of the solution was kept low by constant acid addition

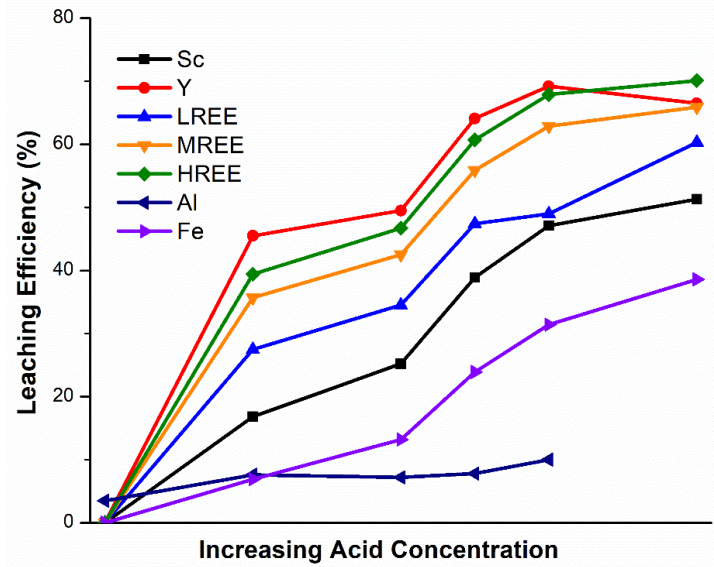


Figure 3.9: Leaching efficiency vs acid concentration for as-received H Bed lignite.

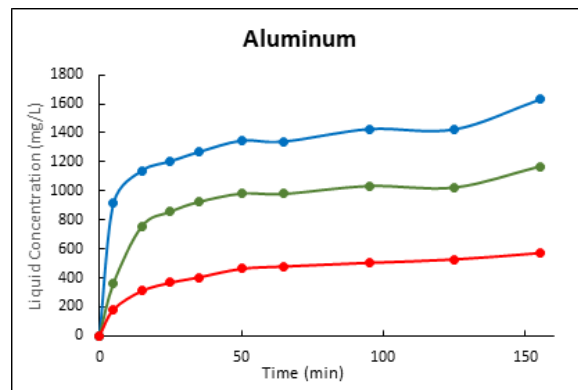


Figure 3.10: Leaching kinetics (through association with Al) in the as-received H Bed lignite.

Utilizing these optimized leaching conditions, impurity removal experiments were performed at various pH values. Based on impurities removal results it was found that, despite higher iron (*Fe*) removal at higher pH values, the other desired element's precipitation increased, leading to the understandable decision of reaching pH of 3.0 for the entire solution by addition of base, Na_2CO_3 . Different amounts of oxalic acid loading were used to determine accurate REEs

and CMs recovery. It was found that, at lower oxalate loading a substantial purity and yield of REEs between 70 to 85% was obtained. The medium value of oxalate loading was found to be efficiently recovering these elements showing >90% recovery. Higher oxalate loading leads to no change in REE recovery, however, resulted in excessive use of oxalic acid.

3.2.1.2 Bench-Scale Parametric Testing of H-Bed lignite coal

Bench-scale parametric testing: The bench-scale parametric testing of H-Bed lignite coal was essential due to identification of pH of the leaching process as a significant variable for selectivity and recovery. Additionally, slurry density and residence time of the leaching operation have been identified as key factors for process economics. *Error! Reference source not found.* shows the extraction efficiency of the 3 pH values (pH A, pH B, pH C) and shows the efficiency of extraction of REEs and CMs being lowest at pH A and the highest at pH C. Based on the similar leaching efficiencies between the middle and low pH set points (pH C), the pH B set point was chosen as the set point to be used for further testing.

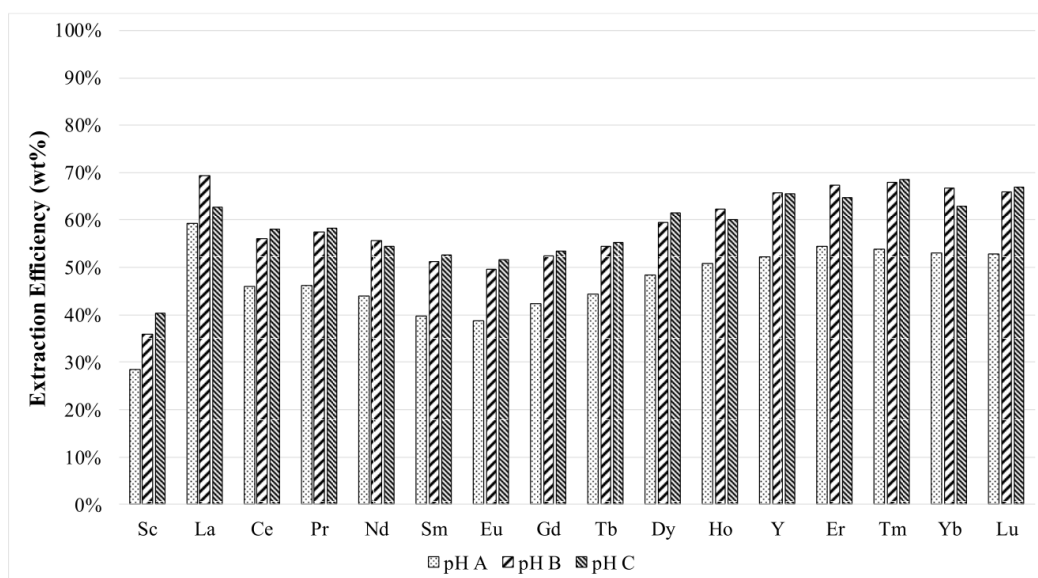


Figure 3.11: Extraction efficiency of REE from lignite coal using a pH-based leaching process at various pH values, with pH A being the high pH, pH B being the medium pH, and pH C being the low pH.

After optimizing the leaching conditions, the ideal pH required for impurity precipitation and removal from the leached solution with minimalistic loss of REEs and CMs was determined. Two different pH values were tested, namely pH 3.0, and pH 3.5. As shown in Figure 3.12, the first test completed at pH 3.0 removed 82% of iron (*Fe*) from solution. In the pH 3 test, a loss of approximately 10% was observed for all of the REE. The pH 3.5 test showed an 87% removal of iron and a significantly higher thorium removal than was observed in the pH 3 test, but also removed an additional 10% of most of the REEs compared to the pH 3 test. The scandium loss in the pH 3.5 test was 35% compared to the 10% loss in the pH 3 test. While the sodium carbonate requirements for the pH 3.5 test were not significantly higher than the pH 3 test (36 g Na_2CO_3/L solution for pH 3 and 37.6 g Na_2CO_3/L solution for pH 3.5), the additional losses in REE and an improvement of only an additional 5% removal of iron made the pH 3.5 test less optimal. Based

on these results a pH of 3 was chosen as the set point to be used for further impurity removal testing.

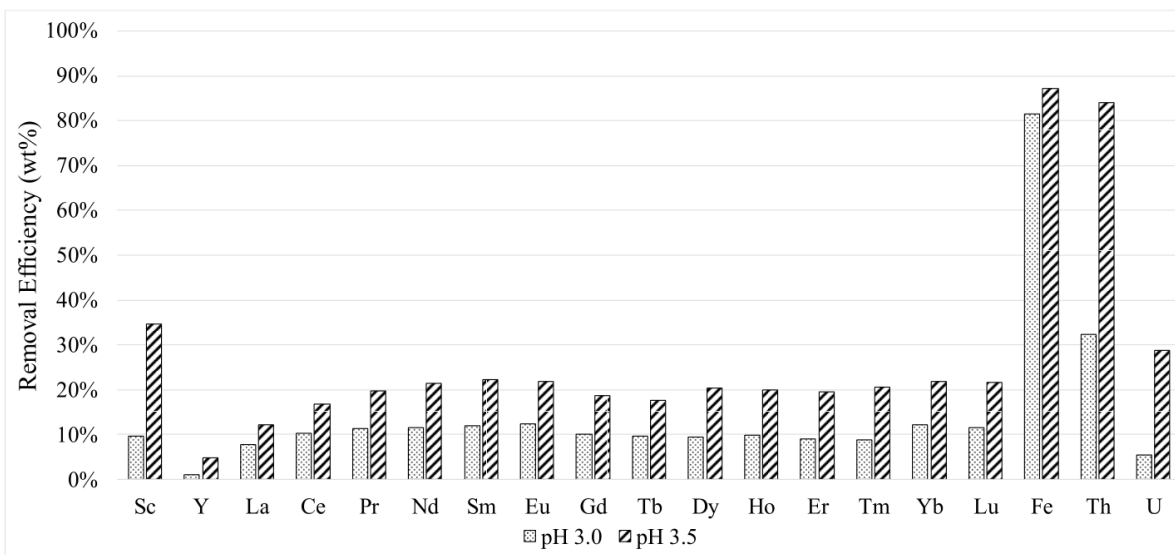


Figure 3.12: Removal efficiencies of REE, iron, thorium, and uranium in the impurity removal step at both pH 3 and pH 3.5.

The recovery efficiencies of REE at oxalic acid concentrates tested are shown in the *Figure 3.13*. With an oxalic acid concentration increment from left to right (Concentration A being the lowest and Concentration D being the highest), the figure shows the cumulative REE recovery at each concentration. It was observed that at Concentration D 95% or higher recovery was achieved for most of the REE. In this testing, two REE products were generated from each test completed. The first REE precipitation test used Concentration A of oxalic acid for precipitation of the primary product, and Concentration C to generate the secondary product. The second REE precipitation test used Concentration B of oxalic acid for the primary product, and Concentration D for the secondary product.

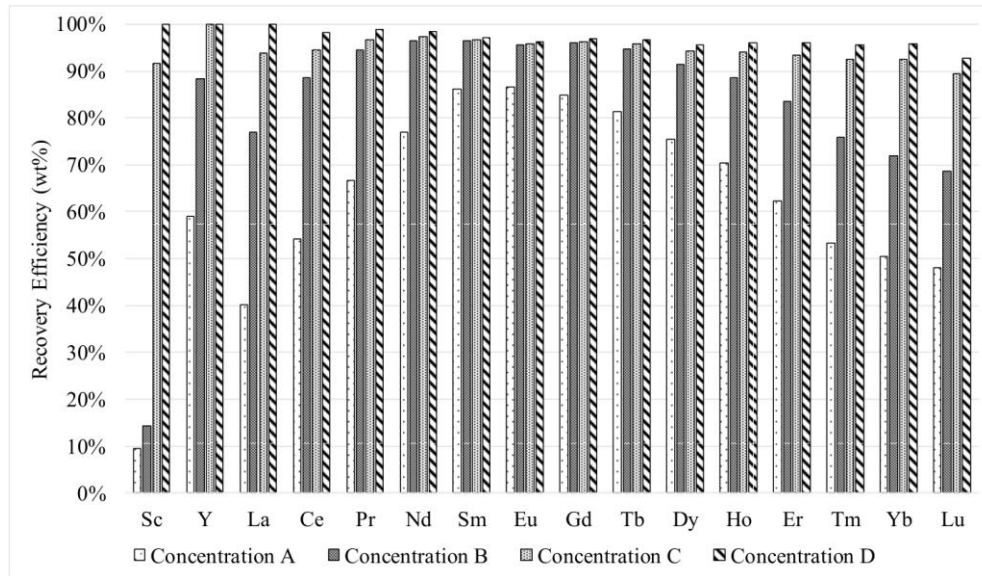


Figure 3.13: Cumulative recovery of REE at different oxalic acid concentrations. oxalic acid concentration increases from left to right (Concentration A is the lowest and Concentration D is the highest).

The purities of the REE in each of these products are shown in *Figure 3.14*. The purity of the Concentration A product is the highest of all of the products, and Concentration D has the lowest. The lower concentration of oxalic acid allows for a more selective precipitation of the REE by utilizing the low solubility of the REE compared to the other elements, such as calcium, which can also precipitate in this reaction and dilute the final product. The precipitation of calcium is the most significant diluent in these products, and accounts for the significant loss in purity between the Concentration A and the Concentration D products. The purity the Concentration A product on a total REE oxide basis was 68%, while the Concentration D product had a purity of 1.6% REE.

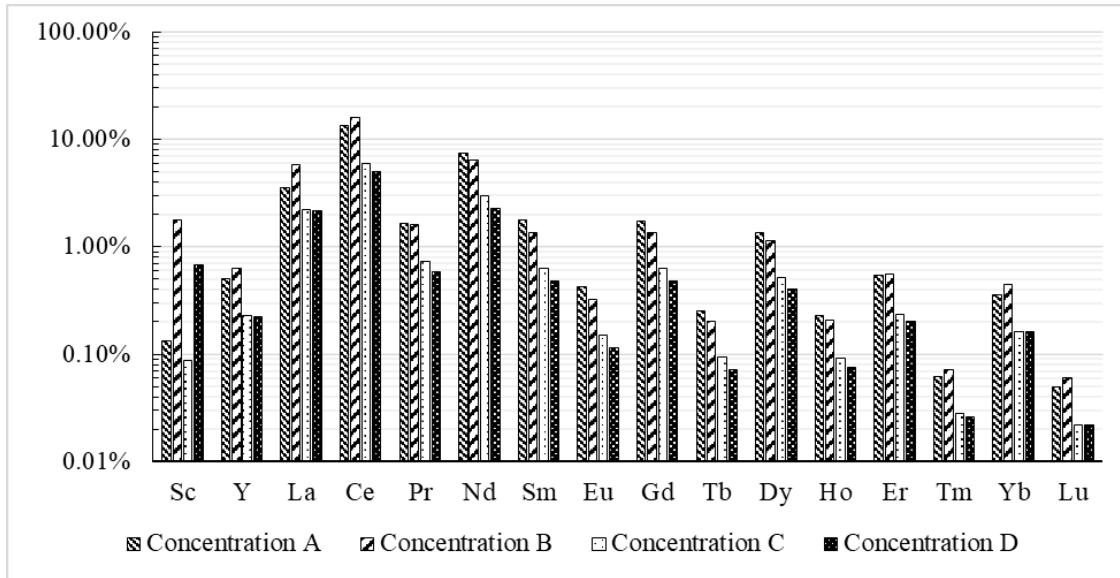


Figure 3.14: Purity of REE products on an oxide basis, which were precipitated at various oxalic acid concentrations. oxalic acid concentration increases from left to right (Concentration A is the lowest and Concentration D is the highest).

Based on these results, the oxalic acid concentration selected for the primary REE product was Concentration A. This will provide a primary REE product with the high purity. The concentration chosen for the secondary product was Concentration D. This was chosen in order to recover the maximum amount of REE from the Pregnant Leach Solution (PLS).

3.2.2 Semi-continuous UND Process modification

The section first presents the process specific aspects of the UND process to be modeled. Based upon the P&ID, the PFD built in METSIM is presented and discussed in Section 3.2.3 with a focus on model calibration and equipment procurement.

Figure 3.15 presents the piping and instrumentation diagram (P&ID) including the liquid recirculation line added to remove clogs and plugs due to thickened slurry in the ports of the filter press. This issue was identified during the shakedown of the entire system. For control of pH-

based set points with addition of concentrated acids/bases, feedback control loops were established. Control parameters including on/off control and PID controls were utilized for both solid and liquid feeds to the system. Evaluation of time delays associated with mixing, measurement, and dispensing of the pH adjustment chemicals was evaluated and included in control logic.

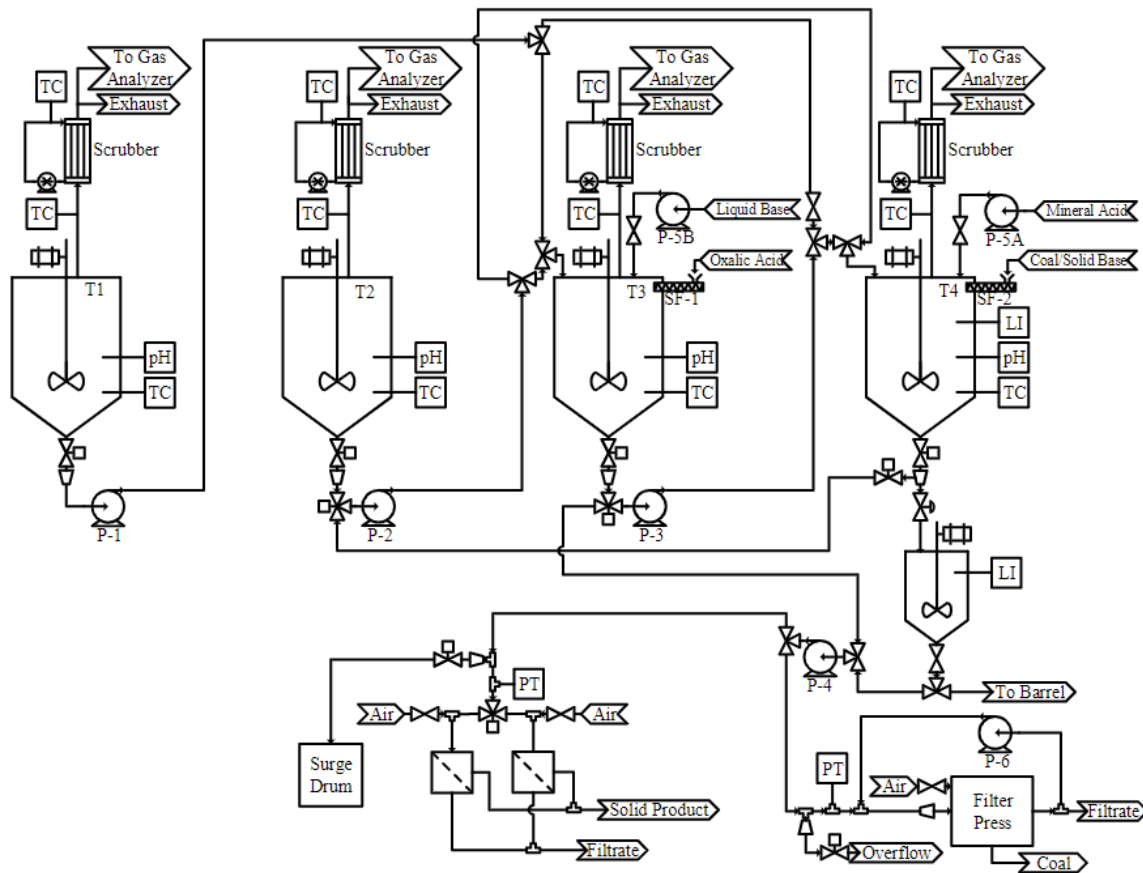


Figure 3.15: Piping and instrumentation diagram for the as-installed semi-continuous REE extraction system.

The operation of each major unit operation as it pertains to the METSIM model development is briefly discussed:

1. Leaching – During leaching tests, the coal feeder (SF-2) is used for feeding the coal into mixing tank (T4). Simultaneously concentrated mineral acid is fed using acid dosing pump (P5A) to generate the desired solids-to-liquid ratio. Slurry wash water generated from previous tests was fed using positive displacement pump (P2). The liquid-to-solid ratio was controlled using process instrumentation along with that acid dosing controlled using a logic-controlled feedback loop. After a preset residence time is achieved in T4, the generated slurry is fed into surge tank (T5) using a cyclic double dump valve. Below T5, a positive displacement peristaltic slurry pump (P4) was attached which created suction from T5 and fed the slurry by creating discharge pressure to meet the filter pressure requirements. Due to inconstancy in the slurry, there was a higher probability of occurrence of clogs in filter press, thus the slurry was diluted with additional liquid flow. However, maintenance of the pH was a critical goal, and thus the additional liquid was gathered from leachate filter press discharge. Continuous flow was maintained through the system until the filter press pressure reached the desired set point. After the completion of leachate generation, the filter pressure blowdown process started for dewatering the solids. In the next step, the coal was washed and wash water was generated for next test. For next experimental setup 35 gallon out of the total leachate was set aside to be used as recirculation fluid. With enough leachate generated, it was ready to process through downstream operations.
2. Impurity Removal – Cleaned leachate combined from multiple leaching tests, and at low flowrate, is fed into T4 continuously. Simultaneously using a PID loop, base is added to increase pH and precipitate impurities. Solids generated during the process were challenging for the inline process filters, thus liquid along with solids were gathered and placed in a barrel with the liquid decanted after 12 hours of solid settlement in the barrel.

3. REE Precipitation – The solution with the impurities removed is processed for recovery of REEs and CMs. The liquid is fed into mixing tank (T1) and then into mixing Tank (T2) using diaphragm pump (P1). In T2 oxalic acid is added to lower the pH as well as precipitation of REEs and CMs. The low pH liquid is then fed into Mixing Tank (T3) using pump (P3). Na_2CO_3 is fed using SF-2 to increase the pH value. Further, the liquid is fed into T4 which then is later fed through inline filters via P5 to gather solid precipitates. Following completion of primary REE precipitation, secondary product precipitation occurred via the same metric, at different oxalic acid concentrations.
4. Aluminum recovery – Filtered, REE-depleted liquids were pumped into the tank with the solid base equipment setup (screw-feeder/PID), and flow was pH controlled to set points. Resultant mixtures were pumped into a separate tank, where liquid base was used to complete the neutralization for product generation. Similar to the impurity removal, Al solids were also allowed to settle in barrels, with the thick slurries recovered from the bottom filtered for product quantification.

With satisfactory performance of all the unit operations the continuous tests were finished with acceptable amount of REE and CM concentrated product.

3.2.2.1 Semi-Continuous Testing on Bench-Scale with H-Bed Lignite Coal

The testing matrix for semi-continuous testing was divided into ‘weeks’. The initialization of semi-continuous testing using the bench-scale system was based upon leachate generation for recirculation to remove plugs in the filter press. Three leaching tests were conducted after leachate generation and the leachates generated during these leaching tests were also used as recirculation.

Figure 3.16 shows the leaching efficiency of each element during each week of testing and the week of leachate generation. The Week 1 processing show a lower percentage of recovery of REEs from coal during leaching, however increasing concentration of REEs and other ions were identified in the wash water after washing coal during leaching of Week 1. Another aspect shown is that through Week 1 to 3 the concentration of mono-, di-, and tri-valent ions increased with the recycle stream; however, do not concentrate the higher valance elements such as U and Th. This can explained through reaching equilibrium of solution at the pH level of interest, allowing recapture of trivalent and multivalent ions into the organic matrix of coal. Furthermore, this equilibrium point of multivalent materials includes deleterious materials such as U and Th. The concentration of REEs and CMs is increasing with time, indicating a true steady-state was not reached. Therefore, it is likely higher REEs and CMs extraction will be achieved during continuous testing. Also, with the addition of a recycle stream (wash water cycle), the weekly acid consumption reduced and an improvement in recovery of REEs and CMs was noted in Week 4 testing of the *Figure 3.16*.

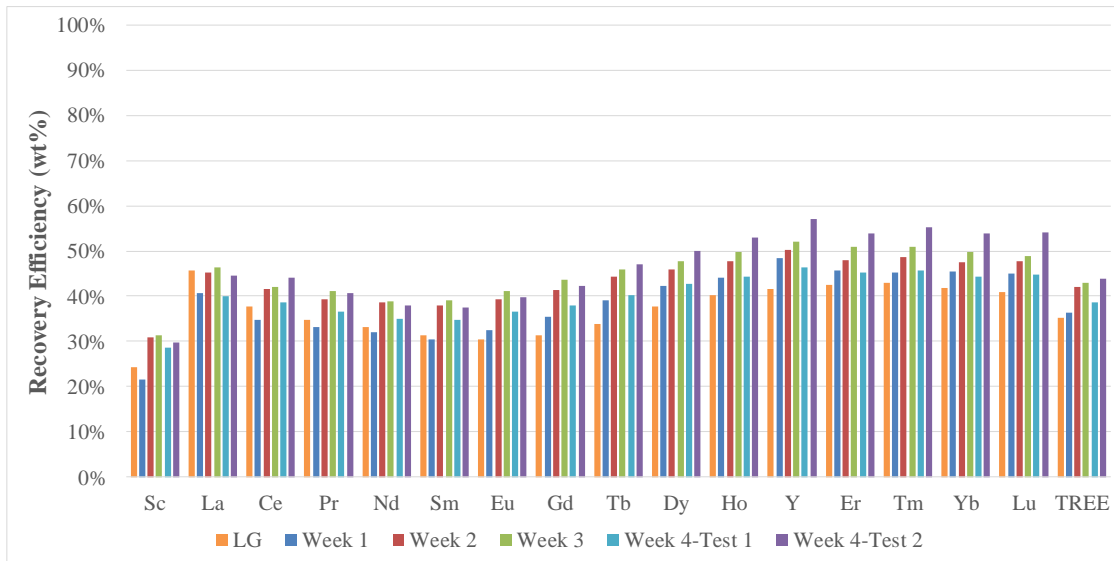


Figure 3.16: REE recovery from coal during leaching tests.

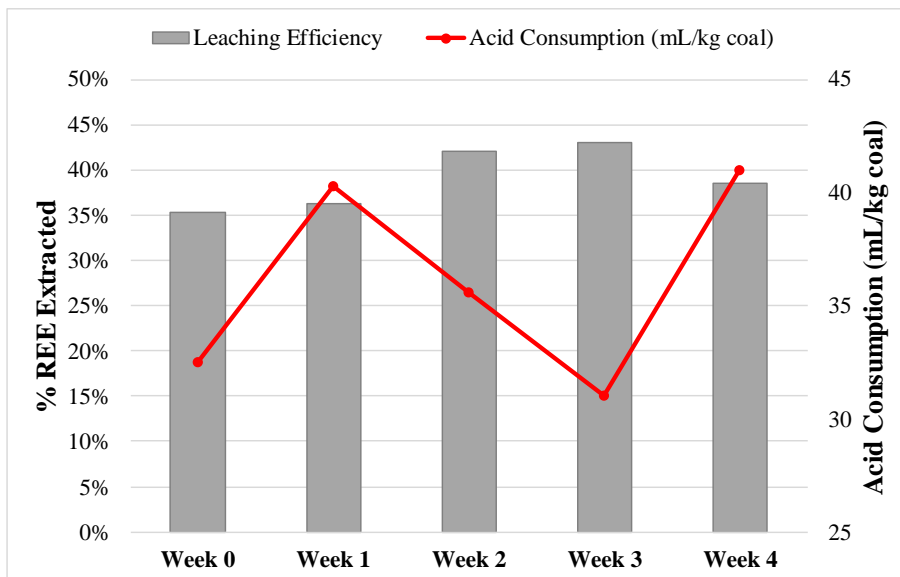


Figure 3.17: Overall REE extraction from the coal, acid consumption during leaching tests.

After generating all the leachate, during the impurities removal process, the results show extraction of over 71% of iron removal (Week 1, 2, 4) and over 25% of calcium removal (except Week 4) in Figure 3.18. During the Week 3 testing only 60% of iron removal with approximately

15% of loss of REEs and CMs was noted. The poor performance in Week 3 is the result of equipment issues, with the control valve under the tank malfunctioning, which required manual control of the valve and a residence time which was 50% shorter than the desired residence time. The shorter residence time did not give sufficient time for the solution to reach equilibrium, resulting in the losses of REE and lower extraction of iron observed in Week 3. The other weeks of testing all had <5% loss of REE.

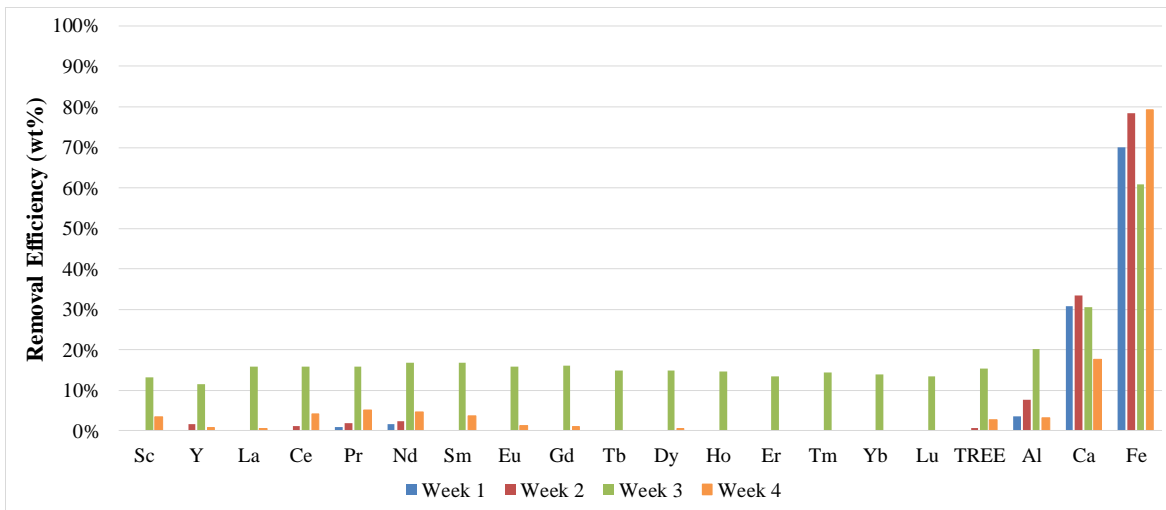


Figure 3.18: Extraction of elements during the impurity removal step for each testing week.

The total recovery of REEs and CMs from PLS using oxalic acid is shown in Figure 3.19. Due to challenges in pump calibrations the manual flowrates resulted in high concentration of oxalic acid in solution resulting in 100% recovery of REEs from solution. However, excessive consumption of oxalic acid, was noted. During Week 3, the experimental run with the correct pump calibration and a lower concentration of oxalic acid feed, the recovery of REEs was slightly lower compared to other weeks, however, the consumption of oxalic acid was significantly lower. However, during Week 3 the impurity removal in the previous step was lowest. The resulting high

iron level consumed oxalic acid, reducing the amount of available oxalic acid to recover the REEs, thus lower yield of REE during the recovery process.

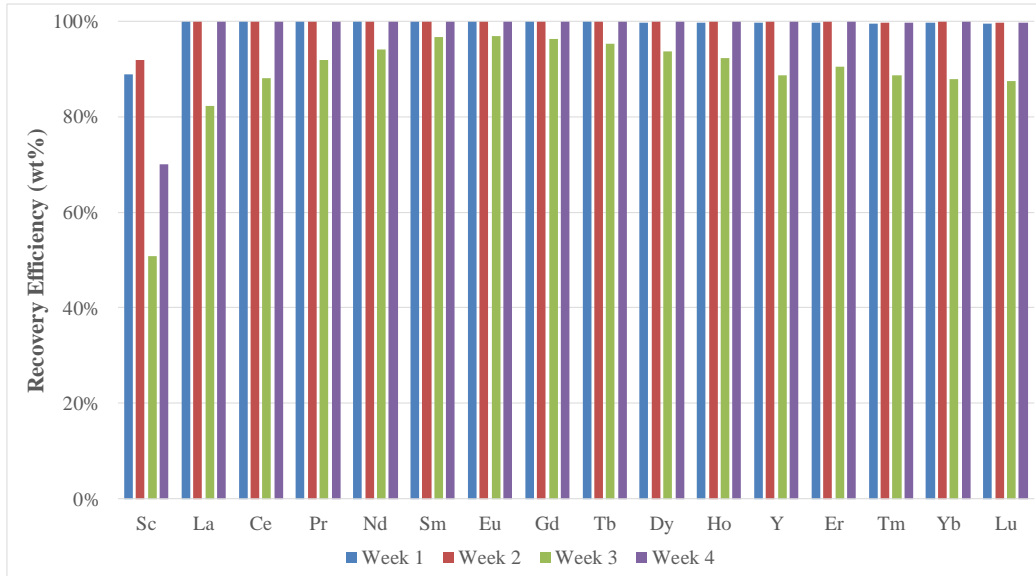


Figure 3.19: Recovery of REE from the PLS for each of the weeks of testing.

The continuous bench-scale based experimental testing was completed based on parametric testing conditions devised prior to continuous testing. Leaching efficiency was lower than expected, with the highest REE recovery being 43% during Week 3 (Figure 3.19). The primary reasons being a lower dewatering efficiency during the process of leaching REE from the coal. A challenge associated with lignite coal is its higher pore volume among its organic matrix, holding higher amount of aqueous media and ions which cannot be driven out with appropriate positive or negative pressure application during process of filtration. During Week 4 testing, the dewatering efficiency, being critical factor to cause lower extraction efficiency, was reduced due to clogs and plugs in filter press filling due to failures of the leachate recirculation pump. The incremental increase in acid consumption on Week 4 is due to setpoint for pH dosing implemented with a lower value

The work performed during Phase-2 of the project provided the experimental data generated from H-Bed lignite coal that can be used to build and validate a METSIM model. Using METSIM and ASPEN software packages, the goal is to provide predictive and reactive results using process model so that fewer tests will be required to determine the economic potential for other types of coals. These results are discussed in next section.

3.2.3 UND Process Modeling of REE Extraction

In this section, the author discusses the METSIM based process flow diagram and results. The previous section 3.2.2 the author presented the process specific aspects of the UND process to be modeled. Based upon the P&ID in section 3.2.2, the PFD built in METSIM is presented and discussed with a focus on model calibration and equipment procurement.

3.2.3.1 Process Modeling Diagrams

The unit operations previously discussed are depicted in PFD diagrams and include the input and output streams associated with these unit operations. The resulting PFDs are shown in *Figure 3.21, Figure 3.22, Figure 3.23, and Figure 3.24, Figure 3.25*. Reactions are not relevant in spiraling and in the leaching process area and therefore not defined. The coal, being a rock comprised of numerous organic complexes, making it impractical to define all the species in reactors. Due to the complexity of the coal matrix certain the following assumptions were made while developing the process model:

1. Process occurs in well mixed reactors
2. Reactions occur in steady-state
3. There are isothermal conditions in the unit operations

4. The REEs and other desired trivalent elements are situated in carboxylic acid bonds, thus coal is defined as amount of carboxylic acid based organic matter (*Figure 3.20*).
5. Based on the proposed reaction mechanism in *Figure 3.20* it is anticipated that the efficiency of REE is inversely correlated to the density fraction of coal, in other words, the best leaching efficiency is achieved for the light density fractions of coal.

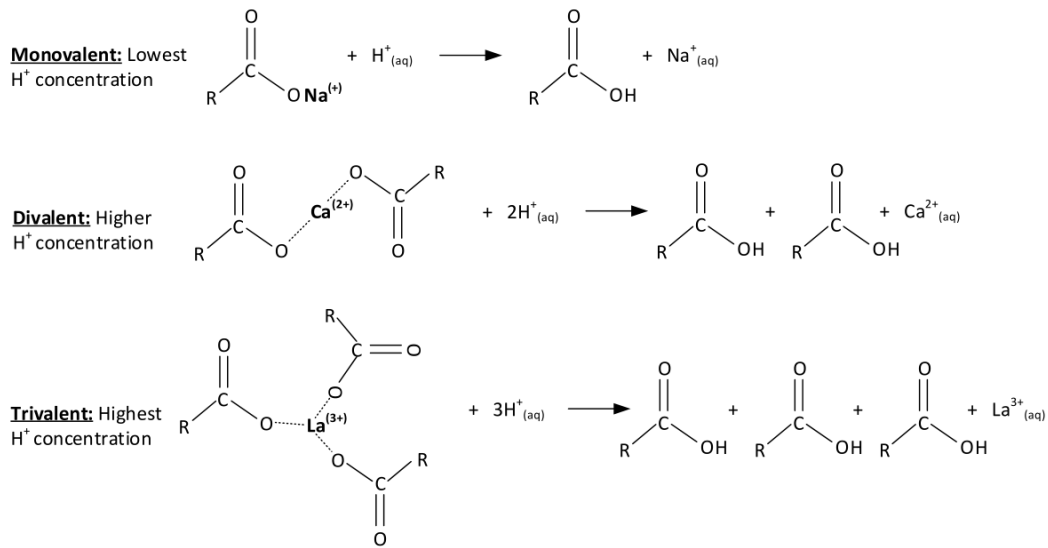


Figure 3.20: The apparent reaction mechanism describing the leaching process insights. Several inorganic species in lignite coal are organically associated in the form of Carboxylic acid salts (monovalent cations). Or complexes of carboxyl functional groups (multivalent cations).

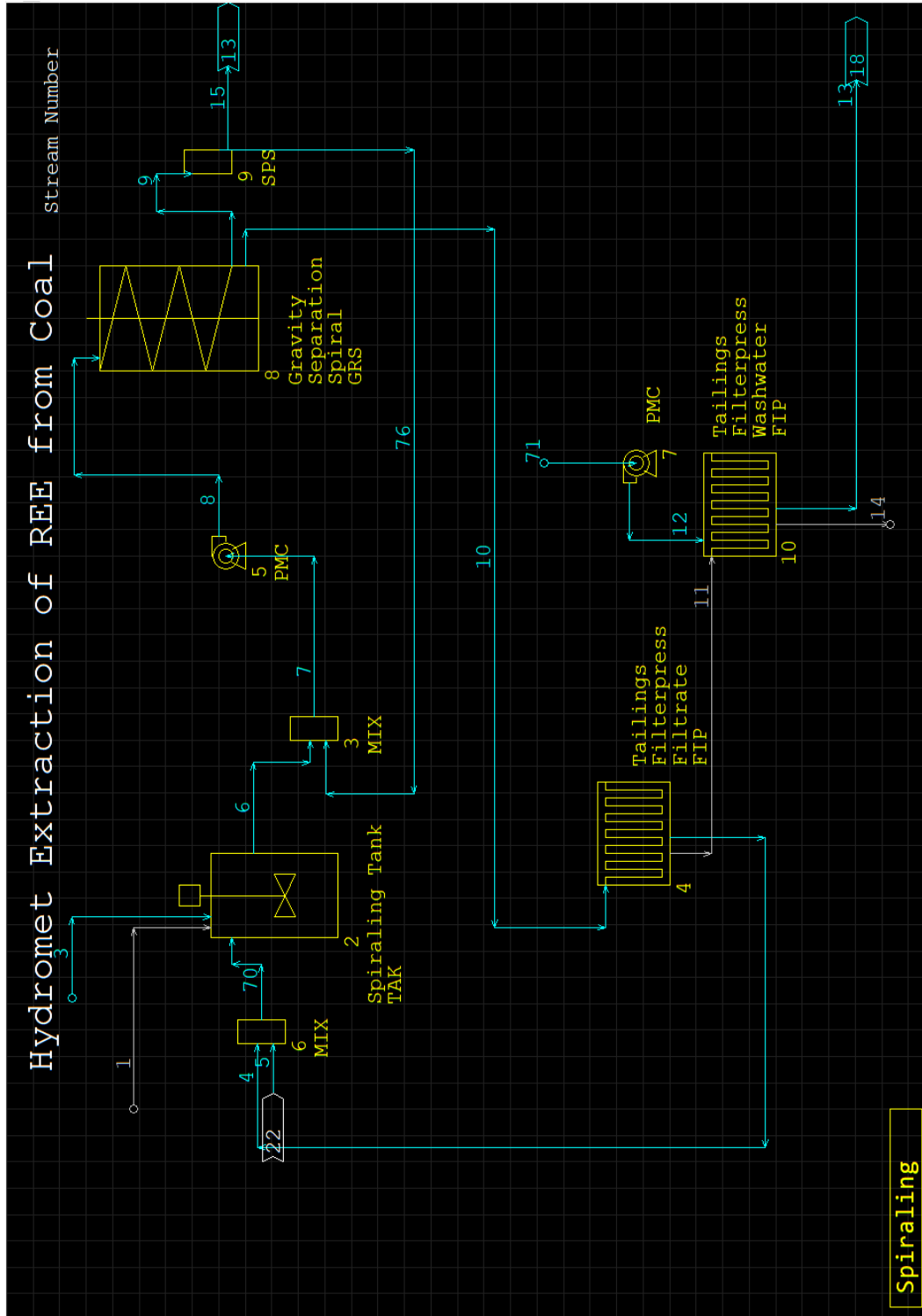


Figure 3.21: Spiraling Process Flow diagram in METSIM consisting of major unit operations

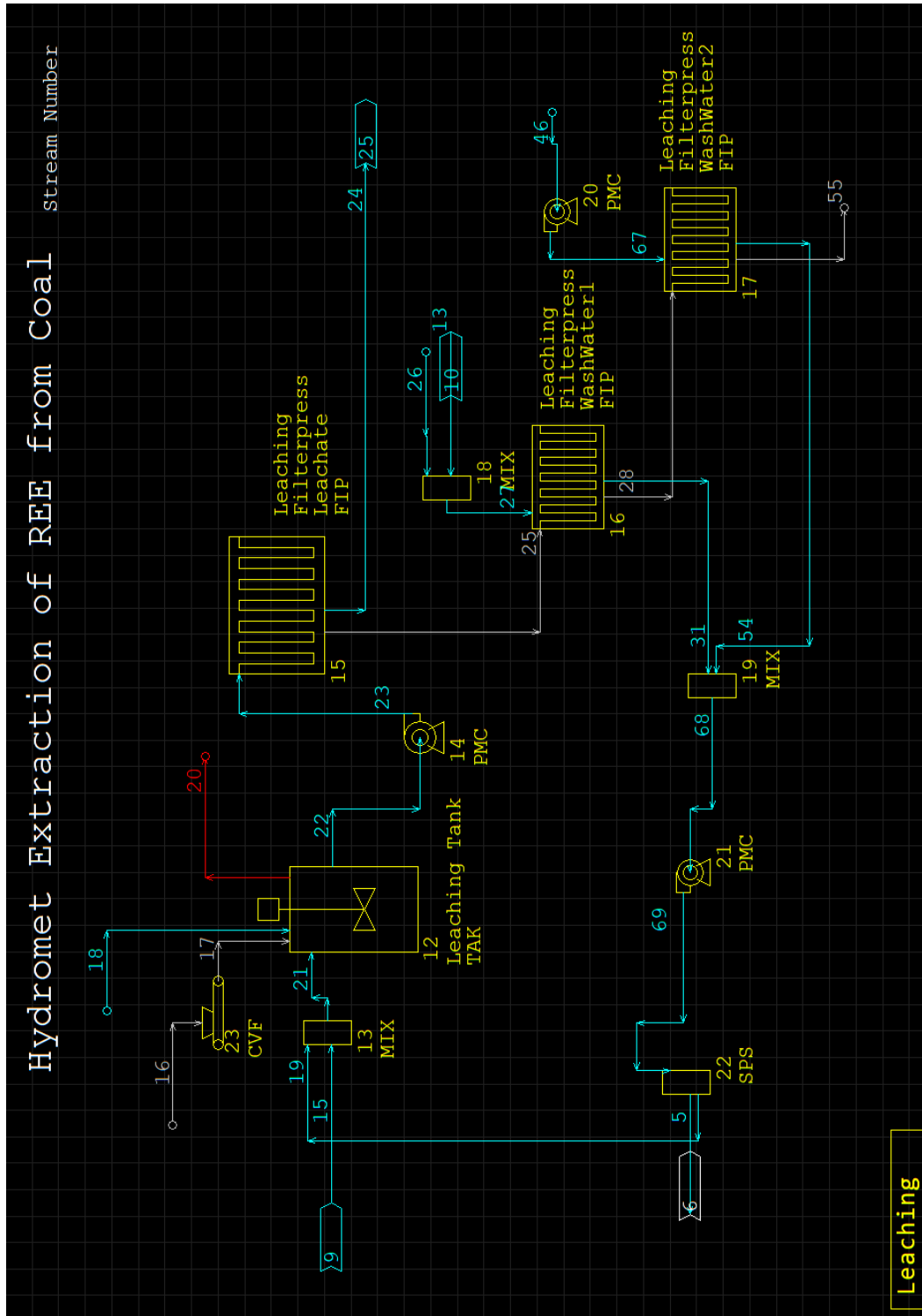


Figure 3.22: Leaching Process Flow diagram in METSIM consisting of major unit operations

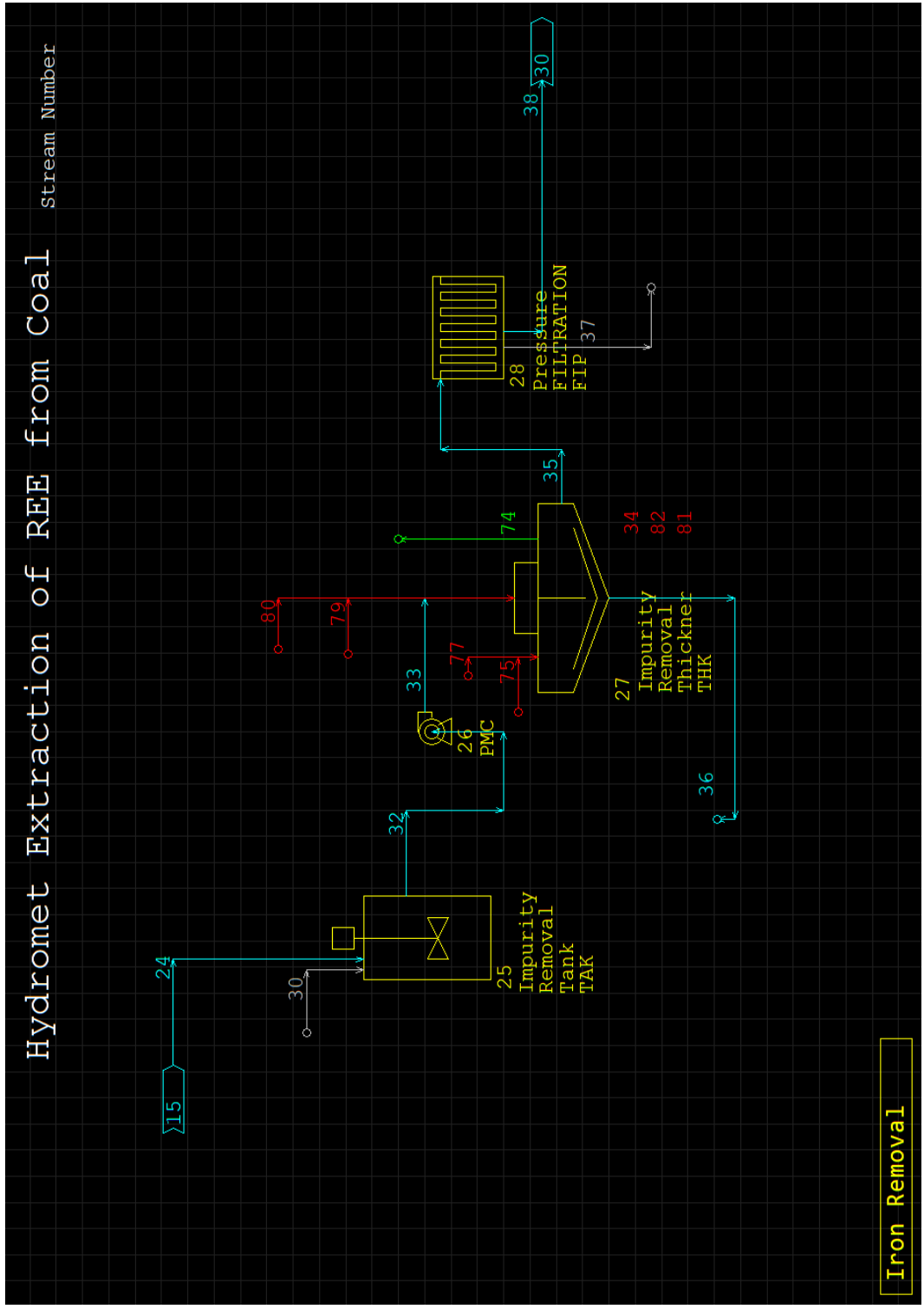


Figure 3.23: Impurity removal process Flow diagram in METSIM consisting of major unit operations

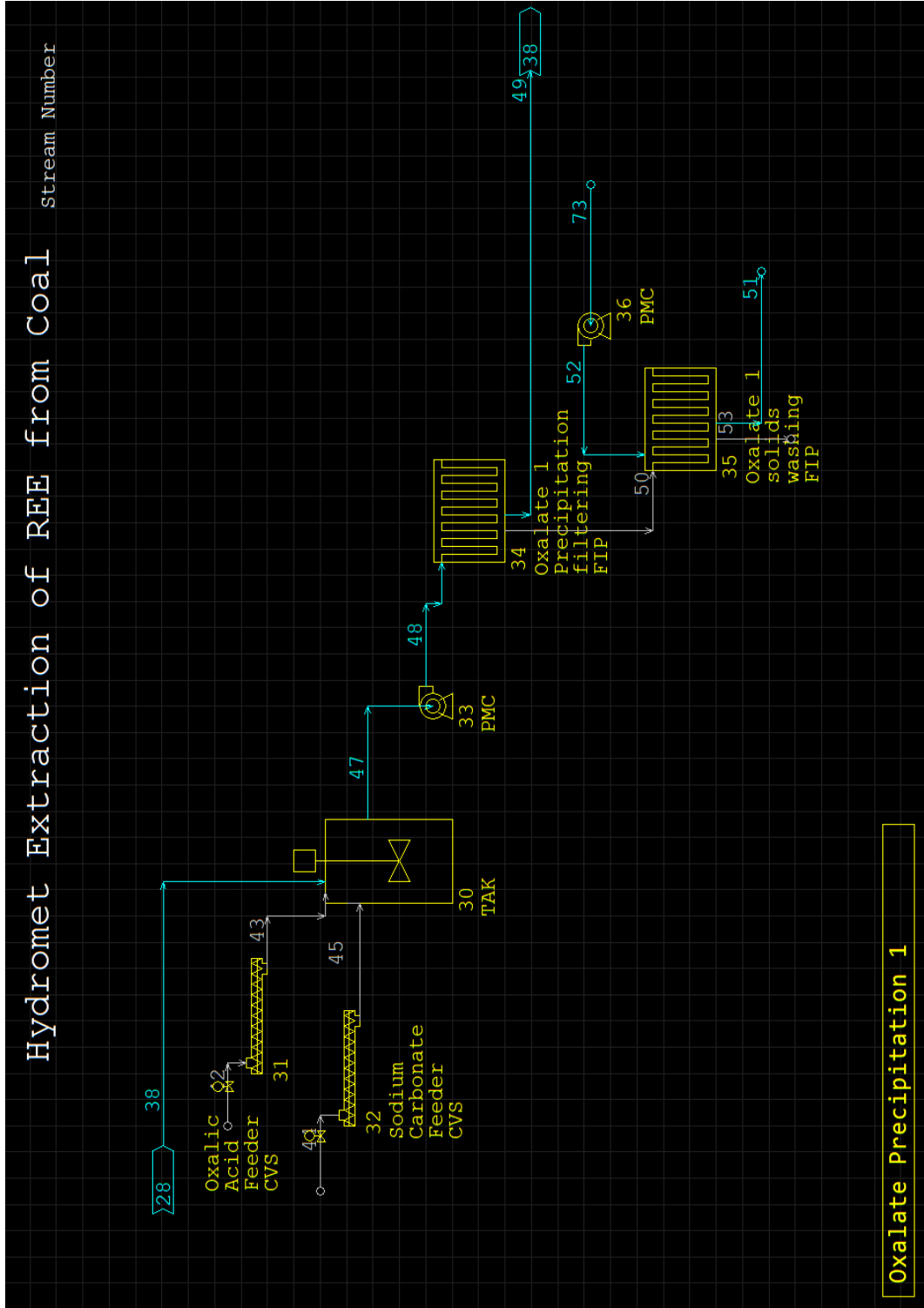


Figure 3.24: Stage-1 oxalate precipitation process flow diagram in METSIM consisting of major unit operations

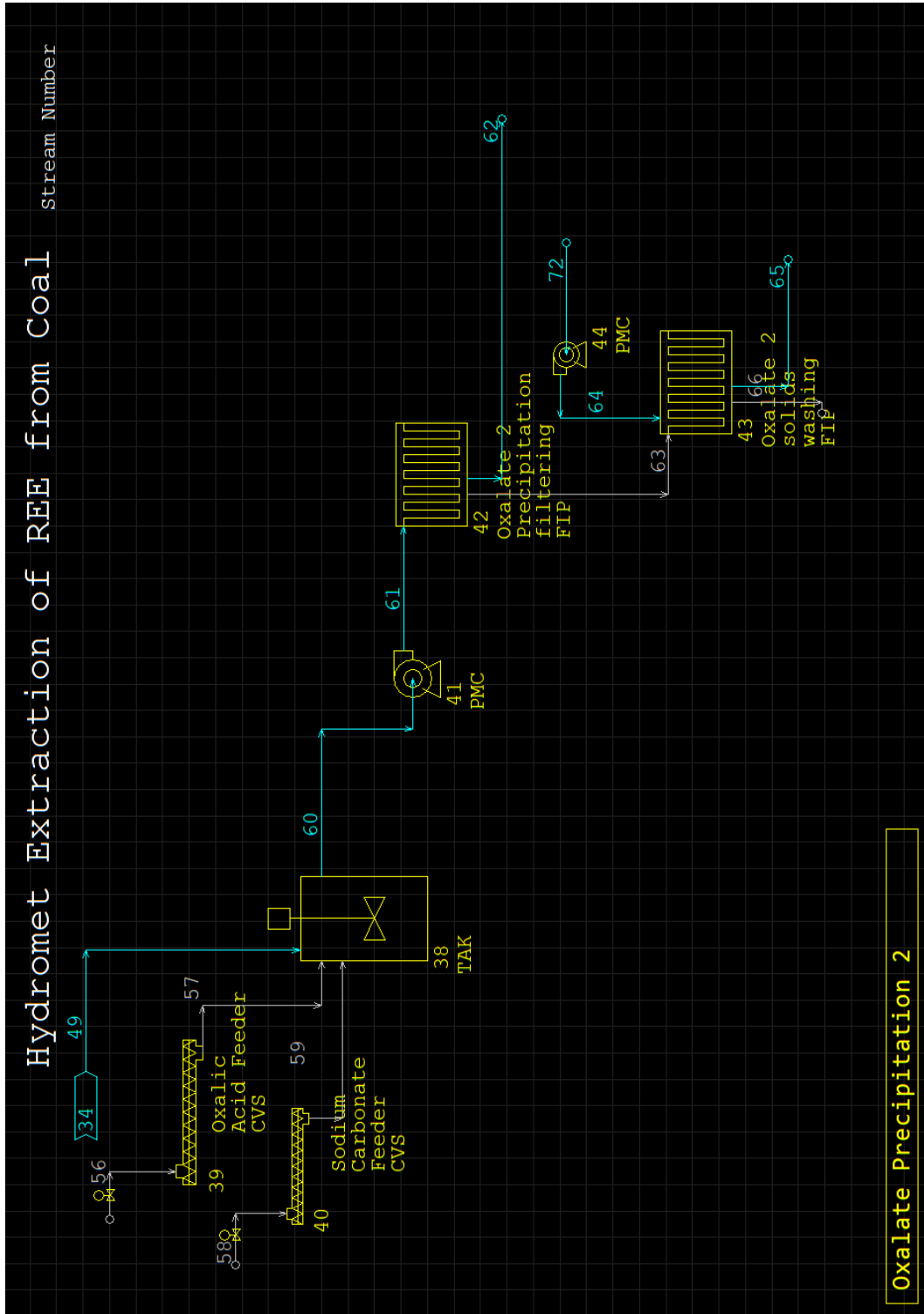


Figure 3.25: Stage-2 oxalate precipitation process Flow diagram in METSIM consisting of major unit operations

These PFDs were created using design of and data from bench-scale system. METSIM's capability to use upstream values and design factors to calculate key data on unit operations based upon new flowrates assists in understanding plant construction and procurement forecasting. The calculations provide valuable information to size the thickener, mixing tanks, and pumps consistent with bench scale data, while the equipment sizing for filter presses in certain process areas illustrates oversizing which may be due to user or software calculations. The spiraling equipment implemented in the software does not calculate concentrates, middlings, and tailings separately due to requirement of coal washability data which can only be obtained from experimental analysis of particular coal, as well as the input of data requires thorough understanding of APL language. Thus, applied spiral in presented process model holds separation of coal into only concentrates and tailings. For this illustration, the concentrates are split using component splitter with a user defined value. As a result, the convergence of stream tailings was difficult to achieve in the process model.

To implement the addition of acid and bases in the process model as a function of rate of feeding of coal in system, the process instrumentation is defined for feed streams of all acids and bases used in the process model. *Table 3-1* is a summary of the instrumentation controls attached to various streams in the process model. These flow controls assist in achieving process modeling convergence. Each flowrate/feedrate controller essentially governs unit operation as well as the stream that is desired to be manipulated by coal feed. In the process flowsheet, acid addition is conducted in three different places; however, it is required to estimate the total value of acid flowrate based on the feedrate of coal. Therefore, the APL expression is divided by 3 and defined

in form of an APL expression in the process flowsheet. In Table 3.1, VKGH represents Volume in Kilo Grams per Hour, SC is defined as component in stream, while SN is called as stream number.

Table 3-1. Flowrates and feedrate controllers implemented in METSIM process modeling calculations.

Description	Type	APL expression for flowrate value function	Stream to be adjusted its flowrate	Controlling Unit Operation
Control Acid flowrate using coal feedrate	FLOW RATE CONTROL	$(VLPH \text{ SN}) \times 1000$	3 (Acid flow stream)	2
Control Water flowrate using coal feedrate	FLOW RATE CONTROL	$(VKGH \text{ SN}) \times 1$	71 (water to wash the tailings)	7
Secondary Coal addition as function of primary coal feedrate	FLOW RATE CONTROL	$(VKGH \text{ SN}) \times 1.0$	16 (coal feed stream in screwfeeder)	23
Na ₂ Co ₃ addition as function of leachate flowrate	FLOW RATE CONTROL	$(SC \text{ VKGH SN}) \times 1000$	30 (Na ₂ Co ₃ feed stream in Tank)	25
H ₂ C ₂ O ₄ addition as function of Iron removed liquid flowrate	FLOW RATE CONTROL	$(VKGH \text{ SN}) \times 1000$	42 (H ₂ C ₂ O ₄ feed stream in screwfeeder)	31
Na ₂ Co ₃ addition as function of Iron removed liquid flowrate	FLOW RATE CONTROL	$(SC \text{ VKGH SN}) \times 100$	44 (Na ₂ Co ₃ feed stream in screwfeeder)	32
H ₂ C ₂ O ₄ addition as function of stage 1 liquid flowrate	FLOW RATE CONTROL	$(VKGH \text{ SN}) \times 1000$	56 (H ₂ C ₂ O ₄ feed stream in screwfeeder)	57
Na ₂ Co ₃ addition as function of stage 1 liquid flowrate	FLOW RATE CONTROL	$(SC \text{ VKGH SN}) \times 100$	58 (Na ₂ Co ₃ feed stream in screwfeeder)	59

Based on lab-scale results of leaching, impurity removal, and two stages of oxalic acid addition processes, coefficients of each process area were calculated and implemented in stirred tank reactors as APL functions. These coefficients are vary distinctively for each element defined in the process model. The ‘User Defined Objects’ (UDOs) are in APL storage memories, while

APL expressions are defined in target unit operations. In this case, all the tanks in all process areas collect information from these memories during iterative calculations. Two types of UDOs are defined in the model, User defined Scalar (US), and User defined Matrix (UM). The US contains singular value identity, while UM store multiple values in columns and rows, where columns are created by spaces between two values.

In *Table 3-2*, the UMWK3 holds all the experimental extraction coefficients, which can be generated from either lab-based tests or bench-scale based tests. The Matrix UMWK3 stores all the values of the coefficients which, during calculation, are called using APL expressions such as UMWK3[26;3] where the [26;3] represents cells as [row;column]. The equations in form of APL expressions locate the variable substitutions. For example, if 43.12% of the Ce is leached out, then 0.4312 is the variable substitution value for the reaction extent in form of APL expression. Using simplified geometric modeling, the author discards the whole reaction taking place with multiple organic complexes in coal and converts the reaction into the following form:



After defining this reduced reaction mechanism in stirred tank reactors, the APL algorithm calculates the number of moles converted to aqueous ionic form and with each iterative calculation converges the mass balance. The other optional UDOs are used to calculate process modeling parameters during bench-scale parametric testing, thus are not used in this process modeling. However, the functioning algorithms of these UDOs is identical as UMWK3. The US can be used as row or column value substitute for UM. By using UDOs, the presented process modeling framework in METSIM is simplified for other users.

Table 3-2. Flowrates and feedrate controllers implemented in METSIM process modeling calculations.

User defined object in METSIM	
Essential	
Name	Type
UMWK3	Matrix
UMSPIRAL	Matrix
Optional	
USLEACHINGPH	Scalar
USPHCOL	Scalar
UMOXAL	Matrix
UMLEACHING	Matrix
UMFEREC	Matrix
UMFESEC	Scalar

Based upon discussions of the process model with the research team, the addition of acid in the stirred tank reactor of the spiraling process area is implemented. The data for this reactor is inadequate, thus no reaction coefficient based APL expressions are defined.

Table 3-3 shows the design of the process equipment inventory by METSIM and its comparison with respect to the process equipment dimensions used for the bench-scale system. The METSIM required design factor is an essential input for stirred tank reactors. METSIM also requested information about bottom of tank as conical or flat. The type of agitation is equivalent to mixing, shear bubbles or suspend solids. The information requested by METSIM is illustrated in the software program, assuming the target audience of equipment sizing to be novice users, thus making preliminary equipment sizing possible. Using a design factor and upstream and downstream flowrates, METSIM calculated the parameters for the stirred tanks in leaching, impurity removal, and oxalate precipitation areas. Residence time predicted by METSIM and actual residence time used during the process show predictive error of $\pm 8.3\%$. The dimensions of the tanks show marginal error between 0.5% and 5%. The error increment is observed while predicting the volume of these tanks, which is between 1% and 15%. The calculations of agitator rotations show consistent 10 more RPMs than actual equipment.

Table 3-3. Tank equipment inventory analysis of the REE extraction bench-scale system using METSIM calculations.

Stirring Tank reactors	Tank Leaching Area	
Parameter	METSIM Calculation	Actual Equipment
Design Factor	1.200	
Diameter (m)	0.553	0.57
Residence time (min)	65.000	60.00
Height (m)	0.950	0.97
Freeboard or Heel (m)	0.500	0.50
Bottom angle (°)	15.000	15.00
Size (m ³)	0.228	0.23
Dimeter of Agitator (m)	0.206	0.17
Impeller to Tank Ratio	0.373	0.31
Agitator speed (RPM)	155.000	145.00
Horse Power / 1000 Gallons	0.332	
	Tank Impurity removal Area	
Parameter	METSIM Calculation	Actual Equipment
Design Factor	1.400	
Diameter (m)	0.558	0.57
Residence time (min)	120.000	120.00
Height (m)	0.970	0.97
Freeboard or Heel (m)	0.500	0.50
Bottom angle (°)	15.000	15.00
Size (m ³)	0.237	0.23
Dimeter of Agitator (m)	0.279	0.17
Impeller to Tank Ratio	0.500	0.31
Agitator speed (RPM)	155.000	145.00
Horse Power / 1000 Gallons	1.172	
	Tank Oxalate stage 1 Area	
Parameter	METSIM Calculation	Actual Equipment
Design Factor	1.200	
Diameter (m)	0.565	0.57
Residence time (min)	73.867	60.00
Height (m)	0.965	0.97
Freeboard or Heel (m)	0.500	0.50
Bottom angle (°)	15.000	15.00
Size (m ³)	0.241	0.23
Dimeter of Agitator (m)	0.183	0.17
Impeller to Tank Ratio	0.324	0.31
Agitator speed (RPM)	155.000	145.00

Horse Power / 1000 Gallons	0.421	
	Tank Oxalate stage 2 Area	
Parameter	METSIM Calculation	Actual Equipment
Design Factor	1.2	
Diameter (m)	0.579	0.57
Residence time (min)	69.207	60.00
Height (m)	0.979	0.97
Freeboard or Heel (m)	0.500	0.50
Bottom angle (°)	15.000	15.00
Size (m ³)	0.257	0.23
Dimeter of Agitator (m)	0.183	0.17
Impeller to Tank Ratio	0.324	0.31
Agitator speed (RPM)	155.000	145.00
Horse Power / 1000 Gallons	0.421	

Table 3-4 presents the predicted METSIM calculations for the continuous filtration system implemented in the bench-scale system. The tabulated data show the predicted dimensions and other filtration parameters of the pressurized filtration and thickening systems with METSIM calculations. METSIM only has a pressurized filtration unit operation as filter presses, thus the manual hand operated inline filtering system in the bench-scale system is replaced with a filter press unit operation in the flowsheet. The Table 3-4 only shows the actual filter press used for solids-liquid separation process during leachate generation.

Four cubic feet ($0.11m^3$) of filter press capacity consisting of 26 filtering plates is used during the filtration process. The filter press unit operation calculated in METSIM shows a plate size of 470 mm which is identical to that value of actual filter press. The entire chamber volume calculated by METSIM also matches with the actual equipment capacity and show marginal difference of only -1.9%. The filtration pressure calculated by METSIM and actual filtration pressure which can be used for the filter press have are essentially the same (<1% difference).

During the impurities removal process, due to smaller particle size, the process of clarification/ thickening is implemented using a barrel. Thus, similar dimensions were provided into METSIM software for the thickener unit operation as an initial condition and the software recalculated the design process and calculated the corrected D50 Diameter as 0.1 μm along with dimensions. This process of calculation predicted similar values as actual equipment implemented during experiment, shown in *Table 3-4*.

Table 3-4. Filtration equipment inventory analysis of the REE extraction bench-scale system using METSIM calculations

Filtration system		
Parameters	Leaching Area Filter Press	
	METSIM Calculations	Actual Equipment
Design Factor	1.250	
Plate Size (mm)	470.000	470
Plate Area (m ²)	0.384	0.4
Chamber Thickness (mm)	32.000	32
Chamber Volume (m ³)	0.108	0.11
Filtration Area		
Based on Cake Volume (m ²)	0.992	
Based on Slurry Filtration (m ²)	0.008	
Number of Plates	26.000	26
Filtration Pressure (kpa)	689.000	691
Parameters	Impurity Area Thickener	
	METSIM Calculations	Actual Equipment
Design Factor		
Diameter (m)	0.711	0.65
Feed Well Diameter (m)	0.510	0.53
Effective Area (m ²)	0.193	0.19
Height (m)	1.000	0.92
Volume (m ³)	0.397	0.25
Corrected D50 Diameter (μm)	0.100	0.10
Flow (m ³ /hr.)	0.001	

METSIM calculates values based on an iterative process, thus convergence is essential to achieve acceptable calculations. *Figure 3.26* shows convergence of the presented steady-state process modeling for recycle streams including all 44 unit operations in the model. The green color represents converged stream and unit operation values. Secondary calculations are performed to check elemental mass balance. The mass balance shows no variations upstream and downstream of each unit operation. The *Figure 3.26* also shows the time required for all streams and unit operations to reach overall convergence in the process model.

The presented model was first compiled for convergence through the design process of each individual unit operation. Later each section in this process model is simulated separately. Once the convergence is achieved for each unit operation, the entire flowsheet including all the process sections were simulated. If at any given time the value in any stream or any unit operation is changed, the entire process is repeated to achieve convergence. Although the process to achieve converged solution is performed, METSIM fails to empty cache of previous calculations, ultimately resulting calculations with convergence but with few warnings.

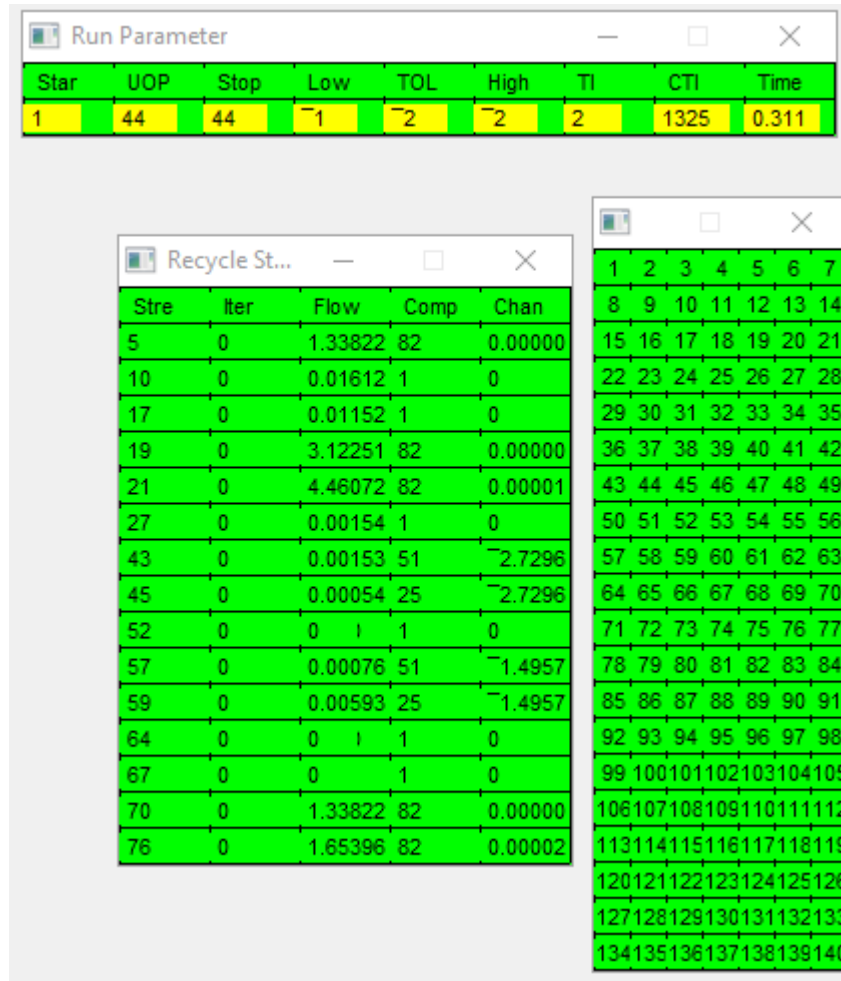


Figure 3.26: METSIM convergence testing for each iteration in steady-state calculations the green color in cell represents acceptable value by software.

For the UND pilot scale facility testing, the necessity to blend two types coals arises due to shorter supply of coal with >300 ppm REEs and CMs. In this case study, Coal 1 contains less than 300 ppm of REEs and CMs, while the Coal 2 contains higher than 300 ppm REEs and CMs. The simulation is simplified geometric modeling, and although both the coal types hold different particle size distribution (PSD), this modeling approach does not affect the leaching process and filtration process. The process modeling is based on the extraction efficiency measured in lab/beaker-scale testing. In this case study, Coal 1 and Coal 2 have the same REE extraction

efficiency, and thus, the case study represents results independent of the acid consumption and leaching efficiency. Both variables are not currently part of the process model.

Figure 3.27 shows the extraction of REEs and CMs from a blend of the two coals with respect to various ratios. The ratios are expressed as Type 1: Type 2. As expected, if the feed rate of coal holding higher concentration of REEs and CMs dry basis as well as better leachability is increased, the concentration of REEs and CMs increased. Thus, additions of coal with higher concentration of REEs and better leachability is sensitive to the process modeling. However, a coal with a higher concentration of REEs, but showing poorer leachability can lead to lower efficiency of extraction for REEs and CMs. In this case study, acid consumption/utilization is considered constant.

The presented METSIM process model is capable of calculations such as the scenarios discussed above. However, the process model is still in preliminary status.

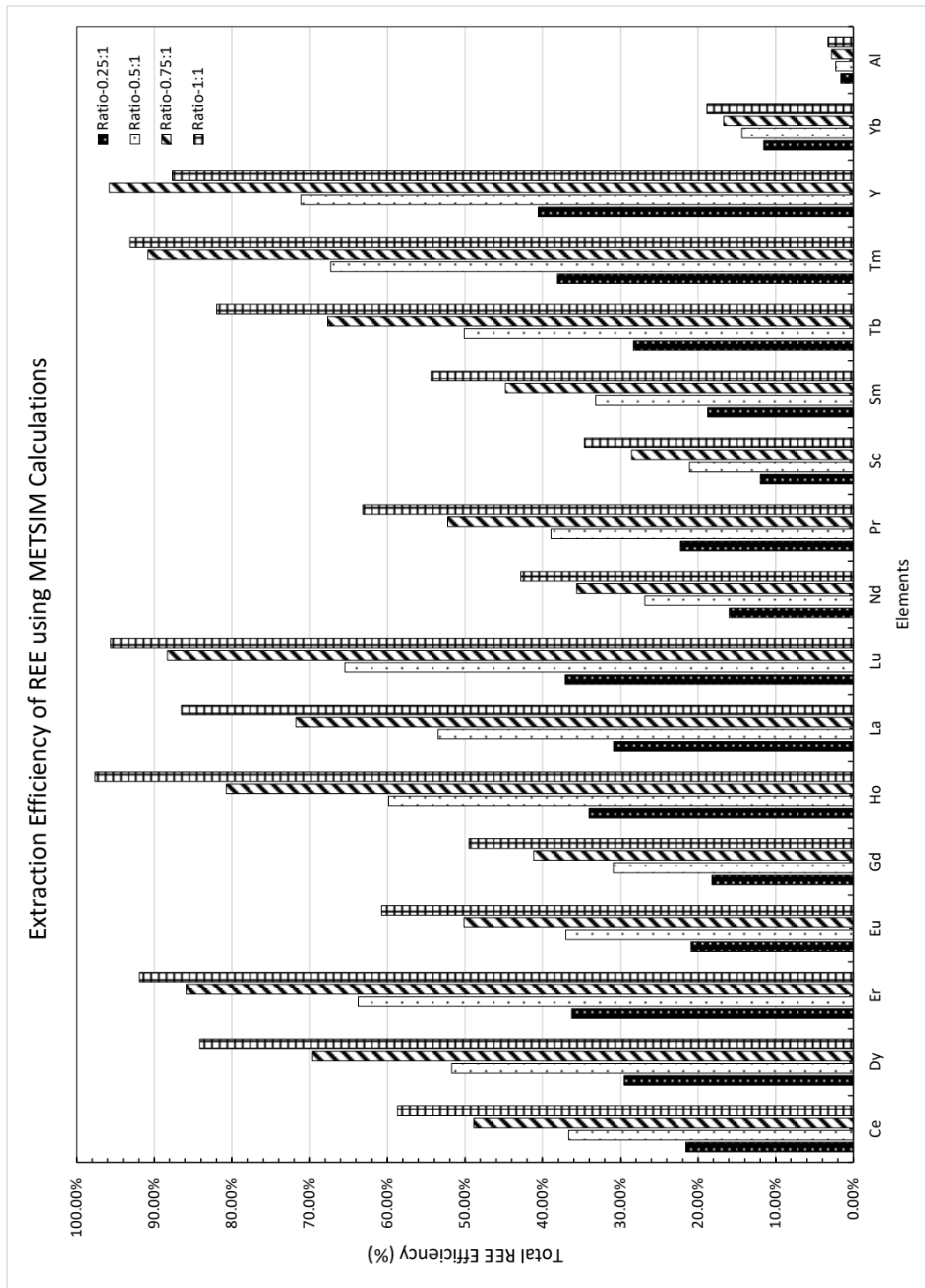


Figure 3.27: Extraction efficiency of REE from blend of two types of coals with respect to their ratios Type 1 and Type 2.

3.3 Conclusion

A fundamental framework of process modeling is created using METSIM software. The process model is capable of performing mass balance calculations, and thus currently presenting basic results. The model can predict equipment inventory with overall accuracy of 1% to 5% as compared to the bench-scale equipment used in the physical testing. To use this model, unit operations require factors of design and other information as such initial conditions, along with detailed information of upstream and downstream flowrates. However, in most scenarios, the unit operations in the model can predict equipment dimensions and other parameters along with downstream mass balance simultaneously.

No reaction mechanisms or any reactions are defined in the unit operations of the presented model. The model lacks the capability of reaction kinetics in unit operations due to the lack of components database as well as the available components having insufficient kinetics and thermodynamics data, and the difficulty of adding reaction data using the advanced METSIM APL functionality. As result, in cases where reaction rates are critical, this model is inferior to the ASPEN model, which has an extensive database of reactions and associated chemical kinetics and thermodynamic data. However, METSIM has unique metallurgical and mining application oriented unit operations not present in other process modeling simulation software packages, thus METSIM is capable of creating preliminary equipment sizing for hydrometallurgical processes using flowrates and other user defined values as initial conditions.

4. CO₂ CAPTURE MODELING

4.1 Introduction: Past CO₂ Modeling efforts

CO₂ Capture by absorption into amine solutions within packed column absorbers has been regarded as one of the most viable options for implementing Carbon Capture and Storage within existing coal and natural gas power stations. However, the high capital and operating costs, particularly the large energy requirement for regeneration, has been a major factor inhibiting the widespread utilization of this technology. For instance, while stable and reliable operation of post combustion capture units for achieving 90% CO₂ capture from coal flue gas have been demonstrated for extended periods, the steam requirement for solvent regeneration using a reference 30% monoethanolamine (MEA) was found to be 3.7GJ/ton CO₂ at 90% removal at an MEA consumption rate of 1.4kg/ton CO₂. To offset this, 20 “elementary” process modifications have been reviewed by Le Moullec et al. and sorted into three categories: absorption enhancement, heat integration, and heat pumps. [106] The goal of absorption enhancement (which is the overarching theme of this proposed project) is to increase CO₂ loading at the absorber bottom or to reduce the excessive driving force in the absorber section. The solvent flow rate to achieve the desired CO₂ capture is thereby reduced and consequently reducing the sensible portion of the boiler heat duty. Further, the lower solvent circulation rate also leads to reduced equipment sizes and pumping duties. Absorption enhancement may be accomplished either by enhancing mass transfer using existing solvents and/or by using novel 2nd generation solvents such as: cyclic amines, hindered amines, ether amines, amino acids, phase change solvents, ionic liquids, or mixtures thereof. Non-aqueous solvent matrix systems such as those developed by ION Engineering also fall under this category. [107] Developing predictive capability for gas absorption

systems for absorption enhancement supporting the 2nd generation post-combustion carbon capture systems (systems that are using second generations solvents such as *MEA*, *MPZ*, *MDEA*, etc. by designing absorbers configuration), is the primary goal of the project. For this, gas-liquid mass transfer rates are targeted while minimizing pressure losses, along with liquid holdup parameters. The kinetics models involving mass-transfer rates; are directly associated with overall hydrodynamics of liquid flow and its characteristics such as pressure drop across the column, the liquid holdup, and mass-transfer coefficients.

4.2 Presented multiphase CFD modeling

The focus of the present chapter will be finding solutions to optimize carbon capture in these structured packings by increasing the surface area for flow with the help of mathematical formulations. Based upon the described algorithms and solution methods in Appendix A, the author presents an approach to transient multiphase flows of two incompressible fluids based upon the Volume of Fluid (VoF) method by Hirt and Nichols [108]. This approach roughly corresponds to interFoam solver from the OpenFOAM C/C++ solvers library [92] [109]. Algorithms such as MULES, PIMPLE, VoF, PISO, etc. are presented. The Author describes algorithms used for solution of the flow of two incompressible fluids in Appendix A.

The VoF model can mathematically generate two or more immiscible, incompressible fluids by solving a single set of momentum equations and tracking the volume fraction of each of the fluids through the domain. The typical applications include the prediction of jet breakup, the motion of liquid after dam break, and steady-state or transient tracking of any gas-liquid interface. [90]

There are certain limitations of VoF model (listed below), and many researchers have tried to improve the solution algorithm to tackle these limitations.

1. The VoF method is a controlled volume-based method, and thus at the initial conditions certain parts of the domain need to be mapped as either 1 or 0 which means either gas or liquid if multiple phases or components of fluids are present such as oil, water, etc. The cell should be marked as per composition required, thus the number of fluid components present is always between 0 and 1. Thus values outside of range 0 and 1 crashes the solver.
2. Only one phase can be defined as compressible either gas or liquid, and mostly it is gaseous phase, which need to be compressed. Thus, physical phenomena where gas is compressing liquid is difficult to formulate under VoF methodology.
3. If the solver is rudimentary or stiff developed then use of a second order implicit time stepping scheme solving technique crashes the solver. This issue is seen multiple times in solvers like OpenFOAM.

While the solution algorithm of VoF methodology holds certain drawbacks, successful implementation of VoF methodology is still dependent on certain assumptions made to solve NS equations. In the current section the fluids for which the computational calculations are processed, show the following assumptions as per [110]

1. All the fluids considered for computational analysis are Newtonian, viscous and incompressible.
2. For particular flowrates and velocities, the physical properties of fluids are considered consistent throughout the fluid flow analysis.
3. For single-phase flow no-mass transfer is assumed.

4. The flowrates and velocities selected for the analysis show no turbulence of fluid occurring in computational domain, all the computational calculations are performed using laminar fluid flow model.
5. No energy balance is assumed while evaluating hydrodynamics of fluid flow, thus energy generation and dissipation is neglected for reactions occurring while capture of CO_2 gas.

Hence, to begin with modeling setup, first we consider the i^{th} cell in computational domain Ω in that cell where the tracking of interface(s) between two phases is accomplished by the solution of the continuity equation for the volume fraction of one or more of the phases. Thus, phase of liquid being phase l and phase of gas being phase g , this equation holds the following format [111] [90]:

$$\frac{1}{\rho_l} \left[\frac{\partial}{\partial t} (\alpha_l \rho_l) + \nabla \cdot (\alpha_l \rho_l \vec{u}_l) \right] = S_{\alpha_l} + \sum_{a=1}^n (\dot{m}_{lg} - \dot{m}_{gl}) \quad (4.1)$$

The volume fraction equation will not be solved for the primary phase, the primary-phase volume fraction will be computed based on the following constraints [108] [112]:

$$\sum_{b=1}^n (\alpha_b) = 1 \quad (4.2)$$

The volume fraction can be solved either through implicit or explicit formulation. In OpenFOAM the VoF equations solving strategy is tend to follow explicit formulation. [109] This is represented using following equation:

$$\frac{\alpha_g^{n+1} \rho_g^{n+1} - \alpha_g^n \rho_g^n}{\Delta t} V + \sum_{b=1}^n (\rho_g U_f^n \alpha_{g,f}^n) = \left[S_{\alpha_l} + \sum_{a=1}^n (\dot{m}_{lg} - \dot{m}_{gl}) \right] V \quad (4.3)$$

In the above equation,

$n + 1$ = index for new (current) time step

n = index of previous time step

$\alpha_{g,f}$ = face value of gas based volume fraction

V = Volume of cell

U_f = Volume flux through the face, based on the normal velocity

Since the volume fraction at the current time step is directly calculated based on the known quantities at the previous time step, the explicit formulation does not require an iterative solution of the transport equation during each time step. [112] [113]

Thus, based on the volume fraction, its properties, particularly for the two incompressible immiscible flows the following variables holds true for the solution [112]:

$$\rho = \alpha \rho_A + (1 - \alpha) \rho_B \quad (4.4)$$

$$\mu = \alpha \mu_A + (1 - \alpha) \mu_B$$

InterFoam utilizes explicit formulation for which it tends to use the Courant Number, based upon the Courant – Frederick – Levy (CFL) condition (equation (4.5)). In InterFoam solver, the cell Courant Number in CFL condition is calculated as:

$$Co_P = (\Delta t) \frac{\|u_p\|}{d_p^e} \approx \frac{\Delta t}{2d_p^e A_p^e} \sum_{(f)_P} |\phi_f^V| = \frac{\Delta t}{2\delta \zeta_P^h} \sum_{(f)_P} |\phi_f^V| \quad (4.5)$$

Where, the $\phi_f^V == \mathbf{S}_f \cdot \mathbf{u}_f$ is the volume flux of fluid through the face f . The formula shown above is based upon the assumption of unidirectional flow in the vicinity of the cell (defined here as ζ_p^h). The above OpenFOAM co-relation is formulated through original formulation of CFL condition which speculates convergence. The stability of finite difference numerical scheme and the stability of the order of difference equation to converge to the solution of the underlying partial differential equation, the numerical scheme is predicted on the assumption that of the information contained in the initial data that influence the solution be used.

A single momentum equation is involved throughout the computational domain, as resulting velocity field is shared among all the phases. [114] The momentum equation (4.6) is dependent on the volume fraction of all the phases through the properties ρ and μ . [115]

$$\frac{\partial}{\partial t}(\rho \vec{v}) + \nabla \cdot (\rho \vec{v} \vec{v}) = -\nabla p + \nabla \cdot [\mu \{\nabla \vec{v} + \nabla \vec{v}^T\}] + \rho \vec{g} + \vec{F} \quad (4.6)$$

While the continuity equation defined by following manner:

$$\frac{\partial \rho}{\partial t} + \nabla \cdot (\rho \vec{v}) = 0 \quad (4.7)$$

One limitation of shared-fields approximation is that in cases where large velocity differences exist between cases, the accuracy of velocity computed near interfaces can be adversely affected. [115]

4.2.1 Surface forces and their implementation

Surface tension in multiphase flow is modelled by the inclusion of a source term in the momentum equation. Surface tension contribute to the balance of momentum and its calculation

which is shown in equation (4.8). [116] [117] In the equation (4.8), the normal forces of the wall (n_w), the unit vector normal to the wall and (t_w) which is shown in *Figure 4.1* the unit vector tangential to the wall which is shown. Here, n points into the liquid phase

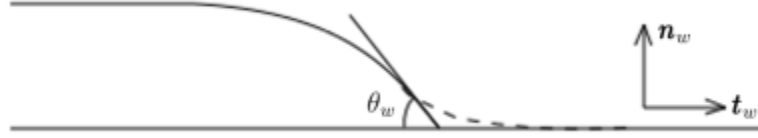


Figure 4.1: Definition of the contact angle, θ_w , unit vector normal to the wall, n_{wall} and unit vector tangential to wall, t_w .

In the overall N-S equation, the surface force term, f_s , is evaluated via the continuous surface force model of Brackbill, Kothe, and Zemach [117] [118] [119] The equation corresponding to surface tension forces is defined as:

$$\mathbf{f}_s = \gamma \hat{\mathbf{n}} \cdot \kappa(\mathbf{x}) \quad (4.8)$$

Where, the γ is the surface tension force coefficient, $\hat{\mathbf{n}}$ is the outer limit unit normal to the gas – liquid interface and κ is the mean surface curvature. [120] Moreover, it is possible to evaluate the vector $\hat{\mathbf{n}}$ and the interface curvature, κ , based upon the volume fraction function as follows:

$$\hat{\mathbf{n}} = \frac{\nabla \alpha}{\|\nabla \alpha\|}, \quad (4.9)$$

$$\kappa(\mathbf{x}) = -\nabla \cdot \hat{\mathbf{n}}$$

Near the wall boundary, the cells have to be adjusted in order to take into account the liquid dynamic contact angle, β which is as follows:

$$\hat{n}_{wall} = \hat{n}_w \cos \beta + t_w \sin \beta \quad (4.10)$$

Where \hat{n}_w and t_w are the unit vector tangent to the wall accounting near wall forces. One of the critical factors of this study, is that the dynamic contact angle model is applied as boundary condition along with surface tension forces. The code as a part of the boundary condition, is provided as a core part of OpenFOAM solver library, [88] [121] which in some other proprietary software is accounted as Add-on. The dynamic alpha contact angle (referred as dynamicAlphaContactAngle, or constantAlphaContactAngle), is given by:

$$\beta = \beta_0 + (\beta_A - \beta_R) \tanh\left(\frac{u_w}{u_\beta}\right) \quad (4.11)$$

Where, β_0 , β_A , and β_R are the equilibrium, advancing and receding contact angles, respectively, u_w is the speed of the moving contact line relative to the speed of adjacent to the wall and u_β is an appropriate scale for u_w .

4.2.2 Film layer mass transfer modeling and implementation

There are various ways of showing the addition of mass transfer in VoF modeling. In this dissertation, the modeling of mass transfer occurring on thin film layers inside the CCS systems;

is based upon the methods of Harun et.al [16]. This approach is a direct numerical simulation method, eliminating the need for additional models, such as Higbie penetration theory [17], to resolve the mass transfer process. The equation uses an additional set of equations to determine the evolution of species concentration throughout the domain which is given by:

$$\frac{\partial C_i}{\partial t} + \nabla \cdot (\mathbf{u} C_i) = -\nabla \cdot (D_i \times \nabla C_i + \Phi_i) + W_i \quad (4.12)$$

$$\text{where, } \Phi_i = - \left(\mathbf{D}_i \times \frac{C_i(1 - He_i)}{\alpha + He_i(1 - \alpha)} \nabla \cdot \alpha \right)$$

Where C_i is the concentration of i^{th} species, D_i is the diffusivity of the i^{th} species and the W_i is the production term for the i^{th} species. The current dissertation presents VoF formulation of mass transfer modeling as only physical mass transfer and therefore the production term, W_i term is neglected. Haroun show the detailed derivation of the along with flux implementation as well [16].

Equation (4.13) is modeled to account for scalar transport with an additional flux term to account for discontinuities in the concentration field at the interface between two isothermal immiscible fluids Thus, at the interface, following mass transfer equation can be accounted for:

$$\sum_{L,G} |j_i \cdot n \delta_i| = 0 \quad (4.13)$$

and the discontinuity in the concentration of species at the specific gas – liquid interface given by:

$$C_{G,i}^{int} = He_i \times C_{L,i}^{int} \quad (4.14)$$

The H denoting Henry's law is defining the equilibrium condition in chemical species, which value eventually shows the reaction status. Here, C_i represents the concentration for species at i^{th} . The diffusivity \mathbf{D}_i is computed with mathematical manipulations called harmonic averaging

methodology. Thus, the diffusivity is calculated using a harmonic formulation, and the term is given by:

$$D_i = \frac{D_{i,L} \times D_{i,G}}{\alpha_1 D_{i,G} + (1 - \alpha_1) D_{i,L}} \quad (4.15)$$

It has been demonstrated by Haroun that the above-mentioned approach reduces the chances of spurious fluxes arising in the species concentration as a result of interface curvature. The choice of a harmonic equation for diffusion over linear diffusion does not affect the species transport equation.

4.3 Multiphase modeling setup

In the previous section 4.2 the generalized solution algorithms for numerical equations describing continuum of multiphase flows were presented. The algorithms and equation solving strategies that were described in previous section were used to solve the multiphase flows in complex computational domains such as the geometry of Mellapak packings showing the hydrodynamics of flows (*Figure 4.2*).

4.3.1 Introduction to Packings with Numerical Strategies

Carbon capture units consist of absorption and separation columns having multiphase flows. The behavior of these multiphase flow columns are not totally understood. Such columns are used in chemical engineering to carry out large-scale mass transfer operations. These columns hold complex geometries for generation of thin-film fluid flows to perform the chemical reactions on surface of the film to capture the CO₂ in reactions. The numerical solutions of multiphase flows computed in these complex corrugated Mellapak packings are calculated using the OpenFOAM computational fluid dynamics software. Using previously described algorithm techniques, the

multiple tasks focus on; mainly on the primary goal which is to construct a Volume of Fluid – based CFD model of the multiphase flows.

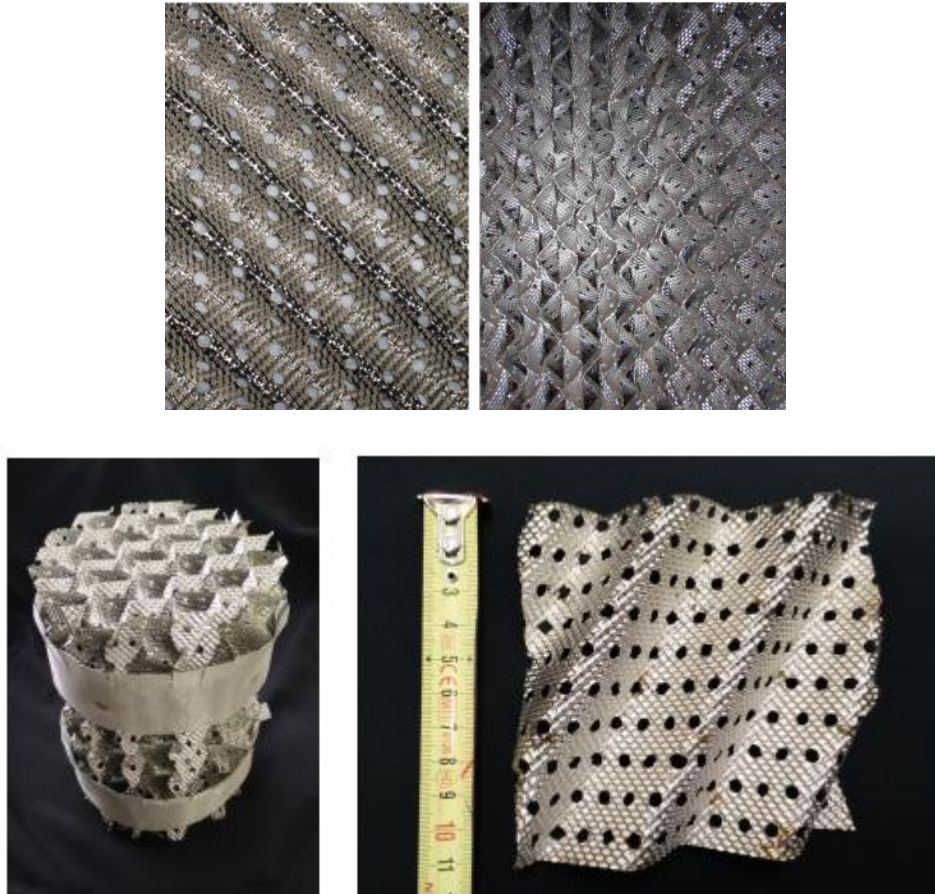


Figure 4.2: Metallic structured packings above shown packings are ‘MellapakPlus,252.Y’ while the lower pictures are of ‘MellapakPlus,250.X’ packing.

Due to the geometrical complexity of the packings and the size of the column itself, modeling of entire column using computational fluid dynamics is yet to be developed. Thus, Rynal and Royon-Lebeaud [93] proposed one particular approach to model the separation columns such as carbon capture columns by segregating the numerical formulations in three scales, 1.) microscale representation of thin film flow and its characteristics study in section of column for example a single panel of corrugated sheet. 2.) scale-up of these numerical problem to meso-scale

to one packing element of structured packing, and 3.) macro-scale study by considering key factors of previous results of meso-scale study to simulate the entire column. Thus, according to that at the beginning, flow pattern and flow behavior is analyzed in in linear lined wall column which represents the particular wall of one packing element in corrugated sheet in 2D format. Flow patterns and behavior in the corrugated wall column is analyzed with the two-phase flow solver while the dry pressure drop is analyzed using single-phase solver. Although, it has been analyzed by previous researchers [122], the calculations have not been achieved using courser mesh which is performed in this research. In addition, this work looked at flow patterns using the same geometrical domain gas–liquid counter–current flow with solvent falling down the straight vertical wall and a corrugated vertical wall in form of thin film flow coupled with mass transfer and the absorption of gas species using Henry’s constant. This approach was previously performed by Cook et. al [123]. The two–phase gas–liquid flow behavior is studied, and results were analyzed with previously performed computational calculations by CCSI team researchers from NETL [82]. Simultaneously, the wet pressure drop for two–phase gas–liquid counter–current flow is analyzed in the same packing geometry.

In the following sections author shall discuss about the overall computational setup for 2D gas–liquid flows in vertical straight and vertical corrugated wall columns, with original interFoam solver which provides the capability of computing two immiscible and incompressible fluids and their sharp interfaces.

4.3.2 OpenFOAM file structure and introduction

Before dwelling in simulation setup with boundary conditions as other things, author would first prefer to explain OpenFOAM file structure and brief introduction to OpenFOAM environment. Unlike any other software, OpenFOAM which is short for, ‘Open-source Field(s) Operations and

Manipulations’, primarily develop for UNIX based computing system and has terminal like interface. [109] [124] [125] [115] OpenFOAM is generally considered as C/C++ computing language based numerically solution providing framework for complex partial differential equations which are generally derived from nature occurring physics-based phenomena. OpenFOAM is framework for developing application executables using ‘build-system architecture’ that use packaged functionality contained with collection of over 100 C/C++ *libraries*. This advanced numerical framework holds over 200 pre-built utilities which can be segregated in two categories which are *solvers* built towards specific applications for example interFoam (specifically targeted towards multiphase VoF methodology) and *Utilities* that are designed to perform tasks involving multiple data manipulation. Open-FOAM is the only currently available open-source numerical environment which supplied with Pre – and Post – processing functions and utilities further providing assurance towards seamless data handling across all environments. The following *Figure 4.3* shows the overall architecture of OpenFOAM framework.

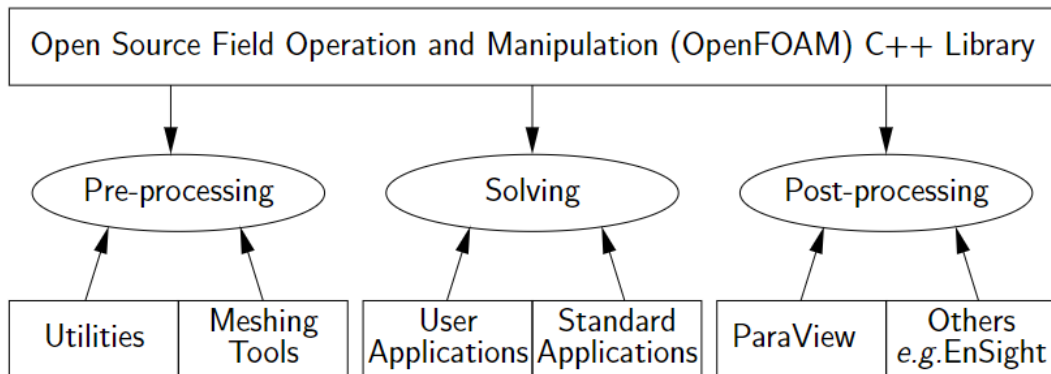


Figure 4.3: Overview of OpenFOAM architecture.

The post-processing steps in OpenFOAM are graphically handled by ParaView software, which is provided in the overall software bundle. Critically, three major folders are categorically required for a successful run of simulations by OpenFOAM. These are ‘*0 folder*’ which also can

be considered as ‘time-step folder’, ‘*Constant folder*’ where constant parameters particular to the case are stored such as mesh, transport properties, etc., and ‘*System folder*’ where the Finite Volume Method (FVM) based discretization parameters and options are defined. *Figure 4.4* shows the OpenFOAM simulations case file structure, showing a typical ‘build system’ type software architecture in which the files are arranged in a specific manner inside folders and subfolders inside folders. This allow certain commands to execute in terminal over the defined directory as well as the full path to the file which can be considered as a terminal command in certain cases.

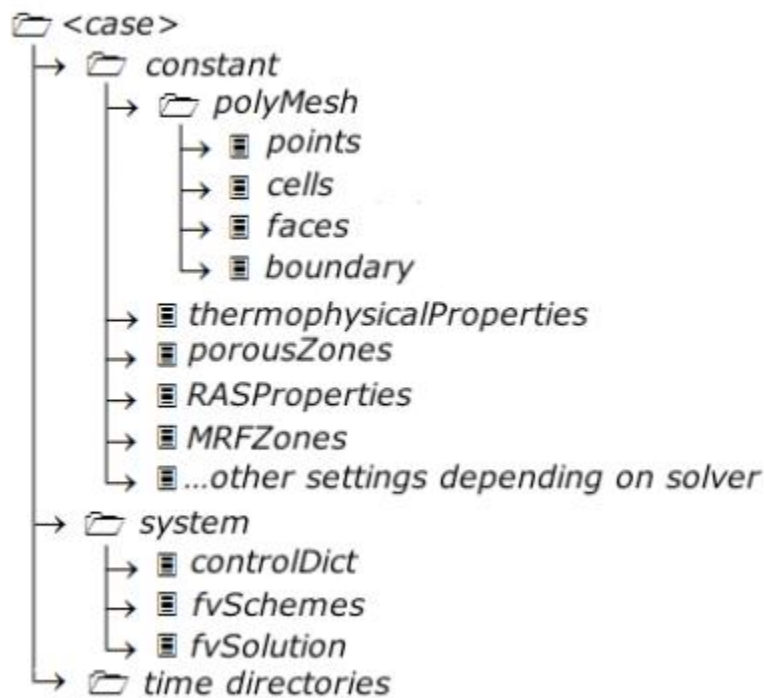


Figure 4.4: Directory structure of an OpenFOAM case in general scenario.

As an example, if the name of the file ‘*blockMeshDict*’ is kept inside ‘constant’ folder, and then in the above main case directory if the terminal command is given as ‘*blockMesh*’, then it develops hexahedral elements containing mesh inside a constant folder. Similar to that, for the

solvers related to multiphase flows, if the ‘*setFieldsDict*’ titled file is inside the folder called system, and then the command is applied in the terminal over case directory as the ‘*setFields*’, then the *alpha.liquid* (in this case *alpha.water*) file receives a certain set of volume fraction values in defined spots of the mesh as the initial position of liquid. These specified spots are defined in the ‘*setFieldsDict*’ file.

4.3.3 OpenFOAM hydrodynamics problem setup

In this section, the problem setup and overall framework generation of the project is discussed in detail for future researchers. The standard operating procedure (SOP) of the model for is also explained.

The problem setup is divided in two parts which are: 1) single-phase flow in complex geometrical domain and 2) multiphase flow in the same complex geometrical domain. In the single-phase case the mesh study is carried out to find the optimized element configuration, while for multiphase flow setup, the objective was to find the coarser mesh to run the simulation at high-fidelity state while achieving reduction in computational resources. Although the studies are carried out with different modeling approaches, the fundamental geometrical domain development and the mesh development, which is essential for the overall model development, is performed identical for both studies.

4.3.3.1 Geometrical development

The Mellapak 250.Y and 250.X packings are geometrically highly complex and large computational resources consuming structures. In this project the 250.Y packing is utilized which shows to a certain degree, similar characteristics with Koch-Glitsch Gempak-3A structured packing (*Figure 4.5*). For these complex geometrical structures, a robust tool is needed to for

suitable FVM mesh creation. The geometrical domain was developed using Autodesk inventor 2019, which is 3D Computer Aided Designing (CAD) software. A proprietary 3D CAD tool provides the research team of the project leverage towards multifaceted geometry development without a steep learning curve. In a specific section of absorber tower, the packing is formed by series of channels with triangular cross-section. This cross-section forms the whole sheet of panels in a section of packing which as shown in *Figure 4.5*.

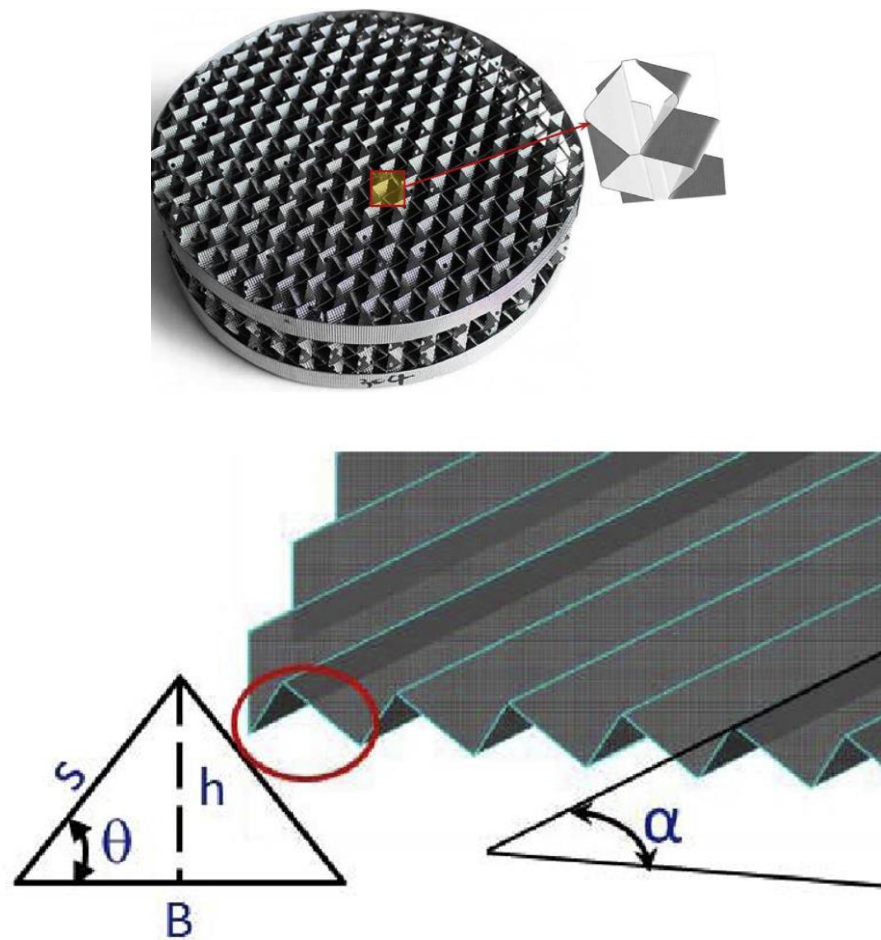


Figure 4.5: A corrugated sheet structured assembly, a predominant motivation towards the REU development for present project.

The Representative Elementary Unit (REU) is developed by using data and dimensions of cutting a certain section of two corrugated sheets aligned together as shown in *Figure 4.5*. The

resulting geometry is two individual parts of the sheets and its triangular sections placed next to each other with a hollow gap between them. This is further developed as a 3D CAD model for continuum domain assignment. The reactive continuum mechanics is observed between two gaps; thus, the gaps are filled with solid material in an Autodesk inventor resulting in the final geometrical domain chosen for discretization for use in the meshing tool and for the simulations. The *Table 4-1* shows values of the packing triangular section.

Table 4-1: The dimensions of the triangular section which are utilized for development of REU.

Design of Corrugated sheet of Mellapak 250.Y packing	
Corrugation angle (α)	45°
Crimped Angle (θ)	45°
Corrugation base (B)	18 mm
Corrugation height (h)	9 mm
Corrugation Side (s)	12.73 mm

After drawing the baseline triangle with defined height and side, the procedure to design and draft the section is elegant and recursive for the whole REU (*Figure 4.6*). First, a baseline triangle is created with 2D sketch the triangle is extruded along defined axis. Now, the extrusion of 2D triangle over plane in 3D space is tricky process since the defined axis is at 45° tilted to the main Y axis due to requirement of crimped angle which is defined above. Thus, first a line is generated using a 3D points perturbation method in 3D space of the Inventor at 45°. Later the drawn line is defined as a support line for extrusion and the first triangle of packing is designed. Later this triangle is patterned across the space as long as desired. The excessive pattern of these triangles is then trimmed by various cutting options available in Autodesk Inventor. In the final 3D CAD model cosmetics, the thin cuts were marked at the top portion to mark the liquid inlet

line and similarly at bottom to mark the liquid outlet line. For gas-liquid counter-current flow development, at the centerline of packing, a solid area created on different levels is comparable to the liquid inlet and outlet lines, near the top and bottom of the packing. The *Figure 4.6* shows the completed the 3D CAD model.

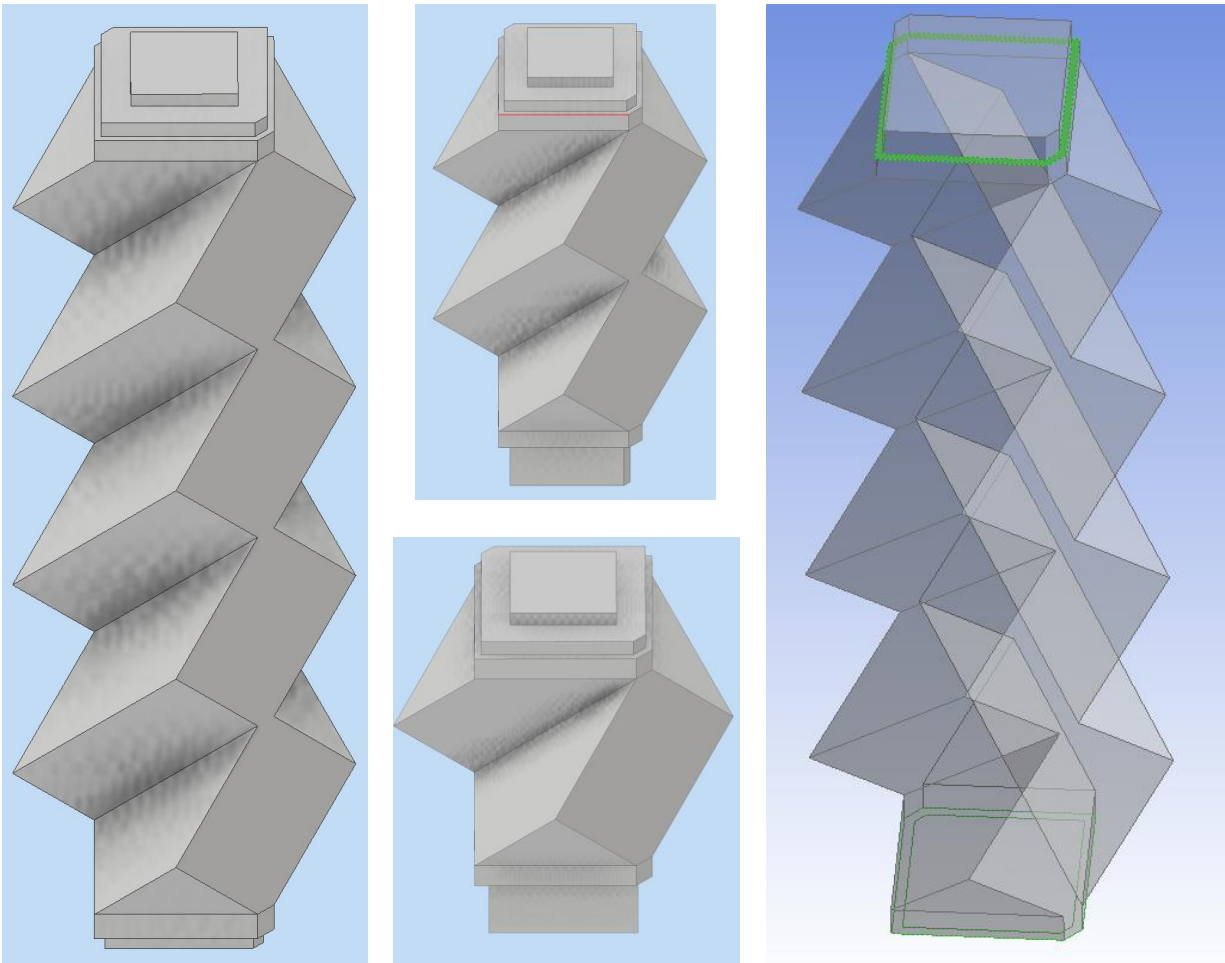


Figure 4.6: Finalized 3D CAD model of Representative Elementary Unit (REU) Multiple levels of REU is shown 3 Sections, 2 Sections, 1 Sections.

4.3.3.2 Discretization Grid Algorithm Development

The computational flow domain is then imported for volume discretization towards different software tools which are ICEM-CFD (previously known as GAMBIT), snappyHexMesh

(the tool provided with OpenFOAM for discretization of geometrical domain), and FLUENT MESHING module. Later on, after computational study and failure of certain methods, it was decided to use the discretization method of ICEM-CFD software which is owned by ANSYS Corporation.

The goal of the discretization study and final product is to capture the hydrodynamics of flow over thin filament generation at a specific flowrate, thus CutCell Cartesian scheme is critical towards development of multilayered mesh generation. First, tri-cell based multivariant mesh is generated using the FLUENT meshing module. The mesh was later imported into the OpenFOAM environment by providing the command 'fluent3DMeshToFoam'. A basic mesh study was also performed using single-phase flow equations. The results failed to produce as time-steps gradually decreasing, eventually failing to reach a time-step of value 1. OpenFOAM solvers provide an advantage of allowing to import any software based discretized domain by command 'fluent3DMeshToFoam' which converts 3D non-binary mesh to OpenFOAM readable point system.

With the goal of producing a CutCell based all hexahedral mesh, the OpenFOAM founded open-source meshing tool called snappyHexMesh, which is part of OpenFOAM pre-processing package, is utilized. The snappyHexMesh utility generates 3-Dimensional meshes containing hexahedra (hex) and split-hexahedra (split-hex) automatically from surfaced or solid geometries. The meshing algorithm approximately conforms to the surface by iteratively refining starting mesh morphing and the final result as surface mesh on the outer surface. Although, stating several advantages, the meshing utility lacks the ability to develop conformal meshes for the boundary-conditions defined for each surface and acts independently of the solver software. This generates large confinement of errors for complex boundary conditions such as periodic boundary conditions.

The periodic boundary condition requires the identical elements placement on both faces which are under discretization algorithm this fails to achieve using snappyHexMesh tool. Apart from that, snappyHexMesh tool requires a certain degree of programming and in-depth knowledge of Linux bash command which forces the team to devote ample time towards the steep learning curve and eventually, due to all these reasons, the tool was omitted from the computational procedure as a pre-processing tool.

After snappyHexMesh, the ICEM-CFD tool is utilized which is part of ANSYS pre-processing software utilities package and previously known as GAMBIT. ICEM-CFD provided correct all hexahedral CutCell scheme-based mesh, after multiple tries. ICEM-CFD also developed an identical grid on faces that defined the periodic boundary condition surfaces. The flow of the mesh generation via ICEM-CFD tool is complicated for complex geometries such as the geometry of Mellapak packing REU; however, due to seamless GUI and availability of software in Windows environment, agreement arose with the unified opinion of using ICEM-CFD as meshing software. Once the ICEM-CFD based mesh is saved with a non-binary ASCII based container, the command 'fluent3DMeshToFoam' is utilized on the terminal to transform the mesh to interFoam recognizable discretized all hexahedral CutCell scheme-based grid. Figure 4.6 shows the meshing of REU. The resulting REU is created with ~ 500,000 elements. The grid study is performed with multiple meshes and the 500,000 elements.

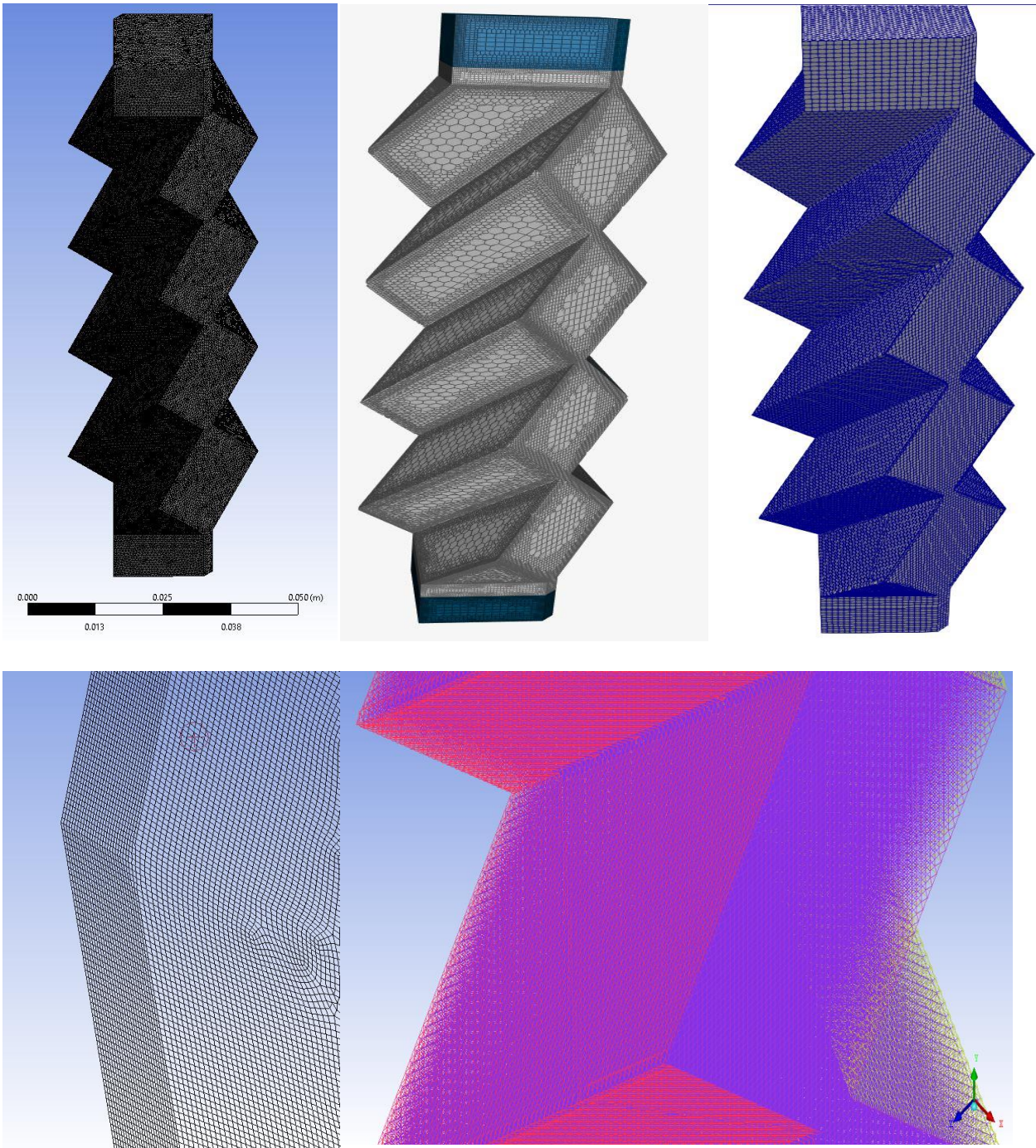


Figure 4.7: Finalized 3D grid of REU the meshes above are tetrahedral prism-based elements, multilayered hexahedral snappyHexMesh tool based elements, and uniform ICEM-CFD based CutCell based mesh. Below two images are showing enlarged views of ICEM-CFD based mesh showing uniformity with single layer inflation at boundary for capturing hydrodynamics of flow along boundary layers.

4.3.3.3 Computational Solver Development

The computational solver development was performed using two flow physics, namely 1) single-Phase flow physics, and 2) multiphase flow physics. The results of the multiphase flow physics are more critical to the overall projects thus the results based upon the single-phase flow physics were analyzed less.

4.3.3.3.1 Single-Phase Flow Study Solver Setup

As the first step to multiphase CFD model development the OpenFOAM compatible grid was first implemented in the single-phase CFD modeling solver. The overall approach used for the simulations setup is similar to the work of Owens et. al. [126] [127], however with flow behavior modeling as laminar. The computational domain and the mesh structure are built upon Autodesk Inventor, ANSYS ICEM-CFD, thus the pre-process workflow is 3rd party software suits. The modeling approach provides researchers an impression of ‘dry pressure drop’.

A single-phase flow of fluid is passed through the model with the fluid having transport properties of carbon dioxide (CO₂). All the transport properties of the implemented fluid are assumed as constant, and the flow is non-reactive in representative domain. A single-phase solver from OpenFOAM library implemented as ‘simpleFoam’, a steady-state solver for incompressible, isothermal, turbulent or laminar flows using SIMPLE algorithm for computations of pressure-velocity coupling was used for this phase of the modeling. The partial differential equations (PDE’s) representing the nature of single-phase fluid flow physics embedded in solver and solver equation solving algorithm is described in section 4.2 of this chapter, while adding in-depth understanding in appendix B.

The system needs to be completed with suitable boundary conditions for better convergence for the PDE's. The overall computational domain under mathematical symbol, shown as Ω and the boundary to the domain defined as $\partial\Omega$, is devised in three sections as follows [88]:

$$\partial\Omega_{Total} = \partial\Omega_{inlet} \cup \partial\Omega_{outlet} \cup \partial\Omega_{wall} \quad (4.16)$$

The boundary conditions and initial conditions shows mathematical interpretations are described in *Table 4-2* form as follows:

Table 4-2: The Boundary Conditions (BC's) are asserted for REU under single-phase solver configuration [88].

Boundary	Condition
$(\partial\Omega_{inlet}) = \left\{ (x, y, z) \in \mathbb{R}^3 : x = \frac{h_{col}}{2}, y^2 + z^2 \leq r_{col}^2 \right\}$	$u = [-u_i, 0, 0]^T$ $S_f \cdot \nabla p = 0$
$(\partial\Omega_{outlet}) = \left\{ (x, y, z) \in \mathbb{R}^3 : x = -\frac{h_{col}}{2}, y^2 + z^2 \leq r_{col}^2 \right\}$	$S_f \cdot u = [0, 0, 0]^T$ if $\Phi_f^V > 0$, else $u = [0, 0, 0]^T, p = 0$
$(\partial\Omega_{wall}) = \left\{ (x, y, z) \in \mathbb{R}^3 : x = \left[\frac{h_{col}}{2}, -\frac{h_{col}}{2} \right], y^2 + z^2 = r_{col}^2 \right\}$	$u = [0, 0, 0]^T$ $S_f \cdot \nabla p = 0$

At inlet(s) of the geometry regardless of the fluid transport properties, the prescribed boundary conditions are Dirichlet boundary conditions for velocity u , due to flow nature being laminar no turbulence parameters needed to define. Also, the complex condition for velocity is not required due to flow being simplified assumptions.

For the outlet(s) of the geometry, being independent of the fluid flow transport properties, the inlet-outlet boundary condition is defined for velocity field u . The boundary condition is a combination of Dirichlet and Neumann which is also known as Robin boundary condition. This

acts as Neumann boundary conditions due to flow flux being non-zero, and otherwise acts as a Dirichlet boundary condition. For pressure, the pure Dirichlet boundary condition is applied which is a fixed pressure value.

For the walls of the geometrical domain, the standard no-Slip boundary condition is prescribed for velocity while the pressure boundary condition is constant with the value defined as zero. At the near wall treatment, to capture the hydrodynamics of the boundary layer, a thin single layer inflation is applied. The latter two walls of the geometry faces which are termed as '*frontWall*', and '*backWall*', are defined with more complex boundary condition called '*Periodic boundary condition*'. For this application, conformal mapping is required over the structured CutCell grid that is having elements number with identical value.

During the OpenFOAM computational setup, first the pre-prepared '*simpleFoam*' solver template is obtained from the OpenFOAM installation directory, which is usually inside '/opt/utilities' folder. From the template the '*blockMeshDict*' file is removed and replaced by the '*polyMesh*' folder which contained all the Mesh files regarding to REU. Then, certain transport properties are changed in '*transportDict*' file. All other files and code remains similar to the template. Later in the process, the files are changed in 'Ø' folder, which is the boundary conditions defining folder. The values inside 'u' and 'p' files are changed as required. All the files are stored in the system path of OpenFOAM, defined under '\$FOAM_DIR' as system variable. After opening 'terminal' software, first command '`checkMesh -allTopology -allGeometry`' provides checking the geometry for any issues and certain failure warning. After that the case is decomposed for running over parallel core configuration by dividing the case in the desired number of cores by providing command '`decomposePar`'. After that '`mpirun -np 4 simpleFoam -parallel > log & tail -f log`' command is executed on the terminal

window. This command essentially allows solver ‘*simpleFoam*’ to run in parallel with 4 core configuration and simultaneously log the residuals in ‘*log*’ file.

4.3.3.3.2 Multiphase Flow Solver and Case Advancement

After development of single-phase flow results, which were promising for mesh study and dry pressure drop analysis, the focus centered towards multiphase flow solver and case development. Since the critical goal of project was directed around multiphase flow physics predictive analysis using *interFoam*, only a few cases were run to calculate dry pressure drop and mesh sensitivity analysis. Thus, this section is devoted towards a brief explanation of the simulation setup of gas–liquid two phase flow in the geometry of structured packings of Mellapak family.

The multiphase flow study is developed based upon the identical geometrical domain which was used for single-phase flow study. It is Representative Elementary Unit (REU). Before divulging in the actual REU, the author first develops a 2D cross section based 2-dimensional study of gas–liquid two phase flow in zigzag Mellapak packings cross sectional geometrical domain. Although the behavior of flow shows laminar thin film layer-based flow, the flow is gas–liquid two phase counter–current flow. The study is concentrated towards estimation of parameters such as time needed for the simulation to finish. Convergence and divergence criteria are established for the *interFoam* solver and the thin flow generation pattern and liquid wetting properties. The author also utilizes ‘*reactingParcelFilmFoam*’ for thin film study while development of *interFoam* solver. The resulting information provides readers a Code-to-Code comparison with the ANSYS FLUENT solver and the local distribution of the liquid in the column and on the REU of the gas-liquid interface.

InterFoam solver is one of many multiphase solvers which are available in OpenFOAM numerical C/C++ framework. As described, interFoam is a solver for 2 incompressible, isothermal immiscible fluids using a VOF (volume of fluid) phase-fraction based interface capturing approach, with optional mesh motion and mesh topology changes including adaptive re-meshing. [109]. The CO2 capture technology is progressed with advanced chemical usage in recent decades, unfortunately, experimental data focusing on third and second generation solvent behavior in structured packings of Mellapak family based upon gas-liquid interface is limited. Much of data indicates liquid holdup, which is amount of liquid present in the packing at time t .

Thus, based upon previous section discussion about the fundamental equations of fluid flow if spatial computational domain is defined as $\Omega \subseteq \mathfrak{R}^3$ as a part of liquid occupied domain in at an instance of time t defined as Ω_A and therefore $\Omega_A \subset \Omega$. So the resultant total liquid holdup in domain and 2D slice of domain is as follows:

$$\bar{\alpha}^{\Omega} = \frac{V(\Omega_A)}{V(\Omega)} = \frac{1}{V(\Omega)} \int_{\Omega} \alpha \, dV, \quad (4.17)$$

$$\bar{\alpha}^{\eta^{y-z}_{x_i}} = \frac{1}{Area(\eta^{y-z}_{x_i})} \int_{\eta^{y-z}_{x_i}} \alpha \, dS,$$

The liquid holdup in the column such as REU is usually measured in dependence on the intensity of liquid and gas flow. The intensity of liquid flow which is also termed as ‘liquid load’ is defined as:

$$B = \frac{Q}{S_{col}} = \left[\frac{m^3 h^{-1}}{m^2} = m \cdot h^{-1} = m/h \right] \quad (4.18)$$

Where Q is the liquid flow rate at inlet and $S_{col} = \pi \times D_{col}^2/4$ is the area of the column cross-section. [82]

The computational setup for 2-dimensional structured grid is configured using two types of geometries, firstly a straight-wall column which measures the hydrodynamics of wetting over a vertical straight wall, and secondly a zigzag-wall column imitating where parameters over the zigzag vertical wall mimic the geometrical domain of certain 2D sections of the overall REU. The proposed geometry developed as per requirement of two-dimensional counter-current gas-liquid flow. Thus, the solvent inlet and outlet are respectively located at the top-left and bottom-left corners, while the gas inlet and outlet are respectively located at top-right and bottom-right corners of domain. The boundary conditions do not differ from previously stated boundary conditions in *Table 4-1*. After geometrical domain development, a domain discretization is necessary. By Hu et al. and Xu et al. [95] [128] it was found that the mesh size of $0.1 \times h$ where ' h ' is film thickness is sufficient to capture the liquid behavior. Thus, the resultant grid is all quad dominated uniformly structured grid with the boundary layer developed over the left wall of the domain, hence the 'constantAlphaContactAngle' boundary condition is applied. To generate the all quad dominant mesh, the terminal 'blockMesh' command is executed. However, in order to develop mesh using block mesh utility of OpenFOAM, first a 'blockMeshDict' file needs to be created. Using geometrical coding language, certain co-ordinates are plotted in 2D space and blocks are created using those points and hence the 'blockMeshDict' is generated. Later transport properties of fluid are checked in 'transportPropertiesDict' these are listed in *Table 4-4*. Using 'setFields' command, an initial condition is modeled in meshed domain. If the user tends to visualize the initial conditions, the block of liquid for a certain section of the domain is initiated at the time $t = 0$ instance. Later, the interFoam solver was executed over the case directory and

results were produced. An identical procedure is followed for zigzag geometry, a *blockMeshDict* based design generation, followed by grid generation over 2D CAD model of zigzag left wall geometry, after that implementation of initial conditions using *setFields*, and accomplishment of results by simulations of case study using *interFoam* solver.

The next step of the multiphase flow solver advancement focused on the 3D domain setup. Investigation focused on the hydrodynamics (i.e. liquid holdup and interfacial area) in REU of 250.Y packings of the Mellapak family. The 3D geometrical domain is of identical dimensions and shape described in previous sections of this chapter. The geometry is a single unit of lateral directions defined from a system consisting of two of those smooth corrugated sheets arranged perpendicularly to each other. A 2 mm gap is specified between two sheets, and in addition, the computational domain consists of three of these repeating units in vertical directions. A top-down view of this REU motivated by the structure shown in figure 4.5. Since the computational domain shows higher complexity than previously stated 2D domains, the domain is developed in Autodesk inventor and meshed in ICEM-CFD, previously popularized as most validated mesh generation software called GAMBIT. The prescribed initial conditions representing a dry column is mathematically formulated at time $t = 0$ with all fields set to zero, i.e., the velocity u , dynamic pressure p_d , and the volume fraction depicting function α , are set as zero. Near the inlet, a small meshed domain of elements is characterized as 1 to show the start of fluid in the domain. As described in the previous single-phase study section, the overall computational domain is given under the mathematical symbol shown as Ω and the boundary to the domain defined as $\partial\Omega$. Thus, the domain is devised in three sections as follows:

$$\partial\Omega_{Total} = \partial\Omega_{inlet} \cup \partial\Omega_{outlet} \cup \partial\Omega_{wall} \cup \partial\Omega_{atmosphere} \quad (4.19)$$

The atmosphere boundary added at the topmost surface of the geometry states pressure flux and gradient to open boundary conditions, in other words it is set to zero throughout the simulations acting as vicious undesirable spurious eddy currents which eventually arises during the simulations, disrupting overall momentum balance and causes divergence in simulation. Thus, the overall boundary conditions are as follows [88]:

Table 4-3: The Boundary Conditions (BC's) are asserted for REU under two phase gas-liquid solver configuration.

Boundary	Condition
$(\partial\Omega_{inlet}) = \left\{ \begin{array}{l} (x, y, z) \in \mathbb{R}^3 : x = \frac{h_{col}}{2}, \\ y^2 + z^2 \leq r_{col}^2 \end{array} \right\}$	$u = [-u_i, 0, 0]^T$ $S_f \cdot \nabla p_d = 0$ $\alpha = 1$
$(\partial\Omega_{outlet}) = \left\{ \begin{array}{l} (x, y, z) \in \mathbb{R}^3 : x = -\frac{h_{col}}{2}, \\ y^2 + z^2 \leq r_{col}^2 \end{array} \right\}$	$S_f \cdot \nabla u = [0, 0, 0]^T$ <i>if</i> $\Phi_f^V > 0,$ $u = [0, 0, 0]^T, S_f \cdot \nabla \alpha = 0$ <i>else</i> $S_f \cdot \nabla p_d = 0, \alpha = 0$
$(\partial\Omega_{atmosphere}) = \left\{ \begin{array}{l} (x, y, z) \in \mathbb{R}^3 : x = 0, \\ y^2 + z^2 \leq r_{col}^2 \end{array} \right\}$	$S_f \cdot \nabla u = [0, 0, 0]^T$ <i>if</i> $\Phi_f^V > 0,$ $u = [0, 0, 0]^T, S_f \cdot \nabla \alpha = 0$ <i>else</i> $S_f \cdot \nabla p_d = 0, \alpha = 0$
$(\partial\Omega_{wall}) = \left\{ \begin{array}{l} (x, y, z) \in \mathbb{R}^3 : x = \left[\frac{h_{col}}{2}, -\frac{h_{col}}{2} \right], \\ y^2 + z^2 = r_{col}^2 \end{array} \right\}$	$u = [0, 0, 0]^T$ $S_f \cdot \nabla p_d = 0$ $S_f \cdot \nabla \alpha = \text{constantAlphaContactAngle}(\alpha)$

Along with these boundary conditions which define the fundamental continuum forces by solving PDE's, a complex set of boundary conditions is implemented called 'periodic'. This

boundary condition demands identical elements across the surfaces to which the boundary condition is prescribed. Essentially, the periodic boundary condition defines an approximately large (relatively infinite) system by using a small part called a unit cell, which governs the linear momentum of the system towards principle of conservation. The angular momentum is not converged. The periodic boundary condition is mathematically described as follows [109]:

$$\frac{\partial^m \Omega_{wall_{left}}}{\partial x_n^m} \phi(x_1, x_2, x_3 \dots, a_n) = \frac{\partial^m \Omega_{wall_{right}}}{\partial x_n^m} \phi(x_1, x_2, x_3 \dots, b_n) \quad (4.20)$$

Hence, with application of boundary conditions and structured grid, the computational model setup now considers transport properties in the ‘transportPropertiesDict’ file inside ‘constant’ folder.

Table 4-4 shows the implied fluid transport properties.

Table 4-4: Transport properties of selected liquids solutions.

Liquid Type	Density (ρ) (kg/m ³)	Viscosity (μ) (mPa.s)	Surface Tension (σ) (mN/m)
Water	997	0.89	72.8
40% MEA	979	3.71	54.8
0.51x MPZ	946.41	13.48	34.37
48.8% MDEA	1016.6	9.25	47.56

Along with that, five values of examining flowrates are selected which are 0.000483 m³/s, 0.000869 m³/s, 0.003477 m³/s, 0.008694 m³/s, 0.013041 m³/s, and six different values of constant liquid contact angles are considered, which are 20°, 30°, 40°, 60°, 70°, 90°. Therefore, based upon that a large size design of experiment (DOE) is created to test all the possibilities. The Table 4-5 shows the DOE.

Table 4-5: Design of Experiment using Taguchi design showing number of cases in this project

Test Case	Solvents	Flowrate	Contact Angle	Test Case	Solvents	Flowrate	Contact Angle
1	Water	0.000483	20	31	MEA	0.000483	20
2	Water	0.000483	30	32	MEA	0.000483	30
3	Water	0.000483	40	33	MEA	0.000483	40
4	Water	0.000483	60	34	MEA	0.000483	60
5	Water	0.000483	70	35	MEA	0.000483	70
6	Water	0.000483	90	36	MEA	0.000483	90
7	Water	0.000869	20	37	MEA	0.000869	20
8	Water	0.000869	30	38	MEA	0.000869	30
9	Water	0.000869	40	39	MEA	0.000869	40
10	Water	0.000869	60	40	MEA	0.000869	60
11	Water	0.000869	70	41	MEA	0.000869	70
12	Water	0.000869	90	42	MEA	0.000869	90
13	Water	0.003477	20	43	MEA	0.003477	20
14	Water	0.003477	30	44	MEA	0.003477	30
15	Water	0.003477	40	45	MEA	0.003477	40
16	Water	0.003477	60	46	MEA	0.003477	60
17	Water	0.003477	70	47	MEA	0.003477	70
18	Water	0.003477	90	48	MEA	0.003477	90
19	Water	0.008694	20	49	MEA	0.008694	20
20	Water	0.008694	30	50	MEA	0.008694	30
21	Water	0.008694	40	51	MEA	0.008694	40
22	Water	0.008694	60	52	MEA	0.008694	60
23	Water	0.008694	70	53	MEA	0.008694	70
24	Water	0.008694	90	54	MEA	0.008694	90
25	Water	0.013041	20	55	MEA	0.013041	20
26	Water	0.013041	30	56	MEA	0.013041	30
27	Water	0.013041	40	57	MEA	0.013041	40
28	Water	0.013041	60	58	MEA	0.013041	60
29	Water	0.013041	70	59	MEA	0.013041	70
30	Water	0.013041	90	60	MEA	0.013041	90

Test Case	Solvents	Flowrate	Contact Angle	Test Case	Solvents	Flowrate	Contact Angle
61	MDEA	0.000483	20	91	MPZ	0.000483	20
62	MDEA	0.000483	30	92	MPZ	0.000483	30
63	MDEA	0.000483	40	93	MPZ	0.000483	40
64	MDEA	0.000483	60	94	MPZ	0.000483	60
65	MDEA	0.000483	70	95	MPZ	0.000483	70
66	MDEA	0.000483	90	96	MPZ	0.000483	90
67	MDEA	0.000869	20	97	MPZ	0.000869	20
68	MDEA	0.000869	30	98	MPZ	0.000869	30
69	MDEA	0.000869	40	99	MPZ	0.000869	40
70	MDEA	0.000869	60	100	MPZ	0.000869	60
71	MDEA	0.000869	70	101	MPZ	0.000869	70
72	MDEA	0.000869	90	102	MPZ	0.000869	90
73	MDEA	0.003477	20	103	MPZ	0.003477	20
74	MDEA	0.003477	30	104	MPZ	0.003477	30
75	MDEA	0.003477	40	105	MPZ	0.003477	40
76	MDEA	0.003477	60	106	MPZ	0.003477	60
77	MDEA	0.003477	70	107	MPZ	0.003477	70
78	MDEA	0.003477	90	108	MPZ	0.003477	90
79	MDEA	0.008694	20	109	MPZ	0.008694	20
80	MDEA	0.008694	30	110	MPZ	0.008694	30
81	MDEA	0.008694	40	111	MPZ	0.008694	40
82	MDEA	0.008694	60	112	MPZ	0.008694	60
83	MDEA	0.008694	70	113	MPZ	0.008694	70
84	MDEA	0.008694	90	114	MPZ	0.008694	90
85	MDEA	0.013041	20	115	MPZ	0.013041	20
86	MDEA	0.013041	30	116	MPZ	0.013041	30
87	MDEA	0.013041	40	117	MPZ	0.013041	40
88	MDEA	0.013041	60	118	MPZ	0.013041	60
89	MDEA	0.013041	70	119	MPZ	0.013041	70
90	MDEA	0.013041	90	120	MPZ	0.013041	90

After setting all the cases are per the DOE, every case was simulated with standard operating procedure. As described in the previous section, the first command executed as ‘checkMesh -allTopology -allGeometry’ provided for checking the geometry with any issues and failure warning. Then, the ‘setFields’ command is mandated to setup the initial liquid conditions in the domain, then the case is decomposed for running over parallel core configuration by dividing the case in the desired number of cores by providing command

'decomposePar', after that 'mpirun -np 4 interFoam -parallel > log & tail -f log' command is executed on the terminal window.

4.4 Results and Discussions

The primary goal of this project was to develop a predictive Computational Fluid Dynamic (CFD) capability targeting absorption enhancement during the scale-up of 2nd generation post-combustion CO_2 capture technologies. Specifically, absorber packing configurations and the solvent flow rates that enhances mass transfer rates while minimizing pressure losses and liquid hold-up were targeted.

4.4.1 OpenFOAM Computational Environment Creation

Before presenting results of the hydrodynamics of multiphase flow simulation, the author first explains the OpenFOAM simulation development and the path taken to reach the main objective of research. To fully understand and model the multiphase flow hydrodynamics of 3D complex structured REU, it helps to first understand simulations using the interFoam solver with a 2D simplified geometrical domain-based and simplified boundary conditions. Secondly, an understanding of the 3D REU domain and its implantation with hybrid complex boundary conditions with involvement of multiphase flow algorithms is needed.

The reason to delve into these other aspects before tackling the primary goal is due to significant challenges encountered during early stages of project resulting from the formulation of "spurious currents" in the numerical simulation. These spurious currents resulted in local gas velocity magnitudes that were unreasonably enlarging over the period of computational time which further increased residuals. These issues also caused a rapid deterioration of delta time stepping

after every timestep in the transient simulations. After a lot of trial and error and changing of boundary conditions including different patches of the domain reasonable results were obtained.

4.4.1.1 Single-Phase Simulations

This section discusses the single-phase simulations showing velocity and pressure drop profiles in the 3D REU unit. The computational study was developed using SIMPLE algorithm. In OpenFOAM the solver is called as *simpleFoam*, while the ANSYS FLUENT software has the option to select the SIMPLE algorithm. In the past, researchers have predicted dry pressure drop by a single-phase solver simulations by using transport properties of gas phase only.

The *Figure 4.8* shows the pressure and velocity profile of single-phase flow passing through 3D REU. The observation of these profiles shows similarity in the solutions for OpenFOAM and ANSYS FLUENT. The results also give an intuition of simulation duration as per wall clock time. To finish the single-phase flow for ~ 400,000 elements with 500 timesteps, it takes 3 hours of wall clock time for single-phase simulation. This gives an approximate time required for two-phase simulations, although the two-phase simulations tend to vary due to the use of the different algorithms used during two-phase simulations.

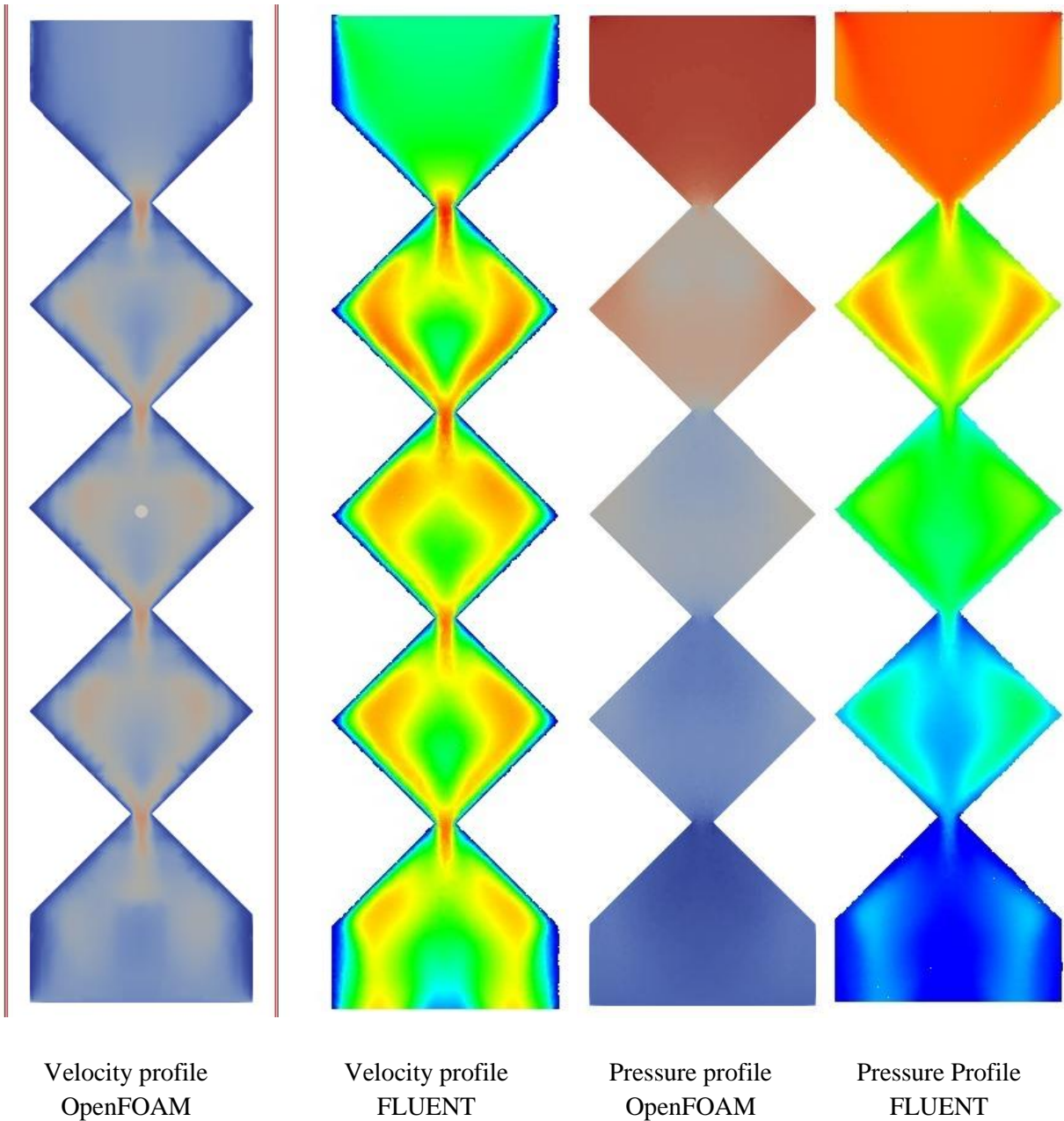


Figure 4.8: Snapshot of the vertical plane along Y axis of REU indicating velocity and pressure contours using single-phase flow.

4.4.1.2 Multiphase Simulations

The 2D multiphase simulations are devised after single-phase flow and its success, as indicated by no occurrences of divergence, which boosted confidence to proceed toward the primary goal of this research. A single vertical column is created in `blockMeshDict` and

numerically modelled under *interFoam* solver. These were gas-liquid two-phase simulations utilizing simplified boundary conditions. This part of numerical modeling was inspired by a solver and case study called “Wetted Wall Column” provided by Carbon Capture and Sequestration Initiative (CCSI) governed by National Energy Technology Laboratory (NETL) [121], and “Separation Research Program” organized by University of Texas, Austin. Transient simulations in *interFoam* created a profile of liquid rolling down the vertically straight column, with respect to time which his shown in *Figure 4.9*:

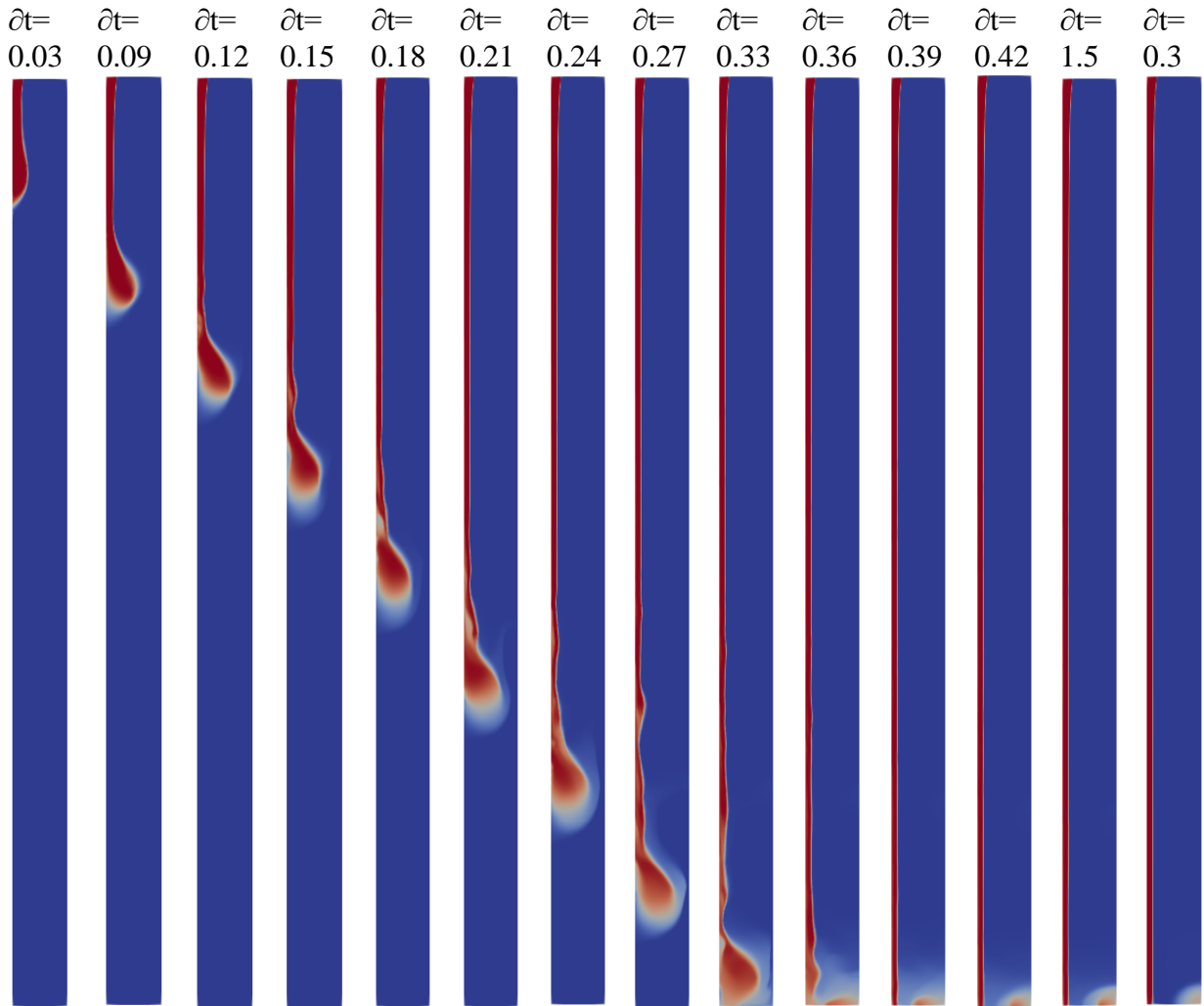


Figure 4.9: Temporal profile Snapshots of the wetting of left wall of the column using gas-liquid two-phase flow solver. The transport properties of liquid utilized were water.

The observation of *Figure 4.10* allows readers and author to understand the hydrodynamics of thin film flow over vertical wall in time dependent snapshots. The flow pattern indicates thin film formation over a vertical wall as a function of contact angle as well as surface tension of liquid. After the 2D simulations, author developed an understanding of theory of boundary conditions for use in the 3D geometry for less divergence.

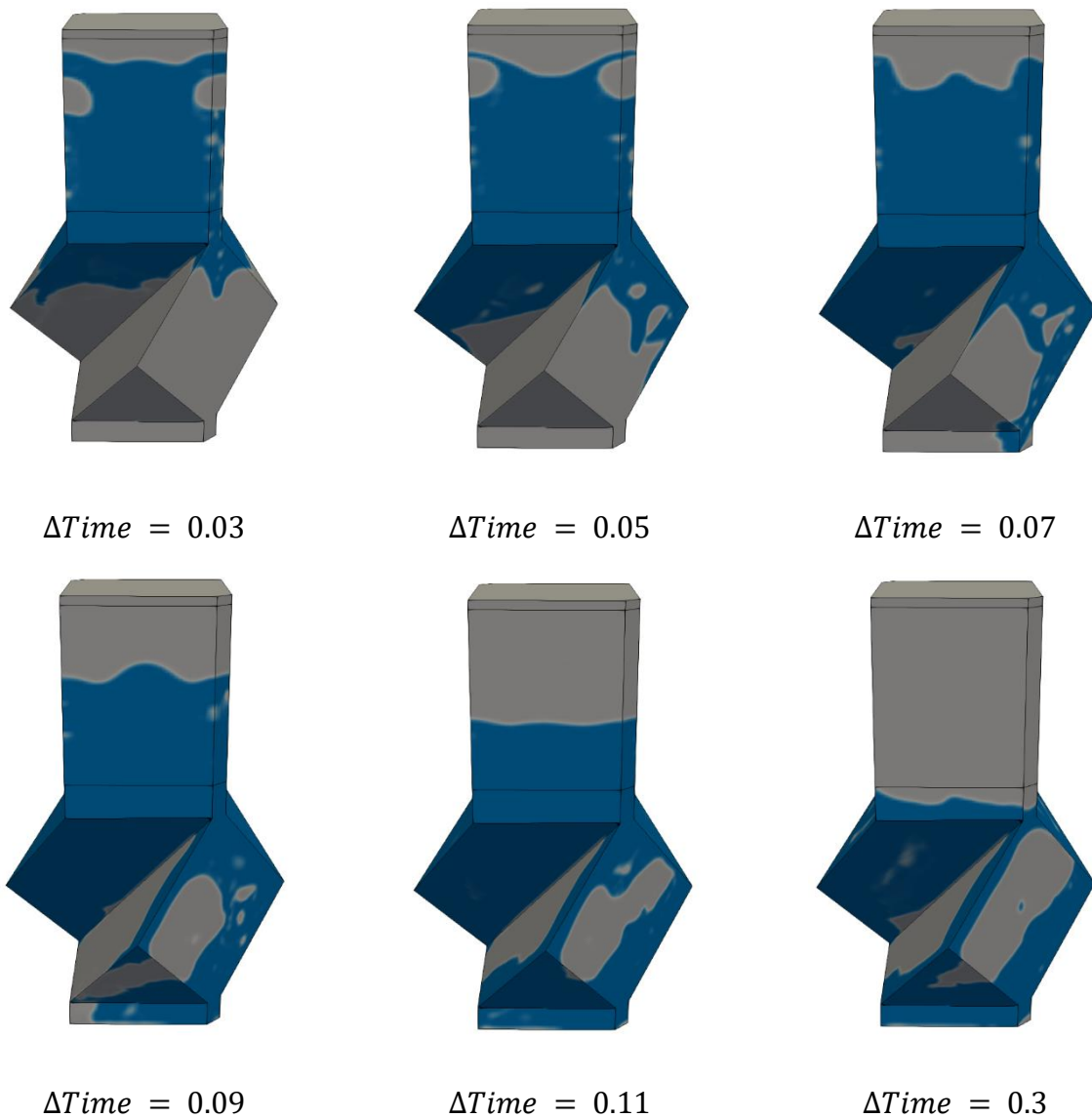


Figure 4.10: A time varying snapshots of the 1-part corrugation of REU with simplified conditions of boundary, which is gravity driven flow, inspired by Dam break case in OpenFOAM tutorials.

With indications of the speculative notion of boundary conditions from 2D simulations, the author portrays the time consecutive snapshots for flow of liquid in single corrugation geometry with tank at top. In this simulation a Tank was built overhead of the geometry and a gravity assisted flow is simulated to capture the rivulet pattern over a triangular section of the corrugated sheet. The flow hydrodynamics show wetting of the corners of the triangular corner section of the corrugation. Simplified boundary conditions (Dirichlet boundary conditions) are implemented, thus flow travels over the front wall, not providing insights of helical curve-based flow. Due to the simplified boundary conditions, the flow interacts between two sheets, thus voiding further validation of the previously published research. As a result, hybrid boundary conditions such as ‘periodic boundary conditions’ were implemented in this research. In terms of OpenFOAM, the periodic boundary condition is called ‘cyclicAMI’, where AMI stands for Arbitrary Mesh Interface. As previously discussed, the cyclicAMI boundary condition is categorized under Robin type boundary conditions which is a hybrid combination of Neumann and Dirichlet type boundary conditions.

4.4.2 3D REU Multiphase Flow Hydrodynamics

Based upon previously reported validation of VoF simulations and corresponding experimental investigation, the current study was carried out. The hydrodynamics in an REU of packing structure are explored for 4 different types of solvents with different flowrates and multiple values of contact angles. The design of experiment is comprised of a large amount of simulations. Each transport properties-based fluid simulation is comprised of six different contact angles and each contact angle comprised of five different flowrates. Thus, the total amount of simulations framework involves $5 \times 6 \times 4 = 120$ simulations. The effects of transport properties

and solvent flow rate are presented with respect to two types of dimensionless numbers; the Kapitza number (Ka) and Weber Number (We) shown below:

$$We = \rho_l u_l^2 \times \frac{h_{in}}{\sigma} = 7.72 \times 10^{-8} \left(\rho_l q_l^2 \times \frac{h_{in}}{\sigma} \right), \quad (4.21)$$

$$Ka = \sigma \left(\frac{\rho_l}{\mu_l^4 \times g} \right)^{\frac{1}{3}}$$

As the formula appears, the Weber number is calculated based upon the inlet conditions where h_{in} is the inlet height and u_l is the inlet velocity. Here the inlet velocity is based upon the amount of liquid load over structured packing, which is:

$$u_l = \frac{Q_l}{3600}, \text{ units} = m. s^{-1} \quad (4.22)$$

The Weber number, which is commonly used in these types of studies, generically represents the relative effects of inertia and surface tension. When flow transition starts occurring such as rivulet to thin film flow towards thick film covering all of the surface area, then the Weber number is considered more relevant compared to Reynold's number since the flow behavior is still under laminar regime. The Kapitza number is a dimensionless number here representing only fluid transport properties. Solvents with high Ka value are characterized by low viscosity and/or high number surface tension.

4.4.3 Grid Independent test

One of the critical steps of CFD analysis is conducting grid independent tests for computational fluid flows. Generally, a course grid can cause divergence in simulations and can reduce the accuracy of results. However, considering various variables as critical parts of this study,

such as required computational power, invested computational time, etc., minimalistic percentage error occurring between large scale simulations and small scale simulations was acceptable. One can substantially reduce the element size and can perform high-fidelity simulations of particular physics phenomenon with high-cost computational resources. In OpenFOAM framework, the code architecture changes the iterations based upon the type of elements and number of elements, similar to other codes such as COMSOL, or FLUENT. However, the algorithm is efficient compared to other software packages, thus allowing courser cell size meshes. Although, it leads to reduced accuracy, the percentage error is trivial compared to previous validation based experimental or computational results.

Thus, with that in consideration, the current research does not follow the older understanding of ‘higher the elements/cell in mesh, better the accuracy’. In fact, for simulations presented initialized with 0.5M cells, instead of reported cells/Elements configuration of 1.3M [82], the value of volume fraction with respect to time captured and post-processed using ParaView shows that, the values do not change and even if changes the change is trivial. Hence the number of cell configuration reduced to ~ 410,000 elements and the accuracy reduced by 0.75%, and the cell type is identical as the previous research which is CutCell all hexagonal with boundary layer.

At this stage, the time taken by single-phase simulation using simpleFoam solver is still 3 to 5 days on single core computing while it took 1.5 to 3 days with quad core computing. Thus, the element configuration is reduced to ~366,000 elements/cell and the accuracy reduced by 1.0 to 1.5%. What is of importance to the readers is that the process of finding interfacial area capture or dry pressure drop is not affected by substantial change in mesh size while the computational cost is significantly changed. The simulations which were taking 1.5 days now finished within 12 hours of wall clock time using quadcore basic configuration computing power. Thus, with faster

computing power the framework using regular PC takes 12 to 24 hours to finish one single-phase flow simulation, while with same grid size the multiphase simulations take a maximum of 48 hours to finish one simulation.

4.4.4 Transient flow with hybrid BCs

The process of developing transient flow in OpenFOAM is relatively easier due to all the main classes and their header files are connected to time iterations in terms of a loop. The implementation of periodic boundary conditions is substantially difficult, especially while generating meshes using ICEM CFD. By default, *interFoam* solver simulates multiphase flow dynamics in transient conditions. The periodic boundary conditions allow the flow to re-enter the flow domain on the left boundary after it exited from the right boundary. The process continues until the flow is exited from bottom boundary condition of flow outlet. In the process of the flow movement, the rivulet pattern starts appearing over the corrugated sheet.

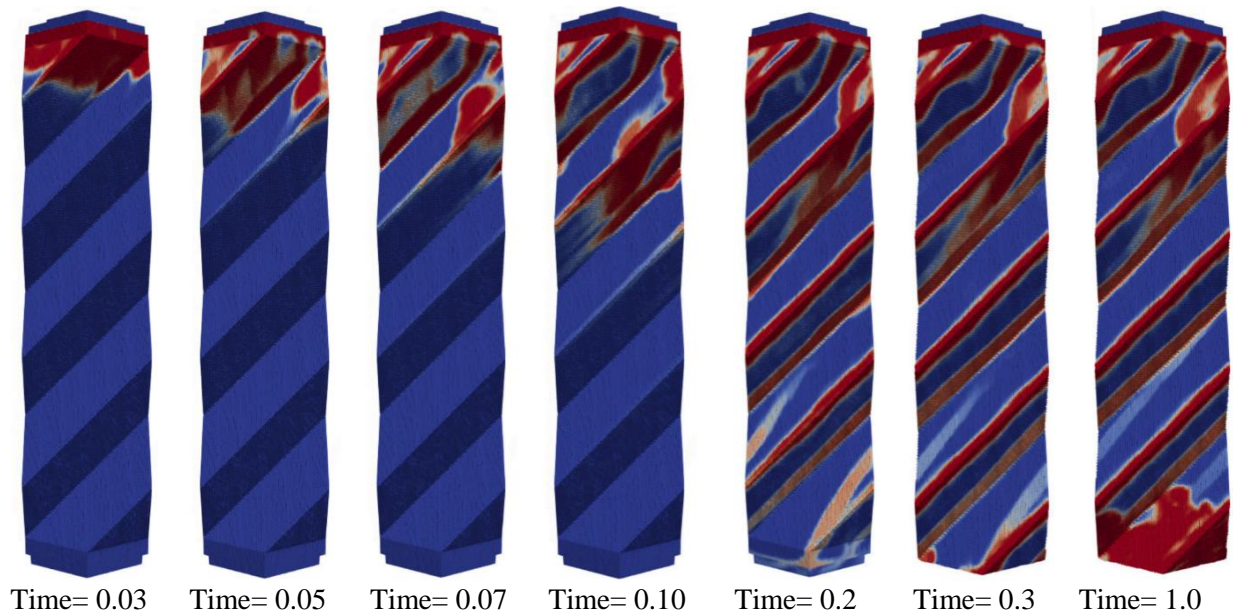


Figure 4.11: Snapshot of the gas-liquid interface depicting the temporal evolution of the wetting along corrugated sheet. Water ($Ka = 3969$) at $q_L = 180m^3/m^2$ here gas indicted by blue

The transient evolution of the wetting of a single sheet in the REU is illustrated in *Figure 4.11*, with a series of snapshots with liquid transport properties as surface tension = 72.8 mN/m and contact angle (γ) = 70°. The red color indicates wetting of liquid, while the blue color indicates dryness of surface. Based upon the snapshot, it can be observed that the flow of liquid is predominantly constrained to triangular channel valley generated due to attachment of two corrugated sheets, while the rivulets tend to fall down through 2mm gap between two sheets. Through observational aspects, it is worth noting that liquid flow behavior in the corrugated sheets is complex and liquid may not be constrained to a channel valley but also fall over the cap of 2mm between two sheets. However, apparently liquid does not cross the gap and flow over the other corrugated sheet. The hydrodynamic variables of the interest, such as wetted and interfacial area and liquid holdup, are computed for further analysis. In the present research, the computational value of interfacial area (A_I) is normalized by specific area of the packing (A_p) as $A_{In} = A_I/A_p$.

4.4.5 Effect of Solvent Properties

The local hydrodynamics in structured packing is predominantly dependent on the transport properties of the solvent. Thus, as part of this research a wide range of solvent properties was examined with simulations. For example, for every solvent and its property, the flowrate is changed and for every flowrate the contact angle changed. The results of physical properties on both liquid holdup and normalized interfacial area are explained in terms of Kapitza number of liquid.

Since the interfacial area is the crucial factor influencing the mass transfer in the solvent absorption system, the variable value needs to be accessed with high accuracy. Several experimental studies implicitly estimated the effective mass transfer area, based upon the results

of total absorption, or liquid holdup data of the experiment. The computational research, for example this presented research, tends to show interfacial area based upon time as well as per surface area of geometry derived from fundamental equations gives more insights towards intrinsic variables of flow which are yet in-deterministic in experiments.

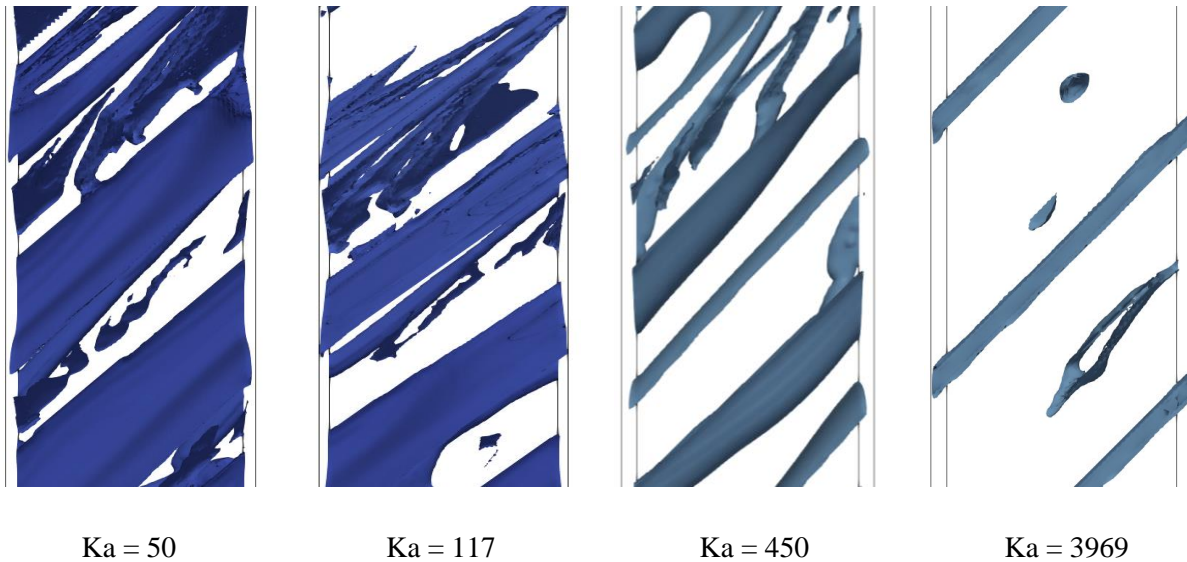


Figure 4.12: Snapshot of the liquid interface in one side of REU, for four indicated solvents by Ka number with fix load $q_L=72m^3/m^2$ and fix contact angle(γ) of 70°

The *Figure 4.12* shows the snapshot of the gas–liquid interface at $f = 0.5$ in one side of REU for four different solvents defined by Kapitza number (Ka) with fixed conditions of liquid load and constant contact angle. The shape resembling the helix arises due to the periodic boundary conditions applied as well as the iso-surface defined at the gas-liquid interface over a range of values from 0.5 to 1.0. The flow shows the behavior of rivulet pattern as well as thin film within the laminar regime, thus as it has been observed, the rivulets do not follow the hybrid boundary condition applied to the structured grid. Rather, the flow follows gravity driven short paths between two slanted/corrugated parts of sheets.

A certain co-relation can be established between interfacial area and Ka number of solvent: the interfacial area seems to be increasing as the value of Ka number starts decreasing.

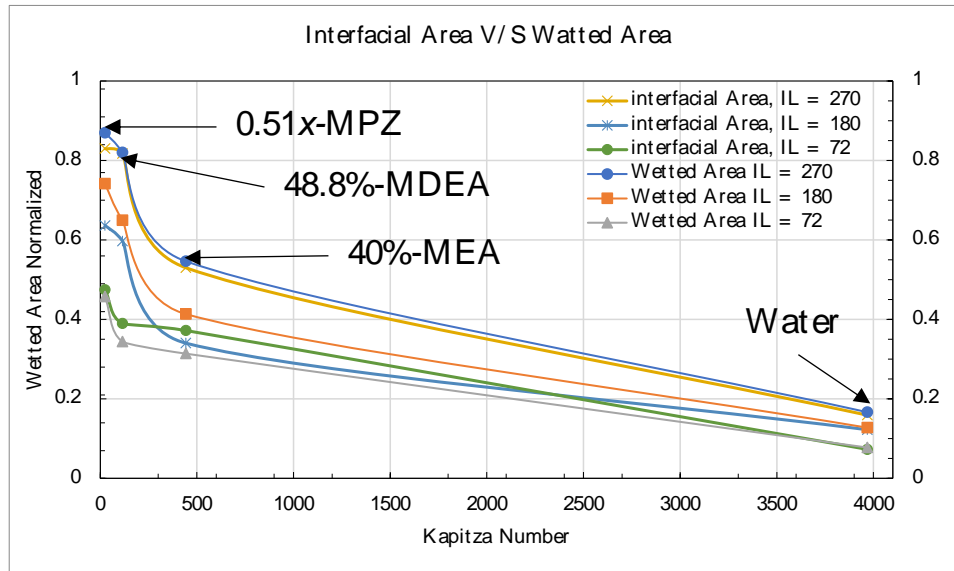


Figure 4.13: Variations of Normalized wetted, and interfacial area compared against Ka number of fluid loads varying $q_L=72, 180, 270 m^3/m^2$ and fix contact angle(γ) of 70°

In Figure 4.13 the graph shows the variation of wetted and interfacial area normalized with respect to fluid transport properties based on the Kapitza number. The graphed lines in terms of wetted and interfacial area do not significantly change for a specific liquid; however, drastic differences can be visualized between various liquids. For example, water having the highest ‘Kapitza number’ value shows the lowest wetting over the sheet, while the 0.51x-MPZ having the lowest ‘Kapitza number’ value shows the highest wetting among the four solvents. Although interfacial area is observed to be higher than wetted area for inclined flat plate studies done by previous researcher [82], simulations of REU show the wetted area gives a higher value than interfacial area, which is due to presence of the rivulet pattern for a particular fluid. Under these circumstances, the liquid pooling that is dead liquid zone may develop, and this region does not actively participate in mass transfer.

During the simulations which resulted the data used in Figure 4.13, the constant contact angle (γ) is maintained constant. Reduced surface tension was observed leading to an enhancement of effective interfacial area for Mellapak 250.Y packing due to a reduction in liquid pooling effects.

Liquid holdup is another important hydrodynamic parameter that controls overall performance of the structured packing. Its activity impacts the pressure drop and resulting gas velocity, therefore affecting the overall efficiency. Some 3D CFD simulations of flow using pseudo single-phase solver codes have estimated liquid holdup as part of their simulations. For example, a liquid holdup based on classic film theory and assumptions of complete wetting of a column for corrected gas theory and wall conditions setup for pseudo single-phase simulations was performed by Fernandes et.al [69]. The presence of a liquid film was indirectly accounted for while calculating wet pressure drop by Raynal et.al [129], however, the value of liquid holdup was estimated based off 2D simulations, which do not carry all the calculated presence of forces due to absence of z-dimension.

In the presented research, liquid holdup (h_L) is the fraction of REU volume occupied by solvent (V_L) over total REU volume (V_T), thus in terms of mathematical formulation: $h_L = V_L/V_T$. As expected, with respect to previous results of interfacial area, the value h_L decreases if the value of Ka increases. *Figure 4.14* shows variation of liquid holdup with Kapitza number with conditions as constant contact angle (γ) = 70°, and liquid load $q_L = 72 \text{ m}^3/\text{m}^2$. The graph shows that the previously hypothesized statement about the liquid holdup (h_L) proves true. This has also been observed in experimental conditions demonstrated by Zakari et.al [130]. The experiment also proves liquid holdup increase along with an increase in viscosity.

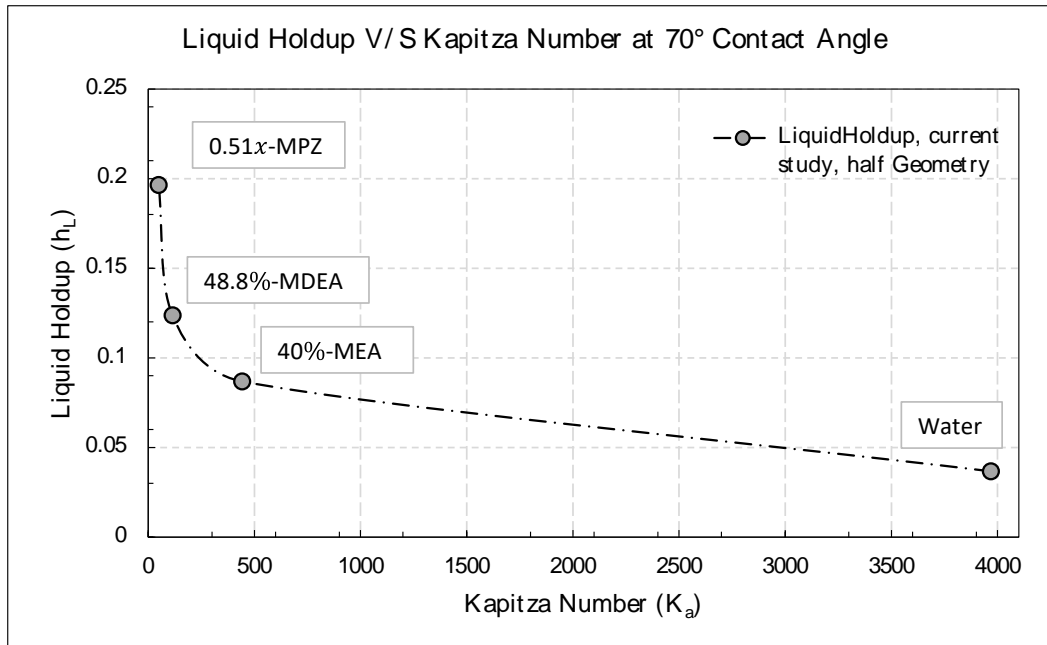


Figure 4.14: Variations of Normalized liquid holdup compared against Ka number of fluid $q_L=72 \text{ m}^3/\text{m}^2$ and fix contact angle(γ) of 70°

The effect of contact angle is inversely proportional to the wetting and interfacial area of the geometry. Former research done at NETL extensively studied the effect of contact angles over inclined surface area and as well as REU corrugated sheets. Multiple solvents and their transport properties and the effect of contact angles were examined. The conditions were primarily analyzed with MDEA 48.8% and 0.51xMPZ solvents study with contact angles of $20^\circ, 30^\circ, 40^\circ, 60^\circ, 70^\circ, 80^\circ, 90^\circ$.

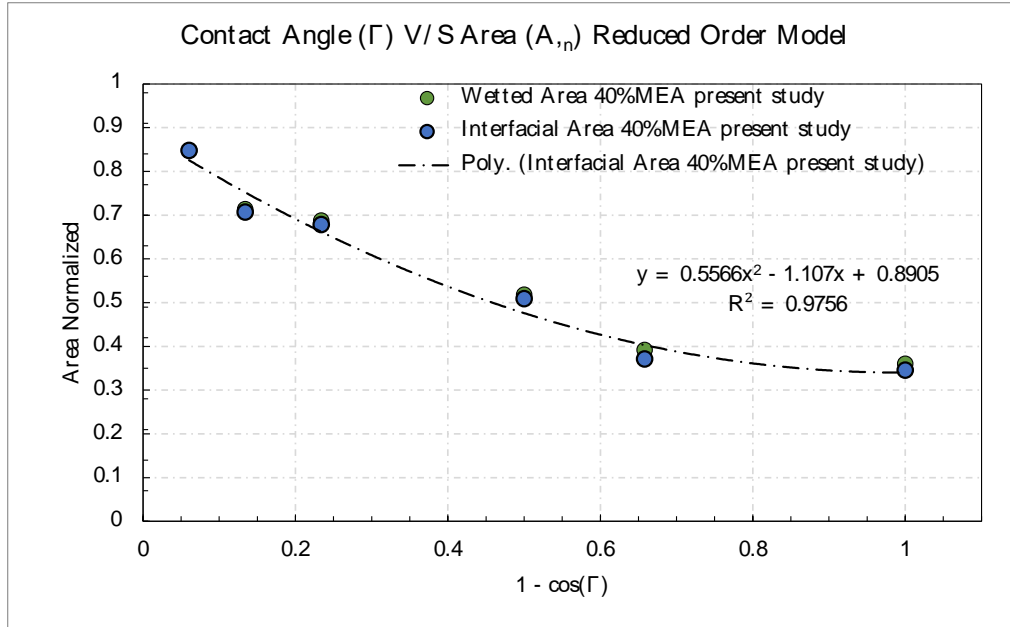


Figure 4.15: Variations of Normalized wetted and interfacial area compared against contact angles of fluid $q_L=72 \text{ m}^3/\text{m}^2$ and fix liquid = 40% – MEA

Figure 4.15 shows the relationship of contact angle on the normalized wetted and interfacial area for 40% – MEA liquid with a fixed liquid load of $q_L=72 \text{ m}^3/\text{m}^2$. The graph shows the effect of contact angle directly interacting with wetted and interfacial area as inversely proportionality. This has been visualized by previous researchers: that both wetted and interfacial areas are significantly in contact with each the represented contact angle in the simulation or experimental results. In contrast to the rivulet pattern over inclined plate study done by previous researchers, the current REU behavior of flow shows wetted area value being slightly higher than the interfacial area value; however, this might not be true for the lowest contact angle where the values are approximately identical. In previous research performed at NETL [84] the contact angle investigation was studied using pseudo-state shaper of gas-liquid interface: the results showed at higher values of γ the liquid does not spread and its constrained to a valley with a 2 mm gap between two corrugated sheets.

4.4.6 Code-to-Code Comparison & Simplified Geometric Modeling

Based upon the investigative computational and/or experimental analysis performed by many researchers in the past [95] [131] [68] [92], the micro-scale CFD simulations utilizing the volume of fluid (VoF) interface capturing methodology for resolving the thin film flows over absorber packing elements have been deemed to be computationally very expensive. Spatial grid resolution on the order of 10^{-4} to 10^{-5} m is necessary to resolve the film flow and the wetting characteristics accurately resulting in simulations times on the order of 100+ CPU days per operating conditions! Therefore, the primary goal of the project was to uncover a more computationally efficient modeling methodology that will enable investigations of different operating and packing configurations in an expedient manner. This goal is discussed by comparing the simulations performed between two CFD solver software in this section.

The previous CFD simulations with REU were performed with ANSYS FLUENT, where multi-millions of cells were employed and adequately captured the characteristics of the multiphase gas-liquid flow for range of operating conditions. However, the present research reports simulation analytics using OpenFOAM. The author had to be judicious in the spatial resolution employed in the simulations. The solvers and utilities in OpenFOAM numerical framework implement a Courant number constraint explicitly time-stepping scheme where time stepping size varies over the course of simulation by constraining the Courant number in the computational domain within specific limits of 1 to 3. As result the implementation of parameters over the computational grid at the inlet, such as gas and liquid velocities, can lead to a very small time stepping of $< 10^{-7}$ seconds, resulting in simulations running for prolonged durations. Although such a situation does not arise with implicit time stepping with fixed value while employing FLUENT solver, the repercussions of fixed time steps creates a dominating demand for

a highly-resolved mesh with smaller grid resolution than Kolmogorov scale ($\delta\mathcal{O} = 10^{-5} m$) for reduction of chances of calculation divergence. Thus, this implements higher computational costs to run a single simulation, which may not be case for solvers of OpenFOAM.

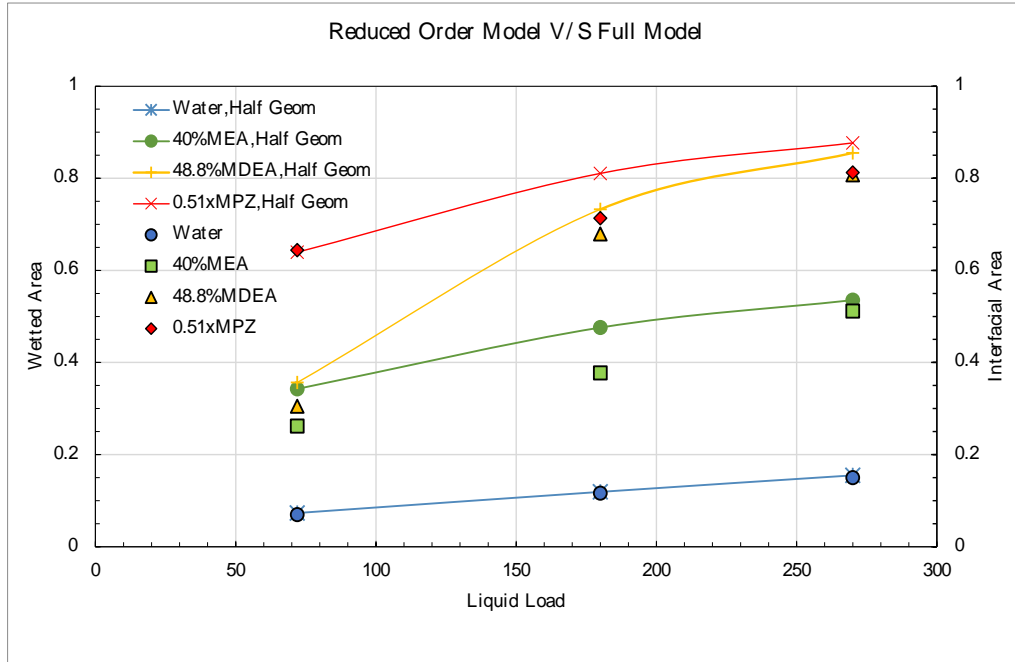


Figure 4.16: The normalized wetted area comparisons for all four solvents in the full scale REU geometry and half (symmetric)REU geometry fixed constant contact angle $\gamma = 70^\circ$

Figure 4.16 compares the normalized wetted area for all 4 solvents in the full-scale geometry and the half scale (symmetric) REU geometry at different flow rates. While excellent agreement between two geometries is seen for water at all flowrates, the results from the two geometries start to deviate from one another at different flowrates and for various liquids. Although results show variations, the error of deviation from baseline results is negligible, between 1% to 3%. Thus, researcher’s judgement allows implementation in techno-economic analysis while scale-up of equipment inventory of course-grid open-source numerical framework with cheaper resources.

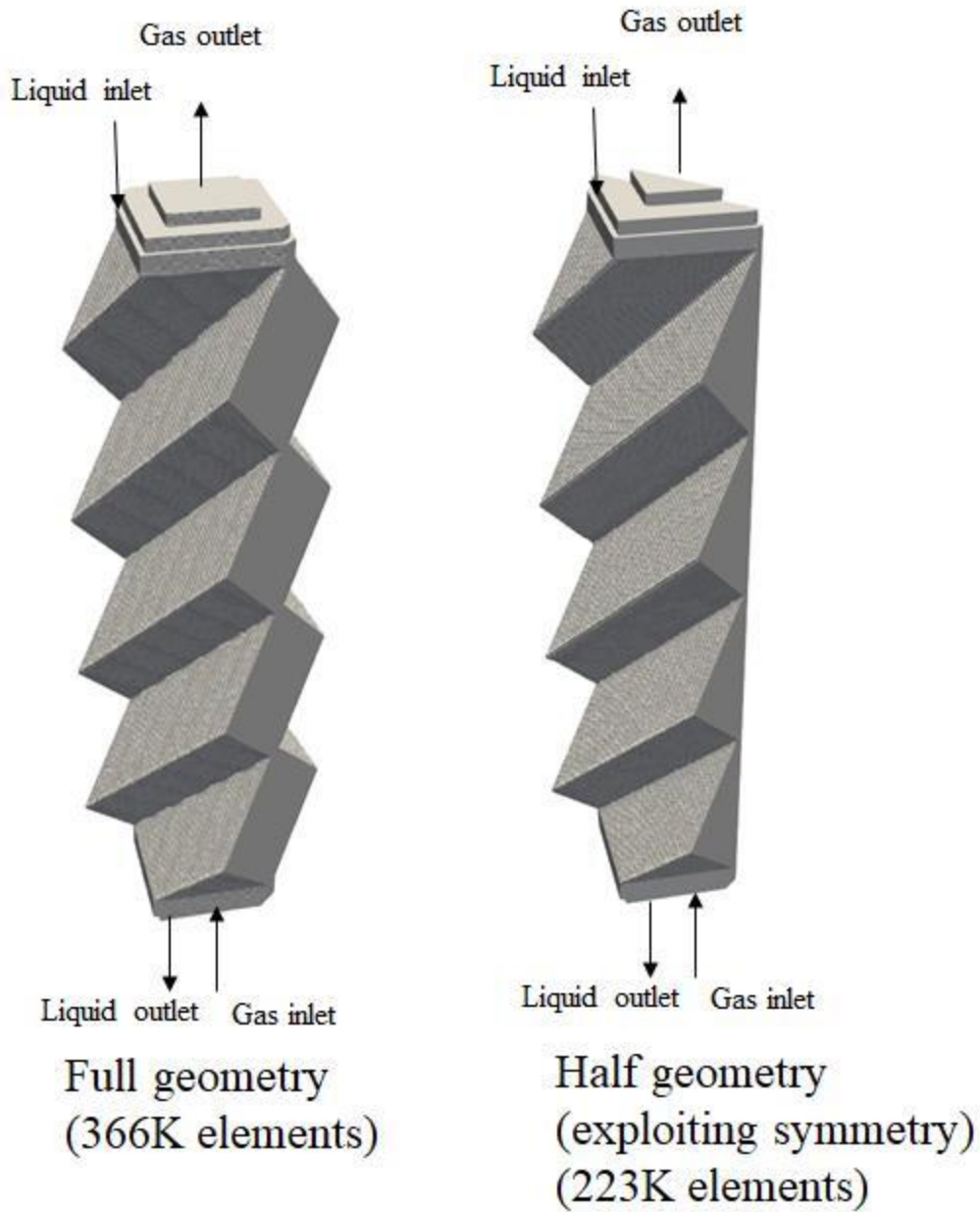


Figure 4.17: The REU geometries employed in the OpenFOAM simulations.

The full geometry shown in *Figure 4.17*, required 1-2 CPU days to investigate each set of operating conditions such as solvent transport properties, solvent flowrates, and contact angle. In addition to the full REU, a similar to simplified geometric model phenomenon based geometrical domain was developed. A symmetrical boundary condition dependent REU geometry is created

which is the same as shown in *Figure 4.17* (the left side utilizing the flow behavior in REU). This resulted in a further 50% reduction in simulation time while interfacial area predictions did not vary more than 3% from the values obtained from the full-scale simulations. The complex flow conditions are implemented and complexed geometrical domains created, and as a result the degrees of freedom increased. In this scenario, the computational costs and time acts as major limiting factor in CFD simulations along with accuracy of results. For conquering the factor, a model reduction based upon geometrical grid is critical which is performed in the project.

Figure 4.18 show comparison between ANSYS FLUENT based simulations done by NETL researchers and OpenFOAM performed simulations yielded in this study.

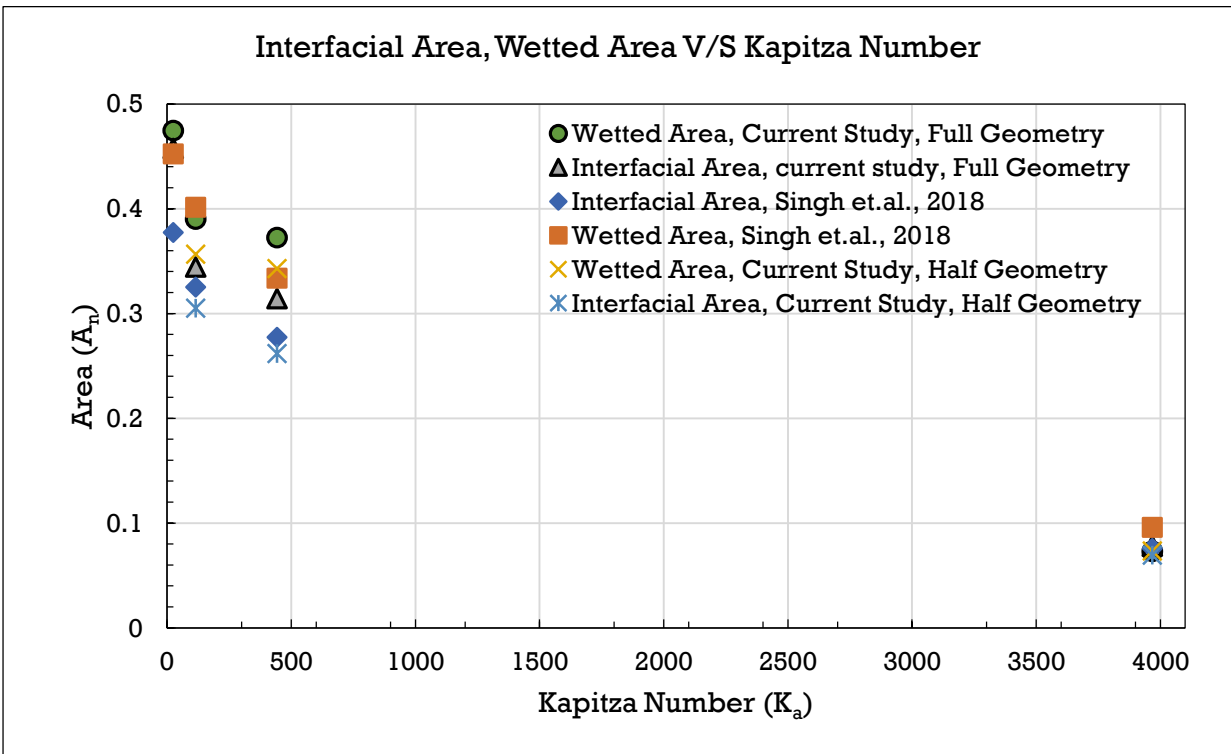


Figure 4.18: The normalized wetted area comparisons for all four solvents in the full scale REU geometry and half (symmetric)REU geometry fixed constant contact angle $\gamma = 70^\circ$

The graph shows interfacial and wetted area results comparison. As the solvent properties are changed the results deviate slightly from the previous study, with a percentage deviation between 1% to 3%. As previously mentioned, the graph shows no deviation of results for water between previous research and the current investigation.

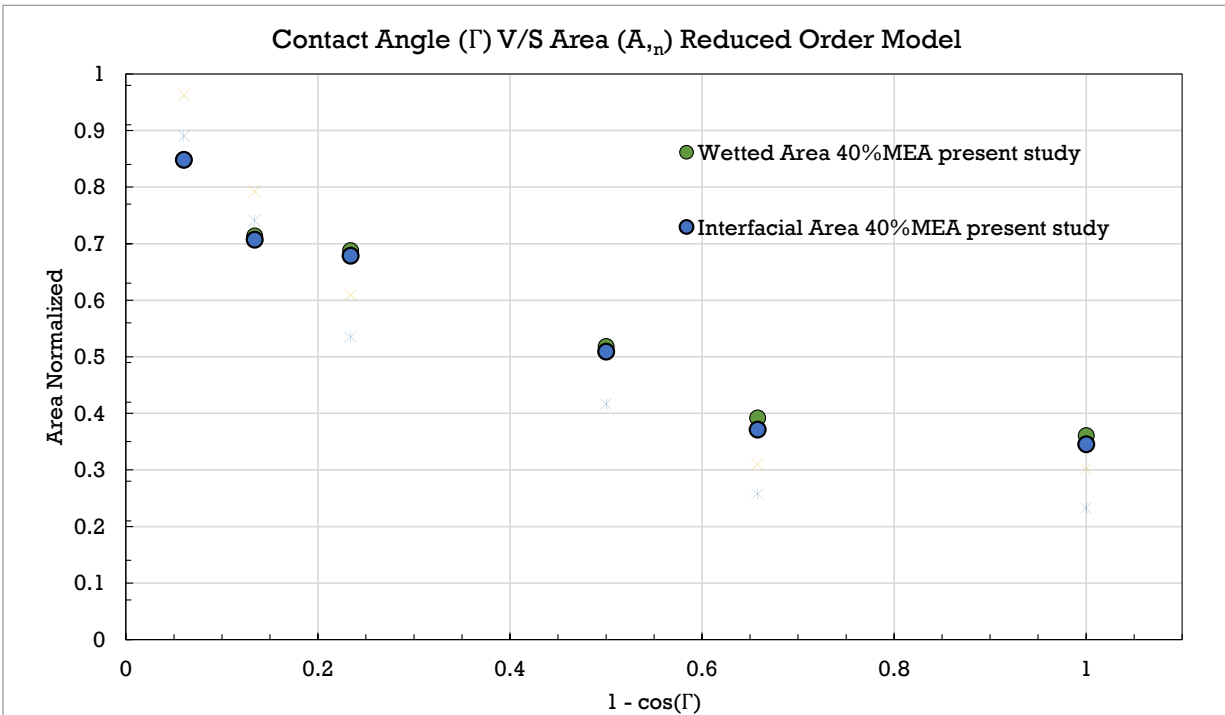


Figure 4.19: The normalized wetted and interfacial area comparisons for MEA 40% in the full scale REU geometry and half (symmetric)REU geometry and previous research study by Singh and others, varying constant contact angle γ

Figure 4.19 shows the wetted area and the interfacial area comparison with respect to this investigation and the analysis of NETL researchers using 40%MEA solvent transport properties and its significance over contact angle. The contact angle implementation in OpenFOAM is simplified compared to ANSYS FLUENT due to its integral singularity holding code structure in C/C++ language, unlike FLUENT where contact angle is a separate add-on module for FLUENT software, or it needs to be written using UDF methodology. In OpenFOAM the constant or

dynamic contact angle for specific operating conditions can be applied in the ‘*alpha.liquid*’ file using regular expressions in C/C++, and this appended as boundary condition patch.

To expand the comparison further the liquid holdup parameter is considered apart from the interfacial area and wetted area which is previously discussed. In this section the author discusses the comparison of the present study with Singh’s research along with liquid holdup co-relations which are empirically developed by other researchers.

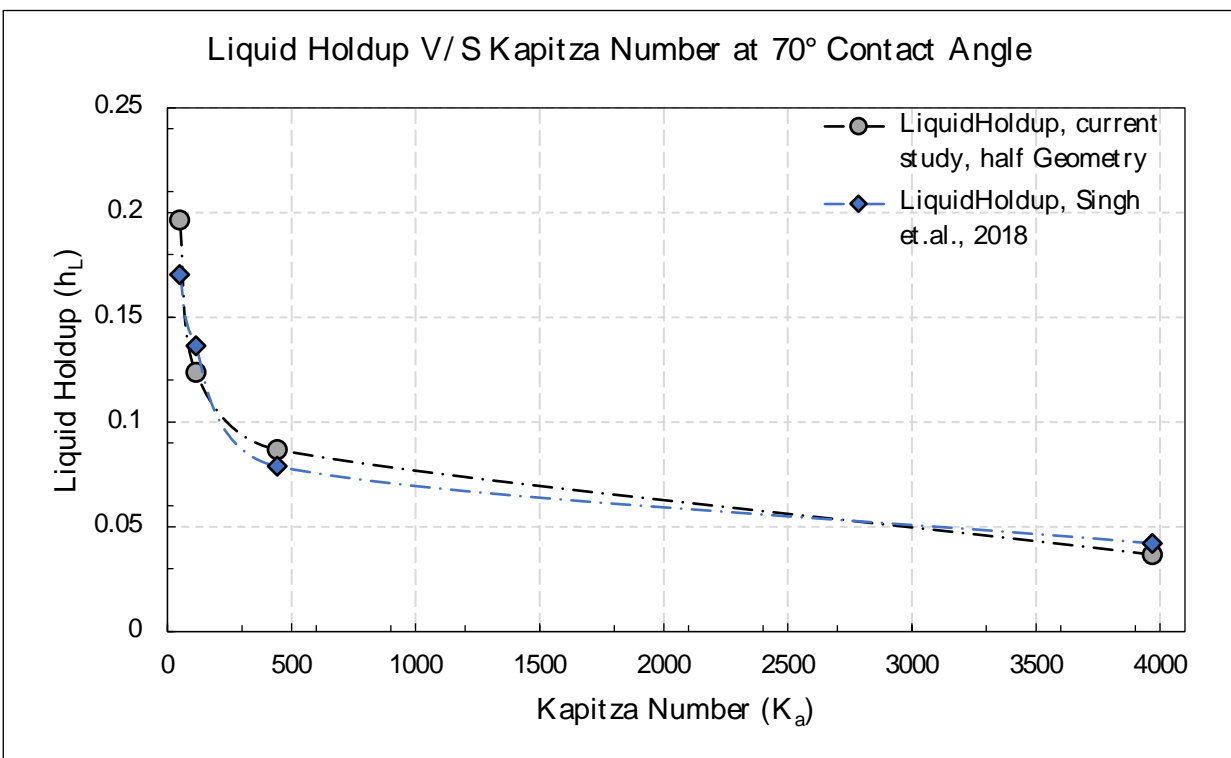


Figure 4.20: The liquid holdup comparison for all four solvents with respect to their K_a number in the previous computational study by Singh and others and half (symmetric)REU geometry in present investigation, fixed constant contact angle $\gamma = 70^\circ$ and liquid = Water

The observations from *Figure 4.20* brings understanding of identicalness between the current study and previous investigation for liquid holdup in REU. The graph also shows that the liquid holdup is directly proportional to transport properties of liquid solvent designated by K_a number. While the deviation parentage from previous study values and values from present study

show negligible for liquid like water, the same does not hold true for other solvent such as 0.51x MPZ and 48.8% MDEA.

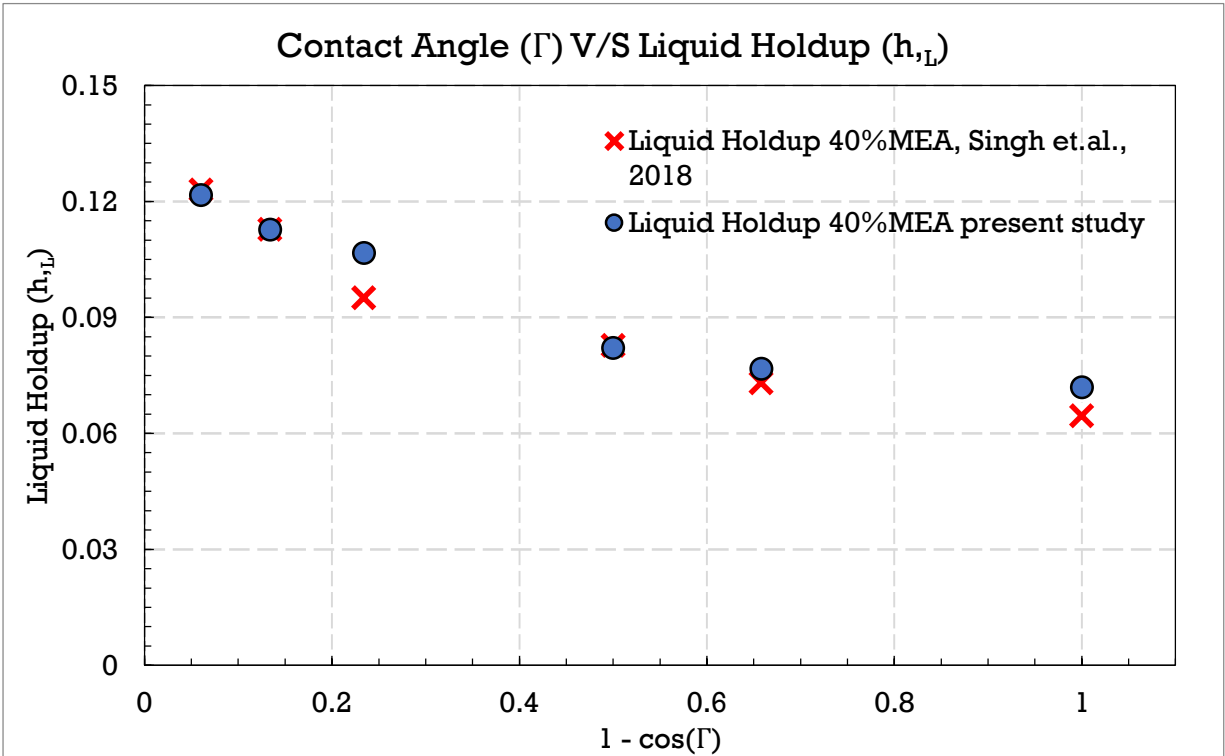


Figure 4.21: The liquid holdup comparison with respect to contact angle in the previous computational study by Singh and others and half (symmetric)REU geometry in present investigation, varying constant contact angle γ , and liquid = 40%MEA

The Figure 4.21 provides validity of computationally efficient approach by showing comparison between previous study and present analysis of liquid holdup against contact angle. The graph also denotes the fact that variations between data points are higher because of different methodology of implementation of contact angle in the solver.

4.4.7 Comparison with Existing Correlations

The comparison between computational results show variations. The present investigative analysis also put to test its validity of results among existing experimental correlations. A comparison of observed liquid holdup is shown in *Figure 4.22*.

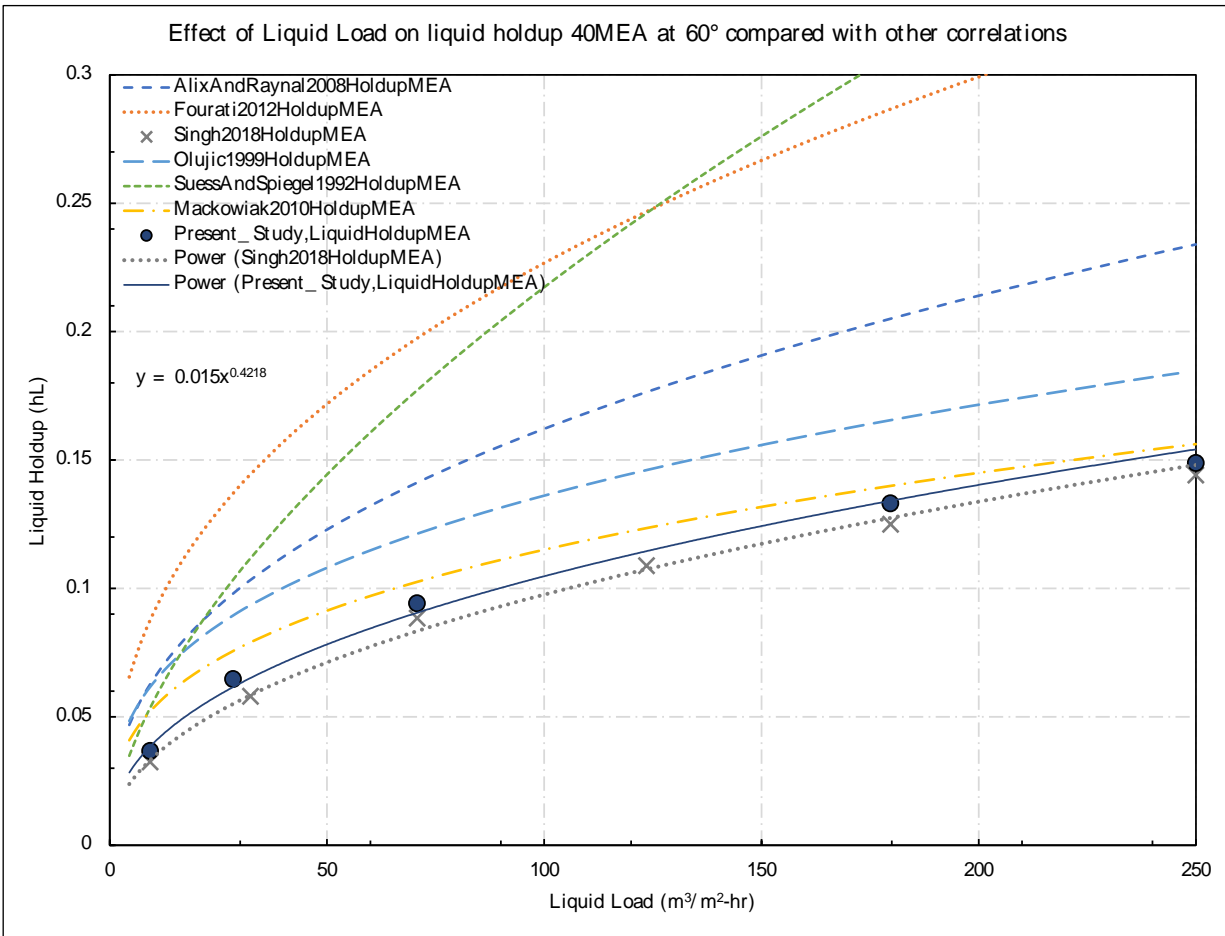


Figure 4.22: The liquid holdup against liquid load in comparison with previous computational and experimental studies by various researchers and half (symmetric)REU geometry applied in present investigation, constant contact angle $\gamma = 60^\circ$, and liquid = 40%MEA

Figure 4.22 depicts the comparison of the existing study with other experimentally investigated empirical co-relations, along with Singh and other's computational investigation. For 40%MEA at $\gamma = 60^\circ$, all the models overestimate the value of h_L . Among the correlations

examined the model of Mackowiak [132] shows the closest agreement with the CFD simulation predictions. Furthermore, the difference between the predicted and computed value decreased with increasing liquid load.

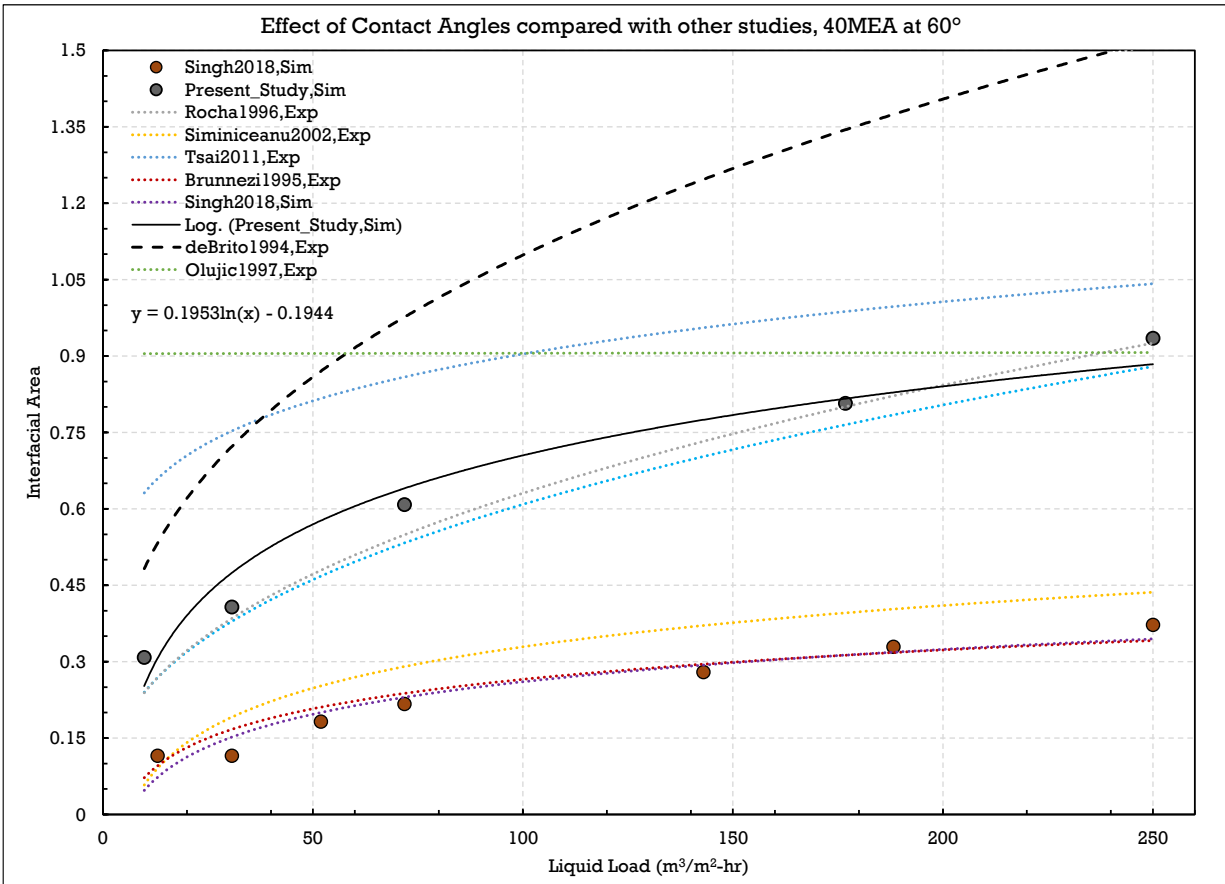


Figure 4.23: The interfacial area against liquid load in comparison with previous computational and experimental studies by various researchers and half (symmetric)REU geometry applied in present investigation, constant contact angle $\gamma = 60^\circ$, and liquid = 40%MEA

Figure 4.23 depicts the comparison of the existing study with other experimentally investigated empirical co-relations, along with Singh and other’s computational investigation. For 40%MEA at $\gamma = 60^\circ$, all the models overestimate the value of A_n . The plotted graph shows various interfacial area normalized values, in which the reader can understand the factor of contact angle being critical to simulations. Due to change in contact angle, the transport properties of liquid

show unmatched behavior against study published by Singh et. al. [82]. The presented study over predicts compared to Singh's modeling study in which the correlations were established.

4.5 Conclusion

Through appropriate modifications to the flow boundary conditions, a REU geometry consisting of 366 K elements predicted interfacial areas that were in excellent agreement with published results at 1-2 CPU days per operating condition.

Upon examining the symmetry in the liquid flow pattern over the REU elements, the REU geometry was decomposed along a symmetry plane and meshed with 223K geometric elements. Simulations run with this geometry resulted in a further 50% reduction in CPU time (at 0.5 – 1 CPU days/simulation scenario) while resulting in interfacial area predictions that did not vary by more than 10% from those obtained from the full-scale predictions.

Given that the inclination angle of different structured packing elements can vary significantly (in general between 30 to 60 degrees), a simplified single passage representation of the REU geometry was also attempted in ANSYS FLUENT for the aforementioned solvents and flow rates. These simplified representations gave good qualitative agreement with the fully resolved geometry simulations and can be employed to quickly examine the effects of variations in the packing inclination angles without the need to undertake time-consuming geometry modifications to the full REU geometry.

It should be mentioned, however, that these simulations tend to give rather optimistic predictions (e.g., interfacial areas, liquid holdup, etc.) for the more corrugated structured packings, and therefore the confidence level of such predictions should be approached with caution. This work shows that the approach of using OpenFOAM as a simulation framework with ANSYS

FLUENT as a pre- and post-solver is an effective way to increase the speed and ease of large-scale simulation work with interfacial area calculations.

5. OVERALL CONCLUSION AND FUTURE WORK

The current chapter offers an overall conclusion of this dissertation, encompassing both technologies and their outcomes. The chapter also gives a brief idea of the near future work that can be performed to make efficient, accurate, and faster mathematical modeling. While the discussion focuses on the main work conducted as a part of this dissertation, the author also provides insights into coal value-added chain management models for future coal-operated power generation industries.

5.1 UND Hydrometallurgical Process Synopsis

This dissertation presents a process of extraction and recovery of REEs and CMs utilizing hydrometallurgical methodology. The process developed within the scope of the project targets the extraction of REEs and CMs from pre-combustion lignite, which is different compared to other extraction processes involving either post-combustion fly-ash or coal byproducts. This was based upon the high concentration of HREEs found in many North Dakota lignite samples as compared with mineral resources found, as well as comparatively uncomplicated extraction as compared with mineral-based REE resources. Testing conducted in Phase-2 of the related DOE project involved the potential use of a sequential extraction method for impurity control, however, was adjusted to a one-step semi-continuous leaching process for economic benefit. The leaching process is successfully able to extract and recover REE and other deleterious elements which later are disposed of. A by-product of upgraded coal is produced at minimal cost, allowing significantly improved properties producing cleaner post-combustion emissions. Following the leaching process, the REE recovery process was designed from aqueous ionic media to generate REE

concentrates of various purities, including a primary concentrate averaging greater than 50% purity REOs, containing more than 70% of the total REE mass, and a secondary concentrate of ~ 7% purity REO containing essentially all of the Sc mass. Overall REE recoveries from coal into salable products of 30-50% were achieved at the bench-scale semi-continuous testing, with dewatering efficiency from the lignite found to be the largest contributor for the lack of recovery.

The process was developed, including leaching, impurity control, and removal. The REE recovery utilizes industrially-proven equipment and requires no novel expensive reagent usage compared to other REE metallurgical extraction processes. The developed process also requires normal ambient temperature ranges, and moderate pH control for mineral processing technologies, and has minimized potential waste streams. The process offers low-cost and environmentally viable and sustainable solutions. The upgraded lignite coal also can be used for multiple products generation opportunities including activated carbon production, combined heat, and power, humic acid production as well as upgraded cleaner emission generating fuel for coal-fired utility/industrial use. The techno-economic assessment conducted under this work by the overall research team evaluated two configurations of combined facilities: 1) an activated carbon/combined heat and power facility, and 2) a combined humic acid production facility. In each base case, both showed promising economics utilizing results of bench-scale testing conducted in Phase-2.

UND is in the process of building and operating a pilot-scale facility for the continuous process of hydrometallurgical extraction of REEs and CMs. The pilot-scale is planned to process 0.5 ton per hour of lignite coal.

5.2 Current Work in Process Modeling

The process modeling for hydrometallurgical extraction was conducted based on comprehensive experimental work completed during Phase-2 of the project and extensive experimental work involved under Phase-3 of the project. The modeling framework involves two software packages namely METSIM and ASPEN.

The presented dissertation discusses a novel approach aimed at using the process modeling simulations capabilities of METSIM and bench-scale test work to calibrate the modeling framework. The availability of this model is intended to reduce the future testing-related work and expenditures related to developing rare earth element separation processes for potential feedstocks from other seams and other ranks of coals. The modeling framework holds fewer chemical reactions under the leaching process, unlike leaching processes mathematically modeled for ores and clays.

The reduced number of reactions, as well as simplified reactions used in the current model, is due to the difficulty of accounting for all the species and their chemical reactions occurring in coal during the process of leaching. Thus, the current model in METSIM software needs input on multiple streams before calculations of mass/energy balance. These inputs can be generated from either experimental evidence or the ASPEN process modeling framework. The process of defining leaching efficiency for each rare earth element and other deleterious elements using experimental data assists ASPEN in calculating streams and unit operations in leaching, impurity control and removal, and REE recovery areas. In addition, this dissertation also explains the extensive efforts required during database development in METSIM, involving possible accounted compounds and their data for chemical reactions to accommodate the lack of database packaged with the software.

This differs from ASPEN where streamlined property and component setup assist less experienced user to process model complex scenarios with robust chemical property database banks.

The METSIM modeling framework is very capable of estimating and predicting accurate extraction metallurgical and mining application-specific results, however, the user is required to surpass the steep learning curve of handling software package effectively. This dissertation described the standard operating procedure of handling, utilizing this software package efficiently.

5.3 Future Work in Process Modeling Required

The presented model with its standard operating procedure is essentially a basic model that is calibrated along with experimental data points. While this model, like all models, cannot be used as a validation and forecasting study case with 100% reliance, if the species in lignite coal are mapped the input data supported by experimental studies, one can use the model along with all the species and their reaction data for mass and energy balance forecasting economics of other potential feedstocks in addition to the one which is studied during Phase-2 of the project.

Coal being sedimentary rock, unlike clays and ores, holds a vast amount of species in the organic state, inorganic state, and in certain scenarios organometallics. It's impractical to map and characterize all the species and their reactions with various acids and bases. Hence one can apply a reduced-order modeling approach. Extensive research has shown that REEs are more likely to bond with carboxylic compounds complexes in coal with a loose ionic exchange. Thus, one can create an estimated analysis where the percentage presence of carboxylic acid complexes can be directly proportional to the presence of REEs. Now a prospective researcher can study and experimentally find the percentage presence of carboxylic complexes. This data point is one of the input parameters in REE modeling framework. Essentially, the METSIM model is needed to

forecast the potential recovery of REEs from that specific rank of coal or within the same rank of coal; a sample gathered from the different seam along with potential acid consumption and leachability of the sample. The method proposed is based on many assumptions including empirical correlations between the presences of REEs in carboxylic complexes. Coal samples gathered from different ranks or different seams may show bonds of REEs with different complexes, for example, the presence of REEs in form of organometallics. Coals samples with significantly different rare-earth associations cannot be assessed by this modeling framework and require an entirely different approach.

In 1998 team of researchers from South Africa followed by an investigation study in 2007 in India [133] & [134] showed that Neural Network and the process of machine learning can simulate and model rare earth extraction by hydrometallurgical processes.

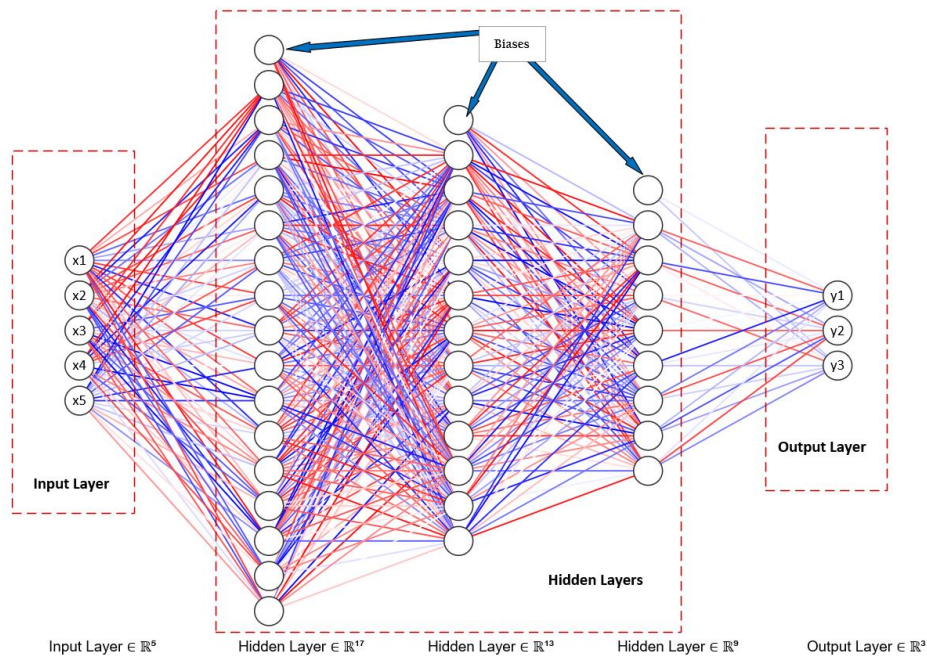


Figure 5.1: A schematic of a typical Neural Network showing hidden layers, an input layer, and an output layer as well as biases.

As proposed in future research, this type of neural network and/or other machine learning techniques can be applied to simulation and modeling for hydrometallurgical extraction of REEs and CMs using proprietary software packages such as MATLAB neural network toolbox or open-sources packages PyTorch, TensorFlow. The inputs in this neural network can be data points from past publications or experimental data points.

5.4 Current Numerical Modeling Status

The state-of-the-art modeling framework is developed using an open-source software package called OpenFOAM. From geometry development to numerical analysis with optimization strategies, the current framework helps to understand the CO_2 capture mechanism using second-generation solvents. The framework provides enhancements of mass transfer coefficients for these solvents with help of numerical methodology of the volume of fluid.

The efficiency of CO_2 adsorption is closely tied to the structure of liquid films within the packing materials. These solvent-generated liquid films can exhibit a range of flow regimes, including full-film, rivulet, and droplet flow. The VoF-based numerical framework developed in this thesis assists to capture and understand these flow behaviors. In general, the volume of fluid methodology tends to consume higher computational resources for the prolonged duration due to the underlying grid requiring smaller resolution, and the time step size is in the range of $1e-7$. For example, in a typical VoF formulation problem to reach a flow time of 10 seconds with an average $1e-7$ time step it takes approximately 5 to 7 days using 8 logical processors to acquire an accurate solution. However, the presented framework shows lower time requirements compared to typical simulations to reach a flow time of 10 seconds due to adaptive time-steps calculations per iteration and courser mesh adaptation, while achieving similar accuracy.

During the framework development, an adequate understanding of multiphase modeling methodology at the mesoscale is also needed to deduce the fidelities required in interphase exchange model formulations that are likely to impact the micro-scale predictions. Although reaction kinetics-based transport equations are not involved in this framework, the hydrodynamics of flow patterns dictates fidelity level for interphase exchange as discussed in earlier chapters. While the mesh coarseness does emanate accuracy of the results compared to multi-million cells based HPC simulations.

Multiple solvent properties were explored in this project with multiple contact angle values. Proper documentation is created in this dissertation for the presented modeling framework with detailed instructions to change the values in desired files to simulate the different types of solvents and geometrical domains. The open-source software-based modeling approach can be acquired by research personnel having little to no prior knowledge of programming, although the framework does not hold ease of access to GUI functionality.

5.5 Future Work in CO_2 Capture CFD Analysis

The framework which has been discussed in this dissertation is developed for the CO_2 capture modeling initiative project with a short duration. Thus, after delivering objectives defined under the project scope, various types of novel concepts can be implemented which are discussed in this section.

With respect to the present status of the discussed framework in this dissertation, a functional code with all desired aspects has been created for CO_2 capture for simulations involving any liquid CO_2 capturing reagent, the lack of chemical kinetics and its coupled solution with flow hydrodynamics, and turbulence reduces the model's fidelity. One can attach a stiff chemistry

solver, or Chemkin based chemical solver as an external routine to be solver per time step or per iteration.

Faster simulations are possible even over daily available quad-core computers due to advancements in chip technology. Novel algorithms can run calculations of non-linear equations with less occupancy of random access memory. With no hesitation, it is possible to state that, with help of near future advancements in high performance computing (HPC) systems, one can run simulations involving geometrical domains of entire column. Thus, in the near future numerical modeling, using current results of simulations as inputs, one can calculate liquid holdup, interfacial mass transfer coefficients, and pressure drop variables for entire columns. This methodology first was defined by Rynal and Others [93]. However, during that period the technology advancement restricted the whole column simulations. With near future advancement in chips it is possible to develop whole column simulations using direct numerical simulation (DNS), or Large Eddy Simulation (LES) methodology.

Due to recent progress in machine learning and artificial intelligence, it is possible to implement computer automata thinking in the field of computational fluid dynamics, where complex fluid equations such as Navier Stokes equations can solve by the process of computational neural networks as shown recently by team at Google Deepmind [99]. With implementation of computational automata thinking, it possible to tackle these system-of-equations with greater efficiency, more accurately predictable results, and with overall utilization of less computational resources. An article published by Vnuesa followed by Usman in 2021 discusses the multiple possibilities of machine learning enhanced CFD. [135] As per the articles, machine learning can be implemented to accurately predict the residuals of the system of equations which can accelerate the convergence of simulation.

One of the caveats of this methodology is that datasets are needed priori for building a reduced-order modeling approach. Large sets of data are needed to feed to the machine to learn the process of CO_2 capture using solid or liquids in columns. This critical requirement can be fulfilled by developing a vast experimental test matrix or it can be done by conventional numerical simulations. To achieve successful machine learning-based reduced-order modeling either neural network algorithms should be able to learn the adaptable, system verbose machine learning model from fewer datasets, or one needs to develop thousands of datasets using various geometrical domains. [136]

5.6 Efficient Coal Power Plants

An evolution of coal and other fossil fuel markets has been occurring over the past couple of decades, two critical reasons being, 1) growing competition with renewable energy resources, and 2) rising CO_2 levels due to these power generation facilities. Thus, as the market requirements, changes upgrading the mined product to the market requirements becomes essential. This type of product upgrading dates back the early days of the industry in the U.S., and beneficiation and separation, chemical processing, and hydro-thermal treatment have been used as per the desired market essential product. However, based upon recent environmental challenges and overall cost and efficiency benefits, the coal operated power stations are required to pre-process coal for better emissions with less pollutants, while capturing remaining pollutants from flue gases for ecologically beneficial power generation, and to be working in conjunction with renewable power resources.

Figure 5.2 shows opportunities to collect the REEs and CMs from various sections of coal value chain. The processes prior to energy conversion process shown in figure 5.2 (which are also pre-combustion processes) not only provide better efficiency for the recovery of the REEs and

CMs but also reduces sulfur containing compounds which reduces post-combustion sulfur containing flue gases and generates ecologically sustainable emissions.

Many opportunities for REEs recovery span the Coal Value Chain

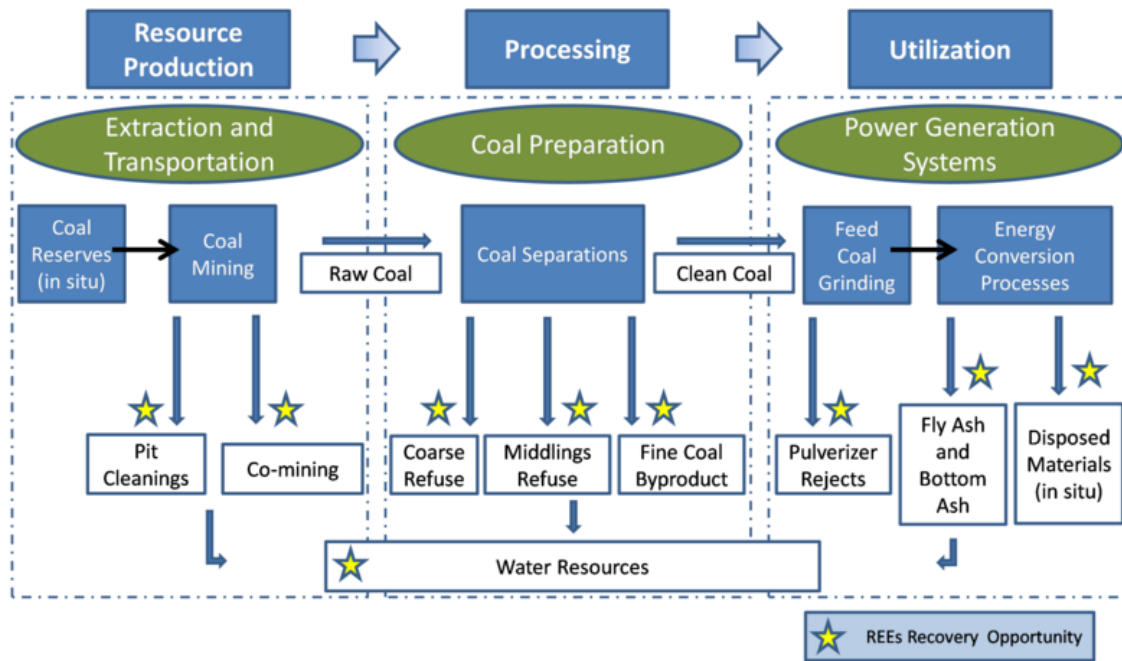


Figure 5.2: Opportunities to recover REE from various sections of coal value added chain management. (courtesy: NETL, DoE)

In the future, the next generation coal operated power plants may have coal chemical processing units as pre-combustion processes which involve extraction of critical minerals (CMs) and REEs, while simultaneously upgrading value of coal to generate cleaner emissions. Figure 5.3 presents a schematic of a proposed coal operated power facility where coal is processed and precious minerals such as REEs are recovered. During the process coal is mixed with mineral extracting acids which simultaneously help to reduce pollutants causing elements such as sulfur. As a result the coal now holds upgraded value as well as reduced pollutants, ultimately generating cleaner emissions. After combustion of coal, the flue gases consist of CO_2 as one of major

constituents. A well-researched and developed CO_2 capturing unit can remove CO_2 from these flue gases in form of hydrocarbons, and other CO_2 bonded compounds. Although, it is almost impossible to achieve 100% efficiency, with near 97% efficiency, the proposed system will emit only a minimal amount of greenhouse gases. This may allow coal operated power plants to work in conjunction with renewable energy power resources.

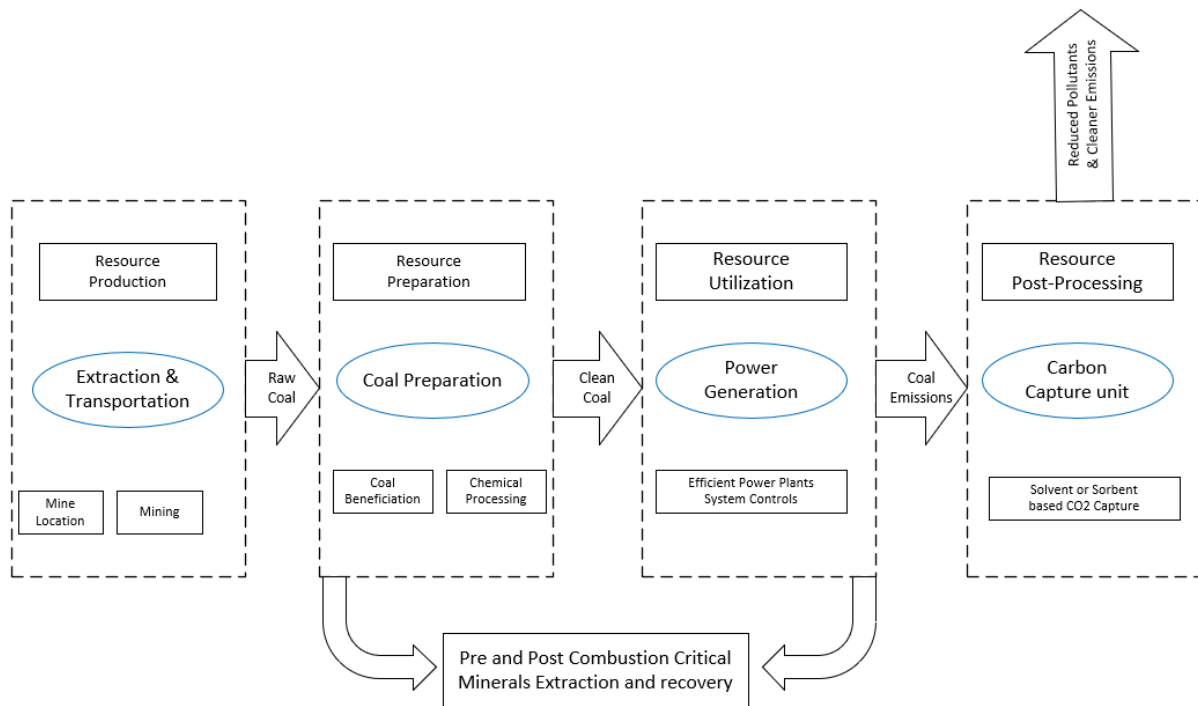


Figure 5.3: Proposed Near future or next generation coal operated power plant system process flow.

The work done in this dissertation allows future researchers to develop models for efficient metallurgical extraction using reduced capital expenses and/or operational expenses to generate cleaned and upgraded coal as well as extract minerals during the pre-combustion process. Simultaneously, improved CO_2 post-combustion capturing system models to reduce CO_2 as well as other pollutant consisting emissions towards atmosphere can be developed.

BIBLIOGRAPHY

- [1] U.S. Environmental Protection Agency (EPA), "Greenhouse Gas Emissions: Understanding Global Warming Potentials," U.S. Environmental Protection Agency (EPA), 2018. [Online]. Available: <https://www.epa.gov/ghgemissions/understanding-global-warming-potentials>. [Accessed 2018].
- [2] U.S. Energy Information Administration, "Annual Energy Outlook 2020," U.S. Energy Information Administration, 29 01 2020. [Online]. Available: <https://www.eia.gov/outlooks/archive/aeo20/>. [Accessed 29 01 2020].
- [3] R. Andrews, J. Duddy, J. Gellici, K. Johnson, L. Meyers and G. Skoptsov, "Carbon Forward: Advanced Markets for Value-Added Products from Coal," National Coal Council, Annapolis, Maryland, 2021.
- [4] K. Bisaka, I. C. Thobadi and C. Pawlik, "Sustainable Hydrometallurgical Extraction of Metals Cape Town," 2016.
- [5] R. K. Pachauri, L. Meyer, S. Brinkman, L. v. Kesteren, N. Leprince-Ringuet, F. v. Boxmeer and The Core Writing Team, "Climate Change 2014: Synthesis Report," Intergovernmental Panel on Climate Change (IPCC), Geneva, Switzerland, 2014.
- [6] C. Littlecott, L. Roberts, Ö. Şenlen, J. Burton, M. Joshi, C. Shearer and M. Ewen, "No New Coal by 2021: The Collapse of The Global Coal Pipeline," E3G Publishing, 2021.
- [7] D. A. Laudal, S. A. Benson, R. S. Addleman and D. Palo, "Leaching behavior of rare earth elements in Fort Union lignite coals of North America," *International Journal of Coal Geology*, vol. 191, no. 11, pp. 112-124, 2018.
- [8] M. K. Jha, A. Kumari, R. Panda, J. Rajesh Kumar, K. Yoo and J. Y. Lee, "Review on hydrometallurgical recovery of rare earth metals," *Hydrometallurgy*, vol. 165, no. 2, pp. 77-101, 1 2016.
- [9] D. Laudal, "Evaluation Of Rare Earth Element Extraction From North Dakota Coal-related Feed Stocks," UND Dissertations & Theses, Grand Forks, 2017.
- [10] b. B. Anusha Kothandaraman Chem Eng, "Carbon Dioxide Capture by Chemical Absorption: A Solvent Comparison Study," 2010.

- [11] L. E. Øi, Aspen HYSYS Simulation of CO₂ Removal by Amine Absorption from a Gas Based Power Plant, L. Øi, Ed., Gøteborg, Norway: Society of Industrial Mathematics, 2007, pp. 73-82.
- [12] Y. Amini and M. Nasr Esfahany, CFD simulation of the structured packings: A review, vol. 54, Taylor and Francis Inc., 2019, pp. 2536-2554.
- [13] D. Asendrych, P. Niegodajew and S. Drobniak, CFD modelling of CO₂ capture in a packed bed by chemical absorption, vol. 34, 2013, pp. 269-282.
- [14] F. Chu, L. Yang, X. Du and Y. Yang, CO₂ capture using MEA (monoethanolamine) aqueous solution in coal-fired power plants: Modeling and optimization of the absorbing columns, vol. 109, Elsevier Ltd, 2016, pp. 495-505.
- [15] M. Isoz, CFD Study of Gas Flow Through Structured Separation Columns Packings Mellapak 250.X and Mellapak 250.Y, Czech Technical University in Prague - Central Library, 2017, pp. 171-184.
- [16] Y. Haroun and L. Raynal, "Use of Computational Fluid Dynamics for Absorption Packed Column Design," Editions Technip, 2016.
- [17] R. W. Higbie, "The Rate of Absorption of a Pure Gas into a Still Liquid During Short Periods of Exposure," University of Michigan, Ann Arbor, 1934.
- [18] T. Cook and F. Harlow, "Virtual Mass in Multiphase Flows," *International Journal of Multiphase flows*, vol. 10, no. 6, pp. 691-696, 1984.
- [19] N. Verbaan, K. Bradley, J. Brown and S. Mackie, "A review of hydrometallurgical flowsheets considered in current REE projects," *Symposium on critical and strategic materials.*, pp. 147-162, 11 2015.
- [20] V. V. Seredin and S. Dai, "Coal deposits as potential alternative sources for lanthanides and yttrium," *International Journal of Coal Geology*, vol. 94, no. 3, pp. 67-93, 2012.
- [21] X. Yang, J. Werner and R. Q. Honaker, "Leaching of rare Earth elements from an Illinois basin coal source," *Journal of Rare Earths*, vol. 37, no. 3, pp. 312-321, 3 2019.
- [22] N. Krishnamurthy and C. K. Gupta, Extractive metallurgy of rare earths, second edition, 2015.
- [23] K. Yoo, "Modeling and simulation on extraction of rare earth by computational fluid-particle dynamics in a batch reactor," *Journal of Mechanical Science and Technology*, vol. 31, no. 12, pp. 5887-5895, 12 2017.

- [24] D. A. Laudal, S. A. Benson, R. S. Addleman and D. Palo, "Rare Earth Elements in North Dakota Lignite Coal and Lignite-Related Materials," *Journal of Energy Resources Technology*, vol. 191, pp. 112-124, 4 2018.
- [25] J. Zhang, B. Zhao and B. Schreiner, Separation hydrometallurgy of rare earth elements, 2016.
- [26] A. Jordens, Y. P. Cheng and K. E. Waters, "A review of the beneficiation of rare earth element bearing minerals," *Minerals Engineering*, vol. 41, no. 0892-6875, pp. 97-114, 2013.
- [27] G. Özbayoğlu and M. Ü. Atalay, "Beneficiation of bastnaesite by a multi-gravity separator," *Journal of Alloys and Compounds*, vol. 303–304, no. 3, pp. 520-523, 2000.
- [28] A. Jordens, R. Sheridan, N. Rowson and K. Waters, "Processing a rare earth mineral deposit using gravity and magnetic separation," *Minerals Engineering*, vol. 62, no. 0892-6875, pp. 9-18, 2014.
- [29] Z. Huang, M. Fan and H. Tiand, "Coal and coal byproducts: A large and developable unconventional resource for critical materials – Rare earth elements," *Journal of Rare Earths*, vol. 36, no. 4, pp. 337-338, 2018.
- [30] W. Zhang, M. Rezaee, A. Bhagavatula, Y. Li, J. Groppo and R. Honaker, "A review of the occurrence and promising recovery methods of rare earth elements from coal and coal by-products," *International Journal of Coal Preparation and Utilization*, vol. 35, no. 6, pp. 295-330, 11 2015.
- [31] A. Akcil, N. Akhmediyeva, R. Abdulvaliyev, Abhilash and P. Meshram, "Overview On Extraction and Separation of Rare Earth Elements from Red Mud: Focus on Scandium," *Mineral Processing and Extractive Metallurgy Review*, 2018.
- [32] A. Kumari, R. Panda, M. K. Jha, J. R. Kumar and J. Y. Lee, "Process development to recover rare earth metals from monazite mineral: A review," *Minerals Engineering*, vol. 79, pp. 102-115, 6 2015.
- [33] T. Qiu, D. Zhu, X. Fang, Q. Zeng, G. Gao and H. Zhu, "Leaching kinetics of ionic rare-earth in ammonia-nitrogen wastewater system added with impurity inhibitors," *Journal of Rare Earths*, 2014.
- [34] R. Honaker, X. Yang, A. Chandra, W. Zhang and J. Werner, "Hydrometallurgical Extraction of Rare Earth Elements from Coal," *Extraction 2018: Proceedings of the First Global Conference on Extractive Metallurgy*, vol. 1, pp. 2309-2322, 2018.

- [35] J. C. Hower, D. Qian, N. J. Briot, K. R. Henke, M. M. Hood, R. K. Taggart and H. Hsu-Kim, "Rare earth element associations in the Kentucky State University stoker ash," *International Journal of Coal Geology*, vol. 189, 2018.
- [36] M. D. Mann, N. L. Theaker, B. J. Rew, S. A. Benson, A. Benson, D. Palo, C. Haugen and D. Laudal, "Investigation of Rare Earth Element Extraction from North Dakota Coal-Related Feedstocks (Phase 2 Final Technical Report)," Department of Energy, United States, 2021.
- [37] M. Yi, B.-X. Xu and O. Gutfleisch, "Computational study on microstructure evolution and magnetic property of laser additively manufactured magnetic materials," *Computational Mechanics*, vol. 64, no. 4, pp. 917-935, 2019.
- [38] M. Karl-Hartmutand, S. Simonand, G. Rolandand and O. Gutfleisch, "Permanent Magnet Materials and Applications," *Handbook of Magnetism and Magnetic Materials*, pp. 1369-1433, 2021.
- [39] F. Vasilyev, "Model-based Design And Optimization Of Hydrometallurgical Liquid-liquid Extraction Processes," Lappeenranta University of Technology, Lappeenranta, 2018.
- [40] Y. Yun, S. Stopic and B. Friedrich, "Valorization of Rare Earth Elements from a Steenstrupine Concentrate Via a Combined Hydrometallurgical and Pyrometallurgical Method," *Minerals*, vol. 10, no. 3, 2020.
- [41] W. D. Judge and G. Azimi, "Recent progress in impurity removal during rare earth element processing: A review," *Hydrometallurgy*, vol. 196, 9 2020.
- [42] L. Niinistö, "Industrial applications of the rare earths, an overview," *Inorganica Chimica Acta*, vol. 140, pp. 339-343, 1987.
- [43] B. Gupta, P. Malik and A. Deep, "Extraction of uranium, thorium and lanthanides using Cyanex-923: Their separations and recovery from monazite," *Journal of Radioanalytical and Nuclear Chemistry*, vol. 251, no. 3, pp. 451-456, 2002.
- [44] V. I. Kuzmin, G. L. Pashkov, V. G. Lomaev, E. N. Voskresenskaya and V. N. Kuzmina, "Combined approaches for comprehensive processing of rare earth metal ores," *Hydrometallurgy*, Vols. 129-130, pp. 1-6, 2012.
- [45] A. Yörükoğlu, A. Obut and İ. Girgin, "Effect of thiourea on sulphuric acid leaching of bastnaesite," *Hydrometallurgy*, vol. 68, no. 1, pp. 195-202, 2003.
- [46] G. A. Moldoveanu and V. G. Papangelakis, "Recovery of rare earth elements adsorbed on clay minerals: II. Leaching with ammonium sulfate," *Hydrometallurgy*, Vols. 131-132, pp. 158-166, 2013.

- [47] S. Peelman, Z. H. I. Sun, J. Sietsma and Y. Yang, "Leaching of Rare Earth Elements: Review of Past and Present Technologies," *Rare Earths Industry*, pp. 319-334, 2016.
- [48] R. Otto and A. Wojtalewicz-Kasprzak, "Method for recovery of rare earths from fluorescent lamps". United States Patent US Patent 7,976,798, 12 7 2011.
- [49] Y. Chunhua, J. Jiangtao, L. Chunsheng, W. Sheng and X. Guangxian, "Rare Earth Separation in China," *Tsinghua Science And Technology*, vol. 11, no. 2, pp. 241-247, 4 2006.
- [50] N. V. Thakur, "Separation of rare earths by solvent extraction," *Mineral Processing and Extractive Metallurgy Review*, 2000.
- [51] K. Binnemans and P. T. Jones, "Perspectives for the recovery of rare earths from end-of-life fluorescent lamps," *Journal of Rare Earths*, vol. 32, no. 3, pp. 195-200, 2014.
- [52] N. A. Danilov, G. V. Korpusov, Y. S. Krylov, K. V. Puzitskii and Y. T. Eidus, "Trends in the distribution of individual rare earth elements during extraction with α α α -dialkylcarboxylic acids and with normal carboxylic acids," *Inst. of Physical Chemistry, Moscow*, vol. 19, no. 1, pp. 194-199, 6 1974.
- [53] H. Liu, Y. Zhang, Y. Luan, H. Yu and D. Li, "Research progress in preparation and purification of rare earth metals," *Metals*, vol. 10, no. 10, pp. 1-13, 10 2020.
- [54] F. Liu, "Fundamental electrochemical study on neodymium molten salt electrolysis in fluoride bath," Colorado School of Mines. Arthur Lakes Library, Golden, 2019.
- [55] S. Dai, I. T. Graham and C. R. Ward, "A review of anomalous rare earth elements and yttrium in coal," *International Journal of Coal Geology*, vol. 159, pp. 82-95, 4 2016.
- [56] T. A. Henrie, E. Morrice and E. S. Shedd, "Direct electrolysis of rare-earth oxides to metals and alloys in fluoride melts(Preparation of high-purity rare earth metals and alloys by electrolysis of rare earth oxides in fluoride media)," 1967., pp. 715-727, 1967.
- [57] T. A. Henrie, "Electrowinning rare-earth and uranium metals from their oxides," *JOM*, vol. 16, no. 12, pp. 978-981, 1964.
- [58] E. Morrice and M. M. Wong, "Fused-salt electrowinning and electrorefining of rare-earth and yttrium metals," *Min. Sci. Eng.*, vol. 11, no. 3, pp. 125-136, 1979.
- [59] S. Pang, W. Lu, Z. Yang, X. Zhang, D. Chen, D. Wu, L. Zhou and R. Miao, "Mechanism of removing ferrum impurity in lanthanum refined by electron beam melting," *Journal of Rare Earths*, vol. 39, no. 7, pp. 875-880, 2021.

- [60] V. S. Cvetković, D. Feldhaus, N. M. Vukićević, T. S. Barudžija, B. Friedrich and J. N. Jovićević, "Investigation on the Electrochemical Behaviour and Deposition Mechanism of Neodymium in NdF₃-LiF-Nd₂O₃ Melt on Mo Electrode," *Metals*, vol. 10, no. 5, 2020.
- [61] N. Krishnamurthy and C. K. Gupta, "Rare Earth Metals and Alloys by Electrolytic Methods," *Mineral Processing and Extractive Metallurgy Review*, vol. 22, no. 4-6, pp. 477-507, 1 2002.
- [62] X. Guo, Z. Sun, J. Sietsma and Y. Yang, "Semiempirical Model for the Solubility of Rare Earth Oxides in Molten Fluorides," *Industrial & Engineering Chemistry Research*, vol. 55, no. 16, pp. 4773-4781, 4 2016.
- [63] Q. Guo, J. Wu, Y. Yang, X. Liu, W. Sun, Y. Wei, Z. Lan, J. Lin, M. Huang, H. Chen and Y. Huang, "Low-temperature processed rare-earth doped brookite TiO₂ scaffold for UV stable, hysteresis-free and high-performance perovskite solar cells," *Nano Energy*, vol. 77, p. 105183, 2020.
- [64] J. Thonstad, S. Rolseth and R. Keller, *Light Metals 2013: On the mechanism behind low voltage PFC emissions*, 883-885: Springer, 2003.
- [65] H. Herzog, *Carbon Capture*, Boston, MA: MIT Press, 2018.
- [66] R. Stuart Haszeldine, *Carbon capture and storage: how green can black be?*, vol. 325, 2009, pp. 1647-1652.
- [67] R. Surampalli, *Carbon Capture and Storage: Physical, Chemical, and Biological Methods*, R. Surampalli, Ed., Reston, VA: American Society of Civil Engineers, 2015, p. 553.
- [68] P. Sues and L. Spiegel Sulzer, "Hold-up of Mellapak structured packings," 1992.
- [69] J. Fernandes, P. F. Lisboa, P. C. Simões, J. P. Mota and E. Saadjan, "Application of CFD in the study of supercritical fluid extraction with structured packing: Wet pressure drop calculations," vol. 50, 2009, pp. 61-68.
- [70] S. Q. Wang, L. M. Wang, F. Wang and D. Fu, "Study on the surface tensions of MDEA-methanol aqueous solutions," Institute of Physics Publishing, 2017.
- [71] A. Meisen and X. Shuai, "Research and development issues in CO₂ capture," *Energy Conversion and Management*, vol. 38, no. 3, pp. S37-S42, 1997.
- [72] S. Aforkoghene Aromada and L. Øi, "Simulation of improved absorption configurations for CO₂ capture," Linköping University Electronic Press, 2015.
- [73] U. S. P. Arachchige and M. C. Melaaen, *Aspen plus simulation of CO₂ removal from coal and gas fired power plants*, vol. 23, Elsevier Ltd, 2012, pp. 391-399.

- [74] J. Bao, R. Singh and Z. Xu, "Milestone Report Device-scale CFD study for mass transfer coefficient and effective mass transfer area in packed column Revision Log Acknowledgment of Funding Contents," 2018.
- [75] S. M. Damián, *An Extended Mixture Model for the Simultaneous Treatment of Short and Long Scale Interfaces*, Santa Fe, Argentina, 2013, pp. 1-231.
- [76] A. Ataki and H. J. Bart, "Experimental and CFD simulation study for the wetting of a structured packing element with liquids," 2006.
- [77] R. E. Treybal, *Mass Transfer Operations*, New York: McGraw-Hill Book Company, 1980.
- [78] E. Kenig, R. Schneider and A. Gorak, "Reactive absorption: Optimal process design via optimal modelling," *Chemical Engineering Science*, vol. 56, no. 2, pp. 343-350, 2001.
- [79] "Aspen plus 11.1. User Manual guide," Aspen Technology, 2011.
- [80] G. Qi, S. Wang, H. Yu, L. Wardhaugh, P. Feron and C. Chen, "Development of a rate-based model for CO₂ absorption using aqueous NH₃ in a packed column," *International Journal of Greenhouse Gas Control*, vol. 17, no. 3, pp. 450-461, 2013.
- [81] Z. Ying, C. Hern , C. Chau-Chyun, P. Jorge , R. Dugas and G. T. Rochelle, "Rate-Based Process Modeling Study of CO₂ Capture with Aqueous Monoethanolamine Solution," *Industrial & Engineering Chemistry Research*, vol. 48, no. 20, pp. 9233-9246, 2009.
- [82] R. K. Singh, J. E. Galvin and X. Sun, "Multiphase flow studies for microscale hydrodynamics in the structured packed column," Elsevier B.V., 2018.
- [83] R. Billet and M. Schultes, "Prediction of mass transfer columns with dumped and arranged packings: Updated summary of the calculation method of Billet and Schultes," IChemE, 1999.
- [84] R. K. Singh, J. E. Galvin and X. Sun, "Hydrodynamics of the rivulet flow over corrugated sheet used in structured packings," Elsevier Ltd, 2017.
- [85] J. J. Cooke, S. Gu, L. M. Armstrong and K. H. Luo, "Gas-Liquid Flow on Smooth and Textured Inclined Planes," 2012.
- [86] R. K. Singh, J. E. Galvin and X. Sun, "Three-dimensional simulation of rivulet and film flows over an inclined plate: Effects of solvent properties and contact angle," Elsevier Ltd, 2016.
- [87] V. Boniou, T. Schmitt and A. Vié, Comparison of interface capturing methods for the simulation of two-phase flow in a unified low-Mach framework, 2021.

- [88] M. Isoz, "Dynamics of rivulets and other multiphase flows," Prague, 2018.
- [89] M. Isoz, "Study of rivulet type flow of liquid on inclined plate," Prague, 2013.
- [90] D. Drew, "Mathematical modeling of two-phase flows," *Annual Review of Fluid Mechanics*, vol. 3, no. 15, pp. 261-291, 1983.
- [91] S. Shrikant, CFD modeling of Dry Pressure Drop in Structured Packings, Roorkee, India, 2012, pp. 1-56.
- [92] M. J. Nieves-Remacha, L. Yang and K. F. Jensen, "OpenFOAM Computational Fluid Dynamic Simulations of Two-Phase Flow and Mass Transfer in an Advanced-Flow Reactor," American Chemical Society, 2015.
- [93] L. Raynal and A. Royon-Lebeaud, A multi-scale approach for CFD calculations of gas-liquid flow within large size column equipped with structured packing, vol. 62, 2007, pp. 7196-7204.
- [94] S. H. Hosseini, S. Shojaei, G. Ahmadi and M. Zivdar, Computational fluid dynamics studies of dry and wet pressure drops in structured packings, vol. 18, 2012, pp. 1465-1473.
- [95] Z. Xu, R. Kumar Singh, J. Bao and C. Wang, Direct Effect of Solvent Viscosity on the Physical Mass Transfer for Wavy Film Flow in a Packed Column, vol. 58, American Chemical Society, 2019, pp. 17524-17539.
- [96] G. Lavalley, M. Lucquiaud, M. Wehrli and P. Valluri, Cross-flow structured packing for the process intensification of post-combustion carbon dioxide capture, vol. 178, Elsevier Ltd, 2018, pp. 284-296.
- [97] C. Wang, Z. Xu, C. Lai, G. Whyatt, P. Marcy and X. Sun, "Hierarchical calibration and validation for modeling bench-scale solvent-based carbon capture. Part 1: Non-reactive physical mass transfer across the wetted wall column," Blackwell Publishing Ltd, 2017.
- [98] J. E. Carney and J. R. Finn, "Device Scale Modeling of Solvent Absorption using MFIX-TFM," Albany, OR, 2016.
- [99] D. Kochkov, J. A. Smith, A. Alieva, Q. Wang, M. P. Brenner and S. Hoyer, "Machine learning accelerated computational fluid dynamics," *Proceedings of the National Academy of Sciences*, vol. 118, no. 21, pp. 1 - 8, 2021.
- [100] R. G. A. Montero, "Estudio De Actualización Del Balance De Masa Para La Simulación Del Proceso De Refinación De Ferróníquel En Horno Cuchara De Cerro Matoso S.a Empleando METSIM®," Universidad Industrial De Santander, Bucaramanga, 2010.

- [101] M. W. Kennedy, "Metallurgical Plant Optimization Through The Use Of Flowsheet Simulation Modelling," *Celebrating the Megascale: Proceedings of the Extraction and Processing Division*, vol. 11, no. 1, pp. 367-368, 2014.
- [102] T. Larochelle and H. Kasaini, "Predictive Modeling Of Rare Earth Element Separation By Solvent Extraction Using METSIM," *IMPC 2016: XXVIII International Mineral Processing Congress Proceedings*, pp. 1-7, 2016.
- [103] Z. Qiuyue, Z. Tingan, L. Guozhi, Z. Xiaofeng and liuyan, "Application of Process Simulation Software METSIM in Metallurgy," *TELKOMNIKA*, vol. 10, no. 8, pp. 2202-2208, 2012.
- [104] F. N. Yahya, W. H. Tbrahim, R. A. Rasid, A. Hisham and L. N. Suli, "Modelling and simulation of lanthanum (La) and neodymium (Nd) leaching from monazite ore using METSTM," *IOP Conference Series: Materials Science and Engineering*, vol. 736, no. 2, 3 2020.
- [105] T. QIU, D. ZHU, C. WU and L. WANG, "Lattice Boltzmann model for simulation on leaching process of weathered elution-deposited rare earth ore," *Journal of Rare Earths*, vol. 35, no. 10, pp. 1014-1021, 10 2017.
- [106] H. Li, Y. Le Moullec, J. Lu, J. Chen, J. Carlos Valle Marcos and G. Chen, "Solubility and energy analysis for CO₂ absorption in piperazine derivatives and their mixtures," *International Journal of Greenhouse Gas Control*, vol. 31, no. 12, pp. 25-32, 2014.
- [107] D. Heldebrant, P. Koech, V.-A. Glezakou, R. Rousseau, D. Malhotra and D. Cantu, "Water-Lean Solvents for Post-Combustion CO₂ Capture: Fundamentals, Uncertainties, Opportunities, and Outlook," *Chemical Reviews*, vol. 117, no. 14, pp. 9594-9624, 2017.
- [108] C. Hirt and B. Nichols, "Volume of fluid (VOF) method for the dynamics of free boundaries," *Journal of Computational Physics*, vol. 39, no. 1, pp. 201-225, 1981.
- [109] H. Rusche, "Computational Fluid Dynamics of Dispersed Two-Phase Flows at High Phase Fractions," Imperial College of Science, Technology & Medicine, London, 2002.
- [110] A. Y. C. & T. C. Kotwal, "Two-Phase Flow Behavior in Channels With Sudden Area Change Using Experimental and Computational Approach," in *Proceedings of the ASME 2017 International Mechanical Engineering Congress and Exposition. Volume 7: Fluids Engineering.*, Tampa, Florida, USA., November 3–9, 2017.
- [111] A. Chorlin, "Numerical solution of the Navier-stoke's equations," *Mathematical Computational Physics*, vol. 22, pp. 745-760, 1978.
- [112] A. Ataki and H. J. Bart, "The use of the VOF-model to study the wetting of solid surfaces," 2004.

- [113] P. Frolkovič, D. Logashenko and G. Wittum, "Flux-Based Level Set Method for Two-Phase Flow," 2011.
- [114] D. Spalding, "A general purpose computer program for multi-dimensional one- and two-phase flow," *Mathematics and Computers in Simulation (MATCOM)*, vol. 23, no. 3, pp. 267-276, 1981.
- [115] G. H. Yeoh and J. Tu, *Computational techniques for multiphase flows*, Butterworth-Heinemann, 2010, p. 643.
- [116] J. J. Cooke, "Modelling of reactive absorption in gas-liquid flows on structured packing," 2016.
- [117] M. S. X. Cai, "Interface-Resolving Simulations of Gas-Liquid Two-Phase Flows in Solid Structures of Different Wettability," Karlsruhe, Germany, 2016.
- [118] C. Wang, Z. Xu, C. Lai and X. Sun, *Beyond the standard two-film theory: Computational fluid dynamics simulations for carbon dioxide capture in a wetted wall column*, vol. 184, Elsevier Ltd, 2018, pp. 103-110.
- [119] C. Wang, "PNNL Report on the Development of Bench-scale CFD Simulations for Gas Absorption across a Wetted Wall Column Revision Log Acknowledgment of Funding Table of Contents," 2016.
- [120] S. Mirjalili, S. S. Jain A N and D. M. S. Dodd, "Interface-capturing methods for two-phase flows: An overview and recent developments," 2017.
- [121] DOE Carbon Capture Simulation Initiative, "CCSI CFD Models User Manual," Berkeley, 2018.
- [122] S. G. T. R. T. F. E. Freguia, "Modeling of CO₂ Removal from Flue Gases with Monoethanolamine," pp. 1-201, 5 2002.
- [123] J. J. Cooke, L. M. Armstrong, K. H. Luo and S. Gu, "Adaptive mesh refinement of gas-liquid flow on an inclined plane," 2014.
- [124] F. Moukalled, L. Mangani and M. Darwish, *Fluid Mechanics and Its Applications The Finite Volume Method in Computational Fluid Dynamics*, 1 ed., vol. 113, M. Darwish, L. Mangani and F. Moukalled, Eds., Beirut: Springer, 2016, pp. 1-816.
- [125] s. Tim Behrens, "OpenFOAM's basic solvers for linear systems of equations," 2009.
- [126] S. A. Owens, M. R. Perkins, B. Eldridge, K. W. Schulz and R. A. Ketcham, "Computational Fluid Dynamics Simulation of Structured Packing," *Industrial & Engineering Chemistry Research*, vol. 52, no. 5, pp. 2032-2045, 2013.

- [127] C. Soullaine, P. Horgue, J. Franc and M. Quintard, "Gas-liquid flow modeling in columns equipped with structured packing," John Wiley and Sons Inc., 2014.
- [128] B. Kumar, M. Crane and Y. Delauré, "On the volume of fluid method for multiphase fluid flow simulation," World Scientific Publishing Co. Pte Ltd, 2013.
- [129] L. Raynal, C. Boyer and J.-P. Ballaguet, "Liquid Holdup and Pressure Drop Determination in Structured Packing with CFD Simulations," 2004.
- [130] A. Zakeri, A. Einbu and H. F. Svendsen, "Experimental investigation of liquid holdup in structured packings," *Chemical Engineering Research and Design*, vol. 90, no. 5, pp. 585-590, 2012.
- [131] E. Ryan, C. Montgomery, C. Storlie and J. Wendelberger, "CCSI Validation and Uncertainty Quantification Hierarchy for CFD Models," 2012.
- [132] J. Mackowiak, *Fluid Dynamics of Packed Columns: Principles of the Fluid Dynamic Design of Columns for Gas/Liquid and Liquid/Liquid Systems*, 1 ed., vol. 1, J. Mackowiak, Ed., Germany: Springer, 2012, pp. 1-368.
- [133] M. Anitha and H. Singh, "Artificial neural network simulation of rare earths solvent extraction equilibrium data," *Desalination*, vol. 232, no. 1-3, pp. 59-70, 11 2008.
- [134] A. E. Giles, C. Aldrich and J. S. J. Van Deventer, "Modelling of rare earth solvent extraction with artificial neural nets," ELSEVIER, 1996.
- [135] M. R. M. S. A. N. A. A. a. M. L. A. Usman, "Machine Learning Computational Fluid Dynamics," in *2021 Swedish Artificial Intelligence Society Workshop (SAIS)*, Luleå, SE-97187, Sweden, 2021.
- [136] T. Karras, M. Aittala, J. Hellsten, S. Laine, J. Lehtinen and T. Aila, "Training Generative Adversarial Networks with Limited Data," in *34th Conference on Neural Information Processing Systems (NeurIPS 2020)*, Vancouver, Canada, 2020.
- [137] L. Schiller and A. and Naumann, "A drag coefficient correlation.;" *Z. Ver. Deutsch. Ing.*; vol. 1, no. 77, p. 318–320, 1935.
- [138] B. E. Launder, G. J. Reece and W. Rodi, "A new correlation for the two-phase pressure recovery downstream from a sudden enlargement," *Experimental Heat Transfer, Fluid Mechanics and Thermodynamics*, vol. 6, no. 20, pp. 537-566, 1975.
- [139] B. Launder and D. Spalding, "The numerical computation of turbulent flows," *Computer Methods in Applied Mechanics and Engineering*, vol. 11, no. 3, pp. 269-275, 1974.
- [140] O. Ubbink, "Numerical prediction of two fluid systems with sharp interfaces," Imperial College of Science, Technology & Medicine, London, 1997.

- [141] G. H. Yeoh and J. Tu, *Computational Techniques in Multiphase flows*, London : Elsevier, 2010.
- [142] B. Leonard, "Locally modified QUICK scheme for highly convective 2-D and 3-D flows," *Numerical methods in laminar and turbulent flow*, vol. 5, no. 1, pp. 35-47, 1987.
- [143] S. Patankar, "A calculation procedure for two-dimensional elliptic situations," *Numerical heat transfer*, vol. 4, no. 4, pp. 409-425, 1981.
- [144] L. Yang, "CFD MODELING OF MULTIPHASE COUNTER-CURRENT FLOW IN PACKED BED REACTOR FOR CARBON CAPTURE," 2015.
- [145] X. Y. Wu and A. F. Ghoniem, "Hydrogen-assisted Carbon Dioxide Thermochemical Reduction on La_{0.9}Ca_{0.1}FeO_{3-Δ} Membranes: A Kinetics Study," Wiley-VCH Verlag, 2018.
- [146] M. Wehrli, T. Kögl, T. Linder and W. Arlt, "An unobstructed view of liquid flow in structured packing," vol. 69, *Italian Association of Chemical Engineering - AIDIC*, 2018, pp. 775-780.
- [147] K. E. Wardle and H. G. Weller, "Hybrid multiphase CFD solver for coupled dispersed/segregated flows in liquid-liquid extraction," 2013.
- [148] H. J. Verschoof, Z. Olujic and J. R. Fair, "A general correlation for predicting the loading point of corrugated sheet structured packings," vol. 38, *ACS*, 1999, pp. 3663-3669.
- [149] A. Technology, "Rate-Based Model of the CO₂ Capture Process by K₂CO₃ using Aspen Plus Aspen Plus," 2008.
- [150] X. Sun, Z. Xu, C. Lai, W. Pan, C. Wang, J. Gattiker, P. Marcy, L. Alamos, N. Laboratory, S. Sundaresan and A. Ozel, "A Validation Hierarchy for CFD Models of Solvent-based Carbon Capture Systems," 2015.
- [151] C. P. Stemmet, "Gas-liquid solid foam reactors : hydrodynamics and mass transfer," Africa, 2008.
- [152] L. Spiegel and W. Meier, "Distillation columns with structured packings in the next decade," vol. 81, *Institution of Chemical Engineers*, 2003, pp. 39-47.
- [153] T. L. Sønderby, K. B. Carlsen, P. L. Fosbøl, L. G. Kiørboe and N. von Solms, "A new pilot absorber for CO₂ capture from flue gases: Measuring and modelling capture with MEA solution," vol. 12, 2013, pp. 181-192.
- [154] E. Solnes Birkelund, "CO₂ Absorption and Desorption Simulation with Aspen HYSYS," 2013.

- [155] W. Said, M. Nemer and D. Clodic, "Modeling of dry pressure drop for fully developed gas flow in structured packing using CFD simulations," 2011.
- [156] S. Rebughini, A. Cuoci and M. Maestri, "Hierarchical analysis of the gas-to-particle heat and mass transfer in micro packed bed reactors," Elsevier, 2016.
- [157] S. Rebughini, A. Cuoci, A. G. Dixon and M. Maestri, Cell agglomeration algorithm for coupling microkinetic modeling and steady-state CFD simulations of catalytic reactors, vol. 97, Elsevier Ltd, 2017, pp. 175-182.
- [158] N. Razi, O. Bolland and H. Svendsen, "Review of design correlations for CO₂ absorption into MEA using structured packings," 2012.
- [159] C. F. Petre, F. Larachi, I. Iliuta and B. P. A Grandjean, "Pressure drop through structured packings: Breakdown into the contributing mechanisms by CFD modeling," 2003.
- [160] W. Pan, J. Galvin, W. L. Huang, Z. Xu, X. Sun, Z. Fan and K. Liu, Device-scale CFD Modeling of Gas-liquid Multiphase Flow and Amine Absorption for CO₂ Capture, vol. 5, Madison, 2012, pp. 1-41.
- [161] K. Meredith, Y. Xin and J. De Vries, A numerical model for simulation of thin-film water transport over solid fuel surfaces, 2011, pp. 415-428.
- [162] K. V. Meredith, A. Heather, J. De Vries and Y. Xin, A numerical model for partially-wetted flow of thin liquid films, 2011.
- [163] R. Lu, K. Li, J. Chen, H. Yu and M. Tade, "Rate-based modelling and simulation of large-scale CO₂ capture using a piperazine-promoted aqueous ammonia solution," Italian Association of Chemical Engineering - AIDIC, 2017.
- [164] H. Liepmann and A. Roshko, Elements of Gasdynamics, 1 ed., vol. 1, H. Liepmann, Ed., Pasadena, CA: California Institute of Technology, 1957, pp. 1-232.
- [165] B. H. Li, N. Zhang and R. Smith, "Simulation and analysis of CO₂ capture process with aqueous monoethanolamine solution," Elsevier Ltd, 2016.
- [166] A. Kothandaraman, L. Nord, O. Bolland, H. J. Herzog and G. J. McRae, Comparison of solvents for post-combustion capture of CO₂ by chemical absorption, vol. 1, 2009, pp. 1373-1380.
- [167] I. Kataoka, K. Yoshida, M. Naitoh, H. Okada and T. Morii, "Transport of Interfacial Area Concentration in Two-Phase Flow," Nuclear Energy Safety Organization Japan, Nuclear Energy Safety Organization Japan, 2012.

- [168] M. Isoz and J. Haidl, Computational-Fluid-Dynamics Analysis of Gas Flow through Corrugated-Sheet-Structured Packing: Effects of Packing Geometry, vol. 57, American Chemical Society, 2018, pp. 11785-11796.
- [169] Y. Iso, J. Huang, M. Kato, S. Matsuno and K. Takano, "Numerical and experimental study on liquid film flows on packing elements in absorbers for post-combustion CO₂ capture," Elsevier Ltd, 2013.
- [170] Y. Iso and X. Chen, "Flow transition behavior of the wetting flow between the film flow and rivulet flow on an inclined wall," 2011.
- [171] Z. Idris, J. Han, S. Jayarathna and D. A. Eimer, "Surface Tension of Alkanolamine Solutions: An Experimentally Based Review," Elsevier Ltd, 2017.
- [172] A. Hoffmann, I. Ausner, J. U. Repke and G. Wozny, Detailed investigation of multiphase (gas-liquid and gas-liquid-liquid) flow behaviour on inclined plates, vol. 84, Institution of Chemical Engineers, 2006, pp. 147-154.
- [173] H. Hikita, S. Asai, H. Ishikawa and M. Honda, "The Kinetics of Reactions of Carbon Dioxide with Monoethanolamine, Diethanolamine and Triethanolamine by a Rapid Mixing Method," 1977.
- [174] S. Higgins, Y.-A. Liu, L. E. Achenie, D. G. Baird and P. L. Durrill, "Design and Optimization of Post-Combustion CO₂ Capture in Chemical Engineering," 2016.
- [175] M. Hettel, C. Diehm, H. Bonart and O. Deutschmann, "Numerical simulation of a structured catalytic methane reformer by DUO: The new computational interface for OpenFOAM® and DETCHEM™," Elsevier, 2015.
- [176] J. Han, J. Jin, D. A. Eimer and M. C. Melaaen, Density of water (1) + monoethanolamine (2) + CO₂ (3) from (298.15 to 413.15) K and surface tension of water (1) + monoethanolamine (2) from (303.15 to 333.15) K, vol. 57, 2012, pp. 1095-1103.
- [177] M. H. Gutknecht, "A Brief Introduction to Krylov Space Methods for Solving Linear Systems," 2011.
- [178] V. Gupta, A. Paula Vieira Soares Pereira Dias in, K. Sztekler, E. Caetano Fernandes Supervisor and A. Paula Vieira Soares Pereira Dias, "Modelling of CO₂ capture using Aspen Plus for EDF power plant, Krakow, Poland Energy Engineering and Management Examination Committee," 2016.
- [179] D. Gueyffier, J. Li, A. Nadim, R. Scardovelli and S. Zaleski, "Volume-of-Fluid Interface Tracking with Smoothed Surface Stress Methods for Three-Dimensional Flows," Academic Press Inc., 1999.

- [180] M. Fourati, V. Roig and L. Raynal, "Experimental study of liquid spreading in structured packings," 2012.
- [181] D. Darmana, R. L. Henket, N. G. Deen and J. A. Kuipers, Detailed modelling of hydrodynamics, mass transfer and chemical reactions in a bubble column using a discrete bubble model: Chemisorption of CO₂ into NaOH solution, numerical and experimental study, vol. 62, 2007, pp. 2556-2575.
- [182] Y. Yu, L. Yu, K. Y. Koh, C. Wang and J. P. Chen, "Rare-earth metal based adsorbents for effective removal of arsenic from water: A critical review," *Critical Reviews in Environmental Science and Technology*, vol. 48, no. 22-24, pp. 1127-1164, 12 2018.
- [183] R. T. Yang, S. K. Das and B. M. Tsai, "Coal demineralization using sodium hydroxide and acid solutions," *Fuel*, vol. 156, no. 3, pp. 12-19, 1985.
- [184] F. Xie, T. A. Zhang, D. Dreisinger and F. Doyle, "A critical review on solvent extraction of rare earths from aqueous solutions," *Minerals Engineering*, 2014.
- [185] N. Wijaya and L. Zhang, "A critical review of coal demineralization and its implication on understanding the speciation of organically bound metals and submicrometer mineral grains in coal," *Energy and Fuels*, vol. 25, no. 1, pp. 1-16, 1 2011.
- [186] V. Vaccarezza, "Beneficiation And Hydrometallurgical Treatment Of Norra Kärr Eudialyte Mineral," Colorado School of Mines, Golden, 2018.
- [187] P. L. Rozelle, A. B. Khadilkar, N. Pulati, N. Soundarrajan, M. S. Klima, M. M. Mosser, C. E. Miller and S. V. Pisupati, "A Study on Removal of Rare Earth Elements from U.S. Coal Byproducts by Ion Exchange," *Metallurgical and Materials Transactions E*, vol. 3, no. 1, pp. 6-17, 3 2016.
- [188] E. O. Opare, E. Struhs and A. Mirkouei, "A comparative state-of-technology review and future directions for rare earth element separation," *Renewable and Sustainable Energy Reviews*, vol. 143, 6 2021.
- [189] S. N, E. B, C.-H. Lee, G. E and T. N, "A hydrometallurgical process for the recovery of cerium from Khuren khad ore," *Proceedings of the Mongolian Academy of Sciences*, vol. 59, no. 01, pp. 32-37, 4 2019.
- [190] S. Mukherjee and P. C. Borthakur, "Chemical demineralization/desulphurization of high sulphur coal using sodium hydroxide and acid solutions," 2001.
- [191] F. R. Karner, H. H. Schobert, S. K. Falcone and S. A. Benson, "Elemental Distribution And Association With Inorganic And Organic Components In North Dakota Lignites," in *ACS Symposium Series*, Philadelphia, 1986.

- [192] G. M. Eskenazy, "Aspects of the geochemistry of rare earth elements in coal: An experimental approach," *International Journal of Coal Geology*, 1999.
- [193] C. Tunsu, C. Ekberg and T. Retegan, "Characterization and leaching of real fluorescent lamp waste for the recovery of rare earth metals and mercury," *Hydrometallurgy*, Vols. 144-145, pp. 91-98, 2014.
- [194] S. Tang, C. Zheng, M. Chen, W. Du and X. Xu, "Geobiochemistry characteristics of rare earth elements in soil and ground water: a case study in Baotou, China," *Scientific Reports*, vol. 10, no. 1, p. 11740, 2020.
- [195] A. Sedat, T. Yavuzand and O. Gulhan, "Extraction of rare earths from a Turkish ore," *Physicochemical Problems of Mineral Processing*, vol. 27, no. 1, pp. 69-76, 1993.
- [196] A. Rout, J. Kotlarska, W. Dehaen and K. Binnemans, "Liquid–liquid extraction of neodymium(iii) by dialkylphosphate ionic liquids from acidic medium: the importance of the ionic liquid cation," *Physical Chemistry Chemical Physics*, vol. 15, no. 39, pp. 16533-16541, 2013.
- [197] T. Müller and B. Friedrich, "Development of a recycling process for nickel-metal hydride batteries," *Journal of Power Sources*, vol. 158, no. 2, pp. 1498-1509, 2006.
- [198] M. Gergoric, C. Ekberg, B.-M. Steenari and T. Retegan, "Separation of Heavy Rare-Earth Elements from Light Rare-Earth Elements Via Solvent Extraction from a Neodymium Magnet Leachate and the Effects of Diluents," *Journal of Sustainable Metallurgy*, vol. 3, no. 3, pp. 601-610, 2017.

APPENDIX A.


Tutorial to create METSIM model.

In this appendix Author discusses a tutorial to build METSIM model. Although, resources to perform process modeling using METSIM software are available on YouTube more than 91% resources are behind payment wall, while remaining resources maximum explained in Chinese or Spanish language. Apart from that, the resources do not discuss in detail about various options available in METSIM. These resources mostly discusses available simplified process models available in software directory. Thus, author discusses standard operating procedure to build process model using METSIM. Also, following this tutorial, any peer reviewing publication can validate author's results and discussion. The tutorial is in simplified English language with no scientific tone. Thus, inexperience less-scientific user can understand how to use software.

Step.1:

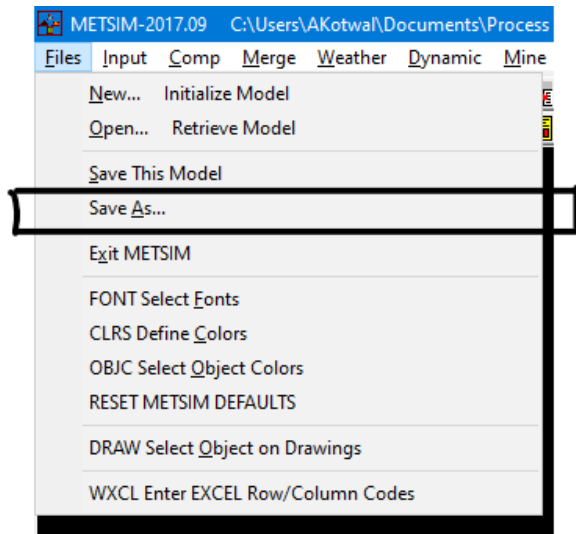
In process modeling and simulations, it is essential to understand required components (reactants and products in reactions) and elements that are planned to implement in process model. The METSIM specifically requests user defined as well as database based components. Thus, with help of research team or through various publications gather data for all the components that are established in process model. Also it is beneficial to establish reactions between these components.

Step.2:

Now start METSIM and click on first icon (new model)  from the button bar which is shown below




Then click on File option from menu bar, in File manu, click on 'Save As' option shown below:



After that write model name with no spaces (special characters such as underscore and dash can be used) and save the model.

Step.3:

After saving model click on  (model parameters) icon and add model related information in first tab called '**Project**' such as *Owner, Location, Title, Engineer*, etc. This information does not affect any part of modeling and simulations, however it allows user to create effortless report from METSIM

On the Second Tab called '**Site data**', add information such as *Geographic location, Ambient Conditions, Standard/Normal Conditions for Gas, Estimated moisture content in that area*, etc. The information applied in this tab does create significant effect while running simulation of model and should be added vary carefully with well researched data.

In '**Calc Options**', the modeler or user of the model activates the required utilities which are provided by METSIM for example '*Mass Balance*' allow software to do calculations involving only mass balance. By default, '*Mass Balance*' is active and user or modeler does not required any further action. The user can activate other utility options as well as per the requirements. However, the subsequent information will be asked by METSIM. The information applied in this tab does create significant effect while running simulation of model

In ‘**Calc Parameters**’, the modeler or user define the *units of mass and time* which acts as global time and mass related units. *Calculations range* to define the tolerances *On/Off controls* for unit operations run *time displays* to show monitors of steady-state or dynamic simulations of models. The information applied in this tab does create significant effect while running simulation of model

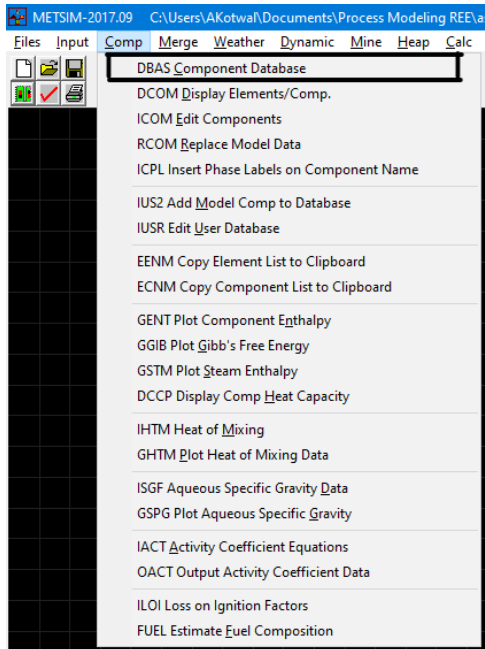
If the time dependent dynamic simulation is planned to performed, then options in ‘**Dynamic Parameters**’ tab are essential to defined. Along with activations of dynamic simulation option under Calc Options tab, the information defined under this tab is critical for model if it is time dependent. Under this tab, *time step, starting date and time, dynamic plotting of functions* is defined.

Under ‘**Convergence**’ tab *steady state recycle stream convergence, Feedback control based convergence, ‘Minimum stream values’* for convergence of each stream, etc. are defined. The information applied in this tab does create significant effect while running simulation of model. This data is also critical for convergence occurrence.

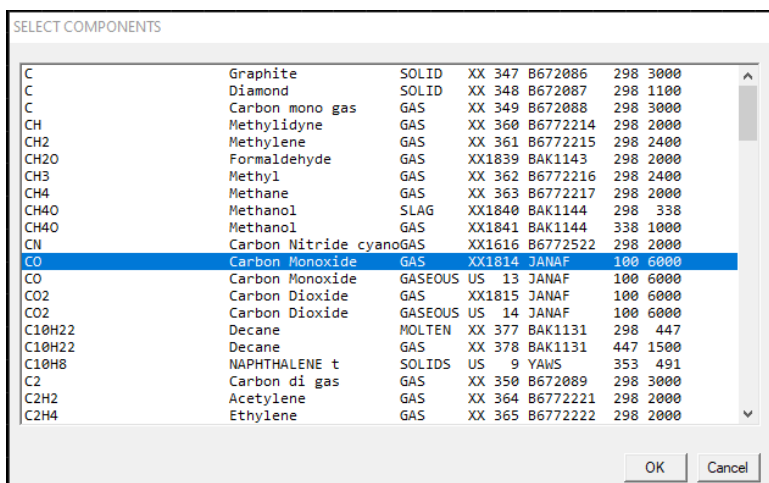
Step.4:

Go to ‘**Comp**’ menu, → select DBAS Component Database → Left click on each element that are essential for this process model to work. → Click OK.

If the Carbon element is added then software ask, → ‘include YAWS hydrocarbon database?’ → click yes if the database has any compounds that are associated with your model.

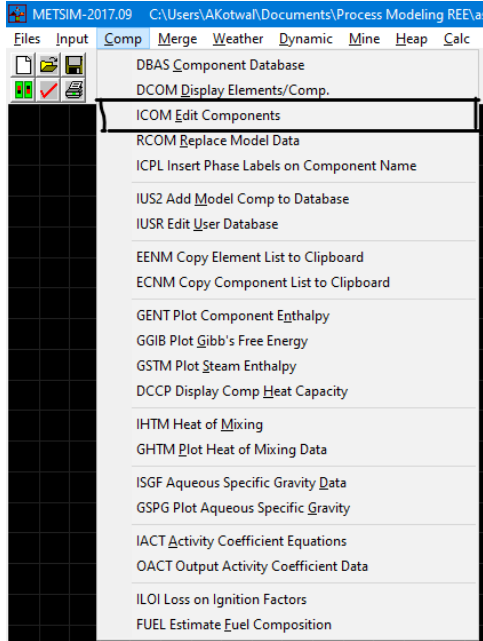


As result METSIM database of components opens up, look for all the components that are essential for the simulation of model work. Do first left click on the first ever component that is requested, then before each left click, hold control key on keyboard. This allow user to select multiple components in single session. If anytime between component selection if the OK button is pressed by mistake then fear not the all of the previously selected components are added to model registry, along with that, METSIM algorithm pops up again giving modeler a second chance. However, after popping the SELECT COMPONENTS window second time, make sure all previously selected components are deselected, that way modeler does not duplicate the entries in model registry.

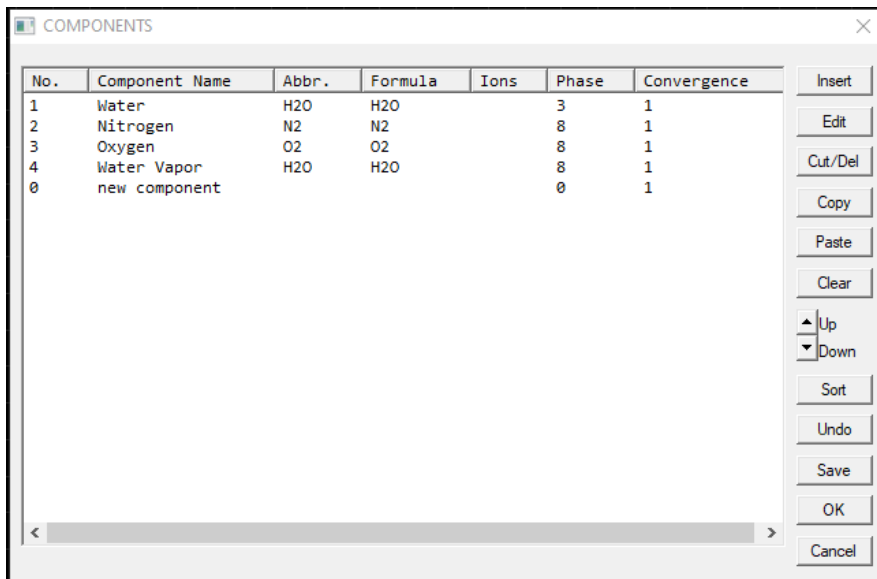


Step.5:

After adding all the reactant components and products components in model registry, certain components need to be added manually. Thus, the METSIM components registry can be accessed by going to 'Comp' menu, → select ICOM Edit Components option.



This opens window called 'COMPONENTS' where components registry is stored.






Using *Insert, Edit, Cut/Del, Copy, Paste, Clear*, options each component can be added as well as modified the previously added component default from the database. For example, a solid bounded elements such as Neodymium can be added from inbuilt database of METSIM but Neodymium ion in aqueous form is not present in database. For that following operations are needed:

Select Component name → left click ‘*Copy*’ option → left click ‘*Paste*’ option → left click ‘*Edit*’ option. Change its abbreviation and name and all other properties and click OK. For now the component number can be ignored because METSIM arrange it correctly.

Like that change the data of default component or add completely new component, modeler’s choice!

Step.6:


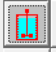



From side panel which is shown below, click  (GEN) option which activates general options and unit operations which are required for modelling flowsheet. → Left Click  (section) option → hover mouse over flowsheet space → left click anywhere → Left click  (redraw Flowsheet) option from top tool bar panel. This procedure adds sections in model. The sections are benefitted towards adding various process areas and distinguishing those amongst each other.



Step 7:

Deploy all the unit operations which are required in first section.

An example of adding Unit operation:

From side panel which is shown below, click  (GEN) option which activates general options and unit operations which are required for modelling flowsheet. → Left Click  (Tank, TNK) option → hover mouse over flowsheet space → left click anywhere → Left click  (redraw Flowsheet) option from top tool bar panel. → Left click  (Change the object size) option from top tool bar panel. → again Left click  (redraw Flowsheet) option from top tool bar panel.

Like the example procedure add all desired unit operations in current section of model and design the flowsheets which are shown in this dissertation.

APPENDIX B.

In this Appendix an OpenFOAM case files codes are described which are typically used in all the cases that are simulated in this dissertation. These codes can be used as tutorials also a way to crosscheck for the peer review publications.

Files in 0 folder of Case Directory

The structure of 'U' file (located at \$CASE_DIR\0\U) in OpenFOAM simulation

```
1. /*-----*- C++ -*-----*/
2.
3.  \ \ / / F i e l d      | OpenFOAM: The Open Source CFD Toolbox
4.  \ \ / / O peration    | Website: https://openfoam.org
5.  \ \ / / A nd          | Version: 7
6.  \ \ / / M anipulation |
7.  /*-----*- C++ -*-----*/
8. FoamFile
9. {
10.     version      2.0;
11.     format        ascii;
12.     class         volVectorField;
13.     location      "0";
14.     object        U;
15. }
16. // *****
17.
18. dimensions      [0 1 -1 0 0 0];
19.
20. internalField   uniform (0 0 0);
21.
22. boundaryField
23. {
24.
25.     atmosphere
26.     {
27.         type      noSlip;
28.     }
29. /*
30.     {
31.         type      pressureInletOutletVelocity;
32.         value     uniform (0 0 0);
33.     }
34. */
35.     liquidinlet
36.     {
37.         type      flowRateInletVelocity;
38.         massFlowRate constant 0.0036116;
39.         value     uniform (0 0 0);
40.     }
41. /*
42.     wall
43.     {
44.         type      uniformFixedValue;
45.         uniformValue constant (0 0 0);
46.         value     uniform (0 0 0);

```



```

47. }
48. */
49. gasinletwall
50. {
51.     type          noSlip;
52. }
53. /*
54. {
55.     type          fixedValue;
56.     value         uniform (0 0.238 0);
57. }
58. */
59. gasoutletwall
60. {
61.     type          noSlip;
62. }
63. /*
64. {
65.     type          fixedValue;
66.     value         uniform (0 0 0);
67. }
68. /*
69. uppergasoutlet
70. {
71.     type          inletOutlet;
72.     inletValue    uniform (0 0 0);
73.     value         $internalField;
74. }
75.
76. lowerliquidoutlet
77. {
78.     type          inletOutlet;
79.     inletValue    uniform (0 0 0);
80.     value         $internalField;
81. }
82. */
83. liquidoutlet
84. {
85.     type          pressureInletOutletVelocity;
86.     value         uniform (0 0 0);
87. }
88.
89. frontwall
90. {
91.     type          cyclicAMI;
92. }
93.
94. backwall
95. {
96.     type          cyclicAMI;
97. }
98.
99. corrugatedwall
100. {
101.     type          noSlip;
102. }
103.
104. topwall
105. {
106.     type          noSlip;
107. }
108.
109. bottomwall
110. {

```

```

111.     type          noSlip;
112.   }
113.
114.   symmetry
115.   {
116.     type          symmetry;
117.   }
118.
119.   defaultFaces
120.   {
121.     type          empty;
122.   }
123.
124. }
125.
126. // ***** //

```

The structure of 'alpha.water' file (located at \$CASE_DIR\0\alpha.water.orig) in OpenFOAM simulation

```

1.  /*-----*- C++ -*-----*/
2.  =====
3.  \ \ / / F i e l d      | OpenFOAM: The Open Source CFD Toolbox
4.  \ \ / / O p e r a t i o n | Website: https://openfoam.org
5.  \ \ / / A n d           | Version: 7
6.  \ \ / / M a n i p u l a t i o n |
7.  /*-----*/
8.  FoamFile
9.  {
10.   version      2.0;
11.   format       ascii;
12.   class        volScalarField;
13.   object       alpha.water;
14. }
15. // ***** //
16.
17. dimensions    [0 0 0 0 0 0];
18.
19. internalField uniform 0;
20.
21. boundaryField
22. {
23.
24.   atmosphere
25.   {
26.     type       zeroGradient;
27.   }
28. /*
29.   {
30.     type       inletOutlet;
31.     inletValue uniform 0;
32.     value      uniform 0;
33.   }
34. */
35.   liquidinlet
36.   {
37.     type       fixedValue;
38.     value      uniform 1.0;           //Liquid volume fraction
39.   }
40.

```

```

41.  gasinletwall
42.  {
43.      type          zeroGradient;
44.  }
45.  /*
46.  {
47.      type          fixedValue;
48.      value         uniform 0.0;          //Gas volume fraction
49.  }
50.  */
51.  gasoutletwall
52.  {
53.      type          zeroGradient;
54.  }
55.  /*
56.  {
57.      type          inletOutlet;
58.      inletValue   $internalField;
59.      value        $internalField;
60.  }
61.  */
62.  liquidoutlet
63.  {
64.      type          zeroGradient;
65.      value         uniform 0.0;
66.  }
67.  /*
68.  {
69.      type          inletOutlet;
70.      inletValue   $internalField;
71.      value        $internalField;
72.  }
73.
74.  /*
75.  wallfront
76.  {
77.      type          zeroGradient;
78.  }
79.
80.  wallback
81.  {
82.      type          zeroGradient;
83.  }
84.  /*
85.  frontwall
86.  {
87.      type          cyclicAMI;
88.      //value      uniform 0;
89.  }
90.
91.  backwall
92.  {
93.      type          cyclicAMI;
94.      //value      uniform 0;
95.  }
96.  /*
97.  walleleft
98.  {
99.      type          zeroGradient;
100. }
101.
102. wallright
103. {
104.     type          zeroGradient;

```

```

105.     }
106. */
107.
108.     corrugatedwall
109.     {
110.         type            constantAlphaContactAngle;
111.         theta0          72;
112.         limit           gradient;
113.         value           uniform 0;
114.     }
115.
116.     bottomwall
117.     {
118.         type            zeroGradient;
119.     }
120.
121.     topwall
122.     {
123.         type            zeroGradient;
124.     }
125.
126.     symmetry
127.     {
128.         type            symmetry;
129.     }
130.
131.     defaultFaces
132.     {
133.         type            empty;
134.     }
135.
136. }
137.
138. // ***** //

```

The structure of p_rgh file (located at \$CASE_DIR\0\p_rgh) in OpenFOAM simulation

```

1. /*-----*- C++ -*-*/
2.
3.  ===== |
4.  \ \ / /   F i e l d       | OpenFOAM: The Open Source CFD Toolbox
5.  \ \ / /   O p e r a t i o n   | Website: https://openfoam.org
6.  \ \ / /   A n d               | Version: 7
7.  \ \ / /   M a n i p u l a t i o n |
8.  /*-----*/
9.  FoamFile
10. {
11.     version      2.0;
12.     format       ascii;
13.     class        volScalarField;
14.     object       p_rgh;
15. }
16. // ***** //
17. dimensions      [1 -1 -2 0 0 0];
18.
19. internalField   uniform 0;
20.
21. boundaryField
22. {
23.
24.     atmosphere

```

```

25.  {
26.      type          fixedFluxPressure;
27.      //gradient    uniform 0;
28.      value         uniform 0;
29.  }
30. /*
31.  {
32.      type          totalPressure;
33.      rho           rho;
34.      psi           none;
35.      gamma        1;
36.      p0           uniform 0;
37.      value         uniform 0;
38.  }
39. */
40.  liquidinlet
41.  {
42.      type          fixedFluxPressure;
43.      //gradient    uniform 10;
44.      value         uniform 0;
45.  }
46. /*
47.  lowerGasInlet
48.  {
49.      type          zeroGradient;
50.  }
51.
52.  upperLiquidInlet
53.  {
54.      type          fixedFluxPressure;
55.      gradient      uniform 0;
56.      value         uniform 0;
57.  }
58. */
59.  gasinletwall
60.  {
61.      type          fixedFluxPressure;
62.      //gradient    uniform 0;
63.      value         uniform 0;
64.  }
65. /*
66.  upperGasOutlet
67.  {
68.      type          totalPressure;
69.      //rho         rho;
70.      //psi         none;
71.      //gamma       1;
72.      p0           uniform 0;
73.      //value       uniform 0;
74.  }
75. */
76.  gasoutletwall
77.  {
78.      type          fixedFluxPressure;
79.      //gradient    uniform 0;
80.      value         uniform 0;
81.  }
82. /*
83.  {
84.      type          fixedValue;
85.      value         uniform 0;
86.  }
87. */
88.  liquidoutlet

```

```

89.  {
90.      type          totalPressure;
91.      rho           rho;
92.      psi           none;
93.      gamma         1;
94.      p0            uniform 0;
95.      value         uniform 0;
96.  }
97.
98.  frontwall
99.  {
100.     type          cyclicAMI;
101.     value         uniform 0;
102.  }
103.
104.  backwall
105.  {
106.     type          cyclicAMI;
107.     value         uniform 0;
108.  }
109.
110.  corrugatedwall
111.  {
112.     type          fixedFluxPressure;
113.     //gradient    uniform 0;
114.     value         uniform 0;
115.  }
116.
117.  topwall
118.  {
119.     type          fixedFluxPressure;
120.     //gradient    uniform 0;
121.     value         uniform 0;
122.  }
123.
124.  bottomwall
125.  {
126.     type          fixedFluxPressure;
127.     //gradient    uniform 0;
128.     value         uniform 0;
129.  }
130.
131.  symmetry
132.  {
133.     type          symmetry;
134.  }
135.
136.  defaultFaces
137.  {
138.     type          empty;
139.  }
140.
141. }
142.
143. // ***** //

```

The boundary file of particular mesh that is used during the simulations how to create it, and how it modify it can be understandable with little knowledge of OpenFOAM programming and modeling

```

1. /*-----*- C++ -*-----*/
2.  =====
3.  \ \ / / F i e l d           | OpenFOAM: The Open Source CFD Toolbox
4.  \ \ / / O p e r a t i o n   | Website: https://openfoam.org
5.  \ \ / / A n d                | Version: 7
6.  \ \ / / M a n i p u l a t i o n |
7.  /*-----*- C++ -*-----*/
8.  FoamFile
9.  {
10.     version      2.0;
11.     format        ascii;
12.     class         polyBoundaryMesh;
13.     location      "constant/polyMesh";
14.     object        boundary;
15. }
16. // *****
17.
18. 11
19. (
20.     atmosphere
21.     {
22.         type          wall;
23.         inGroups      List<word> 1(wall);
24.         nFaces        553;
25.         startFace     638803;
26.     }
27.     gasoutletwall
28.     {
29.         type          patch;
30.         nFaces        225;
31.         startFace     639356;
32.     }
33.     liquidinlet
34.     {
35.         type          patch;
36.         nFaces        171;
37.         startFace     639581;
38.     }
39.     liquidoutlet
40.     {
41.         type          patch;
42.         nFaces        604;
43.         startFace     639752;
44.     }
45.     gasinletwall
46.     {
47.         type          patch;
48.         nFaces        119;
49.         startFace     640356;
50.     }
51.     topwall
52.     {
53.         type          wall;
54.         inGroups      List<word> 1(wall);
55.         nFaces        1251;
56.         startFace     640475;
57.     }
58.     corrugatedwall
59.     {
60.         type          wall;
61.         inGroups      List<word> 1(wall);
62.         nFaces        35915;
63.         startFace     641726;
64.     }

```

```

65.   frontwall
66.   {
67.       type                cyclicAMI;
68.       inGroups             List<word> 1(cyclicAMI);
69.       nFaces               3575;
70.       startFace            677641;
71.       matchTolerance       0.0001;
72.       transform             translational;
73.       neighbourPatch       backwall;
74.       method                faceAreaWeightAMI;
75.       lowWeightCorrection   0.2;
76.       separationVector      (-0.023622 0 0);
77.   }
78.   backwall
79.   {
80.       type                cyclicAMI;
81.       inGroups             List<word> 1(cyclicAMI);
82.       nFaces               3650;
83.       startFace            681216;
84.       matchTolerance       0.0001;
85.       transform             translational;
86.       neighbourPatch       frontwall;
87.       method                faceAreaWeightAMI;
88.       lowWeightCorrection   0.2;
89.       separationVector      (0.023622 0 0);
90.   }
91.   bottomwall
92.   {
93.       type                wall;
94.       inGroups             List<word> 1(wall);
95.       nFaces               2107;
96.       startFace            684866;
97.   }
98.   symmetry
99.   {
100.      type                symmetry;
101.      inGroups             List<word> 1(symmetry);
102.      nFaces               13052;
103.      startFace            686973;
104.   }
105. )
106.
107. // ***** //

```


The g file which describes the status of gravity application in OpenFOAM simulations.
 (Location: \$CASE_DIR\constant\g)

```

1. /*-----*- C++ -*-----*/
2.  =====
3.  \ \ / / F i e l d           | OpenFOAM: The Open Source CFD Toolbox
4.  \ \ / / O p e r a t i o n   | Website: https://openfoam.org
5.  \ \ / / A n d               | Version: 7
6.  \ \ / / M a n i p u l a t i o n |
7. /*-----*/
8. FoamFile
9. {
10.  version      2.0;
11.  format       ascii;
12.  class        uniformDimensionedVectorField;
13.  location     "constant";
14.  object       g;
15. }
16. // *****
17.
18. dimensions   [0 1 -2 0 0 0 0];
19. value        (0 -9.81 0);
20.
21.
22. // *****
  
```

turbulenceProperties file describing the status of turbulence model implemented in OpenFOAM simulation (Location: \$CASE_DIR\constant\turbulenceProperties)

```

1. /*-----*- C++ -*-----*/
2.  =====
3.  \ \ / / F i e l d           | OpenFOAM: The Open Source CFD Toolbox
4.  \ \ / / O p e r a t i o n   | Website: https://openfoam.org
5.  \ \ / / A n d               | Version: 7
6.  \ \ / / M a n i p u l a t i o n |
7. /*-----*/
8. FoamFile
9. {
10.  version      2.0;
11.  format       ascii;
12.  class        dictionary;
13.  location     "constant";
14.  object       turbulenceProperties;
15. }
16. // *****
17.
18. simulationType laminar;
19.
20.
21. // *****
  
```

transportProperties file of modelled case, here the liquid name is water but that can be changed along with other properties of that liquid in this file, prior to running model

(Location: \$CASE_DIR\constant\transportProperties)

```
1. /*-----*- C++ -*-----*\
2.
3.  =====
4.  \ \ / / F i e l d           | OpenFOAM: The Open Source CFD Toolbox
5.  \ \ / / O p e r a t i o n   | Website: https://openfoam.org
6.  \ \ / / A n d                | Version: 7
7.  \ \ / / M a n i p u l a t i o n |
8.  /*-----*\
9.  FoamFile
10. {
11.     version      2.0;
12.     format        ascii;
13.     class         dictionary;
14.     location      "constant";
15.     object        transportProperties;
16. }
17. // *****
18. phases (water air);
19.
20. water
21. {
22.     transportModel  Newtonian;
23.     nu              1e-06;
24.     rho             997.3;
25. }
26.
27. air
28. {
29.     transportModel  Newtonian;
30.     nu              1.831e-05;
31.     rho             1.185;
32. }
33.
34. sigma            0.0728;
35.
36. // *****
```

Now the files inside system folder of typical OpenFOAM cases that are modelled in this research. These files are *fvSchemes*, *fvSolution*, *setFieldsDict*, *decomposeParDict*, *controlDict*. These files essentially govern the solution algorithms and modeling development for each time step of the simulation.

fvSchemes file code of typical modelled case, this file governs the solution methodology and time stepping analysis for case.

```

1. /*-----*- C++ -*-----*/
2.  =====
3.  \ \ / / F i e l d           | OpenFOAM: The Open Source CFD Toolbox
4.  \ \ / / O peration         | Website: https://openfoam.org
5.  \ \ / / A n d               | Version: 7
6.  \ \ / / M anipulation      |
7.  /*-----*-
8.  FoamFile
9.  {
10.     version      2.0;
11.     format        ascii;
12.     class         dictionary;
13.     location      "system";
14.     object        fvSchemes;
15. }
16. // ***** //
17.
18. ddtSchemes
19. {
20.     default       Euler;
21. }
22.
23. gradSchemes
24. {
25.     default       Gauss linear;
26. }
27.
28. divSchemes
29. {
30.     default       none;
31.
32.     div(rhoPhi,U) Gauss linearUpwind grad(U);
33.     div(phi,alpha) Gauss vanLeer;
34.     div(phiRb,alpha) Gauss linear;
35.     div(((rho*nuEff)*dev2(T(grad(U)))) Gauss linear;
36. }
37.
38. laplacianSchemes
39. {
40.     default       Gauss linear corrected;
41. }
42.
43. interpolationSchemes
44. {
45.     default       linear;
46. }
47.
48. snGradSchemes
49. {
50.     default       corrected;
51. }
52.
53. wallDist
54. {
55.     method meshWave;
56. }
57.
58. // ***** //

```

fvSolution file code of typical modelled case, the code defines the algorithmic cycles for each variable of the modelled case for example pressure, velocity, volume fraction, etc.

```

1. /*-----*- C++ -*-----*/
2.      =====
3.      \\      / F i e l d           | OpenFOAM: The Open Source CFD Toolbox
4.      \\      / O peration          | Website: https://openfoam.org
5.      \\      / A nd                 | Version: 7
6.      \\      / M anipulation       |
7. /*-----*- C++ -*-----*/
8. FoamFile
9. {
10.     version      2.0;
11.     format        ascii;
12.     class         dictionary;
13.     location      "system";
14.     object        fvSolution;
15. }
16. // *****
17.
18. solvers
19. {
20.     "alpha.water.*"
21.     {
22.         nAlphaCorr      1;
23.         nAlphaSubCycles 1;
24.         cAlpha          1;
25.
26.         MULESCorr       yes;
27.         nLimiterIter    3;
28.
29.         solver          smoothSolver;
30.         smoother        symGaussSeidel;
31.         tolerance       1e-8;
32.         relTol          0;
33.     }
34.
35.     "pcorr.*"
36.     {
37.         solver          PCG;
38.         preconditioner
39.         {
40.             preconditioner  GAMG;
41.             tolerance       1e-5;
42.             relTol          0;
43.             smoother        GaussSeidel;
44.         }
45.         tolerance       1e-5;
46.         relTol          0;
47.         maxIter         50;
48.     }
49.
50.     p_rgh
51.     {
52.         solver          GAMG;
53.         tolerance       5e-9;
54.         relTol          0.01;
55.
56.         smoother        GaussSeidel;
57.
58.
59.
60.         maxIter         50;
61.     };
62.
63.     p_rghFinal
64.     {

```

```

65.     $p_rgh;
66.     tolerance      5e-9;
67.     relTol         0;
68. }
69.
70. U
71. {
72.     solver          smoothSolver;
73.     smoother        symGaussSeidel;
74.     nSweeps         1;
75.     tolerance       1e-07;
76.     relTol          0.1;
77. }
78. }
79.
80. PIMPLE
81. {
82.     momentumPredictor    no;
83.     //nOuterCorrectors   1;
84.     nCorrectors          2;
85.     nNonOrthogonalCorrectors 0;
86. }
87.
88. relaxationFactors
89. {
90.     equations
91.     {
92.         ".".*" 1;
93.     }
94. }
95.
96.
97. // ***** //

```

setFieldsDict file code of typical modelled case, the file patches the amount of denser phase in cells of mesh as an initial condition for solving inside computational domain.

```

1. /*-----*- C++ -*-----*\
2.  =====
3.  \ \ / / F i e l d       | OpenFOAM: The Open Source CFD Toolbox
4.  \ \ / / O p e r a t i o n | Website: https://openfoam.org
5.  \ \ / / A n d             | Version: 7
6.  \ \ / / M a n i p u l a t i o n |
7.  /*-----*/
8. FoamFile
9. {
10.     version      2.0;
11.     format       ascii;
12.     class        dictionary;
13.     location     "system";
14.     object       setFieldsDict;
15. }
16. // ***** //
17.
18. defaultFieldValues
19. (
20.     volScalarFieldValue alpha.water 0
21. );
22.
23. regions

```

```

24. (
25.   boxToCell
26.   {
27.
28.     box (-0.011811 0.0468247 -0.013) (0.011811 0.0494357 0.0129983);
29.
30.     fieldValues
31.     (
32.       volScalarFieldValue alpha.water 1
33.     );
34.   }
35. /*
36.   boxToCell
37.   {
38.     //boxes((-0.022622 0.0685851 -0.0115858)(-0.001 0.0710851 0.0115858)
39.     //      (-0.023622 0.0686251 -0.013) (0 0.0710851 0.013));
40.
41.     //box (-0.022622 0.0685851 -0.0115858)(-0.001 0.0710851 0.0115858);
42.     box (-0.015 0.0686251 -0.013) (-0.009 0.0710851 0.013);
43.
44.     fieldValues
45.     (
46.       volScalarFieldValue alpha.water 0
47.     );
48.   }
49. */
50.
51.   cylinderToCell
52.   {
53.     p1 (0 0.05 0);
54.     p2 (0 0.045 0);
55.     radius 0.007;
56.
57.     fieldValues
58.     (
59.       volScalarFieldValue alpha.water 0
60.     );
61.   }
62. );
63. );
64.
65.
66. // ***** //

```

decomposeParDict file code of typical modelled case, for faster computational performance this code allow solution domain prior to simulation to divide in multiple sections and for solve each sections by each core of CPU

```

1. /*-----*- C++ -*-----*\
2. =====
3.  \ \ / / F ield      | OpenFOAM: The Open Source CFD Toolbox
4.  \ \ / / O peration  | Website: https://openfoam.org
5.  \ \ / / A nd        | Version: 7
6.  \ \ / / M anipulation |
7.  \*-----*/
8. FoamFile
9. {

```

```

10.  version    2.0;
11.  format     ascii;
12.  class      dictionary;
13.  location   "system";
14.  object     decomposeParDict;
15. }
16. // * * * * *
17.
18. numberOfSubdomains 12;
19.
20. method             scotch;
21.
22. /*
23. numberOfSubdomains 12;
24.
25. method             simple;
26.
27. simpleCoeffs
28. {
29.     n               (2 6 1);
30.     delta            0.001;
31. }
32.
33. hierarchicalCoeffs
34. {
35.     n               (1 1 1);
36.     delta            0.001;
37.     order            xyz;
38. }
39.
40. manualCoeffs
41. {
42.     dataFile         "";
43. }
44.
45. distributed        no;
46.
47. roots              ( );
48.
49.
50. // * * * * *

```

controlDict file code of typical modelled case, this file controls the simulation progress and monitors any variables that needed to plotted over each time step.

```

1.  /*-----*- C++ -*------*\
2.  =====
3.  \ \ / / F ield           | OpenFOAM: The Open Source CFD Toolbox
4.  \ \ / / O peration      | Website: https://openfoam.org
5.  \ \ / / A nd            | Version: 7
6.  \ \ / / M anipulation   |
7.  /*-----*-
8.  FoamFile
9.  {
10.     version    2.0;
11.     format     ascii;
12.     class      dictionary;
13.     location   "system";

```

```

14.     object      controlDict;
15. }
16. // * * * * * //
17.
18. application      interFoam;
19.
20. startFrom        startTime;
21.
22. startTime        0;
23.
24. stopAt           endTime;
25.
26. endTime          3.0;
27.
28. deltaT           1e-5;
29.
30. writeControl     adjustableRunTime;
31.
32. writeInterval    0.3;
33.
34. purgeWrite       0;
35.
36. writeFormat      ascii;
37.
38. writePrecision   6;
39.
40. writeCompression off;
41.
42. timeFormat       general;
43.
44. timePrecision    7;
45.
46. runTimeModifiable yes;
47.
48. adjustTimeStep   yes;
49.
50. maxCo            1;
51. maxAlphaCo       1;
52.
53. maxDeltaT        5e-3;
54.
55.
56. functions
57. {
58.     inletFlux
59.     {
60.         type          surfaceFieldValue;
61.         libs          ("libfieldFunctionObjects.so");
62.         writeControl   timeStep;
63.         log            true;
64.         // Output field values as well
65.         writeFields   false;
66.         regionType    patch;
67.         name          liquidinlet;
68.         operation     sum;
69.
70.         fields
71.         (
72.             rhoPhi
73.             alpha
74.         );
75.     }
76.
77.     outletFlux

```



```

78.  {
79.    $inletFlux;
80.    name      liquidoutlet;
81.  }
82.
83.  fieldAverage2
84.  {
85.    type      fieldAverage;
86.    libs      ("libfieldFunctionObjects.so");
87.    writeControl writeTime;
88.    //writeControl  timeStep;
89.    log       true;
90.    // Output field values as well
91.    writeFields false;
92.    fields
93.    (
94.      U
95.      {
96.        mean      on;
97.        prime2Mean on;
98.        base      time;
99.      }
100.
101.      p
102.      {
103.        mean      on;
104.        prime2Mean on;
105.        base      time;
106.      }
107.
108.      alpha.water
109.      {
110.        mean      on;
111.        prime2Mean on;
112.        base      time;
113.      }
114.    );
115.  }
116.
117.  volumeAverage
118.  {
119.    type      volFieldValue;
120.    libs      ("libfieldFunctionObjects.so");
121.    enabled   true;
122.
123.    log       true;
124.    writeControl writeTime;
125.    writeFields true;
126.
127.    regionType all;
128.    operation  volAverage;
129.
130.    fields
131.    (
132.      alpha.water
133.      p
134.      U
135.    );
136.  }
137.
138.  pressureDropPatch1
139.  {
140.    type      fieldValueDelta;
141.    libs      ("libfieldFunctionObjects.so");

```

```

142.         operation      subtract;
143.         writeControl    timeStep;
144.         writeInterval   1;
145.         log              true;
146.
147.         region1
148.         {
149.             #includeEtc "caseDicts/postProcessing/surfaceFieldValue/surfaceRegion.cfg"
150.             operation    areaAverage;
151.             fields        (p);
152.             regionType    patch;
153.             name          liquidinlet;
154.         }
155.
156.         region2
157.         {
158.             #includeEtc "caseDicts/postProcessing/surfaceFieldValue/surfaceRegion.cfg"
159.             operation    areaAverage;
160.             fields        (p);
161.             regionType    patch;
162.             name          liquidoutlet;
163.         }
164.     }
165. }/*
166. interfaceHeightLeftWallPockets
167. {
168.     type          interfaceHeight;
169.     libs          ("libfieldFunctionObjects.so");
170.     writePrecision 5;
171.     writeToFile   true;
172.     useUserTime   true;
173.     locations     (
174.                 (-0.0058851 0.0409692 0.0121)
175.                 (0.0 0.0232323 0.0121)
176.                 (0.0 -0.0003897 0.0121)
177.                 (0.0 -0.0240117 0.0121)
178.                 (0.0059259 -0.0417078 0.0121)
179.                 );
180.     alpha        alpha.mea;
181. }
182.
183. interfaceHeightLeftWallSurfaces
184. {
185.     type          interfaceHeight;
186.     libs          ("libfieldFunctionObjects.so");
187.     writePrecision 5;
188.     writeToFile   true;
189.     useUserTime   true;
190.     locations     (
191.                 (-0.0031042 0.0381884 0.0071)
192.                 (0.0 0.0291582 0.0067)
193.                 (0.0 0.0173472 0.0067)
194.                 (0.0 0.0055362 0.0067)
195.                 (0.0 -0.0062748 0.0067)
196.                 (0.0 -0.0180858 0.0067)
197.                 (0.0 -0.0298968 0.0067)
198.                 (0.0031368 -0.0389187 0.0071)
199.                 );
200.     alpha        alpha.mea;
201. }
202.
203. interfaceHeightRightWallPockets
204. {
205.     type          interfaceHeight;

```

```

206.     libs      ("libfieldFunctionObjects.so");
207.     writePrecision 5;
208.     writeToFile  true;
209.     useUserTime  true;
210.     locations   (
211.                 (0.0058851 0.0409692 -0.0121)
212.                 (0.0 0.0232323 -0.0121)
213.                 (0.0 -0.0003897 -0.0121)
214.                 (0.0 -0.0240117 -0.0121)
215.                 (-0.0059259 -0.0417078 -0.0121)
216.             );
217.     alpha      alpha.meas;
218. }
219.
220. interfaceHeightRightWallSurfaces
221. {
222.     type      interfaceHeight;
223.     libs      ("libfieldFunctionObjects.so");
224.     writePrecision 5;
225.     writeToFile  true;
226.     useUserTime  true;
227.     locations   (
228.                 (0.0031042 0.0381884 -0.0071)
229.                 (0.0 0.0291582 -0.0067)
230.                 (0.0 0.0173472 -0.0067)
231.                 (0.0 0.0055362 -0.0067)
232.                 (0.0 -0.0062748 -0.0067)
233.                 (0.0 -0.0180858 -0.0067)
234.                 (0.0 -0.0298968 -0.0067)
235.                 (0.0031368 -0.0389187 -0.0071)
236.             );
237.     alpha      alpha.meas;
238. }
239. }/*
240.     atmosphereFlux
241.     {
242.         $inletFlux;
243.         name      upperGasOutlet;
244.     }
245. }
246.
247. // ***** //

```

APPENDIX C.

ParaView Python Script to create and calculate the Interfacial Area as well as Wetted Area
(Working on ParaView version less than 5.9.0)

In this dissertation the Paraview is used for visualization of gas-liquid sharp interfaces simulated using InterFoam, a solver from OpenFOAM numerical framework. Here results of initial conditions from '0' directory and geometrical domain from 'constant' directory are combined together and then Paraview adds time steps followed by that into visualization. The language followed in this tutorial is less scientific so that a less experienced person can post-process data, without knowing much terminology

The following script will create the values of interfacial area and wetted area at $f = 0.5$ clipping value.

Script for Wetted area:

```
1. ##### import the simple module from the paraview
2. from paraview.simple import *
3. ##### disable automatic camera reset on 'Show'
4. paraview.simple._DisableFirstRenderCameraReset()
5.
6. # create a new 'OpenFOAMReader'
7. a3D_Case18_halfGeom_80_FlR_0_0033441_watrfoam =
   OpenFOAMReader(registrationName='3D_Case18_halfGeom_(80)_FlR_0_0033441_watr.foam',
   FileName='F:\CCS\3D_cases\H2O_Cases\halfGeom\3D_Case18_halfGeom_(80)_FlR_0_0033441_watr
   \3D_Case18_halfGeom_(80)_FlR_0_0033441_watr.foam')
8.
9. # get animation scene
10. animationScene1 = GetAnimationScene()
11.
12. # update animation scene based on data timesteps
13. animationScene1.UpdateAnimationUsingDataTimeSteps()
14.
15. # Properties modified on a3D_Case18_halfGeom_80_FlR_0_0033441_watrfoam
16. a3D_Case18_halfGeom_80_FlR_0_0033441_watrfoam.LabelSize = '64-bit'
17. a3D_Case18_halfGeom_80_FlR_0_0033441_watrfoam.MeshRegions = ['corrugatedwall']
18. a3D_Case18_halfGeom_80_FlR_0_0033441_watrfoam.CellArrays = ['alpha.water',
   'alpha.waterMean', 'alpha.waterPrime2Mean', 'p_rgh']
19.
20. # get active view
21. renderView1 = GetActiveViewOrCreate('RenderView')
22.
23. # show data in view
24. a3D_Case18_halfGeom_80_FlR_0_0033441_watrfoamDisplay =
   Show(a3D_Case18_halfGeom_80_FlR_0_0033441_watrfoam, renderView1, 'GeometryRepresentation')
25.
26. # trace defaults for the display properties.
```

```

27. a3D_Case18_halfGeom_80_FlR_0_0033441_watrfoamDisplay.Representation = 'Surface'
28.
29. # reset view to fit data
30. renderView1.ResetCamera()
31.
32. # Uncomment this if the parview version is 5.10.RC1 reset view to fit data
33. # renderView1.ResetCamera(True)
34.
35. # get the material library
36. materialLibrary1 = GetMaterialLibrary()
37.
38. # update the view to ensure updated data information
39. renderView1.Update()
40.
41. # set scalar coloring
42. ColorBy(a3D_Case18_halfGeom_80_FlR_0_0033441_watrfoamDisplay, ('POINTS', 'alpha.water'))
43.
44. # rescale color and/or opacity maps used to include current data range
45. a3D_Case18_halfGeom_80_FlR_0_0033441_watrfoamDisplay.RescaleTransferFunctionToDataRange(True
, False)
46.
47. # show color bar/color legend
48. a3D_Case18_halfGeom_80_FlR_0_0033441_watrfoamDisplay.SetScalarBarVisibility(renderView1,
True)
49.
50. # get color transfer function/color map for 'alphawater'
51. alphawaterLUT = GetColorTransferFunction('alphawater')
52.
53. # get opacity transfer function/opacity map for 'alphawater'
54. alphawaterPWF = GetOpacityTransferFunction('alphawater')
55.
56. # Properties modified on animationScene1
57. animationScene1.AnimationTime = 9.0
58.
59. # get the time-keeper
60. timeKeeper1 = GetTimeKeeper()
61.
62. # create a new 'Threshold'
63. threshold1 = Threshold(registrationName='Threshold1',
Input=a3D_Case18_halfGeom_80_FlR_0_0033441_watrfoam)
64.
65. '''
66. # Properties modified on threshold1 This for ParaView 5.10.RC-1
67. threshold1.LowerThreshold = 0.91
68. threshold1.UpperThreshold = 1.0
69. threshold1.UseContinuousCellRange = 1
70. threshold1.Invert = 0
71. '''
72. # Properties modified on threshold1 for paraview version 5.9.0-RC2
73. threshold1.ThresholdRange = [0.91, 1.0]
74. threshold1.Invert = 0
75.
76. # show data in view
77. threshold1Display = Show(threshold1, renderView1, 'UnstructuredGridRepresentation')
78.
79. # trace defaults for the display properties.
80. threshold1Display.Representation = 'Surface'
81.
82. # hide data in view
83. Hide(a3D_Case18_halfGeom_80_FlR_0_0033441_watrfoam, renderView1)
84.
85. # show color bar/color legend
86. threshold1Display.SetScalarBarVisibility(renderView1, True)
87.

```

```

88. # update the view to ensure updated data information
89. renderView1.Update()
90.
91. # create a new 'Integrate Variables'
92. integrateVariables1 = IntegrateVariables(registrationName='IntegrateVariables1',
    Input=threshold1)
93. integrateVariables1.DivideCellDataByVolume = 1
94.
95. # Create a new 'SpreadSheet View'
96. spreadSheetView1 = CreateView('SpreadSheetView')
97. spreadSheetView1.ColumnToSort = ''
98. spreadSheetView1.BlockSize = 1024
99.
100. # show data in view
101. integrateVariables1Display = Show(integrateVariables1, spreadSheetView1,
    'SpreadSheetRepresentation')
102.
103. # get layout
104. layout1 = GetLayoutByName("Layout #1")
105.
106. # add view to a layout so it's visible in UI
107. AssignViewToLayout(view=spreadSheetView1, layout=layout1, hint=0)
108.
109. # Properties modified on integrateVariables1Display, This is for paraview 5.10.RC-1
110. #integrateVariables1Display.Assembly = ''
111.
112. # update the view to ensure updated data information
113. renderView1.Update()
114.
115. # update the view to ensure updated data information
116. spreadSheetView1.Update()
117.
118. # Properties modified on spreadSheetView1
119. spreadSheetView1.FieldAssociation = 'Cell Data'
120.
121. #=====
122. # addendum: following script captures some of the application
123. # state to faithfully reproduce the visualization during playback
124. #=====
125.
126. #-----
127. # saving layout sizes for layouts
128.
129. # layout/tab size in pixels
130. layout1.SetSize(1099, 747)
131.
132. #-----
133. # saving camera placements for views
134.
135. # current camera placement for renderView1
136. renderView1.CameraPosition = [0.0, -0.0005, 0.2]
137. renderView1.CameraFocalPoint = [0.0, -0.0005, 0.007]
138. renderView1.CameraParallelScale = 0.049
139. #-----
140. # uncomment the following to render all views
141. # RenderAllViews()
142. # alternatively, if you want to write images, you can use SaveScreenshot(...).

```

Script for interfacial area:

```
1. ##### import the simple module from the paraview
2. from paraview.simple import *
3. ##### disable automatic camera reset on 'Show'
4. paraview.simple._DisableFirstRenderCameraReset()
5.
6. # create a new 'OpenFOAMReader'
7. a3D_Case18_halfGeom_80_FlR_0_0033441_watrfoam =
   OpenFOAMReader(registrationName='3D_Case18_halfGeom_(80)_FlR_0_0033441_watr.foam',
   FileName='F:\CCS\3D_cases\H2O_Cases\halfGeom\3D_Case18_halfGeom_(80)_FlR_0_0033441_watr
   \3D_Case18_halfGeom_(80)_FlR_0_0033441_watr.foam')
8.
9. # get animation scene
10. animationScene1 = GetAnimationScene()
11.
12. # update animation scene based on data timesteps
13. animationScene1.UpdateAnimationUsingDataTimeSteps()
14.
15. # Properties modified on a3D_Case18_halfGeom_80_FlR_0_0033441_watrfoam
16. a3D_Case18_halfGeom_80_FlR_0_0033441_watrfoam.LabelSize = '64-bit'
17. a3D_Case18_halfGeom_80_FlR_0_0033441_watrfoam.MeshRegions = ['corrugatedwall']
18. a3D_Case18_halfGeom_80_FlR_0_0033441_watrfoam.CellArrays = ['alpha.water',
   'alpha.waterMean', 'alpha.waterPrime2Mean', 'p_rgh']
19.
20. # get active view
21. renderView1 = GetActiveViewOrCreate('RenderView')
22.
23. # show data in view
24. a3D_Case18_halfGeom_80_FlR_0_0033441_watrfoamDisplay =
   Show(a3D_Case18_halfGeom_80_FlR_0_0033441_watrfoam, renderView1, 'GeometryRepresentation')
25.
26. # trace defaults for the display properties.
27. a3D_Case18_halfGeom_80_FlR_0_0033441_watrfoamDisplay.Representation = 'Surface'
28.
29. # reset view to fit data
30. renderView1.ResetCamera()
31.
32. # Uncomment this if the parview version is 5.10.RC1 reset view to fit data
33. # renderView1.ResetCamera(True)
34.
35. # get the material library
36. materialLibrary1 = GetMaterialLibrary()
37.
38. # update the view to ensure updated data information
39. renderView1.Update()
40.
41. # set scalar coloring
42. ColorBy(a3D_Case18_halfGeom_80_FlR_0_0033441_watrfoamDisplay, ('POINTS', 'alpha.water'))
43.
44. # rescale color and/or opacity maps used to include current data range
45. a3D_Case18_halfGeom_80_FlR_0_0033441_watrfoamDisplay.RescaleTransferFunctionToDataRange(True
   , False)
46.
47. # show color bar/color legend
48. a3D_Case18_halfGeom_80_FlR_0_0033441_watrfoamDisplay.SetScalarBarVisibility(renderView1,
   True)
49.
50. # get color transfer function/color map for 'alphawater'
51. alphawaterLUT = GetColorTransferFunction('alphawater')
52.
53. # get opacity transfer function/opacity map for 'alphawater'
54. alphawaterPWF = GetOpacityTransferFunction('alphawater')
```

```

55.
56. # Properties modified on animationScene1
57. animationScene1.AnimationTime = 9.0
58.
59. # get the time-keeper
60. timeKeeper1 = GetTimeKeeper()
61.
62. # create a new 'Threshold'
63. threshold1 = Threshold(registrationName='Threshold1',
    Input=a3D_Case18_halfGeom_80_FlR_0_0033441_watrfoam)
64.
65. '''
66. # Properties modified on threshold1 This for ParaView 5.10.RC-1
67. threshold1.LowerThreshold = 0.91
68. threshold1.UpperThreshold = 1.0
69. threshold1.UseContinuousCellRange = 1
70. threshold1.Invert = 1
71. '''
72. # Properties modified on threshold1 for paraview version 5.9.0-RC2
73. threshold1.ThresholdRange = [0.91, 1.0]
74. threshold1.Invert = 1
75.
76. # show data in view
77. threshold1Display = Show(threshold1, renderView1, 'UnstructuredGridRepresentation')
78.
79. # trace defaults for the display properties.
80. threshold1Display.Representation = 'Surface'
81.
82. # hide data in view
83. Hide(a3D_Case18_halfGeom_80_FlR_0_0033441_watrfoam, renderView1)
84.
85. # show color bar/color legend
86. threshold1Display.SetScalarBarVisibility(renderView1, True)
87.
88. # update the view to ensure updated data information
89. renderView1.Update()
90.
91. # create a new 'Integrate Variables'
92. integrateVariables1 = IntegrateVariables(registrationName='IntegrateVariables1',
    Input=threshold1)
93. integrateVariables1.DivideCellDataByVolume = 1
94.
95. # Create a new 'SpreadSheet View'
96. spreadsheetView1 = CreateView('SpreadSheetView')
97. spreadsheetView1.ColumnToSort = ''
98. spreadsheetView1.BlockSize = 1024
99.
100. # show data in view
101. integrateVariables1Display = Show(integrateVariables1, spreadsheetView1,
    'SpreadSheetRepresentation')
102.
103. # get layout
104. layout1 = GetLayoutByName("Layout #1")
105.
106. # add view to a layout so it's visible in UI
107. AssignViewToLayout(view=spreadsheetView1, layout=layout1, hint=0)
108.
109. # Properties modified on integrateVariables1Display, This is for paraview 5.10.RC-1
110. #integrateVariables1Display.Assembly = ''
111.
112. # update the view to ensure updated data information
113. renderView1.Update()
114.
115. # update the view to ensure updated data information

```



```
116. spreadsheetView1.Update()
117.
118. # Properties modified on spreadsheetView1
119. spreadsheetView1.FieldAssociation = 'Cell Data'
120.
121. #=====
122. # addendum: following script captures some of the application
123. # state to faithfully reproduce the visualization during playback
124. #=====
125.
126. #-----
127. # saving layout sizes for layouts
128.
129. # layout/tab size in pixels
130. layout1.SetSize(1099, 747)
131.
132. #-----
133. # saving camera placements for views
134.
135. # current camera placement for renderView1
136. renderView1.CameraPosition = [0.0, -0.0005, 0.2]
137. renderView1.CameraFocalPoint = [0.0, -0.0005, 0.007]
138. renderView1.CameraParallelScale = 0.049
139. #-----
140. # uncomment the following to render all views
141. # RenderAllViews()
142. # alternatively, if you want to write images, you can use SaveScreenshot(...).
```